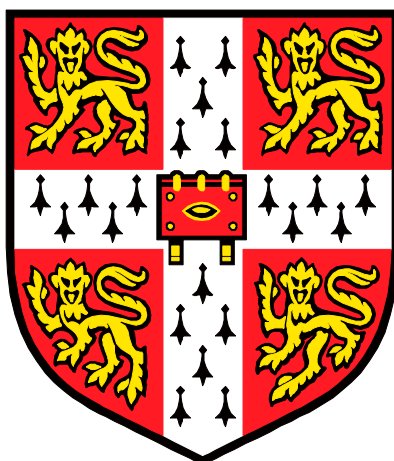


**Dynamics of liquids in porous media:  
Investigating competitive adsorption using  
NMR relaxometry**



University of Cambridge

Department of Chemical Engineering and Biotechnology

Magnetic Resonance Research Centre

**Laura Catharina Maria Rozing**

Newnham College

This thesis is submitted for the degree of Doctor of Philosophy

November 2021



# Preface

The work presented in this dissertation was carried out in the Department of Chemical Engineering and Biotechnology at the University of Cambridge during the period between October 2017 and June 2021. This thesis is the result of my own work and includes nothing which is the outcome of work done in collaboration except where specifically indicated in the text. This dissertation has not been submitted previously in part or in whole to any university for degrees, diplomas or other qualifications. Finally, this thesis contains less than 65,000 words and less than 150 figures, including appendices, tables and equations.



## Summary

“Dynamics of liquids in porous media: Investigating competitive adsorption using NMR relaxometry” – Laura Catharina Maria Rozing

The work presented in this thesis has been focused towards the development of NMR relaxometry methods to investigate competitive adsorption and microphase separation of liquid mixtures imbibed within porous media. The work was done on three different mesoporous catalysts and catalyst supports, namely anatase titania,  $\gamma$ -alumina and silica. The main NMR relaxometry method that was applied was Fast Field Cycling (FFC) NMR, which has been shown to quantitatively probe surface-adsorbate interactions of liquids in porous media.

First, a model study of binary liquid mixtures imbibed within anatase titania and  $\gamma$ -alumina was performed to assess the applicability of FFC-NMR to multi-component systems, and to compare the FFC-NMR data with a high field NMR relaxometry method. In a semi-quantitative analysis, FFC-NMR was shown to provide clear, unambiguous results relating to the surface-adsorbate interactions of both the stronger and weaker interacting species within the liquid mixtures. The high field NMR relaxometry results were more ambiguous, and therefore more open to misinterpretation.

In the following chapters, a theoretical modelling approach was developed to quantitatively describe the interactions of short, linear alcohols with an anatase titania support. The optimized modelling approach was applied to alcohol-water mixtures within the same porous medium, and showed an increased level of microphase separation for aqueous solutions with longer alcohols as well as tetrahydrofuran. This effect was shown not to depend on the bulk miscibility of the mixture, but rather on the surface-adsorbate interaction strength of the weaker interacting species.

The competitive adsorption of ethanol-water mixtures imbibed within silica supports was also studied, initially through fixed field  $T_1 - T_2$  correlation experiments, and subsequently through FFC-NMR methods. Due to overlapping relaxation environments, it was necessary to implement an advanced FFC-NMR pulse sequence with  $T_2$ -encoding. The low field NMR relaxometry experiments and FFC-NMR dispersion profiles were in agreement with one another and found that the form of microphase separation of ethanol-water mixtures depends on the properties of the silica support, thereby explaining a discrepancy in the literature and providing a quantitative analysis of the dynamics of these systems.



## Acknowledgements

First, I would like to express my gratitude to my supervisor, Professor Dame Lynn Gladden. Her incredible insight into the bigger picture and how to contextualise research has truly helped me to bring this PhD together. I would also like to thank Mick Mantle and Andy Sederman for their expertise, advice and suggestions on how to improve my work, which was invaluable to create a complete story.

I also wish to thank everyone at the MRRC, and in particular Jordan Ward-Williams, for mentoring me and teaching me all about FFC-NMR. I am very grateful for the other members of our little FFC-NMR team, Callum Penrose and Julian Beckmann, with whom I have had many useful discussions. Special thanks go to Gemma Siddall, who has always been there for me in scientific or emotional crisis. I am very grateful to have made such a great friend in the lab, and will always remember our walks.

I would not have been able to do most of the experiments in my thesis without Stelar, who created the FFC-NMR relaxometer I have used for nearly four years. I extend my gratitude to Matteo Polello, who came to our rescue many times, and taught me all about the FFC-NMR hardware. Of course, I would also like to thank Shell for their sponsorship. Without their funding I would not have been able to do this PhD, and I look forward to seeing them develop FFC-NMR within Shell.

To my friends, whether they are in Cambridge or back at home in the Netherlands, thank you for all your support. A special shout out must go to my friends at Newnham College. Writing most of my PhD thesis in the presence of friends who understand exactly what I was going through made the process much more manageable, and definitely much more enjoyable.

Finally, I would like to thank my family. My parents have taught me that I can do anything as long as I put my mind to it, but I could not have done this without their unconditional love and support. Mayke, my big sister, you inspire me every day, and Wouter, you challenge me and taught me to stand up for myself. Grandma, your words have encouraged me to push myself, especially when things get hard. They will never be forgotten. Dennis, I don't know what I would do without you. The past few years have been exciting and adventurous, as well as stressful and hard, and I am infinitely happy that now, at the end of it, we are finally together.



# Table of contents

1. Introduction.....	1
1.1 Background and objectives .....	1
1.2 Outline of the thesis.....	3
References .....	4
2. Theory of Nuclear Magnetic Resonance.....	7
2.1 Introduction .....	7
2.2 Basic principles of NMR.....	7
2.2.1 Nuclear spin .....	7
2.2.2 The vector model .....	8
2.2.3 The rotating frame.....	9
2.2.4 Signal detection and processing.....	10
2.2.5 Chemical shift .....	11
2.2.6 Scalar coupling.....	12
2.3 Nuclear relaxation: basics and experimental.....	12
2.3.1 Spin-lattice relaxation .....	12
2.3.2 Spin-spin relaxation .....	14
2.3.3 $T_1 - T_2$ correlation experiments.....	15
2.3.4 Data processing.....	16
2.3.5 Sources of relaxation.....	17
2.3.6 Relaxation in porous media .....	18
2.3.6.1 The two-phase fast exchange model .....	18
2.3.6.2 Internal gradient effects .....	19
2.4 Nuclear relaxation: a theoretical approach.....	20
2.4.1 The autocorrelation function.....	21
2.4.2 The spectral density function .....	22
2.4.3 Bloembergen, Purcell and Pound (BPP) theory.....	24
2.4.4 Intermolecular relaxation .....	25
2.4.5 Combining relaxation mechanisms.....	26
2.4.6 Fast Field Cycling NMR.....	26

2.4.7	Summary .....	28
2.5	Molecular diffusion: Pulsed Field Gradient NMR .....	29
2.5.1	Pulse Gradient Spin Echo .....	29
2.5.2	Pulse Gradient Stimulated Echo .....	30
2.5.3	Alternating Pulse Gradient Stimulated Echo .....	31
	References .....	32
3.	NMR relaxometry methods to investigate liquids and liquid mixtures imbibed within mesoporous media .....	37
3.1	Introduction .....	37
3.2	NMR relaxation methods for porous media investigations.....	38
3.2.1	The spin–lattice interaction parameter ( $T_{1,bulk}/T_{1,pore}$ ratio) .....	38
3.2.2	$T_1 - T_2$ correlation experiments .....	41
3.2.3	FFC-NMR .....	45
3.3	Liquid mixtures .....	50
3.3.1	Bulk liquid mixtures .....	50
3.3.2	Confined liquid mixtures and microphase separation.....	52
3.4	Conclusions and outlook .....	55
	References .....	57
4.	FFC-NMR of binary liquid mixtures: a case study of THF-water and THF-decane mixtures imbibed within anatase titania and $\gamma$ -alumina.....	69
4.1	Introduction .....	69
4.2	Materials and methods .....	70
4.2.1	Sample preparation .....	70
4.2.2	FFC-NMR and processing .....	70
4.2.3	Fixed field NMR methods .....	71
4.2.4	Composition analysis .....	72
4.3	FFC-NMR results.....	75
4.3.1	Surface composition.....	77
4.3.1.1	Filling factor analysis.....	78
4.3.2	Surface dynamics .....	80
4.3.2.1	Power law analysis.....	81

4.4	Fixed field NMR relaxometry results.....	84
4.4.1	Bulk liquids - $T_{1,bulk}$ .....	85
4.4.2	Imbibed liquids - $T_{1,pore}$ .....	85
4.4.3	Bulk/imbibed ratio - $\eta$ .....	88
4.5	Conclusions and outlook .....	90
	References .....	92
5.	Quantitative dynamics of alcohols imbibed within anatase titania.....	97
5.1	Introduction .....	97
5.2	Materials and methods .....	98
5.2.1	Sample preparation .....	98
5.2.2	FFC-NMR methods .....	98
5.2.2.1	Variable temperature experiments .....	99
5.2.3	Computational methods .....	99
5.2.4	Pulsed Field Gradient NMR experiments .....	99
5.3	Results .....	100
5.3.1	$^1\text{H}$ NMR dispersion profiles of alcohols imbibed within anatase titania.....	100
5.3.2	$^1\text{H}$ NMR dispersion profiles of methanol-d and methanol-d3 .....	101
5.4	Theoretical models for FFC-NMR.....	102
5.4.1	Intermolecular relaxation mechanisms .....	104
5.4.1.1	Korb model .....	104
5.4.1.2	$3\tau$ model.....	105
5.4.2	Intramolecular relaxation mechanisms .....	105
5.4.2.1	Reorientations mediated by translational diffusion .....	105
5.4.2.2	Protic model.....	107
5.4.3	Temperature dependent relaxation.....	107
5.4.3.1	Variable temperature experiments results.....	109
5.4.3.1.1	Methanol-d imbibed within anatase titania .....	110
5.4.4	High field relaxation .....	111
5.4.5	Summary .....	112
5.5	RMTD modelling .....	114
5.5.1	Theory and background .....	114
5.5.2	Fitting expressions and parameters .....	117

5.5.2.1	Distance to the surface $\delta$ .....	119
5.5.2.2	Diffusion coefficient $D$ .....	120
5.5.3	Modelling results .....	121
5.5.3.1	Comparison with THF imbibed within anatase titania .....	125
5.6	Comparison with the Korb model .....	126
5.7	Conclusions and outlook .....	128
	References .....	129
6.	Microphase separation of alcohol-water mixtures imbibed within anatase titania.....	133
6.1	Introduction .....	133
6.2	Adaptation of the RMTD model to mixtures .....	135
6.3	Experimental .....	139
6.3.1	Composition analysis .....	139
6.4	Results and discussion.....	141
6.4.1	FFC-NMR dispersion profiles .....	141
6.4.2	RMTD modelling.....	145
6.4.2.1	Effect of the diffusion coefficient .....	146
6.4.2.2	$N_S/N \times \tau_A$ initial analysis.....	150
6.4.2.3	$N_S/N \times \tau_A$ fits.....	152
6.4.2.4	Estimating $N_S/N$ and $\tau_A$ .....	154
6.5	Conclusions and outlook .....	156
	References .....	158
7.	Competitive adsorption of ethanol-water mixtures imbibed within mesoporous silicas.	
	Part I: a fixed field relaxometry study .....	161
7.1	Introduction .....	161
7.2	Experimental .....	163
7.2.1	Materials .....	163
7.2.2	NMR relaxometry experiments.....	164
7.3	Results and discussion.....	165
7.3.1	High field NMR relaxometry results .....	165
7.3.2	Low field NMR relaxometry results .....	168
7.3.2.1	Rehydroxylated silicas .....	171

7.3.3	Comparison between high and low field NMR relaxometry .....	172
7.4	Conclusions and outlook .....	175
	References .....	177
8.	Optimization of a FFC-NMR pulse sequence with CPMG-acquisition for enhanced resolution through $T_2$ -encoding .....	179
8.1	Introduction .....	179
8.2	Background and literature review .....	180
8.2.1	Applications .....	181
8.2.2	Field noise effects .....	181
8.3	Aims and objectives .....	182
8.4	Experimental .....	183
8.4.1	Materials .....	183
8.4.2	FFC-NMR experimental parameters.....	183
8.4.3	NMR relaxation experiments on a permanent 23 MHz magnet .....	184
8.5	Results and discussion.....	184
8.5.1	Acquisition field fluctuations.....	184
8.5.2	Tuning and matching stability .....	185
8.5.3	The effect of the echo delay .....	186
8.5.4	Comparison of $T_2$ with a permanent magnet .....	187
8.5.5	$T_2$ NMRD profiles analysis.....	190
8.5.6	$T_1$ NMRD profiles analysis.....	191
8.6	Conclusions and outlook .....	193
	References .....	195
9.	Competitive adsorption of ethanol-water mixtures imbibed within mesoporous silicas. Part II: correlation times through FFC-NMR relaxometry .....	199
9.1	Introduction .....	199
9.2	Experimental .....	200
9.3	Results and discussion.....	201
9.3.1	FID-FFC-NMR experiments.....	201
9.3.1.1	Pure liquids .....	201
9.3.1.2	Mixtures .....	202

9.3.2	CPMG-FFC-NMR experiments.....	204
9.3.2.1	Validation: a comparison of FID and CPMG acquisition.....	204
9.3.2.2	Mixture NMRD profiles .....	206
9.4	Modelling .....	207
9.5	Conclusions and outlook .....	212
	References .....	214
10.	Conclusions and future work .....	217
10.1	Conclusions .....	217
10.2	Future work .....	221
10.2.1	Different types of liquid mixtures.....	221
10.2.2	Different types of porous media .....	222
10.2.3	Development of FFC-NMR for liquids in porous media.....	223
	References .....	224
	Appendix A: THF-water and THF-decane mixture compositions .....	225

# 1. Introduction

## 1.1 Background and objectives

Adsorption of liquids confined within mesoporous media is essential to optimizing a wide range of industrial applications, such as chemical catalysis, oil recovery, separation technologies and drug delivery. Optimization of these processes is crucial for chemical industry, to reduce costs and to mitigate negative side-effects, such as toxic gas emissions, hazardous waste and high water consumption. In order to improve and develop these processes, the porous media must be optimized to the adsorbed liquid and to the specific application. Over the last several decades, the adsorption of pure liquids in porous media has been heavily investigated, and as such, a good fundamental understanding has been established<sup>1-4</sup>. However, adsorption studies of liquid mixtures in porous media are scarce.

Many industrial processes will encounter more than one liquid species. For example, in catalysis, there will be a reagent and a product, or there can be multiple reagents. For separation technologies, multiple liquid species are obviously involved. Some liquid mixtures that are fully miscible in the bulk state, have been shown to phase-segregate upon confinement in a mesoporous medium. This phenomenon is known as microphase separation, and can have significant consequences for the efficiency of catalytic reactions or mixture separations<sup>5-8</sup>. Unfortunately, the complexity of adsorption problems increases considerably when liquid mixtures and competitive adsorption are studied. For example, not all techniques that investigate adsorption may be able to distinguish molecular species. Additionally, the effect that liquids may have on each other, even in the bulk state, must be taken into account when competitive adsorption is investigated. This means that both the acquisition and the interpretation of data is much more complex compared to the confinement of pure liquids. The main objective of this thesis is to develop methods to gain insight into the competitive adsorption and microphase separation of liquid mixtures imbibed within mesoporous media.

Nuclear magnetic resonance (NMR) has been shown to be a powerful, non-invasive tool to investigate the structure and dynamics of porous media systems. Notably, NMR relaxometry can be used to probe the dynamics of confined liquids and the surface-adsorbate interaction strength<sup>9-11</sup>. Most NMR relaxometry experiments are performed at a high magnetic field. At high field, the chemical resolution is generally very good, which is important for structural

investigations. However, in terms of dynamics, at high field many different processes contribute to the relaxation behaviour. Therefore it is not always possible to distinguish adsorption processes from other chemical processes, which may lead to a misinterpretation of the data. As a result, the development of NMR relaxometry methods is favouring low field experiments<sup>12</sup>. At low field, slower processes are observed, such as surface-adsorbate interactions, and therefore it is easier to unambiguously interpret the data. However, even at low field, the relaxation behaviour of a liquid imbibed within a porous medium is determined by many factors, such as the type of porous support and the presence of paramagnetic impurities on the support, the properties of the imbibed liquid, and the interactions between the support and the liquid. As will be shown, fixed field NMR relaxometry methods often struggle to eliminate effects from the porous support and the liquid, in order to exclusively investigate surface-adsorbate interactions. Thus, the comparison of different samples within a study is not straightforward.

NMR relaxometry measurements can also be obtained at a large range of magnetic fields, using a technique called Fast Field Cycling (FFC) NMR<sup>11,13</sup>. By obtaining relaxation times across a large magnetic field range and therefore across a large range of timescales of molecular motions, it is possible to model the adsorption dynamics. These models provide fully quantitative information about the dynamics in the form of correlation times, which are easily comparable between different samples. FFC-NMR has been successfully applied to porous media systems and the extracted correlation times have been shown to correlate with the surface-adsorbate interaction strength<sup>14</sup>. Due to its high sensitivity to surface-adsorbate interactions, FFC-NMR has great potential in clarifying competitive adsorption and microphase separation processes.

In this thesis, FFC-NMR and other NMR relaxometry methods are developed to gain a deeper understanding of competitive adsorption and microphase separation of liquid mixtures imbibed within porous media. The work is carried out on several types of mesoporous media, namely  $\gamma$ -alumina, anatase titania and silica, which are all widely used catalyst supports<sup>15-17</sup>. Different porous media are used to assess the applicability of the methods to diverse systems, and to present a generalized approach to obtain maximum information from FFC-NMR experiments in a consistent and accurate manner.

## 1.2 Outline of the thesis

Chapter 2 provides an introduction to the theory of NMR and the techniques that are used in this thesis.

Chapter 3 highlights several NMR relaxometry methods and their application to the adsorption of liquids imbibed within porous media. Additionally, the current knowledge on competitive adsorption and microphase separation of confined liquid mixtures is reviewed.

Chapter 4 applies FFC-NMR to model systems of tetrahydrofuran (THF)-water and THF-decane mixtures imbibed within anatase titania and  $\gamma$ -alumina. The advantages of FFC-NMR over fixed field NMR relaxation techniques are discussed, as well as the limitations to FFC-NMR in measuring liquid mixtures in porous media.

Chapter 5 introduces theoretical modelling of  $^1\text{H}$  NMRD profiles. Based on the FFC-NMR data of a range of short, linear alcohols imbibed within anatase titania, several models are described. Following variable temperature experiments, the most appropriate model is identified and applied.

Chapter 6 combines the knowledge from chapters 4 and 5 to investigate the microphase separation of alcohol-water mixtures imbibed within anatase titania.

Chapter 7 introduces a different chemical system, namely ethanol-water mixtures imbibed within porous silicas. Fixed field NMR relaxometry experiments are applied to obtain information about competitive adsorption, which are then compared with the literature.

Chapter 8 demonstrates the optimization of a FFC-NMR pulse sequence with CPMG acquisition, and discusses which limitations should be taken into account.

Chapter 9 connects the knowledge from chapters 4–9, as the microphase separation of ethanol-water mixtures in porous silicas is investigated through the modelling of  $^1\text{H}$  NMRD profiles obtained by (CPMG-)FFC-NMR.

Chapter 10 summarises the main conclusions of the work, and suggests directions for extensions to this work.

## References

1. Granick, S. Motions and relaxations of confined liquids. *Science* **253**, 1374–1379 (1991).
2. Richert, R. Dynamics of nanoconfined supercooled liquids. *Annu. Rev. Phys. Chem.* **62**, 65–84 (2011).
3. Christenson, H. K. Confinement effects on freezing and melting. *J. Phys. Condens. Matter* **13**, 95–133 (2001).
4. Huber, P. Soft matter in hard confinement: phase transition thermodynamics, structure, texture, diffusion and flow in nanoporous media. *J. Phys. Condens. Matter* **27**, 103102 (2015).
5. Chen, W. Phase separation of binary nonadditive hard sphere fluid mixture confined in random porous media. *J. Chem. Phys.* **139**, 154712 (2013).
6. Swenson, J., Elamin, K., Chen, G., Lohstroh, W. & Sakai, V. G. Anomalous dynamics of aqueous solutions of di-propylene glycol methylether confined in MCM-41 by quasielastic neutron scattering. *J. Chem. Phys.* **141**, 214501 (2014).
7. Elamin, K., Jansson, H. & Swenson, J. Dynamics of aqueous binary glass-formers confined in MCM-41. *Phys. Chem. Chem. Phys.* **17**, 12978–12987 (2015).
8. Muthulakshmi, T., Dutta, D., Maheshwari, P. & Pujari, P. K. Evidence for confinement induced phase separation in ethanol-water mixture: a positron annihilation study. *J. Phys. Condens. Matter* **30**, 025001 (2018).
9. Gladden, L. F. & Mitchell, J. Measuring adsorption, diffusion and flow in chemical engineering: applications of magnetic resonance to porous media. *New J. Phys.* **13**, 35001 (2011).
10. D’Agostino, C., Mitchell, J., Mantle, M. D. & Gladden, L. F. Interpretation of NMR relaxation as a tool for characterising the adsorption strength of liquids inside porous materials. *Chem. - A Eur. J.* **20**, 13009–13015 (2014).
11. Korb, J.-P. Multiscale nuclear magnetic relaxation dispersion of complex liquids in bulk and confinement. *Prog. Nucl. Magn. Reson. Spectrosc.* **104**, 12–55 (2018).

12. Mitchell, J., Gladden, L. F., Chandrasekera, T. C. & Fordham, E. J. Low-field permanent magnets for industrial process and quality control. *Prog. Nucl. Magn. Reson. Spectrosc.* **76**, 1–60 (2014).
13. Kimmich, R. & Anoardo, E. Field-cycling NMR relaxometry. *Prog. Nucl. Magn. Reson. Spectrosc.* **44**, 257–320 (2004).
14. Ward-Williams, J., Korb, J.-P., Rozing, L., Sederman, A. J., Mantle, M. D., Gladden, L. F. Characterizing solid-liquid interactions in a mesoporous catalyst support using variable-temperature Fast Field Cycling NMR. *J. Phys. Chem. C* **125**, 8767–8778 (2021).
15. Martínez, A., López, C., Márquez, F. & Díaz, I. Fischer-Tropsch synthesis of hydrocarbons over mesoporous Co/SBA-15 catalysts: the influence of metal loading, cobalt precursor, and promoters. *J. Catal.* **220**, 486–499 (2003).
16. Trueba, M. & Trasatti, S. P.  $\gamma$ -Alumina as a support for catalysts: a review of fundamental aspects. *Eur. J. Inorg. Chem.* **17**, 3393–3403 (2005).
17. Hadjiivanov, K. I. & Klissurski, D. G. Surface chemistry of titania (anatase) and titania-supported catalysts. *Chem. Soc. Rev.* **25**, 61–69 (1996).



## 2. Theory of Nuclear Magnetic Resonance

### 2.1 Introduction

In this chapter, the main principles behind Nuclear Magnetic Resonance (NMR), NMR relaxation and NMR diffusion, are outlined, in order to provide understanding and context to the experiments and results in this thesis. While all core concepts relevant to the thesis are discussed, more detailed explanations can be found in texts by Abragam<sup>1</sup>, Keeler<sup>2</sup>, and Levitt<sup>3</sup>, on which the following discussion is based.

### 2.2 Basic principles of NMR

#### 2.2.1 Nuclear spin

NMR starts with nuclear spin, a fundamental property of every nucleus, that can be characterized by a nuclear spin quantum number,  $I$ . In general, the value of the spin quantum number can be  $I \geq 0$ , with half-integer steps, however in this thesis, NMR experiments are only performed on  $^1\text{H}$ , which has a spin quantum number  $I = 1/2$ . Therefore we will only consider this value of  $I$ .

Each spin is associated with  $(2I + 1)$  different spin states, which are characterized by another quantum number,  $m_I$ . This quantum number has values between  $-I$  and  $I$  in integer steps. For  $I = 1/2$ , this means that  $m_I$  can only hold the values  $-1/2$  and  $1/2$ . In the absence of a magnetic field, the spin states are degenerate. However, if a nucleus is in the presence of an external magnetic field, the so-called Zeeman interaction will give rise to different energy levels for each of the different spin states. The corresponding energy of each spin state is:

$$E_{m_I} = -\gamma\hbar B_0 m_I, \quad (2.1)$$

where  $\gamma$  is the gyromagnetic ratio of the nucleus ( $\gamma_{\text{H}} = 2.675 \times 10^8 \text{ rad T}^{-1} \text{ s}^{-1}$ ),  $\hbar$  is the reduced Planck's constant, and  $B_0$  is the magnetic field.

For a spin  $1/2$  system, the spin states are often denoted  $\alpha$  for  $m_I = 1/2$  (low energy, "spin down"), and  $\beta$  for  $m_I = -1/2$  (high energy, "spin up"). The  $\alpha$  and  $\beta$  spin states, in equilibrium, are populated following the Boltzmann distribution:

$$\frac{N_\alpha}{N_\beta} = \exp\left(\frac{\Delta E}{k_B T}\right), \quad (2.2)$$

where  $N_\alpha$  and  $N_\beta$  are the populations of the  $\alpha$  and  $\beta$  spin states respectively,  $\Delta E = -\gamma\hbar B_0$  is the energy difference between the spin states,  $k_B$  is the Boltzmann constant, and  $T$  is the temperature. NMR occurs when the equilibrium is disturbed and the spins transition from one spin state to another.

### 2.2.2 The vector model

While the transition between nuclear spin states is a quantum mechanical process, a classical description in the form of the Bloch vector model is often used to clarify and justify NMR concepts.

Each nuclear spin leads to a microscopic magnetic moment. In the presence of an external magnetic field,  $B_0$ , the magnetic moments of the  $\alpha$ -spins align with  $B_0$ , and the  $\beta$ -spins magnetic moments oppose  $B_0$ . Following the Boltzmann distribution, this means that there is an equilibrium net magnetization,  $M_0$ , in the direction of  $B_0$ .

The external magnetic field causes a magnetic torque on each magnetic moment:

$$\frac{d\mathbf{M}}{dt} = -\mathbf{M} \times \gamma\mathbf{B}. \quad (2.3)$$

In equation (2.3), the magnetization,  $\mathbf{M}$ , and the external field,  $\mathbf{B}$ , are expressed in vector notation for generality. Because the equilibrium net magnetization,  $M_0$ , is aligned with  $B_0$ , the equilibrium net torque is equal to zero. However, in NMR, a second magnetic field,  $B_1$ , can be applied perpendicular to  $B_0$ .  $B_1$  is significantly weaker than  $B_0$ , and it is applied through a short (<1ms) electromagnetic pulse. At the end of the  $B_1$  pulse, the magnetization is rotated away from equilibrium. This results in a change in torque, which gives rise to a precession of the spins about  $B_0$ , which we call Larmor precession. The Larmor precession frequency,  $\omega_0$ , is proportional to the energy difference between spin states, see equation (2.1). We can relate energy to angular frequency via:

$$E = \hbar\omega, \quad (2.4)$$

from which the Larmor precession frequency can be described as follows:

$$\omega_0 = -\gamma B_0. \quad (2.5)$$

Equally, the Larmor frequency of the  $B_1$  field can be determined. For this pulse, the frequency falls within the radiofrequency (RF) part of the electromagnetic spectrum, and therefore  $B_1$  pulses are often referred to as RF pulses.

### 2.2.3 The rotating frame

Describing the effects of  $B_0$  and  $B_1$  in a stationary frame of reference quickly becomes complex. Therefore, we often apply a frame of reference that is rotating with an angular frequency  $\omega_r$  instead. This means that nuclear spins appear to precess at an effective Larmor frequency,  $\Omega$ :

$$\Omega = \omega_0 - \omega_r. \quad (2.6)$$

Nuclear spins precessing at the frequency of the rotating frame appear to be stationary. These spins are ‘on resonance’.  $\Omega$  is also known as the offset and corresponds to an apparent magnetic field  $\Delta B = -\Omega/\gamma$ .

The  $B_1$  field is generally applied as linearly oscillating RF pulses. It is convenient to decompose the  $B_1$  field into two counter-rotating fields, in order to describe them in the rotating frame. One of the fields is rotating at the Larmor frequency,  $\omega_0$ , and the second is rotating in the opposite direction at the Larmor frequency,  $-\omega_0$ . The latter field has a negligible effect on the magnetization and will therefore be ignored. When spins are on resonance, the effect of the first field, precessing at  $\omega_0$ , is substantial compared to the apparent magnetic field  $\Delta B$ . Therefore RF pulses, even if they are weak, can be used to manipulate spins, as long as they are (nearly) on resonance.

The degree of rotation,  $\theta$ , otherwise known as the flip angle, can be controlled by choosing a desired  $B_1$  field strength and pulse duration,  $t_p$ :

$$\theta = \omega_1 t_p. \quad (2.7)$$

Often in NMR, the field strength and pulse duration will be optimized such that  $\theta$  is equal to  $90^\circ$  or  $\pi/2$ , or  $180^\circ$  or  $\pi$ , depending on the pulse sequence. Most commonly, the  $B_1$  field strength is kept constant, such that the duration for a  $180^\circ$  pulse is twice as long as for a  $90^\circ$  pulse.

## 2.2.4 Signal detection and processing

The precession of the magnetization, after it has been perturbed by a RF pulse, can be decomposed into a component aligned with the  $B_0$  field, conventionally the z-direction, and a component perpendicular to the  $B_0$  field, in the xy-plane. The magnetization in the xy-plane, also known as transverse magnetization, precesses at the effective Larmor frequency, which induces an oscillatory electromotive force. Detection coils in the xy-plane measure this as a current, for which the amplitude corresponds to the transverse magnetization. The frequency of the current corresponds to the effective Larmor frequency or offset of the spins in the sample. The current is digitized, which provides the NMR signal.

In order to measure the magnitude as well as the direction of precession, the x and y components of the transverse magnetization must be measured. Therefore, quadrature detection is applied. In quadrature detection, the current is mixed with locally generated reference fields, which are  $90^\circ$  out of phase with one another. As a result, the x and y components can be measured separately.

The time-domain NMR signal, also known as the Free Induction Decay (FID), consists of a real component (x-direction) and an imaginary component (y-direction). Larmor precession results in an oscillatory, sinusoid signal. As well as this oscillatory behaviour, the time-domain NMR signal decays exponentially due to relaxation effects that will be discussed in more detail in section 2.3. The result is a signal as shown in Figure 2.1a, which is then Fourier transformed to obtain a frequency-domain NMR spectrum.

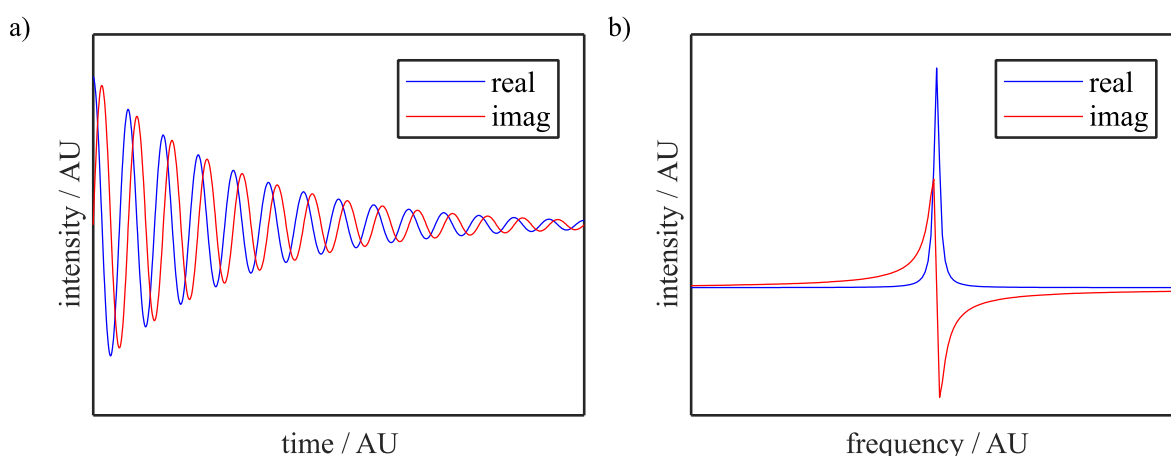


Figure 2.1: The real and imaginary NMR signal components in (a) the time domain, and (b) in the frequency domain after a Fourier transform.

As can be seen in Figure 2.1b, the real signal produces an adsorption lineshape, and the imaginary signal produces a dispersion lineshape. Because the adsorption lineshape is symmetric and narrower than the dispersion lineshape, customarily the real signal is reported. Hardware imperfections will often lead to phase errors, which means that the adsorption and dispersion lineshapes will be distorted. These artefacts can be amended by applying a simple phase correction to the complex signal.

### 2.2.5 Chemical shift

The peak position in Figure 2.1b is determined by the Larmor frequency of the nuclear spins in the sample, which in turn depends primarily on the external magnetic field strength, see equation (2.5). However, the Larmor frequency also depends on the local electronic structure of each individual spin. Electron clouds around the nucleus interact with the  $B_0$  field, effectively producing an opposing magnetic field. As a result, the nucleus is ‘shielded’ by the electron cloud, reducing the local magnetic field, which lowers the Larmor frequency. The shielding strength depends on the local electronic environment, and therefore the chemical environment. Indeed, NMR is sensitive enough to distinguish different chemical functionalities within the same molecule.

It is now clear that the Larmor frequency of each nuclear spin depends on the external magnetic field strength,  $B_0$ , and the local electronic, chemical environment. The level of electronic shielding can be measured independently of  $B_0$  by obtaining a reference Larmor frequency. From the Larmor frequencies of the reference species and the species of interest, the chemical shift,  $\delta$ , can be determined:

$$\delta = \frac{\nu - \nu_{\text{ref}}}{\nu_{\text{ref}}} \times 10^6, \quad (2.8)$$

where  $\nu$  is the Larmor frequency of the species of interest, and  $\nu_{\text{ref}}$  is the Larmor frequency of the reference species, commonly tetramethylsilane (TMS). The unit for chemical shift is parts per million (ppm). For example, in  $^1\text{H}$  NMR, the chemical shift ranges between approximately 0–10 ppm. For  $^{13}\text{C}$  NMR, the chemical shift can go as high as 200 ppm.

### 2.2.6 Scalar coupling

Scalar coupling, also known as J-coupling, is an effect due to the indirect intramolecular interactions between neighbouring nuclear spins through chemical bonds. The orientation of the magnetic moment of one nuclear spin polarizes the surrounding electrons. The polarization of the electrons is transmitted through the molecule, extending over two or three chemical bonds, and affects the local magnetic field of other spin active nuclei. This effect occurs between like spins (homonuclear coupling) or unlike spins (heteronuclear spins). The Larmor frequencies of these spins observe small adjustments, resulting in the NMR signal to be split into multiple peaks. The number and distance between the peaks depend on the specific interactions between nuclei, and how many nuclei are involved. This means that scalar coupling can be used to provide information about the molecular structure of the investigated sample.

## 2.3 Nuclear relaxation: basics and experimental

Relaxation is the process of spins returning to their equilibrium state after a perturbation, e.g. a RF pulse. The relaxation process can be observed in two ways. The first is the restoration of the magnetization aligned with  $B_0$  (z-magnetization), this is spin-lattice ( $T_1$ ) relaxation. The second is the loss of magnetization in the xy plane, also known as spin-spin ( $T_2$ ) relaxation. In this section, the basics of these types of relaxation will be discussed, as well as measurement techniques, sources of relaxation, relaxation mechanisms, Fast Field Cycling (FFC) NMR, and relaxation in porous media.

### 2.3.1 Spin-lattice relaxation

Spin-lattice, or  $T_1$  relaxation, is the first relaxation process that will be discussed. After a perturbation of the  $B_0$  field, for example a RF pulse, the magnetization is not aligned with the  $B_0$  field anymore, and thus the z-component of the magnetization is reduced. In this case, the energy of the system is relatively high, and therefore the system will return to thermal equilibrium, where the magnetization is aligned with the  $B_0$  field again. The return to equilibrium requires the excess energy to be transferred to their surroundings, which is a stimulated process following local fluctuations in the magnetic field. Often, these local fluctuations are caused by reorientations of the magnetic moments of the nuclear spins following molecular motions.

The most efficient relaxation occurs when the correlation time of the reorientations,  $\tau_c$ , is the inverse of the Larmor frequency, i.e.:

$$\omega_0\tau_c = 1. \quad (2.9)$$

The  $T_1$  relaxation time describes how fast the spin-lattice relaxation takes place, and is generally determined through an inversion recovery experiment, or a saturation recovery experiment. In this thesis, only the inversion recovery experiment is used, and therefore we will focus on this pulse sequence, which is shown in Figure 2.2. In the inversion recovery experiment, first a  $180^\circ$  or  $\pi$  pulse is used to invert the magnetization, such that the magnetization is directed along the  $-z$  direction. A delay time,  $\tau$ , allows the system to recover towards thermal equilibrium. Crucially, the value for  $\tau$  is varied, so that the recovery of  $z$ -magnetization can be measured as a function of time. Finally, a  $90^\circ$  or  $\pi/2$  pulse rotates the magnetization in the transverse plane for detection.

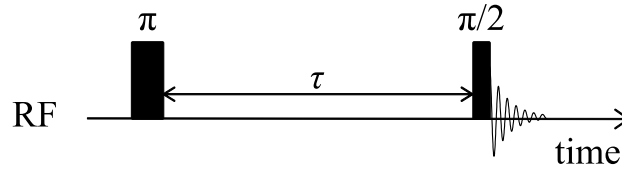


Figure 2.2: The inversion recovery pulse sequence: a radiofrequency (RF)  $\pi$  pulse inverts the magnetization. After a time  $\tau$  the magnetization is rotated into the  $xy$  plane and the FID is recorded. In order to measure the  $T_1$  recovery of the magnetization over time, this experiment is repeated for varying times  $\tau$ .

The time dependence of the longitudinal magnetization,  $M_z$ , can be described according to the Bloch vector model:

$$\frac{dM_z}{dt} = \frac{M_z - M_0}{T_1}, \quad (2.10)$$

where  $M_0$  is the magnetization in equilibrium. In the inversion recovery experiment, the magnetization is first inverted such that  $M_z(0) = -M_0$ . Based on this condition, equation (2.10) can be solved, and provides the time dependence of the magnetization in the inversion recovery experiment:

$$M_z(t) = M_0 \left( 1 - 2 \exp\left(-\frac{t}{T_1}\right) \right). \quad (2.11)$$

Therefore, the  $T_1$  can be extracted through a simple exponential fit.

### 2.3.2 Spin-spin relaxation

Spin-spin or  $T_2$  relaxation is the process of transverse magnetization returning to thermal equilibrium. One part of  $T_2$  relaxation is identical to  $T_1$  relaxation; as the magnetization returns to align with the  $B_0$  field, the magnetization in the xy plane is reduced. However, another process adds to spin-spin relaxation, namely the dephasing of spins. Because of thermal motion, molecules tumble. This creates small variations in the  $B_0$  field across the sample, the Larmor frequency of each nuclear spin becomes dependent on the adjacent spins. In other words, the frequency of some spins is somewhat higher than the average Larmor frequency, and other spins precess at a somewhat lower frequency. As a result, the net transverse magnetization dephases and is reduced according to the Bloch vector model:

$$\frac{dM_{xy}}{dt} = -\frac{M_{xy}}{T_2}, \quad (2.12)$$

with the general solution:

$$M_{xy}(t) = M_{xy}(0) \exp\left(-\frac{t}{T_2}\right). \quad (2.13)$$

Spin-spin relaxation is a thermal, random process, and as such cannot be removed. However, inhomogeneity in the  $B_0$  field or internal field gradients can also contribute to  $T_2$  relaxation. In this case, the observed transverse relaxation time,  $T_2^*$ , can be described as follows:

$$\frac{1}{T_2^*} = \frac{1}{T_2} + \frac{1}{T_{2(\Delta B)}}, \quad (2.14)$$

where  $T_{2(\Delta B)}$  is the  $T_2$  relaxation time due to magnetic field inhomogeneities and gradients. The observed relaxation time is also illustrated in the peak width in NMR spectra; the full width half maximum (FWHM) of the adsorption lineshape corresponds to  $1/\pi T_2^*$ . For example, a less homogeneous  $B_0$  field results in a shorter  $T_2^*$  and a broader NMR spectrum.

As the magnetic field inhomogeneities and internal field gradients are time-independent, spin dephasing as a result of these can be corrected using a spin-echo, as first introduced by Hahn<sup>4</sup> and modified by Carr and Purcell<sup>5</sup>. In the spin-echo by Carr and Purcell, first a  $90^\circ$  pulse is applied along the x-axis to align the magnetization with the y-axis. After a time  $\tau$ , the spins will have started to dephase in the transverse plane. A  $180^\circ$  pulse along the y-axis inverts the spins in the xy plane, however the spins retain their original precession frequency and direction.

This means that after another time  $\tau$ , the magnetization is refocused. As mentioned above, ‘true’  $T_2$  relaxation due to thermal motion is irreversible and will be the only source of  $T_2$  relaxation when using spin-echoes. As such, spin-echoes can be used to obtain the  $T_2$  relaxation time. As the time  $\tau$  is varied, the  $T_2$  decay can be measured as a function of time. In practice, this is done by looping spin-echoes with a fixed echo time,  $\delta$ . This pulse sequence is known as a Carr-Purcell-Meiboom-Gill (CPMG) sequence<sup>6</sup>, shown in Figure 2.3.

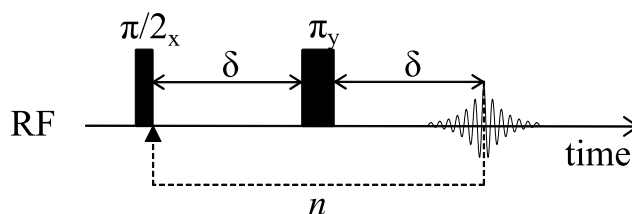


Figure 2.3: The CPMG pulse sequence: a  $\pi/2$  pulse along the  $x$  axis rotates the magnetization along the  $y$  axis. The magnetization is allowed to dephase for a time  $\delta$ , then flipped around the  $y$  axis and allowed to rephase for another time  $\delta$ . This experiment is repeated for  $n$  loops to measure the  $T_2$  decay.

There are two methods to acquire a CPMG decay. First, a full FID can be recorded after a varying number of  $n$  loops. The disadvantage of this method is that between time points, or number of loops, the magnetization has to return to equilibrium and therefore the sample has to be left for  $5 \times T_1$ , which increases the acquisition time for this experiment. The other method is to measure the maximum point of each echo. This means a full CPMG decay can be acquired in a single scan, hence the experiment is also known as a ‘one-shot’ CPMG experiment. The disadvantage of this method is that only one point is obtained for each echo, rather than the full FID, which means there is no spectral resolution. The acquired magnetization data can then be fitted to equation (2.13) to obtain the  $T_2$  relaxation time.

### 2.3.3 $T_1 - T_2$ correlation experiments

It is now clear what  $T_1$  and  $T_2$  relaxation is, and how we can obtain relaxation time constants for both types of relaxation. It is also possible to measure the  $T_1$  and  $T_2$  relaxation time constants in a single experiment. A two-dimensional (2D)  $T_1 - T_2$  correlation experiment is able to correlate the relaxation time constants, which can simplify distinguishing and assigning relaxation environments. Moreover, the  $T_1/T_2$  ratio can be extracted, which can be used as a metric for surface affinity<sup>7-9</sup>. The applications of  $T_1 - T_2$  correlation experiments will be discussed in more detail in chapter 3.

The pulse sequence for a  $T_1 - T_2$  correlation experiment consists of an inversion recovery sequence followed by acquisition using CPMG, see Figure 2.4<sup>10</sup>. If it is necessary to obtain chemical resolution, the conventional CPMG sequence can be used, however this results in an experimental with a long duration, as it is required to vary the  $T_1$  recovery time,  $\tau$ , as well as the number of echo loops,  $n$ . If the one-shot CPMG sequence is applied, the experimental time is significantly reduced, however the chemical resolution is lost.

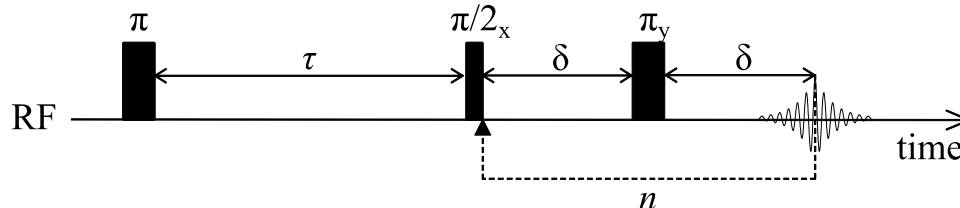


Figure 2.4: The pulse sequence for a  $T_1 - T_2$  correlation experiment: an inversion recovery sequence followed by CPMG acquisition. First a  $\pi$  pulse inverts the magnetization. After a time  $\tau$  the magnetization is rotated along the  $y$  axis. The magnetization is allowed to dephase for a time  $\delta$ , then flipped around the  $y$  axis and allowed to rephase for another time  $\delta$ . This experiment is repeated for varying times  $\tau$  and  $n$  loops to measure the  $T_1$  recovery and  $T_2$  decay respectively.

Many types of 2D NMR correlation experiments exist, such as diffusion- $T_2$  ( $D - T_2$ ) and  $T_2 - T_2$  correlation experiments, however in this thesis only  $T_1 - T_2$  correlation experiments are relevant.

### 2.3.4 Data processing

In the case that the number of relaxation environments is known, data processing is relatively simple. Each relaxation environment corresponds to a monoexponential fit according to equation (2.11) for  $T_1$  relaxation, and equation (2.13) for  $T_2$  relaxation. These equations are linear, and therefore  $n$  relaxation environments can be fitted to a multiexponential fit with  $n$  components.

However, it is common that the number of relaxation environments is not known *a priori*, or that the investigated system corresponds to a distribution of relaxation time constants. In these cases, an inverse Laplace transformation can be used to obtain a probability distribution function of  $T_1$  or  $T_2$ <sup>11,12</sup>. One-dimensional NMR data can be described in matrix form:

$$\mathbf{S} = \mathbf{K}\mathbf{F} + \mathbf{E}, \quad (2.15)$$

where  $\mathbf{S}$  is the NMR signal,  $\mathbf{K}$  is a matrix representing the expected relaxation behaviour,  $\mathbf{F}$  is the true relaxation time distribution, and  $\mathbf{E}$  is a matrix containing experimental noise.

The exponential kernel matrix is ill-conditioned, which means that the solution is sensitive to the experimental noise. To decrease the sensitivity to the signal-to-noise ratio, regularisation can be applied. Regularisation requires the distribution to be non-negative, limited, and continuous, which is assumed to be true for the majority of samples.

In this thesis, Tikhonov regularisation is used to obtain  $\mathbf{F}$ , which requires the minimization of the following expression<sup>13</sup>:

$$\|\mathbf{S} - \mathbf{KF}\|^2 + \alpha\|\mathbf{F}\|^2. \quad (2.16)$$

In this expression, the first term indicates if and how well  $\mathbf{F}$  represents the data. The second term is a penalty term. The smoothing parameter,  $\alpha$ , imposes a level of smoothing on the relaxation time distribution, and as such makes the solution less sensitive to the signal-to-noise ratio. If a too small value is chosen for  $\alpha$ , the noise will be fitted, which results in an unstable solution. However, if a too large  $\alpha$  is chosen, features of the relaxation time distribution may be lost, blurring the solution. Therefore, it is essential that  $\alpha$  is properly optimized. In this thesis, the in-house scripts for inverse Laplace transformations optimize  $\alpha$  using the generalised cross-validation (GCV) methods, which has been shown to provide reliable inversions of NMR data<sup>14,15</sup>.

The inverse Laplace transform described above can be extended to two-dimensional data. If the two dimensions are separable, the matrix equation can be adjusted to:

$$\mathbf{S} = \mathbf{K}_1\mathbf{F}\mathbf{K}_2^T + \mathbf{E}. \quad (2.17)$$

As such, Tikhonov regularisation requires the minimization of:

$$\|\mathbf{S} - \mathbf{K}_1\mathbf{F}\mathbf{K}_2^T\|^2 + \alpha\|\mathbf{F}\|^2. \quad (2.18)$$

### 2.3.5 Sources of relaxation

As was explained previously, relaxation occurs due to local magnetic field fluctuations, which are generally caused by molecular motions. The main sources of relaxation relevant to this thesis are dipolar interactions and paramagnetic interactions. While other sources of relaxation exist, for example quadrupolar coupling and chemical shift anisotropy, we will only discuss the relaxation sources relevant to this thesis.

Dipolar relaxation arises when two spins interact with one another. As the magnetic moment of one spin is reoriented with respect to the  $B_0$  field, this influences the local magnetic field of another spin. Equally, the reorientation of the magnetic moment of spin 2 will cause fluctuations in the local magnetic field surrounding spin 1, thereby causing relaxation. Dipolar interactions are a through-space type of interaction, which are proportional to  $r^{-3}$ , where  $r$  is the internuclear distance. Relaxation induced by dipolar interactions is determined by the dipolar coupling at a time  $t$  and a time  $t + \tau$ . For random motion, the average internuclear distance will be independent of the time, and therefore the relaxation is proportional to the square of the dipolar interaction, and proportional to  $r^{-6}$ . This means that dipolar relaxation can occur between spins within the same molecule (intra-molecular relaxation) or between spins in different molecules (inter-molecular relaxation). It should be highlighted that in dipolar relaxation, the energy is not distributed from one spin to another, but that instead the dipolar interaction induces energy transfer between the spins and the lattice. The lattice, in this case, is molecular motion.

Paramagnetic relaxation occurs when the spin of interest, in this thesis  $^1\text{H}$ , interacts with the unpaired electrons from a paramagnetic species. Due to the high gyromagnetic ratio of electrons, paramagnetic species are highly effective at promoting relaxation. Therefore, only a small amount of paramagnetic species in the system can dominate the relaxation behaviour. Examples of paramagnetic species relevant to this thesis are paramagnetic impurities in porous media and molecular oxygen dissolved within bulk liquids<sup>16-18</sup>.

### 2.3.6 Relaxation in porous media

Imbibing a liquid within a porous medium results in a non-uniform sample. The relaxation behaviour of a liquid at or near a pore surface is often different with respect to its bulk liquid equivalent. This section will discuss the effects of surface relaxation and internal gradients.

#### 2.3.6.1 The two-phase fast exchange model

The relaxation behaviour of a liquid imbibed within a porous medium can often be described using the two-phase fast exchange model<sup>19</sup>. In this model, the liquid is divided into two regions, a surface layer and a bulk-like phase in the centre of the pore. Surface relaxation is significantly faster than liquid relaxation due to paramagnetic impurities on the pore surface, strong adsorption sites leading to the restriction of movement of molecules, and magnetic field gradients at the pore surface. As a result, molecules in the surface layer exhibit considerably

lower  $T_1$  and  $T_2$  relaxation times than molecules in the bulk-like phase. The surface layer thickness,  $\lambda$ , is generally assumed to be one single adsorbate molecule thick. However, the surface layer thickness for water, being a small and highly structured adsorbate, has been shown to be up to 3 molecular layers<sup>20</sup>. The surface relaxation effect becomes negligible for distances larger than  $\lambda$ , therefore the relaxation times for the bulk-like phase are similar to those of the bulk liquid.

The surface layer and bulk-like phase could be measured as two relaxation components, if the system were static. However, in the fast diffusion approximation<sup>21,22</sup>, these phases are in fast exchange with each other, i.e. molecules in the surface layer exchange with molecules in the bulk-like phase at a faster timescale than the measurement. In this thesis, the shortest measured relaxation times are in the order of milliseconds. This is much longer than the dynamical correlation times presented in chapters 5-9, which fall in the range of pico- to microseconds. Therefore, the fast diffusion approximation is considered valid. As a result, all spins sample both the bulk and surface environments and a single relaxation time is obtained, which corresponds to the weighted average of the relaxation times of each phase:

$$\frac{1}{T_{i,\text{obs}}} = p \frac{1}{T_{i,\text{surf}}} + (1 - p) \frac{1}{T_{i,\text{bulk}}}, \quad (2.19)$$

where  $i = 1, 2$ ,  $T_{i,\text{obs}}$  is the observed relaxation time,  $T_{i,\text{surf}}$  the surface relaxation time and  $T_{i,\text{bulk}}$  the bulk relaxation time, and  $p$  is the population fraction of spins at the surface. Because the observed relaxation time of a liquid in a porous material depends on  $p$  and  $T_{i,\text{surf}}$ , the pore characteristics, such as pore geometry and surface chemistry, as well as the surface-adsorbate interactions can be investigated using NMR relaxometry.

### 2.3.6.2 Internal gradient effects

For liquids imbibed within porous media, the liquid and the porous media can have considerably differing magnetic susceptibilities. This means that the level of polarization due to an external magnetic field will be different for the liquid and the solid. At the solid-liquid interface, this creates an internal field gradient<sup>23-27</sup>. When adsorbate molecules diffuse near the pore surface, the field gradients cause enhanced spin dephasing. The observed transverse relaxation time,  $T_2^*$ , is reduced, and therefore the peaks in NMR spectra are broadened; while a bulk liquid can display peaks with a FWHM  $< 0.01$  ppm, the peaks for liquids in porous media are generally  $> 1$  ppm wide.

It is difficult to quantitatively describe the effect of internal field gradients on  $T_2$  relaxation, however three motional regimes can be distinguished<sup>23</sup>:

- First, the short time limit: in this regime, the distance that spins diffuse between CPMG echoes,  $l_e$ , is much shorter than the pore diameter,  $l_s$ , and the distance it takes for a molecule to dephase by  $2\pi$  radians,  $l_g$ . This regime corresponds to large pore systems with weak internal gradients. The contribution of diffusion to  $T_2$  relaxation is similar to free diffusion in a constant gradient, and is proportional to  $\delta^3$ , where  $\delta$  is the echo time. In this case, decay due to internal gradients and true  $T_2$  can be distinguished, and therefore it is possible to apply an internal field gradient correction<sup>23,26</sup>.
- Second, the motional averaging regime: this regime is the opposite of the short time limit, and it corresponds to very small pore size systems. In this case, the pore diameter,  $l_s$ , is much smaller than  $l_e$  and  $l_g$ . Because the spins explore the pore space several times before dephasing, the contribution of diffusion to the observed transverse relaxation varies with  $l_s^2$  and  $\delta$ .
- Finally, the localization regime: in this regime the system contains strong and spatially variant internal gradients. This means that  $l_g$  is much shorter than  $l_e$  and  $l_s$ , and that the contribution of internal field gradients to  $T_2$  relaxation vary with  $\delta$ . As such, it is not possible to distinguish internal gradients and true  $T_2$  relaxation.

In practice, the investigated systems often lie between the regimes, and whether or not internal field gradients can be corrected depends on how much the system resembles each of the regimes.

Because internal field gradients are created by a difference in magnetic susceptibility, the magnitude of the  $B_0$  field will affect the magnitude of the internal gradients. Therefore, the effect of internal field gradients can be reduced by performing low-field NMR<sup>28,29</sup>.

## 2.4 Nuclear relaxation: a theoretical approach

In section 2.3, the basic principles of nuclear relaxation were explained, including how to measure relaxation time constants, general sources of relaxation, and an introduction of relaxation of liquids in porous media. This overview was largely based on macroscopic measurements of  $T_1$  and  $T_2$ , for example following the Bloch vector model. While this is

sufficient to qualitatively discuss nuclear relaxation, this section will describe theoretical concepts that are necessary to discuss the quantitative relaxation behaviour of a molecular system. Specifically, the relaxation behaviour of a bulk liquid is used to demonstrate these concepts.

#### 2.4.1 The autocorrelation function

It has been previously established that molecular motions lead to reorientations of the magnetic moments of nuclear spins. As a result, the local magnetic fields fluctuate, which stimulates nuclear relaxation. Because molecular motions are random, the local field fluctuations are also random, and therefore the long-time average of the local field fluctuations is zero. Additionally, the field fluctuations across a system with a high number of spins also average out to zero. However, a quantitative description of nuclear relaxation requires a definition of the rate and magnitude of the local field fluctuations. Therefore, we consider the mean square fluctuating field:

$$\langle B_{\text{Loc}}^2(t) \rangle \neq 0, \quad (2.20)$$

where the brackets indicate an ensemble average. Figure 2.5a,b visually demonstrates the difference between  $B_{\text{Loc}}(t)$  and  $\langle B_{\text{Loc}}^2(t) \rangle$ .

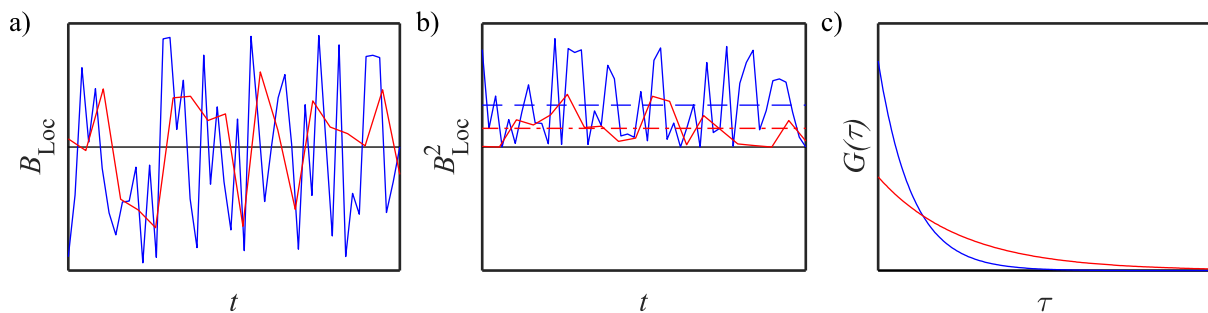


Figure 2.5: (a) Fluctuations in the local field,  $B_{\text{Loc}}$ , over time, (b) the square of the fluctuations over time, and (c) the autocorrelation function based on isotropic rotational motion. Two sets of fluctuations are shown to illustrate different relaxation behaviours; the first is fast and large fluctuations (blue), the second slow and small fluctuations (red). The dashed line in (b) indicates the average of the square of the fluctuations over time, and corresponds to  $G(0)$  in (c).

The rate of field fluctuations can be described by the autocorrelation function, which measures the difference in the local field between a time point  $t$ , and a time point  $t + \tau$ :

$$G(\tau) = \langle B_{\text{Loc}}(t)B_{\text{Loc}}(t + \tau) \rangle. \quad (2.21)$$

As a stationary function, the autocorrelation function is independent of time  $t$ , and only depends on  $\tau$ .  $G(0)$  corresponds to the mean square fluctuating field,  $\langle B_{\text{Loc}}^2(t) \rangle$ , and decays such that  $G(\tau) \rightarrow 0$ . The rate of this decay depends on the rate of the fluctuations; for slow fluctuations, shown in red in Figure 2.5, the difference between  $B_{\text{Loc}}(t)$  and  $B_{\text{Loc}}(t + \tau)$  will be small, and therefore the autocorrelation function will decay slowly, see Figure 2.5c. For fast fluctuations, the opposite occurs, and the autocorrelation function will decay quickly.

The form of the autocorrelation function depends on the type of molecular motions in the system. The simplest form is for isotropic rotational motion, and results in the following autocorrelation function:

$$G(\tau) = \langle B_{\text{Loc}}^2 \rangle \exp\left(-\frac{|\tau|}{\tau_c}\right), \quad (2.22)$$

where  $\tau_c$  is the so-called correlation time, a characteristic time of the corresponding motion. In a recent study, the half of the correlation time,  $\tau_c/2$ , was defined as the mean time for a molecule to rotate one radian<sup>30</sup>. However, it should be noted that the correlation time is not always defined so precisely.

#### 2.4.2 The spectral density function

While the autocorrelation function contains all relevant information to nuclear relaxation, it is more convenient to convert it to the frequency domain, a process similar to converting a FID to a NMR spectrum, see section 2.2.4. The frequency domain spectral density function,  $\mathcal{J}(\omega_0)$ , indicates how much motion is occurring at different frequencies, and can be obtained by Fourier transforming the autocorrelation function:

$$\mathcal{J}(\omega_0) = 2 \int_0^{\infty} G(\tau) \exp(-i\omega_0\tau) d\tau. \quad (2.23)$$

For the autocorrelation function for isotropic rotational motion, shown in equation (2.22), the corresponding spectral density function is:

$$\mathcal{J}(\omega_0) = 2\langle B_{\text{Loc}}^2 \rangle \frac{\tau_c}{1 + (\omega_0\tau_c)^2}. \quad (2.24)$$

Often in the literature the normalized or reduced spectral density is reported. For the remainder of this thesis, the term spectral density function corresponds to the reduced spectral density function:

$$J(\omega_0) = \frac{\tau_c}{1 + (\omega_0\tau_c)^2}. \quad (2.25)$$

The spectral density function in equation (2.25) is a Lorentzian function. Frequencies from zero up to approximately  $1/\tau_c$  are present, for  $\omega_0 > 1/\tau_c$  the spectral density function rapidly decreases. This means that for different correlation times, the Lorentzian curve of the spectral density function changes. A slow correlation time results in a narrow, high magnitude spectral density function, and fast correlation times generate broad, low magnitude spectral density functions, see Figure 2.6.

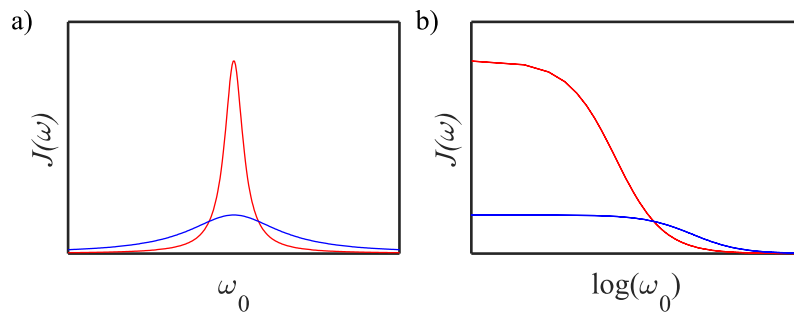


Figure 2.6: Spectral density functions  $J(\omega_0)$ , produced via the autocorrelation functions shown in Figure 2.5c and equation (2.25). For clarity, the data are shown on (a) a linear frequency axis, and (b) a logarithmic frequency axis.

However, it should be noted that the area under the curve always remains the same. This indicates that the contribution to the relaxation behaviour for  $\omega_0 \ll 1/\tau_c$  is decreased, and as such, nuclear relaxation is most efficient and the relaxation times are shortest at  $\omega_0\tau_c = 1$ , see Figure 2.7.

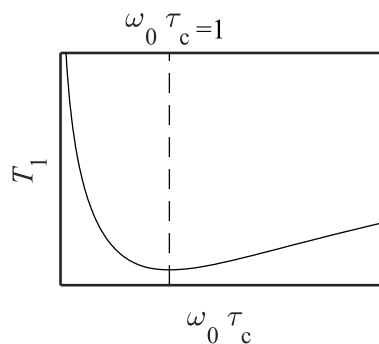


Figure 2.7: The relaxation time  $T_1$  as a function of the dimensionless parameter  $\omega_0\tau_c$ , where the minimum is at  $\omega_0\tau_c = 1$ .

### 2.4.3 Bloembergen, Purcell and Pound (BPP) theory

Simple bulk liquids exhibit relaxation behaviour caused by molecular rotations and translations. In the case of bulk water, approximately 65% of the relaxation behaviour can be ascribed to the rotational motions<sup>30,31</sup>. The dipolar interactions between spins within each molecule are affected by the molecular rotations. This intramolecular relaxation behaviour has been described by Bloembergen, Purcell and Pound (BPP) using the spectral density function in equation (2.25), and they suggested the following expression for intramolecular  $T_1$  and  $T_2$  relaxation<sup>32</sup>:

$$\frac{1}{T_{1,\text{intra}}} = \left(\frac{\mu_0}{4\pi}\right)^2 \frac{3\gamma^4 \hbar^2}{10b^6} [J(\omega_0) + 4J(2\omega_0)], \quad (2.26)$$

$$\frac{1}{T_{2,\text{intra}}} = \left(\frac{\mu_0}{4\pi}\right)^2 \frac{3\gamma^4 \hbar^2}{20b^6} [3J(0) + 5J(\omega_0) + 2J(2\omega_0)], \quad (2.27)$$

where  $\mu_0$  is the vacuum magnetic permeability constant,  $\gamma$  is the gyromagnetic ratio,  $\hbar$  is the reduced Planck constant, and  $b$  is the distance between spins.

Figure 2.8 shows the relaxation time constants as a function of the correlation time for a set Larmor frequency. For  $T_1$  relaxation, there is a minimum at  $\omega_0\tau_c = 1$ , equivalent to Figure 2.7. For short correlation times, i.e.  $\omega_0\tau_c < 1$ , the  $T_2$  relaxation behaviour is identical to that of the  $T_1$ . This means that  $T_1/T_2 \approx 1$  for highly mobile species, such as simple bulk liquids. Samples where the mobility is restricted will display longer correlation times, such that  $\omega_0\tau_c > 1$ . In these cases, the value of  $T_2$  continues to decrease, which is not the case for  $T_1$ , and as a result  $T_1/T_2 > 1$ . Examples of such systems are large, complex molecules and liquids imbibed within porous media, where the mobility of the adsorbate is restricted by surface binding<sup>7,8</sup>.

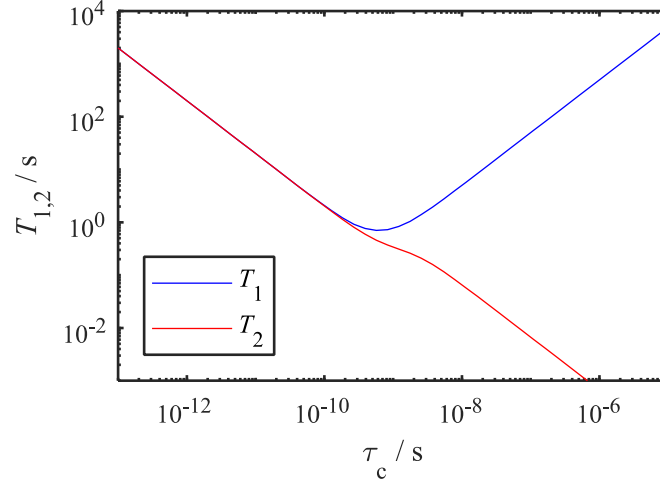


Figure 2.8: The  $T_1$  and  $T_2$  relaxation times for the BPP model plotted against the correlation time,  $\tau_c$ . The prefactor from equation (2.26) was set to  $1 \times 10^9$ , for equation (2.27) the prefactor was  $0.5 \times 10^9$ , and the frequency was set to  $\omega_0 = 1 \times 10^9 \text{ s}^{-1}$ .

#### 2.4.4 Intermolecular relaxation

The dipolar interactions causing the intramolecular relaxation showed previously, also apply to spins of different molecules. The Hwang-Freed model describes the random diffusive motion of two hard spheres, which represent molecules<sup>33</sup>. Through diffusion, the internuclear distances, as well as the orientations of interacting spins are altered. The intermolecular autocorrelation function therefore depends on the minimum distance of approach of the two molecules,  $d$ , which is often estimated to be the molecular diameter, and the diffusion coefficient,  $D$ :  $\tau_t = d/(2D)$ , where  $\tau_t$  is the translational correlation time. The corresponding intermolecular spectral density function is<sup>22,33,34</sup>:

$$J(\omega_0) = \frac{(3/2)u^2 + (15/2)u + 12}{(1/8)u^6 + u^5 + u^4 + (27/2)u^3 + (81/2)u^2 + 81u + 81}, \quad (2.28)$$

where  $u = \sqrt{2\omega_0\tau_t}$ . From the spectral density function the relaxation times can be calculated:

$$\frac{1}{T_{1,\text{inter}}} = \left(\frac{\mu_0}{4\pi}\right)^2 \frac{6\pi}{5} N \frac{\gamma^4 \hbar^2}{d^3} \tau_t [J(\omega_0) + 4J(2\omega_0)], \quad (2.29)$$

$$\frac{1}{T_{2,\text{inter}}} = \left(\frac{\mu_0}{4\pi}\right)^2 \frac{3\pi}{5} N \frac{\gamma^4 \hbar^2}{d^3} \tau_t [3J(0) + 5J(\omega_0) + 2J(2\omega_0)], \quad (2.30)$$

where  $N$  is the number of spins per unit volume.

### 2.4.5 Combining relaxation mechanisms

It is not always the case that a single relaxation mechanism is present in a sample. Multiple relaxation mechanisms can contribute to the overall relaxation behaviour. In the case of  $n$  relaxation mechanisms, the overall relaxation rate,  $1/T_i$ , becomes:

$$\frac{1}{T_i} = \sum_n \frac{1}{T_{i,n}}, \quad (2.31)$$

where  $i = 1, 2$ . In theory, there are many processes that can contribute to the relaxation behaviour, however generally only one or two are dominant. In the case of simple bulk liquids, the expressions for intra- and intermolecular relaxation shown previously may be summed to obtain the observed relaxation rate:

$$\frac{1}{T_i} = \frac{1}{T_{i,\text{intra}}} + \frac{1}{T_{i,\text{inter}}}. \quad (2.32)$$

The summation of relaxation rates is generalized and may be applied to different relaxation behaviours.

### 2.4.6 Fast Field Cycling NMR

Previously, the concepts required to quantitatively describe nuclear relaxation have been discussed. The spectral density function has been introduced, which provides a characterization of the relaxation behaviour as a function of the Larmor frequency. However, data acquisition has not yet been discussed in detail. Conventional NMR relaxometry techniques measure  $T_1$  and  $T_2$  relaxation at a fixed magnetic field. Whilst the information from these experiments can be highly valuable, it is also possible to measure the relaxation behaviour across a range of Larmor frequencies. The advantage is that a more complete picture of the relaxation behaviour can be obtained, which could reduce the chances of misinterpretation of the data.

The  $T_1$  relaxation time can be measured as a function of the Larmor frequency by using Fast Field Cycling (FFC) NMR<sup>22,35,36</sup>. A FFC-NMR relaxometer uses an electromagnet to rapidly switch between different magnetic fields, thereby allowing the measurement of  $T_1$  at a large range of Larmor frequencies. There are two types of FFC-NMR experiments; the pre-polarized (PP) sequence, and the non-polarized (NP) sequence. The PP pulse sequence is shown in Figure 2.9.

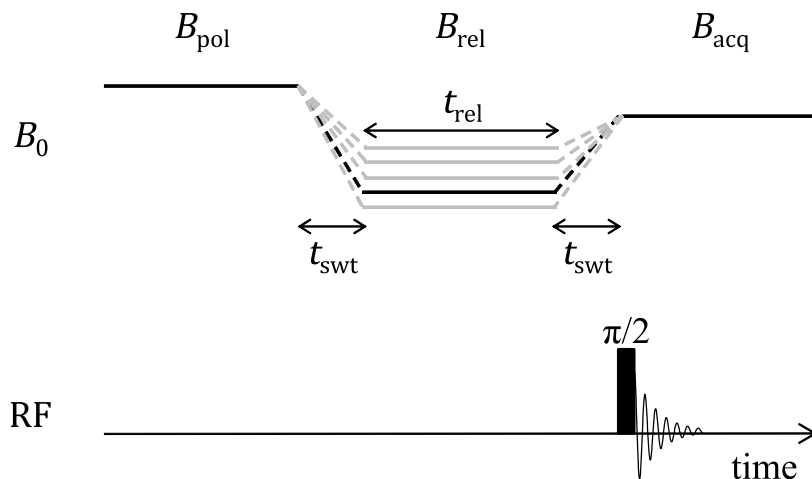


Figure 2.9: The pre-polarized FFC-NMR pulse sequence: the sample is polarized at the polarization field  $B_{pol}$ . Then the magnetic field is switched to a variable relaxation frequency  $B_{rel}$  for a variable time  $t_{rel}$ . Finally, the magnetic field is switched to the acquisition field  $B_{acq}$  and the signal is detected following a  $\pi/2$  pulse.

In a PP FFC-NMR experiment, the sample is polarized at a high magnetic field,  $B_{pol}$ , typically corresponding to 20–25 MHz  $^1\text{H}$  Larmor frequency. Using a relatively high magnetic polarization field ensures that the signal-to-noise ratio is sufficient to obtain accurate data. After a time  $t_{pol}$ , at maximum polarization, the magnetic field is rapidly switched to a variable relaxation field,  $B_{rel}$ . The relaxation field generally ranges between  $0.01 \leq \omega_0 \leq 40$  MHz ( $^1\text{H}$ ). The sample is left at  $B_{rel}$  for a time delay,  $t_{rel}$ , during which relaxation will occur. Finally, the magnetic field is switched to the acquisition frequency,  $B_{acq}$ . For the majority of the experiments in this thesis, the acquisition field is set to  $B_{acq} = 16.3$  MHz. The experiment is then repeated for varying values of  $B_{rel}$  and  $t_{rel}$  to obtain  $T_1$  curves across a large Larmor frequency range. The NP FFC-NMR experiment is equal to the PP FFC-NMR sequence, except the polarization step is excluded. This sequence is typically used to probe  $T_1$  relaxation at high relaxation fields.

An alternative to FFC-NMR is to switch the field by physically moving the sample in a permanent magnet, such that the effective magnetic field changes. This technique is known as shuttling<sup>37,38</sup>. Due to the requirement of physically moving the sample, the minimum switching time of a shuttling experiment is  $\sim 100$  ms, and therefore fast relaxation rates ( $R_1 = 1/T_1 > 10 \text{ s}^{-1}$ ) cannot be detected. In FFC-NMR however, the switching time,  $t_{swt}$  in Figure 2.9, is generally only a few ms, and therefore relaxation rates up to  $R_1 = 1000 \text{ s}^{-1}$  can be measured, which are typical relaxation rates for liquids imbedded within porous media<sup>39–41</sup>.

As mentioned previously, relaxation rates can be measured across a  $^1\text{H}$  Larmor frequency  $0.01 \leq \omega_0 \leq 40$  MHz using FFC-NMR. This means that molecular processes on a timescale from  $\mu\text{s}$  to  $\text{ns}$  can be detected. When the  $R_1$  relaxation rate is plotted against the Larmor frequency, this is known as a NMR dispersion or NMRD profile. An example of a  $^1\text{H}$  NMRD profile of a liquid imbibed within a porous medium, namely water in  $\gamma$ -alumina, is shown in Figure 2.10.

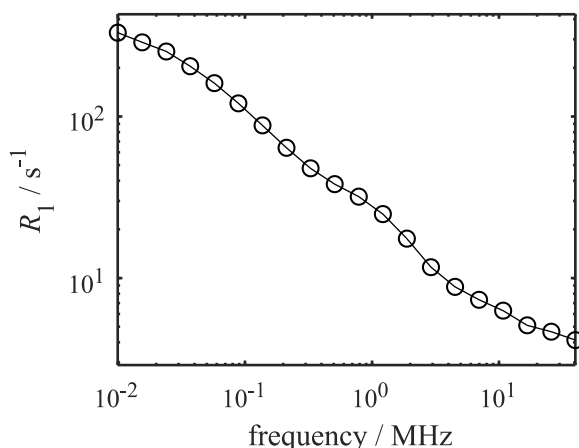


Figure 2.10: The  $^1\text{H}$  NMRD profile of water imbibed within  $\gamma$ -alumina, as an example of a  $^1\text{H}$  NMRD profile of a liquid imbibed within a porous material. Sample and data acquisition information can be found in chapter 4.

The NMRD profiles can then be fitted with theoretical models, such as the models shown in sections 0 and 2.4.4. The result is quantitative information about the liquid dynamics in the form of correlation times, for liquids in porous media this provides insight into the surface-adsorbate interactions<sup>22,41–43</sup>.

#### 2.4.7 Summary

This section presented the core concepts to quantitatively understand relaxation behaviour. A general approach to obtain quantitative information about the dynamics of spins, including liquids in porous media, can be outlined. First, it is necessary to identify any molecular motions and spin interactions relevant to the relaxation of the investigated sample. Based on this information, an appropriate autocorrelation function can be created, which is then Fourier transformed to obtain the spectral density function. With the spectral density function, the relaxation equations as shown in sections 0 and 2.4.4 can be generated. Finally, the relaxation equations can be fitted to the NMRD profiles obtained through FFC-NMR, and physical parameters can be extracted.

While the example of a simple bulk liquid was used, it is possible to extend the theories discussed in this section to other systems featuring different relaxation mechanisms, as will be shown in later chapters in this thesis. The above approach has already been applied to many other relaxation mechanisms, which means that often relaxation equations can be extracted from the literature and fitted to the experimental data directly<sup>41</sup>. The main challenge then lies in identifying the appropriate relaxation mechanisms, a case study of which is shown in chapter 5.

## 2.5 Molecular diffusion: Pulsed Field Gradient NMR

In order to measure molecular diffusion, Pulsed Field Gradient (PFG) NMR can be applied. From PFG NMR experiments, the self-diffusion coefficient,  $D$ , can be extracted, which is an important parameter for some theoretical models.

PFG NMR applies a magnetic field gradient,  $\mathbf{g}$ , which results in a variation in the phase of spins,  $\varphi$ , according to their position:

$$\varphi(\mathbf{r}) = \gamma\delta\mathbf{g} \cdot \mathbf{r}, \quad (2.33)$$

where  $\gamma$  is the gyromagnetic ratio,  $\delta$  is the gradient pulse duration, and  $\mathbf{r}$  is the position. This can be used to obtain phase encoding. The basic experiment is as follows<sup>44</sup>: first, a gradient pulse is applied. After waiting for an observation time,  $\Delta$ , another gradient pulse is applied, such that the effects of the first gradient pulse are reversed. For spins that have not moved, the phases will be the same as before the first gradient pulse. Any spin displacement, on the other hand, will lead to a net phase,  $\varphi_{\text{net}}$ :

$$\varphi_{\text{net}}(\mathbf{r}) = \gamma\delta\mathbf{g} \cdot (\mathbf{r} - \mathbf{r}'), \quad (2.34)$$

where  $\mathbf{r}'$  is the positions of the spins after the observation time. If there has been displacement,  $\varphi_{\text{net}}(\mathbf{r}) \neq 0$  and as such, the signal intensity is reduced. Therefore, the signal attenuation in PFG NMR experiments can be connected to molecular motion.

### 2.5.1 Pulse Gradient Spin Echo

The simplest PFG NMR pulse sequence is the Pulse Gradient Spin Echo (PGSE) sequence, which combines the Carr-Purcell spin echo with field gradients, see Figure 2.11.

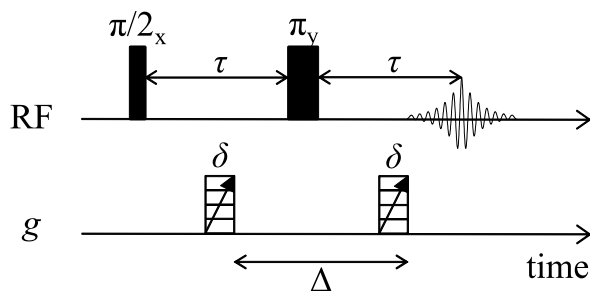


Figure 2.11: The PGSE pulse sequence<sup>44</sup>: a  $\pi/2$  pulse along the  $x$  axis rotates the magnetization along the  $y$  axis. During a time  $\tau$  the spins are allowed to dephase. A magnetic field gradient  $g$  is applied for a duration of  $\delta$  to encode the phase of the spins. A  $\pi$  pulse along the  $y$  axis flips the magnetization, after which the spins will rephase during a time  $\tau$  and another magnetic field gradient is applied to reverse the effects of the initial magnetic field gradient. The total time between magnetic field gradients is  $\Delta$ , the observation time. Finally, the FID is detected.

The signal attenuation,  $S/S_0$ , depends on the molecular motion and the experimental parameters according to the Stejskal-Tanner equation<sup>44</sup>:

$$\frac{S}{S_0} = \exp \left[ -\gamma^2 \delta^2 g^2 \left( \Delta - \frac{\delta}{3} \right) D \right]. \quad (2.35)$$

Often the equation is regrouped such that  $-\gamma^2 \delta^2 g^2 (\Delta - \delta/3)$  is known as the  $b$ -factor. The experimental parameters can then be varied such that the signal attenuation is measured as a function of  $b$  and fitted to equation (2.35). Generally, it is preferred to vary  $b$  by altering the gradient strength, because this does not cause  $T_1$  or  $T_2$  relaxation artefacts as would be the case for changing the gradient pulse duration or the observation time.

### 2.5.2 Pulse Gradient Stimulated Echo

Samples for which the apparent spin-spin relaxation time,  $T_2^*$ , is short will exhibit significant signal loss during the observation time,  $\Delta$ , in the PGSE sequence. For these samples, a Pulse Gradient Stimulated Echo (PGSTE) sequence will provide a better alternative<sup>45</sup>, see Figure 2.12. In this pulse sequence, the Carr-Purcell spin echo is replaced with a stimulated echo. The second  $\pi/2$  pulse rotates the magnetization along the  $z$ -axis, where it undergoes  $T_1$  relaxation. This means that the measurement is not restricted by  $T_2^*$  relaxation, but rather by  $T_1$  relaxation, which is often a longer timescale. The magnetization is stored in this configuration for a time,  $T$ , which comprises a large part of the observation time. Additionally, a homospoil gradient, shown as a grey rectangle in Figure 2.12, eliminates residual  $x$ -magnetization to avoid unwanted echoes. After  $T$ , a third  $\pi/2$  pulse rotates the magnetization back in the transverse plane, after which the second gradient pulse is applied, and the FID is detected.

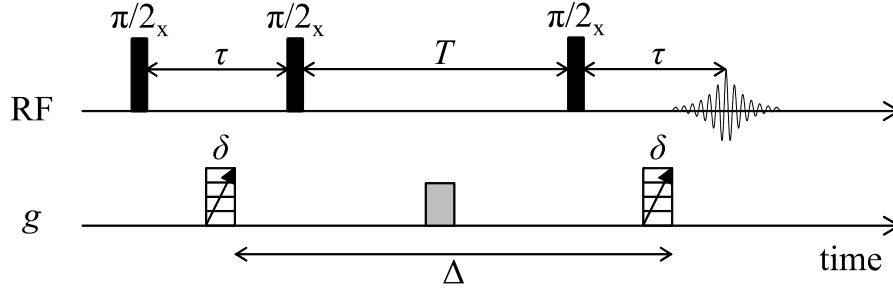


Figure 2.12: The PGSTE pulse sequence<sup>45</sup>: this sequence is similar to the PGSE sequence in Figure 2.11, however the magnetization is stored along the  $z$  axis for a time  $T$  following a  $\pi/2$  pulse along the  $x$  axis. A homospoil gradient, shown as a grey rectangle, eliminates residual  $x$ -magnetization. Another  $\pi/2$  pulse rotates the magnetization back in the transverse plane to continue the PFG experiment.

### 2.5.3 Alternating Pulse Gradient Stimulated Echo

The final PFG NMR pulse sequence described in this chapter, and the sequence that is used for the experiments in this thesis, is the Alternating Pulse Gradient Stimulated Echo (APGSTE) sequence<sup>46</sup>, see Figure 2.13. The APGSTE sequence is designed to suppress the effects from strong background gradients, such as internal field gradients in porous media, see section 2.3.6.2. In the case of strong background gradients, the  $T_2^*$  relaxation time may be severely reduced, which can lead to an underestimation of the diffusion coefficient.

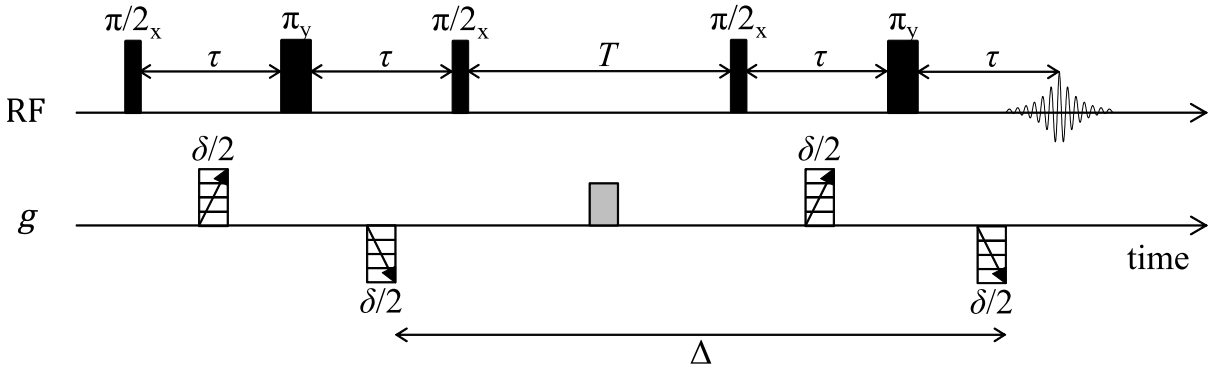


Figure 2.13: The APGSTE pulse sequence<sup>46</sup>: this is an advanced version of the PGSTE sequence in Figure 2.12, where two additional  $\pi$  pulses are added in the middle of the phase encoding interval to minimize  $T_2^*$  dephasing. Correspondingly, the gradient pulses are split into two sets of two pulses.

As can be seen in Figure 2.13, the APGSTE sequence corresponds to the PGSTE sequence with two additional  $\pi$  pulses in the phase encoding interval, which refocus  $T_2^*$  dephasing. The gradient pulses are split such that the  $\pi$  pulses occur between the gradient pulses. It is important to note that the gradient pulses before and after the  $\pi$  pulses must have the opposite polarity to produce the same phase encoding. The description of the signal attenuation for the APGSTE experiment differs slightly from equation (2.35) and is given by:

$$\frac{S}{S_0} = \exp \left[ -\gamma^2 \delta^2 g^2 \left( \Delta - \frac{\tau}{2} - \frac{\delta}{12} \right) D \right]. \quad (2.36)$$

## References

1. Abragam, A. *The principles of nuclear magnetism*. (Clarendon Press, 1983).
2. Keeler, J. *Understanding NMR spectroscopy*. (John Wiley & Sons, Ltd, 1999).
3. Levitt, M. H. *Spin dynamics: basics of nuclear magnetic resonance*. (John Wiley & Sons, Ltd, 2001).
4. Hahn, E. L. Spin echoes. *Phys. Rev.* **80**, 580 (1950).
5. Carr, H. Y. & Purcell, E. M. Effects of diffusion on free precession in nuclear magnetic resonance experiments. *Phys. Rev.* **94**, 630 (1954).
6. Meiboom, S. & Gill, D. Modified spin-echo method for measuring nuclear relaxation times. *Rev. Sci. Instrum.* **29**, 688–691 (1958).
7. Weber, D., Mitchell, J., McGregor, J. & Gladden, L. F. Comparing strengths of surface interactions for reactants and solvents in porous catalysts using two-dimensional NMR relaxation correlations. *J. Phys. Chem.* **113**, 6610–6615 (2009).
8. D’Agostino, C., Mitchell, J., Mantle, M. D. & Gladden, L. F. Interpretation of NMR relaxation as a tool for characterising the adsorption strength of liquids inside porous materials. *Chem. - A Eur. J.* **20**, 13009–13015 (2014).
9. D’Agostino, C., Brett, G., Divitini, G., Ducati, C., Hutchings, G. J., Mantle, M. D. & Gladden, L. F. Increased affinity of small gold particles for glycerol oxidation over Au/TiO<sub>2</sub> probed by NMR relaxation methods. *ACS Catal.* **7**, 4235–4241 (2017).
10. Peemoeller, H., Shenoy, R. K. & Pintar, M. M. Two-dimensional nmr time evolution correlation spectroscopy in wet lysozyme. *J. Magn. Reson.* **45**, 193–204 (1981).
11. Butler, J. P., Reeds, J. A. & Dawson, S. V. Estimating solutions of first kind integral equations with nonnegative constraints and optimal smoothing. *SIAM J. Numer. Anal.* **18**, 381–397 (1981).
12. Song, Y.-Q. Venkataramanan, L., Hürlimann, M. D., Flaum, M., Frulla, P., Straley, C.  $T_1$ - $T_2$  correlation spectra obtained using a fast two-dimensional Laplace inversion. *J. Magn. Reson.* **154**, 261–268 (2002).

13. Reci, A., Sederman, A. J. & Gladden, L. F. Obtaining sparse distributions in 2D inverse problems. *J. Magn. Reson.* **281**, 188–198 (2017).
14. Wahba, G. Practical approximate solutions to linear operator equations when the data are noisy. *SIAM J. Numer. Anal.* **14**, 651–667 (1977).
15. Mitchell, J., Chandrasekera, T. C. & Gladden, L. F. Numerical estimation of relaxation and diffusion distributions in two dimensions. *Progress in Nuclear Magnetic Resonance Spectroscopy* **62**, 34–50 (2012).
16. D’Agostino, C., Bräuer, P., Charoen-Rajapark, P., Crouch, M. D. & Gladden, L. F. Effect of paramagnetic species on  $T_1$ ,  $T_2$  and  $T_1/T_2$  NMR relaxation times of liquids in porous  $\text{CuSO}_4/\text{Al}_2\text{O}_3$ . *RSC Adv.* **7**, 36163–36167 (2017).
17. Korb, J.-P., Whaley Hodges, M., Gobron, T. & Bryant, R. G. Anomalous surface diffusion of water compared to aprotic liquids in nanopores. *Phys. Rev. E* **60**, 3097–3106 (1999).
18. Shikhov, I., Christoph Arns, B. H. & Arns carns, C. H. Temperature-dependent oxygen effect on NMR  $D$ - $T_2$  relaxation-diffusion correlation of n-alkanes. *Appl. Magn. Reson.* **47**, 1391–1408 (2016).
19. Brownstein, K. R. & Tarr, C. E. Importance of classical diffusion in NMR studies of water in biological cells. *Phys. Rev. A* **19**, 2446–2453 (1979).
20. Fripiat, J., Cases, J., Francois, M. & Letellier, M. Thermodynamic and microdynamic behavior of water in clay suspensions and gels. *J. Colloid Interface Sci.* **89**, 378–400 (1982).
21. Godefroy, S., Korb, J.-P., Fleury, M. & Bryant, R. G. Surface nuclear magnetic relaxation and dynamics of water and oil in macroporous media. *Phys. Rev. E* **64**, 021605 (2001).
22. Korb, J.-P. Multiscale nuclear magnetic relaxation dispersion of complex liquids in bulk and confinement. *Prog. Nucl. Magn. Reson. Spectrosc.* **104**, 12–55 (2018).
23. Mitchell, J., Chandrasekera, T. C. & Gladden, L. F. Obtaining true transverse relaxation time distributions in high-field NMR measurements of saturated porous media: removing the influence of internal gradients. *J. Chem. Phys.* **132**, 244705

- (2010).
24. Mitchell, J., Chandrasekera, T. C. & Gladden, L. F. A general approach to  $T_2$  measurements in the presence of internal gradients. *Microporous Mesoporous Mater.* **178**, 20–22 (2013).
  25. Mitchell, J., Chandrasekera, T. C. & Gladden, L. F. Measurement of the true transverse nuclear magnetic resonance relaxation in the presence of field gradients. *J. Chem. Phys.* **139**, 074205 (2013).
  26. Mitchell, J. & Chandrasekera, T. C. Understanding generalized inversions of nuclear magnetic resonance transverse relaxation time in porous media. *J. Chem. Phys.* **141**, 224201 (2014).
  27. Hürlimann, M. D. Effective gradients in porous media due to susceptibility differences. *J. Magn. Reson.* **131**, 232–240 (1998).
  28. Mitchell, J., Chandrasekera, T. C., Johns, M. L., Gladden, L. F. & Fordham, E. J. Nuclear magnetic resonance relaxation and diffusion in the presence of internal gradients: the effect of magnetic field strength. *Phys. Rev. E* **81**, 026101 (2010).
  29. Mitchell, J., Gladden, L. F., Chandrasekera, T. C. & Fordham, E. J. Low-field permanent magnets for industrial process and quality control. *Prog. Nucl. Magn. Reson. Spectrosc.* **76**, 1–60 (2014).
  30. Faux, D. A., Rahaman, A. A. & McDonald, P. J. Water as a Levy rotor. *Phys. Rev. Lett.* **127**, 256001 (2021).
  31. Calero, C., Martí, J. & Guardia, E.  $^1\text{H}$  Nuclear spin relaxation of liquid water from molecular dynamics. *J. Phys. Chem. B* **119**, 1966–1973 (2015).
  32. Bloembergen, N., Purcell, E. M. & Pound, R. V. Relaxation effects in nuclear magnetic resonance absorption. *Phys. Rev.* **73**, 679–712 (1948).
  33. Hwang, L.-P. & Freed, J. H. Dynamic effects of pair correlation functions on spin relaxation by translational diffusion in liquids. *J. Chem. Phys.* **63**, 4017 (1975).
  34. Ayant, Y., Belorizky, E., Aluzon, J. & Gallice, J. Calcul des densités spectrales résultant d'un mouvement aléatoire de translation en relaxation par interaction

- dipolaire magnétique dans les liquides. *J. Phys.* **36**, 991–1004 (1975).
35. Noack, F. NMR field-cycling spectroscopy: principles and applications. *Prog. Nucl. Magn. Reson. Spectrosc.* **18**, 171–276 (1986).
  36. Kimmich, R. & Anoardo, E. Field-cycling NMR relaxometry. *Prog. Nucl. Magn. Reson. Spectrosc.* **44**, 257–320 (2004).
  37. Ferrante, G. & Sykora, S. Technical aspects of Fast Field Cycling. *Adv. Inorg. Chem.* **57**, 405–470 (2005).
  38. Gossuin, Y. Serhan, Z., Sandiford, L., Henrard, D., Marquardsen, T., de Rosales, R. T. M., Sakellariou, D. & Ferrage, F., Sample shuttling relaxometry of contrast agents: NMRD profiles above 1 T with a single device. *Appl. Magn. Reson.* **47**, 237–246 (2016).
  39. Chemmi, H., Petit, D., Levitz, P., Denoyel, R., Galarneau, A. & Korb, J.-P. Noninvasive experimental evidence of the linear pore size dependence of water diffusion in nanoconfinement. *J. Phys. Chem. Lett* **7**, 45 (2016).
  40. Ward-Williams, J., Korb, J.-P. & Gladden, L. F. Insights into functionality-specific adsorption dynamics and stable reaction intermediates using Fast Field Cycling NMR. *J. Phys. Chem. C* **122**, 20271–20278 (2018).
  41. Ward-Williams, J., Korb, J.-P., Rozing, L., Sederman, A. J., Mantle, M. D. & Gladden, L. F. Characterizing solid-liquid interactions in a mesoporous catalyst support using variable-temperature Fast Field Cycling NMR. *J. Phys. Chem. C* **125**, 8767–8778 (2021).
  42. Levitz, P., Bonnaud, P. A., Cazade, P.-A., Pellenq, J.-M. & Coasne, B. Molecular intermittent dynamics of interfacial water: probing adsorption and bulk confinement. *Soft Matter* **9**, 8654–8663 (2013).
  43. Levitz, P. Probing interfacial dynamics of water in confined nanoporous systems by NMRD. *Mol. Phys.* **117**, 952–959 (2019).
  44. Stejskal, E. O. & Tanner, J. E. Spin diffusion measurements: spin echoes in the presence of a time-dependent field gradient. *J. Chem. Phys* **42**, 288 (1965).

45. Tanner, J. E. Use of the stimulated echo in NMR diffusion studies. *J. Chem. Phys.* **52**, 2523 (1970).
46. Cotts, R. M., Hoch, M. J. R., Sun, T. & Markert, J. T. Pulsed field gradient stimulated echo methods for improved NMR diffusion measurements in heterogeneous systems. *J. Magn. Reson.* **83**, 252–266 (1989).

### **3. NMR relaxometry methods to investigate liquids and liquid mixtures imbibed within mesoporous media**

#### 3.1 Introduction

Porous media systems have been widely investigated for decades due to their many applications, such as catalysis<sup>1,2</sup>, separation technologies<sup>3,4</sup>, drug delivery routes<sup>5</sup>, and energy storage<sup>6</sup>. Porous materials can be divided into three pore-size based classes: microporous materials with a pore diameter,  $d_p < 2$  nm, macroporous materials with  $d_p > 50$  nm, and in the middle mesoporous materials, for which the pore diameter ranges between 2–50 nm<sup>7</sup>. In this thesis, the main focus is mesoporous materials.

Micro- and mesoporous media exhibit a high surface-to-volume ratio, which means that when a liquid is imbibed, all liquid molecules will interact with the surface to some degree. As such, the surface properties affect the behaviour of the imbibed liquid, which may affect the applicability of the porous medium. Unlike for microporous materials, the pore diameter of mesoporous materials is large enough that several molecular layers can be contained within the pores. As a result, some of the anomalous confinement effects seen in microporous media, such as severely reduced diffusion coefficients<sup>8,9</sup> and size and shape selective adsorption<sup>10,11</sup>, do not affect mesoporous media. These reasons, and the fact that they can be relatively easily adapted to their application, make mesoporous materials of great interest to the (chemical) industry.

NMR relaxometry is a powerful tool to investigate liquids imbibed within mesoporous media. As was shown in chapter 2, nuclear relaxation depends on molecular motions. Interactions with a pore surface can change the molecular motions of liquids. For example, using the two-phase fast exchange model introduced in section 2.3.6.1, the structure of the liquid inside the pores can be elucidated. Moreover, more advanced NMR relaxometry methods, such as  $T_1 - T_2$  correlation experiments and Fast Field Cycling (FFC) NMR, can provide more detailed information about the surface affinity and dynamics of liquids in porous media. This chapter will discuss the application of NMR relaxometry methods to porous media, including different types of NMR relaxometry experiments, what kind of information can be extracted from these experiments, and how the experimental data can be interpreted.

Additionally, liquid mixtures are investigated. Many porous media applications involve liquid mixtures, for example separation technologies, or catalysis, where the mixture can be two (or

more) reagents, or reagents and (by)products. However, the complexity of the system increases dramatically for liquid mixtures compared to pure liquids. Not only are there more components to be considered, but also liquid mixing effects can occur. Therefore, one section of this chapter is dedicated to bulk liquid mixtures and the liquid mixing effects that should be taken into account when investigating mixtures in porous media. Finally, the limited amount of literature on liquid mixtures in porous media, and in particular the phenomenon of microphase separation, will be presented.

## 3.2 NMR relaxation methods for porous media investigations

NMR relaxometry is a powerful tool to investigate liquids imbibed within porous media, and as such, different techniques have been developed. Some of the most used methods can be divided into two groups: fixed field NMR relaxometry, and variable field NMR relaxometry. In fixed field NMR relaxometry, relaxation times are measured at a single magnetic field strength. Often, a dimensionless ratio of different relaxation times will be created, which can provide information about, for example, the surface-adsorbate interaction strength. In this section, two fixed field NMR relaxometry methods are discussed, namely the spin-lattice interaction parameter, which is the ratio of the longitudinal relaxation times in the bulk and in the pore, and  $T_1 - T_2$  correlation experiments. Variable field NMR relaxometry is done by FFC-NMR. Relaxation rates are measured at a range of Larmor frequencies, and the resulting NMR dispersion (NMRD) profile can be fitted to a theoretical model, which can provide quantitative information about the dynamics of liquids imbibed within porous media.

### 3.2.1 The spin–lattice interaction parameter ( $T_{1,\text{bulk}}/T_{1,\text{pore}}$ ratio)

As was shown in sections 2.3 and 2.4, many different processes and properties can contribute to the longitudinal (spin-lattice,  $T_1$ ) and transverse (spin-spin,  $T_2$ ) relaxation times. For liquids imbibed within porous media, three contributions should be taken into account:

- liquid properties, such as molecular diameter and dissolved oxygen content,
- the porous material properties, e.g. pore size and geometry and (paramagnetic) impurities,
- and the surface-adsorbate interaction strength.

Generally, the aim is to obtain a greater understanding of the surface-adsorbate interaction strength, which means that the liquid and porous material properties should be either accounted for and understood, or excluded from the analysis.

In this first NMR relaxometry method, the  $T_1$  relaxation times of a bulk liquid,  $T_{1,\text{bulk}}$ , and the same liquid imbibed within a porous medium,  $T_{1,\text{pore}}$ , are measured. Note that  $T_{1,\text{pore}}$  corresponds to  $T_{1,\text{obs}}$  from equation (2.19). By taking the ratio of these two relaxation times, the contribution of the liquid properties to the relaxation behaviour is excluded from the analysis. Assuming that the relaxation time constant of the unimbibed bulk liquid is equal to the relaxation time of the bulk-in-the-pore phase of an imbibed liquid, multiplying the two-phase fast exchange model (equation (2.19)) by  $T_{1,\text{bulk}}$  results in the following equation:

$$\frac{T_{1,\text{bulk}}}{T_{1,\text{pore}}} = p \left( \frac{T_{1,\text{bulk}}}{T_{1,\text{surf}}} - 1 \right) + 1, \quad (3.1)$$

where  $T_{1,\text{surf}}$  is the surface relaxation time, and  $p$  is the surface population of spins. When molecules are adsorbed onto the surface, the molecular mobility decreases and therefore the surface relaxation time decreases strongly, such that  $T_{1,\text{surf}} \ll T_{1,\text{bulk}}$ . Assuming this is true, equation (3.1) becomes:

$$\frac{T_{1,\text{bulk}}}{T_{1,\text{pore}}} = p \frac{T_{1,\text{bulk}}}{T_{1,\text{surf}}} + 1. \quad (3.2)$$

It should be noted that this assumption is not always accurate, especially at high frequencies. In mesoporous media the surface-to-volume ratio can be sufficiently high that  $p \frac{T_{1,\text{bulk}}}{T_{1,\text{surf}}} \gg 1$ , in which case:

$$\frac{T_{1,\text{bulk}}}{T_{1,\text{pore}}} \propto \frac{T_{1,\text{bulk}}}{T_{1,\text{surf}}}. \quad (3.3)$$

The  $T_{1,\text{bulk}}/T_{1,\text{surf}}$  ratio is also known as the spin-lattice interaction parameter,  $\eta$ . The spin-lattice interaction parameter approach was used by D'Agostino *et al.* to investigate the surface-adsorbate interaction strengths of a large range of different liquids imbibed within several mesoporous materials<sup>12</sup>. The porous media that were used were  $\gamma$ -alumina, titania, and silica, which are common catalyst supports. Due to the high polarity of the porous media, it was expected that polar liquids would interact more strongly with the supports. Indeed, the highest  $T_{1,\text{bulk}}/T_{1,\text{pore}}$  ratios were found for aldehydes and ketones, indicating that these liquids interact

with the porous supports most strongly. The next strongest interacting liquids were monoalcohols and then alkanes. Interestingly, polyalcohols exhibited lower  $T_{1,\text{bulk}}/T_{1,\text{pore}}$  ratios than alkanes, even though alkanes are considered not to interact with the polar surface. The anomalous behaviour for polyalcohols was interpreted as an effect due to hydrogen bonding. The hydrogen bonding network for polyalcohols is very strong, and hinders molecular motion. As the molecules adsorb onto the surface, the hydrogen bonding network is disrupted and therefore the increased molecular mobility causes an increase in the  $T_1$  relaxation time. Moreover, the  $T_{1,\text{bulk}}/T_{1,\text{pore}}$  approach was compared to a similar approach using PFG NMR experiments. In this approach, the bulk diffusion coefficient was normalized to the effective self-diffusivity of the imbibed liquid, to create a dimensionless parameter  $\xi = D_{\text{bulk}}/D_{\text{pore}}$ . Again, alkanes were considered not to interact with the surface, and therefore the values for  $\xi$  were normalized to the  $\xi$ -value for alkanes. The diffusion results showed the same trends as for the  $T_{1,\text{bulk}}/T_{1,\text{pore}}$  approach, highlighting the enhanced mobility of polyalcohols when imbibed within the porous supports.

An advantage of the  $T_{1,\text{bulk}}/T_{1,\text{pore}}$  approach is that the  $T_1$  measurements can be done via the inversion recovery method, shown in section 2.3.1, or via the saturation recovery sequence. Both of these experiments are simple to execute, and measure full FIDs, which means chemical resolution is obtained via the NMR spectrum. Robinson *et al.* used the chemical resolution to separate out the  $\text{CH}_3$  and OH environments in methanol imbibed within several types of passivated (i.e. treated with tetraethyl orthosilicate (TEOS)) and unpassivated porous media. While the hydroxyl relaxation is complicated due to proton exchange effects, the relaxation behaviour of the methyl group was shown to provide information about the surface-adsorbate interaction strength. The spin-lattice interaction parameter was determined for the methyl groups and subsequently normalized to the spin-lattice interaction parameter of a weakly interacting liquid, namely cyclohexane. For the unpassivated porous media, the spin-lattice interaction parameter ranged between 3.0–6.7, whereas the interaction parameter decreased to 1.3–2.0 for the passivated porous media. From these results, it could be concluded that the surface-methanol interaction was decreased by the TEOS treatment, thereby passivating the supports.

On the other hand, the spin-lattice interaction parameter approach has some limitations. The first is that two separate measurements are required to obtain  $T_{1,\text{bulk}}$  and  $T_{1,\text{pore}}$ . Not only does this increase the experimental acquisition time, it also complicates or obstructs the possibility

of *in situ* experiments. Secondly, as was shown previously, relaxation behaviours of liquids in porous media are affected by the surface-adsorbate interactions, the liquid properties, and the properties of the porous support. While the  $T_{1,\text{bulk}}/T_{1,\text{pore}}$  approach evades the liquid property contributions, it does not take into account the variations between different porous materials. This means that it is not straightforward to compare  $T_{1,\text{bulk}}/T_{1,\text{pore}}$  ratios measured for different porous supports. However, within a single porous medium, the contributions of the porous material properties to the relaxation behaviour can be considered constant, which means that relative differences between different liquids correspond with differences between surface-adsorbate interactions.

### 3.2.2 $T_1 - T_2$ correlation experiments

The pulse sequence for a  $T_1 - T_2$  correlation experiment was first introduced in section 2.3.3. In essence, the experiment consists of an inversion recovery to measure the  $T_1$  component, followed by a CPMG echo train to obtain the  $T_2$  component. A full CPMG echo can be detected if it is necessary to also obtain spectral resolution, or a one-shot CPMG sequence can be used to reduce the experimental acquisition time. If the one-shot CPMG sequence is used, it is often possible to distinguish different relaxation environments based on their  $T_1$  and  $T_2$  relaxation times<sup>13–16</sup>. These relaxation environments can correspond to different molecules, but also to different relaxation environments within the same molecule<sup>16</sup>.

Similarly to the spin-lattice interaction parameter approach, a dimensionless ratio of relaxation times is constructed. For a  $T_1 - T_2$  correlation experiment, this is the  $T_1/T_2$  ratio. Assuming the dominant relaxation mechanisms for  $T_1$  and  $T_2$  are the same, the contributions of the porous material to the relaxation behaviour, e.g. paramagnetic species, can be cancelled out by taking the ratio  $T_1/T_2$ . This effect was demonstrated by D’Agostino *et al.*, who investigated the  $T_1$  and  $T_2$  relaxation times of 1-octanol imbedded within  $\gamma$ -alumina<sup>17</sup>. The support was loaded with  $\text{CuSO}_4$  at concentrations between 8–3500 ppm, creating paramagnetic  $\text{Cu}^{2+}$  relaxation centres on the  $\gamma$ -alumina surface. While the  $T_1$  and  $T_2$  values of 1-octanol were shown to decrease for  $\text{Cu}^{2+}$  concentrations above 100 ppm, the  $T_1/T_2$  ratios stayed approximately constant.

In Figure 2.8, the  $T_1$  and  $T_2$  relaxation times according to the Bloembergen, Purcell and Pound (BPP) model were plotted against the correlation time<sup>18</sup>. While the BPP model is a very simple model, and therefore complex systems such as liquids in porous media cannot be fully described using the BPP model, it provides a useful explanation for simple trends in  $T_1/T_2$

ratios. As can be seen in Figure 2.8, for short correlation times,  $T_1 \approx T_2$ , and therefore  $T_1/T_2 \approx 1$ . Small bulk liquid molecules will generally have short correlation times, and as such, this means that the contribution of the bulk liquid to the relaxation behaviour will also be cancelled out by taking the  $T_1/T_2$  ratio. As a result, the  $T_1/T_2$  ratio provides direct insight into the surface-adsorbate interactions of liquids imbibed within porous media.

The  $T_1/T_2$  ratio approach has been used extensively to investigate liquids in porous media. Often, it is applied as a qualitative probe of surface-adsorbate interaction strengths. Based on the variations between  $T_1/T_2$  ratios of different samples, a considerable amount of information can be obtained. For example, the  $T_1/T_2$  ratios, and therefore the interaction strength of water, 2-propanol and 2-butanone with Pd/Al<sub>2</sub>O<sub>3</sub> and Ru/SiO<sub>2</sub> could be ranked as water > 2-propanol > 2-butanone<sup>19</sup>. It was then shown that displacing one liquid with another was only possible when the  $T_1/T_2$  ratio of the second liquid was higher than that of the first. This study therefore showed that the behaviour of binary liquid mixtures imbibed within these supports can be predicted based on the  $T_1/T_2$  ratios of the pure liquids.

In terms of liquid mixtures, another set of studies especially relevant to this thesis was done by D'Agostino *et al.*, who investigated to what extent the interaction of the surface with a solvent, in this case methanol, influenced the efficiency of oxidation reactions in several precious metal catalysts<sup>20–22</sup>. First, it was shown that the  $T_1/T_2$  ratio of 1,4-butanediol dissolved in methanol on a Au/TiO<sub>2</sub> catalyst was severely decreased by the addition of water to the system, corresponding to a decrease in the 1,4-butanediol conversion to dimethyl succinate<sup>20</sup>. From this study, it could be concluded that the addition of water meant that the 1,4-butanediol could not interact with the surface anymore, and therefore the catalytic activity was reduced. Next, this study was generalized for 1,3-propanediols<sup>21</sup>. Finally, the experiments were performed for 1,4-butanediol dissolved in methanol on a range of precious metal catalysts<sup>22</sup>. It was shown that the ratio of the reactant (1,4-butanediol)  $T_1/T_2$  ratio and the solvent (methanol)  $T_1/T_2$  ratio was directly proportional to the 1,4-butanediol conversion. Based on these studies, it is possible to predict the catalyst efficiency following relatively simple  $T_1 - T_2$  correlation experiments.

Many other examples exist of porous media studies using the phenomenological  $T_1/T_2$  approach<sup>23–26</sup>. However, it is also possible to approach  $T_1/T_2$  ratios from a more theoretical point of view. McDonald *et al.* presented a modelling approach to  $T_1/T_2$  ratios based on a relaxation mechanism dominated by paramagnetic surface relaxation sinks, see Figure 3.1<sup>27</sup>.

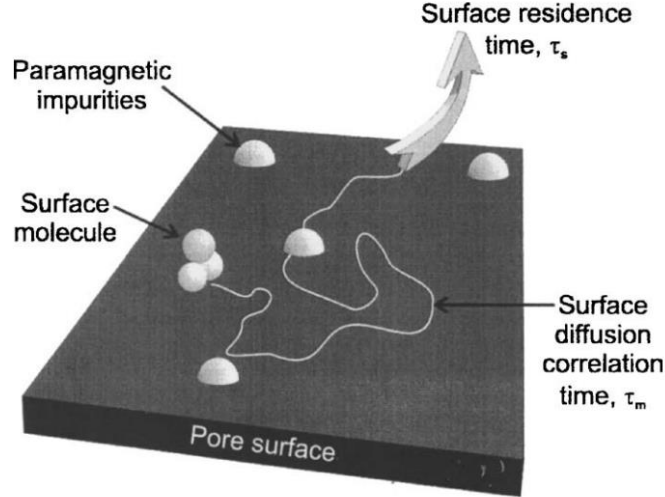


Figure 3.1: Schematic overview of the two-dimensional diffusion of molecules on a surface in the presence of paramagnetic impurities. Reproduced from McDonald *et al.*<sup>27</sup>

By applying a model, it was possible to extract correlation times and a surface affinity parameter,  $A = \tau_s/\tau_m$ , where  $\tau_s$  is the surface residence correlation time, and  $\tau_m$  is the hopping time, which represents the time it takes between successive hops of a molecule on the surface, see Figure 3.1. The surface affinity parameter is important in the oil recovery industry, as it is a measure for the wettability of rocks<sup>28</sup>.

D'Agostino *et al.* then simplified the model used by McDonald *et al.*, which lead to the simple correlation:

$$\frac{T_1}{T_2} \propto \frac{-1}{\ln(\tau_m)}, \quad (3.4)$$

which could be connected to an activation energy for surface diffusion,  $\Delta E$ , to obtain:

$$\frac{T_1}{T_2} \propto \frac{-1}{\Delta E}. \quad (3.5)$$

This correlation was verified by comparing  $e_{\text{surf}} = -T_2/T_1$  values with activation energies measured by temperature programmed desorption, a commonly used characterization technique for porous media. Later, the  $e_{\text{surf}}$  parameter was also connected to adsorption energies calculated using Density Functional Theory (DFT) for a range of alcohols and cyclohexane imbedded within silica<sup>29</sup>.

It is clear that  $T_1 - T_2$  correlation experiments provide great insight into the adsorption of liquids in porous media, either in a phenomenological capacity or developed according to a

theoretical modelling approach. However, it is important to consider the assumptions that were made in analysing  $T_1/T_2$  ratios. One set of assumptions that was made is that  $T_{i,\text{surf}} \ll T_{i,\text{bulk}}$  and  $p/T_{i,\text{surf}} \gg 1/T_{i,\text{bulk}}$ . Based on these assumptions, it was concluded that the observed  $T_1/T_2$  ratio corresponds to the  $T_1/T_2$  ratio of the surface layer. These assumptions are not always true. When the observed intra-pore relaxation times are close to those of the bulk liquid, as is the case for weakly interacting species, the  $T_1/T_2$  ratio will be significantly higher than expected, and as such, the interpretation of the  $T_1/T_2$  ratios can be inaccurate. This effect was demonstrated by Robertson, by comparing the  $T_1/T_2$  ratios of water imbibed within silicas of varying pore size and a uniform surface chemistry<sup>16</sup>. If the  $T_1/T_2$  ratios would be an appropriate measure of the surface-adsorbate interaction strength, the  $T_1/T_2$  ratios should be constant for all silica samples, however it was shown that the  $T_1/T_2$  ratio increased with decreasing pore size, confirming the invalidity of the abovementioned assumptions. On the other hand, the  $T_1/T_2$  ratios of different liquids imbibed within the same silica followed the expected trend for the surface-adsorbate interaction strengths, showing that  $T_1 - T_2$  correlation experiments can still provide qualitative information about weakly interacting species. The dependency of the  $T_1/T_2$  ratio of confined fluids on the pore size was also shown in simulations by Faux & McDonald, again confirming the invalidity of the abovementioned assumptions<sup>106</sup>.

Additionally, it is important to consider internal field gradient effects. Internal gradient effects were described in section 2.3.6.2, and are caused by magnetic susceptibility differences between the porous medium and the imbibed liquid. Internal gradients can severely reduce the observed transverse relaxation time,  $T_2^*$ , leading to an overestimation of the  $T_1/T_2$  ratios. As previously mentioned, internal gradient effects can be reduced by decreasing the magnetic field<sup>30</sup>. However, severe internal gradient effects that would result in an overestimation of the  $T_1/T_2$  ratio and therefore of the surface-adsorbate interaction strength have been shown at field strengths as low as 10 MHz<sup>31</sup>. Alternatively, it is sometimes possible to eliminate gradient effects by optimizing the acquisition parameters<sup>32</sup>, or correct for internal field gradients in post-processing<sup>33,34</sup>. Unfortunately, this is not always the case, and internal gradient effects cannot be evaded, thereby imposing a limitation on  $T_1 - T_2$  correlation experiments as a probe for measuring surface-adsorbate interaction strengths.

Finally, another assumption is that all samples within a study are described by the same relaxation mechanism. For different liquids within the same porous medium<sup>35,36</sup>, or for a single liquid imbibed within different porous media<sup>37,38</sup>, this has previously been shown not to always

be the case. The dominating relaxation mechanism cannot be determined through  $T_1 - T_2$  correlation experiments, and therefore the  $T_1/T_2$  ratios may be misinterpreted. In order to obtain greater insight into the relaxation mechanisms of liquids in porous media, in-depth material characterization<sup>39</sup>, variable temperature experiments<sup>36,40</sup>, and FFC-NMR experiments can be applied.

### 3.2.3 FFC-NMR

The concept and experimental setup for FFC-NMR were described in section 2.4.6. To summarize this section, FFC-NMR uses an electromagnet to rapidly switch the magnetic field. By doing this,  $T_1$  relaxation times across a large Larmor frequency range, typically  $0.01 \leq \omega_0 \leq 40$  MHz for  $^1\text{H}$  NMR corresponding to a timescale ranging between  $\mu\text{s}$ – $\text{ns}$ , can be obtained. The relaxation rate,  $R_1 = 1/T_1$ , is then plotted against the Larmor frequency to create a NMR dispersion or NMRD profile. Some advantages of the Fast Field Cycling technique compared to alternative methods for measuring variable frequency relaxation experiments, are that there is no significant signal loss, because the sample can first be polarized in a high magnetic field, and that fast relaxation rates,  $R_1 \leq 1000 \text{ s}^{-1}$ , can be measured. These fast relaxation rates are common for strongly binding liquids imbibed within porous media<sup>41</sup>.

For frequencies  $\omega_0 \leq 10$  MHz, simple bulk liquids have been shown to exhibit a constant relaxation rate<sup>42,43</sup>. This means that for liquids imbibed within porous media, in this frequency range, a change in  $R_1$  is due to the interaction of the liquid with the pore surface. The simplest method of extracting information from FFC-NMR experiments is a qualitative analysis. By comparing the relaxation rates of different samples and the variation of the relaxation rates with the Larmor frequency, i.e. the slope of the NMRD profiles, Ward-Williams *et al.* ranked the surface-adsorbate interaction strengths of different liquids imbibed within  $\gamma$ -alumina<sup>43</sup>. The difference between  $R_1$  at 0.01 and 10 MHz was defined as the total observable relaxation dispersion (TOD). Polar solvents such as water and methanol displayed a higher TOD than nonpolar solvents such as cyclohexane, following the trend of expected surface-adsorbate interaction strengths based on the high polarity of the support.

However, to obtain more quantitative information, the NMRD profiles can be fitted to theoretical models to provide correlation times. The simplest is the BPP model<sup>18</sup> described in section 2.4.3. Without *a priori* knowledge of the system, a NMRD profile can be described by the BPP model, which is in essence a linear combination of Lorentzian terms:

$$J(\omega_I) = \sum_i C_i \frac{1}{1 + \omega_I^2 \tau_{c,i}^2}, \quad (3.6)$$

$$R_1(\omega_I) = A[J(\omega_I) + 4J(2\omega_I)], \quad (3.7)$$

where  $i$  is the number of relaxation environments,  $J(\omega_I)$  is the spectral density function,  $C_i$  is a scaling factor, and  $\tau_{c,i}$  is the correlation time of environment  $i$ . This approach was used by Hsu *et al.*, who modelled the NMRD profiles of water imbibed within hierarchical H-ZSM-5 using three Lorentzian terms<sup>44</sup>. Each of the three relaxation environments was connected to a different pore size within the sample. The longest correlation times were related to the micropores ( $d_p = 0.5$  nm), which were several orders of magnitude longer than the correlation times that were associated with macropores ( $d_p > 50$  nm). From this, it was concluded that the water inside the micropores had a stronger interaction with the surface than in the macropores. The third correlation time was linked to the mesopores ( $d_p = 4.3$  nm).

If the dominant relaxation mechanism is known, it is possible to construct a formal model that describes the specific spin interactions in the system. Formal models have been constructed for several types of relaxation mechanisms. First, Korb *et al.* have constructed a model to describe a relaxation mechanism dominated by dipolar interactions of  $^1\text{H}$  ( $I$ ) spins in a liquid with paramagnetic impurities ( $S$  spins) on the pore surface<sup>41,45,46</sup>. This modelling approach was also used to describe  $T_1/T_2$  ratios by McDonald *et al.*<sup>27</sup>, as was shown in Figure 3.1. Due to the large gyromagnetic ratio difference between  $^1\text{H}$  spins and the paramagnetic impurities ( $\gamma_S = 658\gamma_I$ ), this relaxation mechanism is dominant even in the presence of a small amount of paramagnetic impurities<sup>38</sup>. As such, it has been applied to a wide range of chemical systems, such as ceramics<sup>47</sup>, cement pastes<sup>48</sup>, metal oxide materials<sup>36,43,49</sup>, porous glasses<sup>38</sup>, biochars<sup>50</sup>, rock cores<sup>28,42,51</sup>, shales<sup>52</sup> and metal supported catalysts<sup>23</sup>. The specific expression for the relaxation rate can be changed slightly depending on the application, however the general form of the model stays consistent:

$$\begin{aligned} \frac{1}{T_{1,\text{obs}}} &= \frac{1}{T_{1,\text{bulk}}} + \left(\frac{\mu_0}{4\pi}\right)^2 \frac{N_s \pi \sigma_s (\gamma_I \gamma_S \hbar)^2 S(S+1)}{15d^2 \delta'^2} \\ &\times \tau_m \left( 3 \ln \left[ \frac{1 + \omega_I^2 \tau_m^2}{\frac{\tau_m^2}{\tau_s^2} + \omega_I^2 \tau_m^2} \right] + 7 \ln \left[ \frac{1 + \omega_S^2 \tau_m^2}{\frac{\tau_m^2}{\tau_s^2} + \omega_S^2 \tau_m^2} \right] \right), \end{aligned} \quad (3.8)$$

where  $\mu_0$  is the vacuum magnetic permeability,  $N_s/N$  is the ratio of spins at the pore surface,  $\sigma_s$  is the density of paramagnetic species on the surface,  $d$  is the molecular diameter, and  $\delta'$  is an effective distance of minimal approach between the  $^1\text{H}$  and paramagnetic spins.

Unfortunately, the assumptions made by Korb in the construction of his model result in limitations of the applicability of the model. The  $\tau_s/\tau_m$  ratio, a parameter that describes the wettability of rocks<sup>28</sup>, was found to often be higher than physically possible, and therefore Faux *et al.* constructed another model by changing some of the assumptions<sup>53–55</sup>. Faux's model, also known as the  $3\tau$  model, specifies three diffusion time constants,  $\tau_b$ ,  $\tau_l$ , and  $\tau_d$ . The time constant  $\tau_b$  characterizes bulk diffusion,  $\tau_l$  – surface diffusion, and  $\tau_d$  – desorption, see Figure 3.2. The  $3\tau$  model was applied to data previously analysed by the Korb model, and showed physically meaningful diffusion correlation times. However, the  $3\tau$  model is mathematically much more complex than the Korb model, and therefore its applications are currently limited.

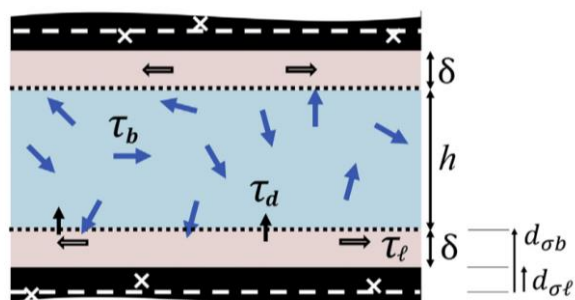


Figure 3.2: A schematic overview of the  $3\tau$  model for a liquid between two pore walls. The surface layer thickness is denoted as  $\delta$  and the layer thickness of the bulk fluid is  $h$ .  $d_{\sigma l}$  and  $d_{\sigma b}$  are the distance from the paramagnetic species, modelled as a uniform layer (white dashes) to the surface and bulk layers respectively.  $\tau_b$  characterizes bulk diffusion,  $\tau_l$  surface diffusion, and  $\tau_d$  desorption. Reproduced from Faux *et al.*<sup>55</sup>

Other types of theoretical models have been created for systems where the relaxation behaviour is not dominated by interactions with paramagnetic impurities. For intramolecular relaxation mechanisms, the dipolar interactions between spins within the same molecule dominate the relaxation behaviour. In the case of the Reorientations Mediated by Translational Diffusion (RMTD) model type, the directional binding of an adsorbate at the pore surface restricts the molecular mobility and therefore affects the relaxation behaviour<sup>56,57</sup>. For the RMTD model, different approaches have been presented. The first approach, by Kimmich, dictates that the RMTD behaviour is determined by the geometry of the porous material, rather than the surface-adsorbate interactions<sup>35,37,58</sup>. The Kimmich-type RMTD model was used to explain the identical NMRD profiles of a range of polar liquids imbedded within porous glasses<sup>37</sup>.

In the second RMTD approach, by Levitz, the surface-adsorbate interactions determine the relaxation behaviour<sup>59–63</sup>. From the Levitz-type RMTD model an adsorption correlation time,  $\tau_A$ , can be extracted, which provides direct, quantitative information about the surface dynamics. More details about the definition of  $\tau_A$  will be shown in chapter 5. For water imbibed within cement,  $\tau_A$ , and therefore the surface-adsorbate interaction strength, was shown to decrease upon addition of an adjuvant, which changes the hydration kinetics, see Figure 3.3<sup>64</sup>.

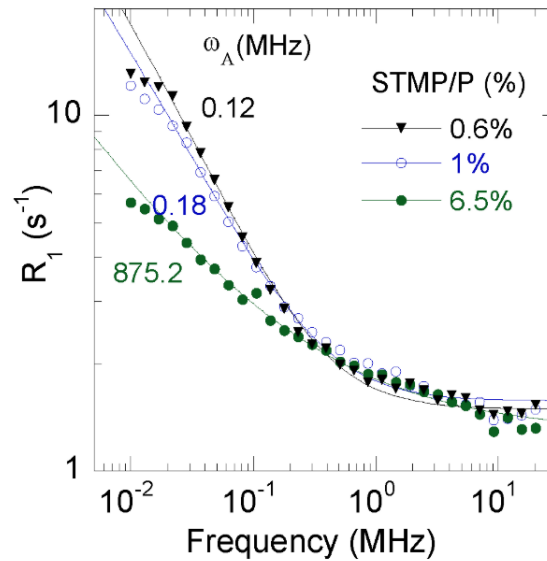


Figure 3.3: NMRD profiles and the Levitz-type RMTD model fits for water imbibed within cement in the presence of a sodium trimetaphosphate adjuvant (STMP), the concentration of which is shown in the graph. The characteristic frequency shown in the graph,  $\omega_A$ , is inversely correlated with the adsorption correlation time,  $\tau_A$ . Reproduced from Korb and Levitz<sup>64</sup>.

Aside from the Korb,  $3\tau$  and RMTD models that have been described in this section, other theoretical models have been developed to describe specific porous media systems. For example, another modelling approach has shown that the NMRD profiles of protic liquids imbibed within  $\gamma$ -alumina are dominated by the interaction of the surface hydroxyls with paramagnetic impurities on the surface, and therefore the NMRD profiles do not appear to provide direct insight into the surface-adsorbate interactions of these systems<sup>36</sup>.

When the relaxation mechanism is known, obtaining quantitative information about the surface-adsorbate interactions from FFC-NMR experiments is relatively straightforward. However, the process of identifying the dominant relaxation mechanism and subsequently developing or applying a theoretical model based on this relaxation mechanism is not trivial. Variable temperature experiments<sup>36,40</sup> and a detailed material characterization<sup>39</sup> can be used to aid the identification of an appropriate theoretical model.

Experimentally, FFC-NMR measurements are more challenging than the other NMR relaxometry techniques presented in this chapter. First, multiple  $T_1$  experiments are performed in a FFC-NMR experiment. As such, the acquisition times are long compared to fixed field experiments. Depending on the signal-to-noise ratio and the  $T_1$  values, FFC-NMR experiments can take up to 24 hours. This not only limits high-throughput applications for FFC-NMR, but also the extent to which FFC-NMR can be used to investigate kinetic processes.

Additionally, because FFC-NMR experiments require rapidly switching magnetic fields generated by an electromagnet, the magnetic field homogeneity is approximately 10–100 ppm<sup>65,66</sup>, and therefore insufficient to obtain spectral resolution. As a result, it is not trivial to distinguish and assign different relaxation environments. It has been shown that if the  $T_1$  values are sufficiently different, it can be possible to separate multiple relaxation environments using an inverse Laplace transform<sup>67</sup>. In this example, by comparing the NMRD profiles of each component to the NMRD profiles of pure liquids, it was possible to assign the relaxation environments to different molecules. If the  $T_1$  values of different environments are similar, an inverse Laplace transform will not be able to separate the environments, and another approach is necessary. It is possible to combine FFC-NMR with other NMR techniques. Neudert *et al.* applied a FFC-NMR pulse sequence with CPMG acquisition to water imbibed within different pore size silica glasses, and was able to separate the NMRD profiles for different pore sizes based on their  $T_2$  value, thereby naming the technique “ $T_2$ -Encoded Acquisition of Relaxation Dispersion for Resolution of Pore Sizes” (TEARDROPS)<sup>68</sup>. Another recently developed method of obtaining spectral resolution in FFC-NMR experiments combines the technique with ultra-low field NMR, in which the J-coupling frequency is measured, providing chemical resolution<sup>69,70</sup>.

Considering the novelty of these advanced NMR relaxometry techniques, it is expected that more aspects, technical and theoretical, of the FFC-NMR technique will be developed in the near future, which could truly solidify FFC-NMR as a standard tool for the investigation of surface-adsorbate interactions of liquids in porous media.

### 3.3 Liquid mixtures

The dynamics of liquids confined within porous media have been widely studied for a number of decades, leading to a strong fundamental knowledge of these nanoconfined liquids<sup>58,66,71–74</sup>. However, much less is known about the confinement dynamics of liquid mixtures. This section will summarize some of the literature about liquid mixtures and their interaction with porous media. Some examples of NMR relaxometry experiments on liquid mixtures in porous media were shown in section 3.2, such as the  $T_1 - T_2$  correlation experiments to investigate the solvent effect in oxidation reactions on metal catalysts<sup>20</sup>, and the FFC-NMR experiments on methanol-THF and THF-cyclohexane mixtures imbibed within  $\gamma$ -alumina<sup>67</sup>. The aim of this section is not to describe methods in order to investigate liquid mixtures, but rather to describe two effects: first, the effects that liquids have on each other upon mixing in the bulk phase, and second, the effect of confining a liquid mixture to a pore.

#### 3.3.1 Bulk liquid mixtures

In order to investigate the dynamics of liquid mixtures imbibed within porous media, it is necessary to consider the effect that one liquid can have on another, when two or more liquids are mixed, especially in terms of their relaxation behaviour. In this thesis, the majority of the investigated mixtures are aqueous solutions. The relaxation behaviour of aqueous solutions has been thoroughly studied by Goldammer and Zeidler<sup>75</sup>. For mixtures of water with a range of organic liquids, the self-diffusion coefficient,  $D$ , and the  $T_1$  relaxation time were determined and plotted against the mixture composition. The example of a tetrahydrofuran (THF)-water mixture is shown in Figure 3.4. Intra- and intermolecular contributions to the relaxation times could be separated by obtaining the  $T_1$  relaxation times for fully protonated mixtures, as well as mixtures where one of the components was deuterated. The deuteron relaxation rate was found to correspond with the intramolecular relaxation rate, and from this, a reorientational correlation time was calculated.

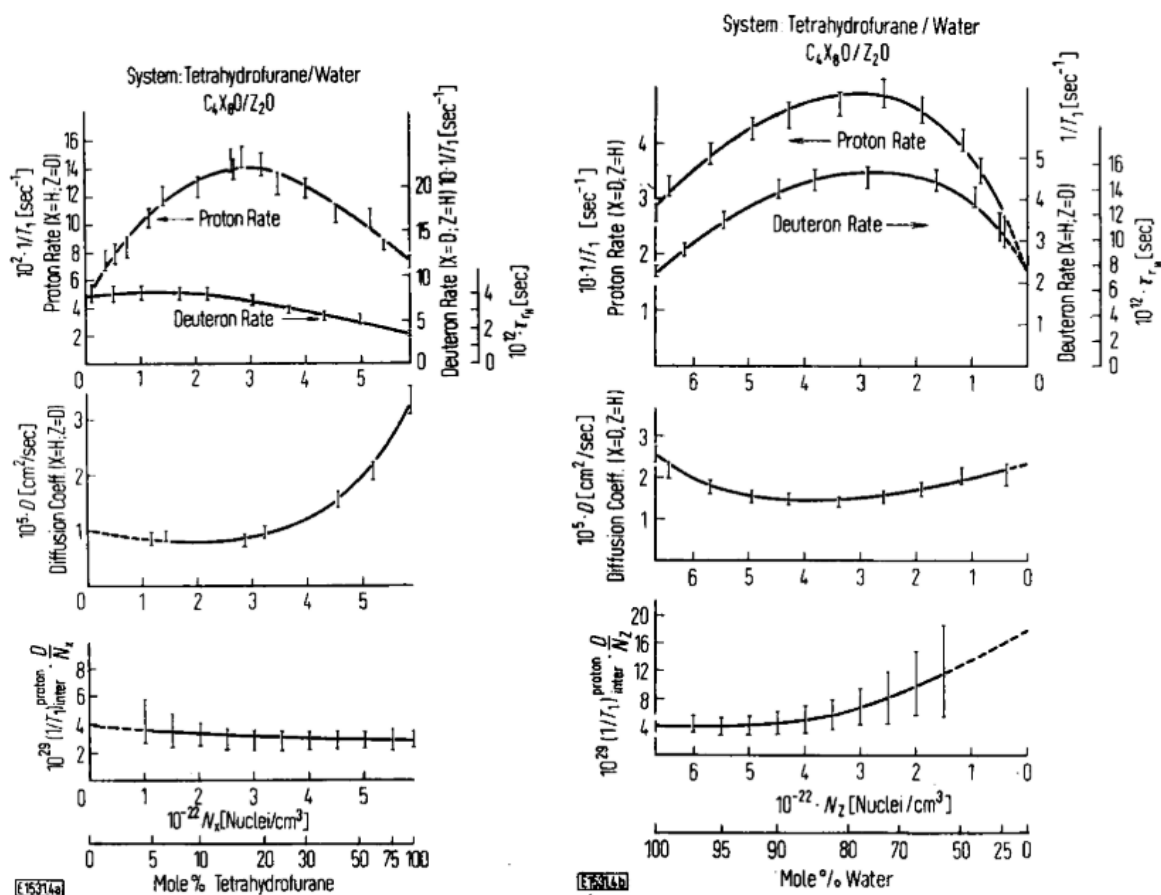


Figure 3.4:  $R_1 = 1/T_1$  relaxation rates (top), diffusion coefficients,  $D$  (middle), and the ratio of the proton and deuteron relaxation rate (bottom), for THF (left) and water (right) in THF-water mixtures, plotted against the mixture composition. The reorientational correlation time  $\tau_{RH}$  corresponds to the deuteron relaxation rate, the scale is shown on the right. Reproduced from Goldammer and Zeidler<sup>75</sup>.

For THF, the intramolecular relaxation is not heavily influenced by the addition of water. However, the proton relaxation rate increases upon addition of water with respect to the relaxation rate of pure THF, indicating that the presence of water is interrupting the translational motion of THF. Below 20 mol% THF, the relaxation decreases again, suggesting that the translational motion of THF increases in a water-heavy mixture. The proton relaxation rate trend for the water component is similar, suggesting similar effects. However, the ratio of the proton and deuteron relaxation rate of the water component increases upon addition of THF, indicating the intramolecular motion of water is disrupted. This is an effect due to the disruption of the hydrogen bonding network. The same effect is also seen for the pyridine, tert-butanol and acetic acid components in their respective aqueous solutions, which in their pure state form a polymer network. This polymer network is then disrupted by the water, resulting in a decrease in the intramolecular relaxation rate.

### 3.3.2 Confined liquid mixtures and microphase separation

It has been shown that liquid mixtures that are miscible in their bulk state can segregate when imbibed within a mesoporous medium<sup>76–81</sup>. Common names for this effect include microphase separation, confinement induced phase separation and nanosegregation. Obtaining greater insight into the dynamics of nanoconfined liquid mixtures and particularly microphase separation is essential to several fields within the chemical industry, such as catalysis, separation technologies, and oil recovery<sup>82,83</sup>. For instance, because of microphase separation effects, nanoconfinement appears to be an energy efficient method for the separation of ethanol-water mixtures, which are difficult to separate through distillation<sup>4,84–87</sup>.

Experimental signs of the possibility of microphase separation of fully miscible liquid mixtures were shown by MD simulations, dielectric spectroscopy and calorimetry experiments on aqueous alcohol solutions confined within MCM-41, where some of the water molecules were concluded to segregate at the pore surface<sup>79–81</sup>. Since then, numerous studies were published on microphase separation, involving a range of theoretical and experimental techniques, including attenuated total reflectance infrared spectroscopy (ATR-IR), sum frequency generation (SFG) vibration spectroscopy, solid-state NMR, neutron scattering and molecular dynamics (MD)<sup>88–96</sup>.

The group of Morineau has studied microphase separation extensively through a combination of quasielastic neutron scattering experiments and molecular dynamics simulations<sup>91,92,95–100</sup>. In recent work, a core shell microphase separation of otherwise miscible tert-butanol (TBA)-toluene mixtures confined within silica nanochannels was shown<sup>96</sup>. Whereas the pure TBA density profile shows peaks for the central layers and the surface layer, the density profile of TBA in the mixture only shows the surface layer peak, see Figure 3.5. The toluene component shows both surface and central layer peaks. This indicates a microphase separation of the mixture, where TBA is at the pore surface. The results of this study exemplify the rapid increase of knowledge about microphase separation and the nature of the dynamics of confined liquid mixtures. However, a quantitative analysis of the dynamics remains unavailable.

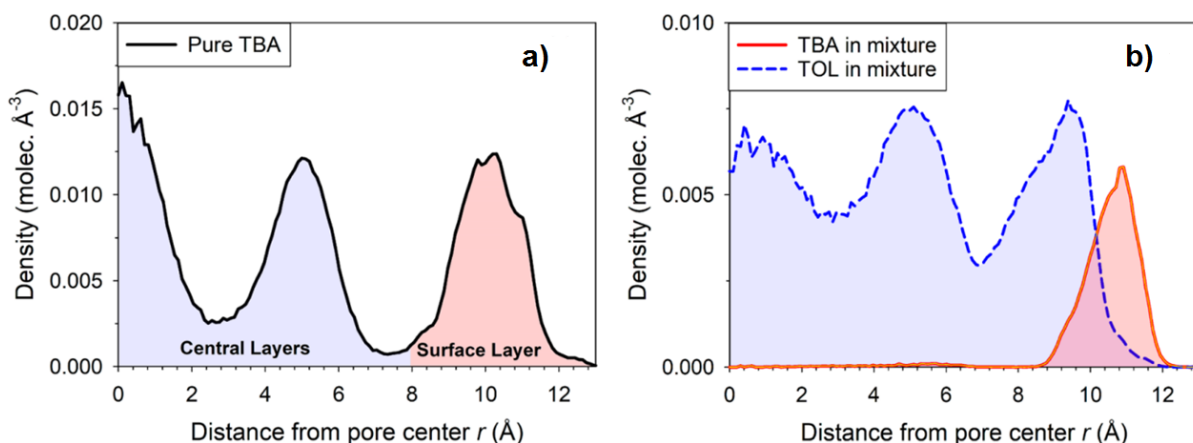


Figure 3.5: Radial density profiles of a) pure TBA, and b) TBA (solid red line) and toluene (dashed blue line) in the confined binary mixture ( $X_{TBA} = 0.24$ ). Reproduced from Mhanna *et al.*<sup>96</sup>

Moreover, many systems are more complex than the seemingly clear case of tert-butanol and toluene imbibed within silica. An example of such a system is ethanol-water mixtures imbibed within silica. Bulk ethanol-water mixtures already show a heterogeneous structure at the molecular level, due to the hydrophobic nature of the alkyl tail<sup>101–105</sup>. Guo *et al.* performed MD simulations on ethanol-water mixtures between silica walls and concluded that water molecules prefer forming hydrogen bonded clusters away from the pore surface. This results in a microphase separation of the mixture, where ethanol molecules are more likely to attach to the silica walls than water<sup>90</sup>.

The MD simulations were later supported by positron annihilation lifetime spectroscopy (PALS) experiments on ethanol-water mixtures within mesoporous silica<sup>94</sup>. In this study, an increase in the interfacial free-volume was detected for ethanol-water mixtures at ethanol concentrations of  $0.3 < X_E < 0.45$ . This excess free-volume, in combination with a more detailed lifetime analysis, was interpreted by the authors as a sign of microphase separation of the mixture, with ethanol attaching to the pore surface.

Contradicting results were found when ethanol-water mixtures imbibed within mesoporous silica were studied by NMR  $T_1 - T_2$  correlation experiments, see Figure 3.6<sup>16</sup>. Upon decreasing the ethanol concentration, the  $T_1/T_2$  ratio of the ethanol component decreases initially but then stabilises. The  $T_1/T_2$  ratio of the water component undergoes a more significant change, increasing drastically with an increase in ethanol concentration. This increase in  $T_1/T_2$  ratio implies an increase in the average surface-water interaction strength, which according to the two-phase fast exchange model described in section 2.3.6.1 is caused by a relatively higher fraction of water molecules being attached to the pore surface than residing in the bulk of the

pore. As a result, it was concluded that the system undergoes partial demixing, forming a water-rich surface layer and an ethanol-rich pore centre.

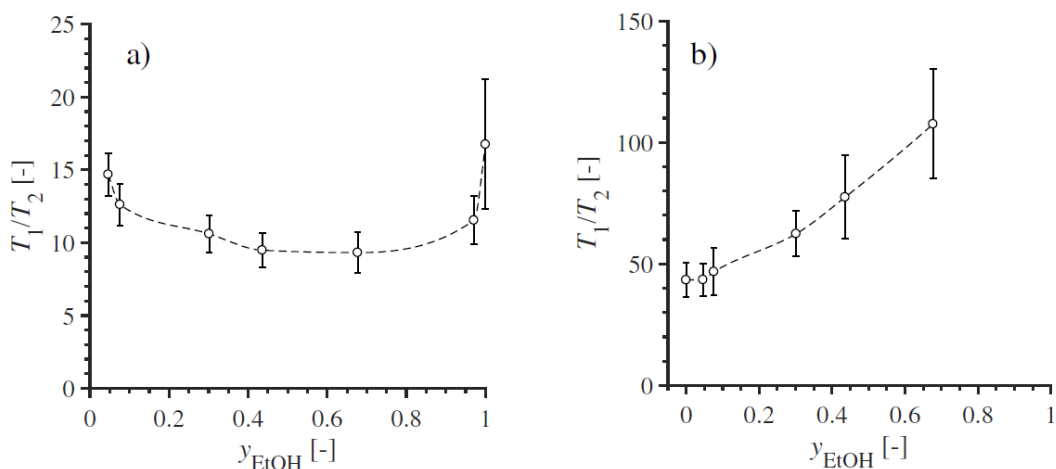


Figure 3.6: Observed  $T_1/T_2$  ratio of a) ethanol, and b) water imbibed within mesoporous silica (pore size 15 nm), as a function of intra-pore mixture composition. Reproduced from Robertson<sup>16</sup>.

At high magnetic fields, the relaxation times are dominated by fast relaxation processes, including rotational and translational processes, mainly originating from the bulk liquid. Comparing the  $T_1/T_2$  ratios of ethanol and water across the composition range to the ratios of the pure liquids should negate the effect of most fast relaxation processes on the interpretation of the chemistry of the system, however this challenge should always be taken into account.

While the understanding of the microphase separation phenomenon is being developed rapidly, it is clear that more investigations are necessary to obtain clear, unambiguous results. Moreover, the work presented in this section describes the qualitative nature of microphase separation in several systems, however a quantitative analysis of the dynamics of the phase-segregated species remains unavailable.

### 3.4 Conclusions and outlook

In the first part of this chapter, NMR relaxometry methods to investigate surface-adsorbate interactions of liquids imbibed within porous media were discussed. The first NMR relaxometry method that was presented was the measurement of the spin-lattice interaction parameter,  $\eta = T_{1,\text{bulk}}/T_{1,\text{surf}}$ . The  $T_1$  interaction parameter was shown to probe surface-adsorbate interactions successfully, the experiments are relatively simple and the interpretation of the data is straightforward. However, the comparison of  $T_{1,\text{bulk}}/T_{1,\text{pore}}$  ratios measured for different porous supports is complicated, as the contribution of the support to the relaxation behaviour is not taken into account.

Different supports can be compared relatively easily in  $T_1 - T_2$  correlation experiments, where the  $T_1/T_2$  ratio was shown to correlate with the surface-adsorbate interaction strength. Pulse sequences for  $T_1 - T_2$  correlation experiments are widely implemented and therefore simple to perform. Moreover, only the confined sample is required to obtain a  $T_1/T_2$  ratio, and therefore the experimental acquisition of this data is very straightforward with respect to the spin-lattice interaction parameter, where the relaxation time must also be measured for the bulk liquid.  $T_1 - T_2$  correlation experiments have been very successful in describing the interactions of liquids imbibed within porous media, however it is assumed in these experiments that the relaxation mechanism for all samples within a study is the same. Different types and strengths of surface interactions as well as internal field gradients can affect the relaxation times. As such, the  $T_1/T_2$  ratios may be distorted, which can lead to misinterpretation of the data.

In order to investigate relaxation mechanisms, variable field NMR relaxometry techniques such as FFC-NMR can be applied. In these experiments, the  $R_1 = 1/T_1$  relaxation rate is measured at a large range of Larmor frequencies, thereby providing insight into the dynamics over a large timescale range. The NMR dispersion profiles can be fitted to theoretical models, which describe the nuclear spin interactions. From these models, correlation times can be extracted, which provide quantitative information about the dynamics of liquids imbibed within porous media and their surface-adsorbate interactions.

While the interactions of pure liquids with porous supports have gained great fundamental understanding, the effect of nanoconfinement on liquid mixtures is much less investigated. The second part of this chapter focuses on the effect of liquid mixing on NMR relaxometry, as well as microphase separation effects for nanoconfined liquid mixtures. First, the effect of bulk liquid mixing on NMR relaxation rates was illustrated. For simple liquids such as tetrahydrofuran (THF), the addition of another liquid, water in this case, decreased the translational mobility and therefore increased the  $R_1$  relaxation rate. As the THF concentration decreased below 20 mol%, the  $R_1$  decreased again, indicating an increase in mobility. For liquids that form a hydrogen bonding or polymer network with itself, such as water or pyridine, the addition of another liquid disrupts this network and therefore the intra- as well as the intermolecular relaxation rate increases. Finally, the state of the art of microphase separation studies is presented. It was shown that liquids that are fully miscible in the bulk state, can nanosegregate when they are imbibed within mesoporous media. Investigations on microphase separation have provided significant insight into the nature of this phenomenon, however some studies presented contradicting results, and a full quantitative analysis of the dynamics of liquid mixtures imbibed within mesoporous media is currently unavailable.

Based on the current literature overview, the main aim of this thesis is to use the NMR relaxometry methods presented in section 3.2, primarily FFC-NMR, to unambiguously and quantitatively describe microphase separation effects of liquid mixtures imbibed within a range of mesoporous media. To this extent, the following chapter presents a case study of the FFC-NMR technique applied to liquid mixtures. This will be followed by a quantitative analysis based on theoretical modelling of alcohol-water mixtures imbibed within anatase titania in chapters 5 and 6.

## References

1. Martínez, A., López, C., Márquez, F. & Díaz, I. Fischer-Tropsch synthesis of hydrocarbons over mesoporous Co/SBA-15 catalysts: the influence of metal loading, cobalt precursor, and promoters. *J. Catal.* **220**, 486–499 (2003).
2. Trueba, M. & Trasatti, S. P.  $\gamma$ -Alumina as a support for catalysts: a review of fundamental aspects. *Eur. J. Inorg. Chem.* **17**, 3393–3403 (2005).
3. Brady, R., Woonton, B., Gee, M. L. & O'Connor, A. J. Hierarchical mesoporous silica materials for separation of functional food ingredients — A review. *Innov. Food Sci. Emerg. Technol.* **9**, 243–248 (2008).
4. Phan, A., Cole, D. R. & Striolo, A. Preferential adsorption from liquid water-ethanol mixtures in alumina pores. *Langmuir* **30**, 8066–8077 (2014).
5. Vallet-Regí, M., Colilla, M., Izquierdo-Barba, I. & Manzano, M. Mesoporous silica nanoparticles for drug delivery: current insights. *Molecules* **23**, 47 (2017).
6. Peng, M., Jeonghun, K., Nanjundan, A. K., Malay, P., Naoya, K., Yoshiyuki, S., & Yusuke, Y. Phosphorus-based mesoporous materials for energy storage and conversion. *Joule* **2**, 2289–2306 (2018).
7. McNaught, A. D.; Wilkinson, M. *IUPAC. Compendium of Chemical Terminology*. (Blackwell Scientific Publications, 1997). doi:<https://doi.org/10.1351/goldbook>
8. Ruthven, D. M. & Post, M. F. M. Chapter 12: Diffusion in zeolite molecular sieves. *Stud. Surf. Sci. Catal.* **137**, 525–577 (2001).
9. Kärger, J., Freude, D. & Haase, J. Diffusion in nanoporous materials: novel insights by combining MAS and PFG NMR. *Processes* **6**, 147 (2018).
10. Davis, M. E. Zeolites and molecular sieves: not just ordinary catalysts. *Ind. Eng. Chem. Res.* **30**, 11 (1991).
11. Sastre, G. & Corma, A. The confinement effect in zeolites. *J. Mol. Catal. A Chem.* **305**, 3–7 (2009).
12. D'Agostino, C., Mitchell, J., Gladden, L. F. & Mantle, M. D. Hydrogen bonding network disruption in mesoporous catalyst supports probed by PFG-NMR

- diffusometry and NMR relaxometry. *J. Phys. Chem. C* **116**, 8975–8982 (2012).
13. Song, Y.-Q., Venkataramanan, L., Hürlimann, M. D., Flaum, M., Frulla, P., Straley, C.  $T_1$ - $T_2$  correlation spectra obtained using a fast two-dimensional Laplace inversion. *J. Magn. Reson.* **154**, 261–268 (2002).
  14. Mitchell, J., Chandrasekera, T. C. & Gladden, L. F. Numerical estimation of relaxation and diffusion distributions in two dimensions. *Progress in Nuclear Magnetic Resonance Spectroscopy* **62**, 34–50 (2012).
  15. Reci, A., Sederman, A. J. & Gladden, L. F. Obtaining sparse distributions in 2D inverse problems. *J. Magn. Reson.* **281**, 188–198 (2017).
  16. Robertson, C. I. Characterising adsorption and mass transfer in porous media. (Doctoral thesis, University of Cambridge, 2017).
  17. D’Agostino, C., Bräuer, P., Charoen-Rajapark, P., Crouch, M. D. & Gladden, L. F. Effect of paramagnetic species on  $T_1$ ,  $T_2$  and  $T_1/T_2$  NMR relaxation times of liquids in porous  $\text{CuSO}_4/\text{Al}_2\text{O}_3$ . *RSC Adv.* **7**, 36163–36167 (2017).
  18. Bloembergen, N., Purcell, E. M. & Pound, R. V. Relaxation effects in nuclear magnetic resonance absorption. *Phys. Rev.* **73**, 679–712 (1948).
  19. Weber, D., Mitchell, J., McGregor, J. & Gladden, L. F. Comparing strengths of surface interactions for reactants and solvents in porous catalysts using two-dimensional NMR relaxation correlations. *J. Phys. Chem.* **113**, 6610–6615 (2009).
  20. D’Agostino, C., Brett, G. L., Miedziak, P. J., Knight, D. W., Hutchings, G. J., Gladden, L. F. & Mantle, M. D. Understanding the solvent effect on the catalytic oxidation of 1,4-butanediol in methanol over Au/TiO<sub>2</sub> catalyst: NMR diffusion and relaxation studies. *Chem. - A Eur. J.* **18**, 14426–14433 (2012).
  21. D’Agostino, C., Kotionova, T., Mitchell, J., Miedziak, P. J., Knight, D. W., Taylor, S. H., Hutchings, G. J., Gladden, L. F. & Mantle, M. D. Solvent effect and reactivity trend in the aerobic oxidation of 1,3-propanediols over gold supported on titania: NMR diffusion and relaxation studies. *Chem. - A Eur. J.* **19**, 11725–11732 (2013).
  22. D’Agostino, C., Feaviour, M. R., Brett, G. L., Mitchell, J., York, A. P. E., Hutchings, G. J., Mantle, M. D. & Gladden, L. F. Solvent inhibition in the liquid-phase catalytic

- oxidation of 1,4-butanediol: understanding the catalyst behaviour from NMR relaxation time measurements. *Catal. Sci. Technol.* **6**, 7896–7901 (2016).
23. Mitchell, J., Broche, L. M., Chandrasekera, T. C., Lurie, D. J. & Gladden, L. F. Exploring surface interactions in catalysts using low-field nuclear magnetic resonance. *J. Phys. Chem.* **117**, 17699–17706 (2013).
  24. Ralphs, K., D'Agostino, C., Burch, R., Chansai, S., Gladden, L. F., Hardacre, C., James, S. L., Mitchell, J. & Taylor, S. F. R. Assessing the surface modifications following the mechanochemical preparation of a Ag/Al<sub>2</sub>O<sub>3</sub> selective catalytic reduction catalyst. *Catal. Sci. Technol.* **4**, (2014).
  25. Krzyzak, A. T. & Habina, I. Low field <sup>1</sup>H NMR characterization of mesoporous silica MCM-41 and SBA-15 filled with different amount of water. *Microporous Mesoporous Mater.* **231**, 230–239 (2016).
  26. D'Agostino, C., Brett, G., Divitini, G., Ducati, C., Hutchings, G. J., Mantle, M. D. & Gladden, L. F. Increased affinity of small gold particles for glycerol oxidation over Au/TiO<sub>2</sub> probed by NMR relaxation methods. *ACS Catal.* **7**, 4235–4241 (2017).
  27. McDonald, P. J., Korb, J.-P., Mitchell, J. & Monteilhet, L. Surface relaxation and chemical exchange in hydrating cement pastes: a two-dimensional NMR relaxation study. *Phys. Rev. E* **72**, 011409 (2005).
  28. Korb, J. P., Freiman, G., Nicot, B. & Ligneul, P. Dynamical surface affinity of diphasic liquids as a probe of wettability of multimodal porous media. *Phys. Rev. E* **80**, 061601 (2009).
  29. Robinson, N., Robertson, C., Gladden, L. F., Jenkins, S. J. & D'Agostino, C. Direct correlation between adsorption energetics and nuclear spin relaxation in a liquid-saturated catalyst material. *ChemPhysChem* **19**, 2472–2479 (2018).
  30. Mitchell, J., Chandrasekera, T. C., Johns, M. L., Gladden, L. F. & Fordham, E. J. Nuclear magnetic resonance relaxation and diffusion in the presence of internal gradients: the effect of magnetic field strength. *Phys. Rev. E* **81**, 026101 (2010).
  31. Mitchell, J., Chandrasekera, T. C. & Gladden, L. F. Measurement of the true transverse nuclear magnetic resonance relaxation in the presence of field gradients. *J. Chem.*

- Phys.* **139**, 074205 (2013).
32. Kleinberg, R. L. & Horsfield, M. A. Transverse relaxation processes in porous sedimentary rock. *J. Magn. Reson.* **88**, 9–19 (1990).
  33. Mitchell, J., Chandrasekera, T. C. & Gladden, L. F. Obtaining true transverse relaxation time distributions in high-field NMR measurements of saturated porous media: removing the influence of internal gradients. *J. Chem. Phys.* **132**, 244705 (2010).
  34. Mitchell, J., Chandrasekera, T. C. & Gladden, L. F. A general approach to  $T_2$  measurements in the presence of internal gradients. *Microporous Mesoporous Mater.* **178**, 20–22 (2013).
  35. Zavada, T. & Kimmich, R. The anomalous adsorbate dynamics at surfaces in porous media studied by nuclear magnetic resonance methods. The orientational structure factor and Lévy walks. *J. Chem. Phys.* **109**, 6929 (1998).
  36. Ward-Williams, J., Korb, J.-P., Rozing, L., Sederman, A. J., Mantle, M. D. & Gladden, L. F. Characterizing solid-liquid interactions in a mesoporous catalyst support using variable-temperature Fast Field Cycling NMR. *J. Phys. Chem. C* **125**, 8767–8778 (2021).
  37. Stapf, S., Kimmich, R., Seitter, R. O., Maklakov, A. I. & Skirda, V. D. Proton and deuteron field-cycling NMR relaxometry of liquids confined in porous glasses. *Colloids Surfaces A Physicochem. Eng. Asp.* **115**, 107–114 (1996).
  38. Korb, J.-P., Whaley Hodges, M., Gobron, T. & Bryant, R. G. Anomalous surface diffusion of water compared to aprotic liquids in nanopores. *Phys. Rev. E* **60**, 3097–3106 (1999).
  39. Plassais, A., Pomiès, M.-P., Lequeux, N., Korb, J.-P., Petit, D., Barberon, F., Bresson, B. Microstructure evolution of hydrated cement pastes. *Phys. Rev. E* **72**, 041401 (2005).
  40. Conte, P., Loddo, V., De Pasquale, C., Marsala, V., Alonzo, G., & Palmisano, L. Nature of interactions at the interface of two water-saturated commercial  $\text{TiO}_2$  polymorphs. *J. Phys. Chem. C* **117**, 5269–5273 (2013).

41. Korb, J.-P. Multiscale nuclear magnetic relaxation dispersion of complex liquids in bulk and confinement. *Prog. Nucl. Magn. Reson. Spectrosc.* **104**, 12–55 (2018).
42. Korb, J. P., Godefroy, S. & Fleury, M. Surface nuclear magnetic relaxation and dynamics of water and oil in granular packings and rocks. *Magn. Reson. Imaging* **21**, 193–199 (2003).
43. Ward-Williams, J., Korb, J.-P. & Gladden, L. F. Insights into functionality-specific adsorption dynamics and stable reaction intermediates using Fast Field Cycling NMR. *J. Phys. Chem. C* **122**, 20271–20278 (2018).
44. Hsu, C.-W., Chen, Y.-W., Rana, B. S., Kumar, R., Sinha, A. K. & Hwang, D. W. Dynamics of water in hierarchical mesoporous H-ZSM-5 by Fast Field-Cycling NMR relaxometry. *J. Phys. Chem. C* **118**, 20481–20487 (2014).
45. Korb, J.-P., Whaley-Hodges, M. & Bryant, R. G. Translational diffusion of liquids at surfaces of microporous materials: theoretical analysis of field-cycling magnetic relaxation measurements. *Phys. Rev. E* **56**, 1934–1945 (1997).
46. Godefroy, S., Korb, J.-P., Fleury, M. & Bryant, R. G. Surface nuclear magnetic relaxation and dynamics of water and oil in macroporous media. *Phys. Rev. E* **64**, 021605 (2001).
47. Muncaci, S., Mattea, C., Stapf, S. & Ardelean, I. Frequency-dependent NMR relaxation of liquids confined inside porous media containing an increased amount of magnetic impurities. *Magn. Reson. Chem.* **51**, 123–128 (2013).
48. Barberon, F., Korb, J.-P., Petit, D., Morin, V. & Bermejo, E. Probing the surface area of a cement-based material by nuclear magnetic relaxation dispersion. *Phys. Rev. Lett.* **90**, 116103 (2003).
49. Chemmi, H., Petit, D., Levitz, P., Denoyel, R., Galarneau, A. & Korb, J.-P. Noninvasive experimental evidence of the linear pore size dependence of water diffusion in nanoconfinement. *J. Phys. Chem. Lett* **7**, 45 (2016).
50. Bubici, S., Korb, J.-P., Kučerik, J. & Conte, P. Evaluation of the surface affinity of water in three biochars using fast field cycling NMR relaxometry. *Magn. Reson. Chem.* **54**, 365–370 (2016).

51. Godefroy, S., Fleury, M., Deflandre, F. & Korb, J.-P. Temperature effect on NMR surface relaxation in rocks for well logging applications. *J. Phys. Chem. B* **106**, 11183–11190 (2002).
52. Korb, J.-P., Nicot, B., Louis-Joseph, A., Bubici, S. & Ferrante, G. Dynamics and wettability of oil and water in oil shales. *J. Phys. Chem. C* **118**, 23212–23218 (2014).
53. Faux, D. A., Cachia, S.-H. P., McDonald, P. J., Bhatt, J. S., Howlett, N. C. & Churakov, S. V. Model for the interpretation of nuclear magnetic resonance relaxometry of hydrated porous silicate materials. *Phys. Rev. E* **91**, 032311 (2015).
54. Faux, D. A. & McDonald, P. J. Explicit calculation of nuclear-magnetic-resonance relaxation rates in small pores to elucidate molecular-scale fluid dynamics. *Phys. Rev. E* **95**, 33117 (2017).
55. Faux, D. A. & McDonald, P. J. A model for the interpretation of nuclear magnetic resonance spin-lattice dispersion measurements on mortar, plaster paste, synthetic clay and oil-bearing shale. *Microporous Mesoporous Mater.* **269**, 39–42 (2018).
56. Bychuk, O. V. & O’Shaughnessy, B. Anomalous surface diffusion: a numerical study. *J. Chem. Phys.* **101**, 772–780 (1994).
57. Stapf, S., Kimmich, R. & Seitter, R.-O. Field-Cycling NMR relaxometry of liquids confined in porous glass: evidence for Levy-walks. *Magn. Reson. Imaging* **14**, 772–780 (1996).
58. Kimmich, R. & Fatkullin, N. Self-diffusion studies by intra- and inter-molecular spin-lattice relaxometry using field-cycling: liquids, plastic crystals, porous media, and polymer segments. *Prog. Nucl. Magn. Reson. Spectrosc.* **101**, 18–50 (2017).
59. Levitz, P. Random flights in confining interfacial systems. *J. Phys. Condens. Matter* **17**, 4059–4074 (2005).
60. Levitz, P., Grebenkov, D. S., Zinsmeister, M., Kolwankar, K. M. & Sapoval, B. Brownian flights over a fractal nest and first-passage statistics on irregular surfaces. *Phys. Rev. Lett.* **96**, 180601 (2006).
61. Levitz, P., Zinsmeister, M., Davidson, P., Constantin, D. & Poncelet, O. Intermittent Brownian dynamics over a rigid strand: heavily tailed relocation statistics in a simple

- geometry. *Phys. Rev. E* **78**, 030102 (2008).
62. Levitz, P., Bonnaud, P. A., Cazade, P.-A., Pellenq, J.-M. & Coasne, B. Molecular intermittent dynamics of interfacial water: probing adsorption and bulk confinement. *Soft Matter* **9**, 8654–8663 (2013).
  63. Levitz, P. Probing interfacial dynamics of water in confined nanoporous systems by NMRD. *Mol. Phys.* **117**, 952–959 (2019).
  64. Korb, J.-P. & Levitz, P. E. Direct probing of the wettability of plaster pastes at the nanoscale by proton Field Cycling Relaxometry. *AIP Conf. Proc.* **1081**, 55 (2008).
  65. Ferrante, G. & Sykora, S. Technical aspects of Fast Field Cycling. *Adv. Inorg. Chem.* **57**, 405–470 (2005).
  66. Kimmich, R. & Anordo, E. Field-cycling NMR relaxometry. *Prog. Nucl. Magn. Reson. Spectrosc.* **44**, 257–320 (2004).
  67. Ward-Williams, J. & Gladden, L. F. Insights into adsorption behaviour of binary liquid mixtures in porous media using fast field cycling NMR. *Magn. Reson. Imaging* **56**, 57–62 (2018).
  68. Neudert, O., Mattea, C. & Stapf, S. Application of CPMG acquisition in Fast-Field-Cycling relaxometry. *Microporous Mesoporous Mater.* **269**, 103–108 (2018).
  69. Tayler, M. C. D., Ward-Williams, J. & Gladden, L. F. NMR relaxation in porous materials at zero and ultralow magnetic fields. *J. Magn. Reson.* **297**, 1–8 (2018).
  70. Bodenstedt, S., Mitchell, M. W. & Tayler, M. C. D. Fast-field-cycling ultralow-field nuclear magnetic relaxation dispersion. *Nat. Commun.* **12**, 4041 (2021).
  71. Granick, S. Motions and relaxations of confined liquids. *Science* **253**, 1374–1379 (1991).
  72. Richert, R. Dynamics of nanoconfined supercooled liquids. *Annu. Rev. Phys. Chem.* **62**, 65–84 (2011).
  73. Christenson, H. K. Confinement effects on freezing and melting. *J. Phys. Condens. Matter* **13**, 95–133 (2001).

74. Huber, P. Soft matter in hard confinement: phase transition thermodynamics, structure, texture, diffusion and flow in nanoporous media. *J. Phys. Condens. Matter* **27**, 103102 (2015).
75. Goldammer, E. & Zeidler, M. Molecular motion in aqueous mixtures with organic liquids by nmr relaxation measurements. *Ber. Bunsenges. Phys. Chem.* **73**, 4–15 (1969).
76. Yabunaka, S., Okamoto, R. & Onuki, A. Phase separation in a binary mixture confined between symmetric parallel plates: capillary condensation transition near the bulk critical point. *Phys. Rev. E* **87**, 032405 (2013).
77. Tanaka, H. & Araki, T. Surface effects on spinodal decomposition of incompressible binary fluid mixtures. *EPL* **51**, 154 (2000).
78. Chen, W. Phase separation of binary nonadditive hard sphere fluid mixture confined in random porous media. *J. Chem. Phys.* **139**, 154712 (2013).
79. Elamin, K., Jansson, H., Kittaka, S. & Swenson, J. Different behavior of water in confined solutions of high and low solute concentrations. *Phys. Chem. Chem. Phys.* **15**, 18437–18444 (2013).
80. Swenson, J., Elamin, K., Chen, G., Lohstroh, W. & Sakai, V. G. Anomalous dynamics of aqueous solutions of di-propylene glycol methylether confined in MCM-41 by quasielastic neutron scattering. *J. Chem. Phys.* **141**, 214501 (2014).
81. Elamin, K., Jansson, H. & Swenson, J. Dynamics of aqueous binary glass-formers confined in MCM-41. *Phys. Chem. Chem. Phys.* **17**, 12978–12987 (2015).
82. Goldemberg, J. Ethanol for a sustainable energy future. *Science* **315**, 808–810 (2007).
83. Vane, L. M. A review of pervaporation for product recovery from biomass fermentation processes. *J. Chem. Technol. Biot.* **80**, 603–629 (2005).
84. Wang, C. H., Bai, P., Siepmann, J. I. & Clark, A. E. Deconstructing hydrogen-bond networks in confined nanoporous materials: implications for alcohol-water separation. *J. Phys. Chem. C* **118**, 19723–19732 (2014).
85. Kumar, S., Singh, N. & Prasad, R. Anhydrous ethanol: A renewable source of energy.

- Renew. Sustain. Energy Rev.* **14**, 1830–1844 (2010).
86. El-Roz, M., Bazin, P., Birsa Čelič, T., Zabukovec Logar, N. & Thibault-Starzyk, F. Pore occupancy changes water/ethanol separation in a metal-organic framework - quantitative map of coadsorption by IR. *J. Phys. Chem. C* **119**, 22570–22576 (2015).
  87. Gravelle, S., Yoshida, H., Joly, L., Ybert, C. & Bocquet, L. Carbon membranes for efficient water-ethanol separation. *J. Chem. Phys.* **145**, 124708 (2016).
  88. Harrach, M. F., Drossel, B., Winschel, W., Gutmann, T. & Buntkowsky, G. Mixtures of isobutyric acid and water confined in cylindrical silica nanopores revisited: a combined solid-state NMR and molecular dynamics simulation study. *J. Phys. Chem. C* **119**, 28961–28969 (2015).
  89. Barnette, A. L. & Kim, S. H. Coadsorption of n-propanol and water on SiO<sub>2</sub>: study of thickness, composition, and structure of binary adsorbate layer using attenuated total reflection infrared (ATR-IR) and sum frequency generation (SFG) vibration spectroscopy. *J. Phys. Chem. C* **116**, 9909–9916 (2012).
  90. Guo, X.-Y., Watermann, T. & Sebastiani, D. Local microphase separation of a binary liquid under nanoscale confinement. *J. Phys. Chem. B* **118**, 10207–10213 (2014).
  91. Abdel Hamid, A. R., Mhanna, R., Lefort, R., Ghoufi, A., Alba-Simionesco, C., Frick, B. & Morineau, D. Microphase separation of binary liquids confined in cylindrical pores. *J. Phys. Chem. C* **120**, 9245–9252 (2016).
  92. Mhanna, R., Abdel Hamid, A. R., Dutta, S., Lefort, R., Noirez, L., Frick, B. & Morineau, D. More room for microphase separation: an extended study on binary liquids confined in SBA-15 cylindrical pores. *J. Chem. Phys.* **146**, 024501 (2017).
  93. Krycka, K. L., Dura, J. A., Langston, L. J. & Burba, C. M. Nanoconfinement-induced phase segregation of binary benzene-cyclohexane solutions within a chemically inert matrix. *J. Phys. Chem. C* **122**, 7676–7684 (2018).
  94. Muthulakshmi, T., Dutta, D., Maheshwari, P. & Pujari, P. K. Evidence for confinement induced phase separation in ethanol-water mixture: a positron annihilation study. *J. Phys. Condens. Matter* **30**, 025001 (2018).
  95. Essafri, I., Morineau, D. & Ghoufi, A. Microphase separation of a miscible binary

- liquid mixture under confinement at the nanoscale. *npj Comput. Mater.* **5**, 1–10 (2019).
96. Mhanna, R., Catrou, P., Dutta, S., Lefort, R., Essafri, I., Ghoufi, A., Muthmann, M., Zamponi, M., Frick, B. & Morineau, D. Dynamic heterogeneities in liquid mixtures confined in nanopores. *J. Phys. Chem. B* **124**, 3152–3162 (2020).
  97. Abdel Hamid, A. R., Lefort, R., Lechaux, Y., Moréac, A., Ghoufi, A., Alba-Simionesco C. & Morineau, D. Solvation effects on self-association and segregation processes in tert-butanol-aprotic solvent binary mixtures. *J. Phys. Chem. B* **117**, 10221–10230 (2013).
  98. Dutta, S., Lefort, R., Morineau, D., Mhanna, R., Merdrignac-Conanec, O., Saint-Jalmesa A. & Leclercq, T. Thermodynamics of binary gas adsorption in nanopores. *Phys. Chem. Chem. Phys.* **18**, 24361–24369 (2016).
  99. Mhanna, R., Lefort, R., Noirez, L. & Morineau, D. Microstructure and concentration fluctuations in alcohol-toluene and alcohol-cyclohexane binary liquids: a small angle neutron scattering study. *J. Mol. Liq.* **218**, 198–207 (2016).
  100. Abdel Hamid, A. R., Mhanna, R., Catrou, P., Bulteau, Y., Lefort, R. & Morineau, D. Multiple glass transitions of microphase separated binary liquids confined in MCM-41. *J. Phys. Chem. C* **120**, 11049–11053 (2016).
  101. Dixit, S., Crain, J., Poon, W. C. K., Finney, J. L. & Soper, A. K. Molecular segregation observed in a concentrated alcohol-water solution. *Nature* **416**, 829–832 (2002).
  102. Price, W. S., Ide, H. & Arata, Y. Solution dynamics in aqueous monohydric alcohol systems. *J. Phys. Chem. A* **107**, 4784–4789 (2003).
  103. Guo, J. H., Luo, Y., Augustsson, A., Kashtanov, S., Rubensson, J. E., Shuh, D. K., Ågren, H., Nordgren, J. Molecular structure of alcohol-water mixtures. *Phys. Rev. Lett.* **91**, 157401 (2003).
  104. Lin, K., Hu, N., Zhou, X., Liu, S. & Luo, Y. Reorientation dynamics in liquid alcohols from Raman spectroscopy. *J. Raman Spectrosc.* **43**, 82–88 (2012).
  105. Corsaro, C., Maisano, R., Mallamace, D. & Dugo, G. <sup>1</sup>H NMR study of water/methanol solutions as a function of temperature and concentration. *Phys. A Stat. Mech. its Appl.* **392**, 596–601 (2013).

106. Faux, D. A. & McDonald, P. J. Nuclear-magnetic-resonance relaxation rates for fluid confined to closed, channel, or planar pores. *Phys. Rev. E* **96**, 063110 (2018).



## 4. FFC-NMR of binary liquid mixtures: a case study of THF-water and THF-decane mixtures imbibed within anatase titania and $\gamma$ -alumina

### 4.1 Introduction

For many years, scientists have worked towards understanding the dynamics of heterogeneous systems. While much progress has been made for single liquids imbibed within a porous material, the complexity of the problem increases significantly when, for example, a mixture of liquids is introduced inside a porous medium<sup>1-3</sup>.

As shown in chapter 3, NMR is a much-used tool that can study liquids inside porous media *in situ*, at high temperature and pressure, as they are used in the chemical industry<sup>4</sup>. Recently, Fast Field Cycling (FFC) NMR has been shown to be highly sensitive to surface-adsorbate interactions, making it a promising additional technique to study the dynamics of liquids in a range of porous media, including porous silica glasses<sup>5-7</sup>, cement pastes<sup>8-10</sup>, rock cores<sup>11-13</sup>, granular packings<sup>14</sup> and catalyst supports<sup>15,16</sup>. Moreover, FFC-NMR has been applied to tetrahydrofuran (THF)-methanol and THF-cyclohexane mixtures in  $\gamma$ -alumina, demonstrating it is possible to measure liquid mixtures imbibed within porous media using FFC-NMR<sup>17</sup>.

In this chapter, FFC-NMR will be used to study surface-adsorbate interactions of liquid mixtures imbibed within anatase titania. The binary mixtures in this study are THF-water and THF-decane, which will be considered as model systems for the binary mixtures studied in later chapters. The titania surface is highly polar. This means it is expected that water, being a highly polar solvent, interacts strongly with the surface. The polarity of THF is moderate, 0.207 relative to a polarity of 1 for water<sup>18</sup>, which means a moderate interaction with the surface is expected. Decane, as a strongly nonpolar solvent, is expected to show weak interaction with the polar titania surface. Therefore the combination of THF-water and THF-decane mixtures on titania provides a full range of possible interaction strengths, which allows us to extrapolate our results to other solvents on the same support. The mixtures will also be imbibed within  $\gamma$ -alumina, in order to make a comparison with the literature<sup>17</sup>.  $\gamma$ -alumina is a highly polar support, much like anatase titania, and therefore the interactions are expected to be similar for both supports.

Considering FFC-NMR is a relatively new technique, the FFC-NMR results will also be benchmarked against a more conventional high field NMR relaxometry technique. At fixed magnetic fields, the fraction between the relaxation rates in a bulk liquid and the liquid adsorbed on a porous medium,  $\eta = T_{1,\text{bulk}}/T_{1,\text{pore}}$ , gives insight on the interaction strength between the liquid and the surface<sup>19</sup>. The comparison of the two techniques will be used to highlight advantages and challenges for each of the techniques.

## 4.2 Materials and methods

### 4.2.1 Sample preparation

Anatase titania and  $\gamma$ -alumina in the form of 1/8" pellets were obtained from Alfa Aesar. A BET and BJH analysis of the anatase titania pellets showed a surface area of 161 m<sup>2</sup> g<sup>-1</sup> and an average pore diameter of 9.5 nm. The pore volume was determined to be 0.39 cm<sup>3</sup> g<sup>-1</sup> by gravimetric measurements. Unfortunately, no further information about the titania, for example about paramagnetic impurities, is available. For  $\gamma$ -alumina, the surface area was 202 m<sup>2</sup> g<sup>-1</sup>, the average pore diameter was 9.1 nm, and the pore volume was 0.60 cm<sup>3</sup> g<sup>-1</sup>. Previously, Electron spin resonance (ESR) measurements showed the presence of paramagnetic Fe<sup>3+</sup> in the  $\gamma$ -alumina<sup>16</sup>. Tetrahydrofuran (THF, with 250 ppm BHT stabiliser) and n-decane were obtained from AlfaAesar at >99% purity, and used as received.

Titania and  $\gamma$ -alumina pellets were dried overnight at 120 °C, after which the pellets were imbibed in the desired pure liquid or liquid mixture overnight. Extra-pellet liquid was removed by drying the sample with filter paper directly before the NMR experiments, leaving only the desired liquid imbibed within the pellets.

### 4.2.2 FFC-NMR and processing

FFC-NMR experiments were performed at room temperature (298 K  $\pm$  1 K) on a Stellar Spinmaster Duo relaxometer. <sup>1</sup>H NMR dispersion (NMRD) profiles were obtained at 25 logarithmically spaced <sup>1</sup>H Larmor frequencies between 10 kHz and 40 MHz. For field strengths above 10 MHz the non-polarized sequence was used, for field strengths below 10 MHz the pre-polarized sequence was used. At each frequency,  $T_1$  curves were produced using 32 logarithmically spaced delay times between 1 ms and 5.69 $T_1$ . The polarization time and recycle delay was optimized to be  $\geq 5.69T_1$ . The polarization field was set at 25 MHz and the acquisition field was set to 16.3 MHz <sup>1</sup>H Larmor frequency.

All data was processed using Matlab 2017b. Figure 4.1 shows an example of the main fitting procedures using a 15:85 mol% THF-water mixture. An in-house script for an inverse Laplace transform (ILT) using Tikhonov regularisation confirmed the presence of one  $T_1$  peak in the FFC-NMR experiments on water, THF and decane imbibed within titania and  $\gamma$ -alumina (Figure 4.1a)<sup>20</sup>. For the THF-water and THF-decane mixtures, the ILT showed two  $T_1$  peaks (Figure 4.1b). Finally, biexponential fits to the  $T_1$  curves obtained by FFC-NMR were used to obtain two  $R_1 = 1/T_1$  components, corresponding to water and THF, or THF and decane (Figure 4.1c). Equivalent plots were obtained for the other mixtures.

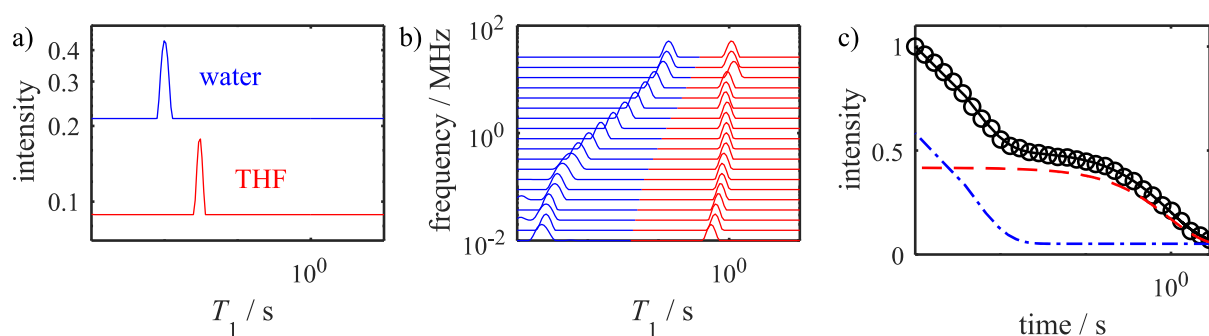


Figure 4.1: An inverse Laplace transform of a) pure water and pure THF, and b) a 15:85 THF-water mixture, each imbibed within anatase titania. c) The corresponding biexponential fit to the  $T_1$  curve obtained at  $\omega_0 = 0.09$  MHz, showing the THF component in red, the water component in blue, and the full fit to the data in black.

Based on the relaxation rates with respect to the pure liquid relaxation rates, and populations of each component, it was concluded that for THF-water mixtures, the higher  $R_1$  component at each frequency corresponds to water, and the lower  $R_1$  component corresponds to THF. For THF-decane mixtures the higher  $R_1$  component corresponds to THF, and the lower  $R_1$  component corresponds to decane.

#### 4.2.3 Fixed field NMR methods

Fixed field NMR experiments were performed at room temperature (298 K) on a Bruker DMX-300 (7 T) NMR spectrometer. For every sample, a single-pulse experiment was performed in order to obtain a high resolution  $^1\text{H}$  NMR spectrum.  $T_1$  values were obtained using an inversion recovery experiment. 4 scans at 32 delay times between 0.01 and 20s were obtained for every  $T_1$  curve. The spectral width was 20 kHz and 2048 points were recorded per FID with a dwell time of 25 $\mu$ s. The RF frequency was 250 kHz for all experiments, and the recycle delay was set to 25s.

All experiments were analysed using Matlab 2017b.  $T_1$  values were determined from mono- (single liquids and bulk mixtures) and biexponential fits (binary liquids in porous media) to the inversion recovery experiments. For the bulk liquids,  $T_1$  values were determined for each species separately. Mixture compositions were obtained from the relative integrals of the high resolution  $^1\text{H}$  NMR spectra. For all experiments, at minimum one of the THF peaks was fully separated from the water/decane peaks. For simplicity, it is assumed the two THF peaks have the same integral. The extracted mixture compositions were subsequently used as initial guess for the intensities in the biexponential  $T_1$  fits on binary liquids on porous media.

#### 4.2.4 Composition analysis

For a range of mixtures on both supports, the intra-pellet mixture compositions were determined using fixed field NMR ( $^1\text{H}$  NMR spectrum and relative intensities of a biexponential  $T_1$  fit) and FFC-NMR (relative intensities of a biexponential  $T_1$  fit, at 7MHz and the average across the full NMRD profile). This allowed for a detailed composition analysis. The compositions for each of the experiments used in this analysis are shown in appendix A. Sample-to-sample errors were determined based on two separately prepared samples. The error corresponds to the standard deviation for a small sample of the full population:  $\text{STD} = \sqrt{\frac{\sum(x_i - \bar{x})^2}{n-1}}$ . The average intra-pore compositions for the two separately prepared samples, the corresponding bulk mixture compositions, and the corresponding sample-to-sample errors are shown in Table 4.1.

*Table 4.1: Mixture compositions in THF mol%, and sample-to-sample composition errors for fixed field NMR and FFC-NMR methods. Bulk compositions correspond to the gravimetrically determined bulk liquid mixtures that were used to imbibe the porous media. For fixed field NMR experiments, the compositions were determined by a spectral analysis and through a biexponential  $T_1$  fit. For the FFC-NMR experiments, two compositions determined through a biexponential fit are shown, namely the composition at 7 MHz, and the average of the compositions across the full frequency range.*

Support	Mixture	Fixed field NMR			FFC-NMR		
		Bulk	Intra-pore		Bulk	Intra-pore	
			$^1\text{H}$ spectrum	$T_1$ fit		7 MHz	Average
titania	THF-water	20.0±0.0	12.4±1.3	11.5±0.6	19.9±0.1	10.8±3.6	11.6±4.5
titania	THF-water	50.1±0.6	30.1±4.5	30.3±2.1	49.8±0.1	31.5±0.8	37.2±1.2
titania	THF-water	69.2±0.1	45.6±6.3	46.6±0.2	-	-	-
titania	THF-water	82.6±0.1	57.6±2.3	59.5±3.1	-	-	-
titania	THF-decane	50.5±0.1	47.8±4.6	43.5±4.0	50.4±0.0	49.0±0.6	43.8±1.6
$\gamma$ -alumina	THF-water	20.0±0.0	12.2±3.2	11.8±1.1	19.9±0.1	9.9±3.2	10.4±3.5
$\gamma$ -alumina	THF-water	50.1±0.6	27.6±4.9	25.2±6.0	49.8±0.1	25.4±5.4	27.7±6.5
$\gamma$ -alumina	THF-decane	50.4±0.4	58.0±2.4	51.7±6.6	50.3±0.2	50.9±1.6	49.8±1.9

For the THF-water samples the intra-pellet composition is higher in water content than the corresponding bulk mixture, indicating strong preferential adsorption of water. This can be explained by the polar nature of the surfaces of  $\gamma$ -alumina and anatase titania. For the THF-decane mixtures, the intra-pellet compositions correspond to the bulk compositions very well. This suggests there is no preferential adsorption for either of the liquids. Considering the relatively low polarities of both THF and decane, this is as expected.

Generally, the high field NMR and FFC-NMR intra-pellet mixture compositions correspond well. However, the “average” FFC-NMR compositions appear to favour the slower component, i.e. the component with the longer relaxation time. The effect is at its most significant for low water content THF-water mixtures. In Figure 4.2, the composition is plotted against the Larmor frequency for three different THF-water mixtures imbibed within anatase titania and  $\gamma$ -alumina, which shows that for low water content mixtures, the water content appears to go down with a decreasing Larmor frequency.

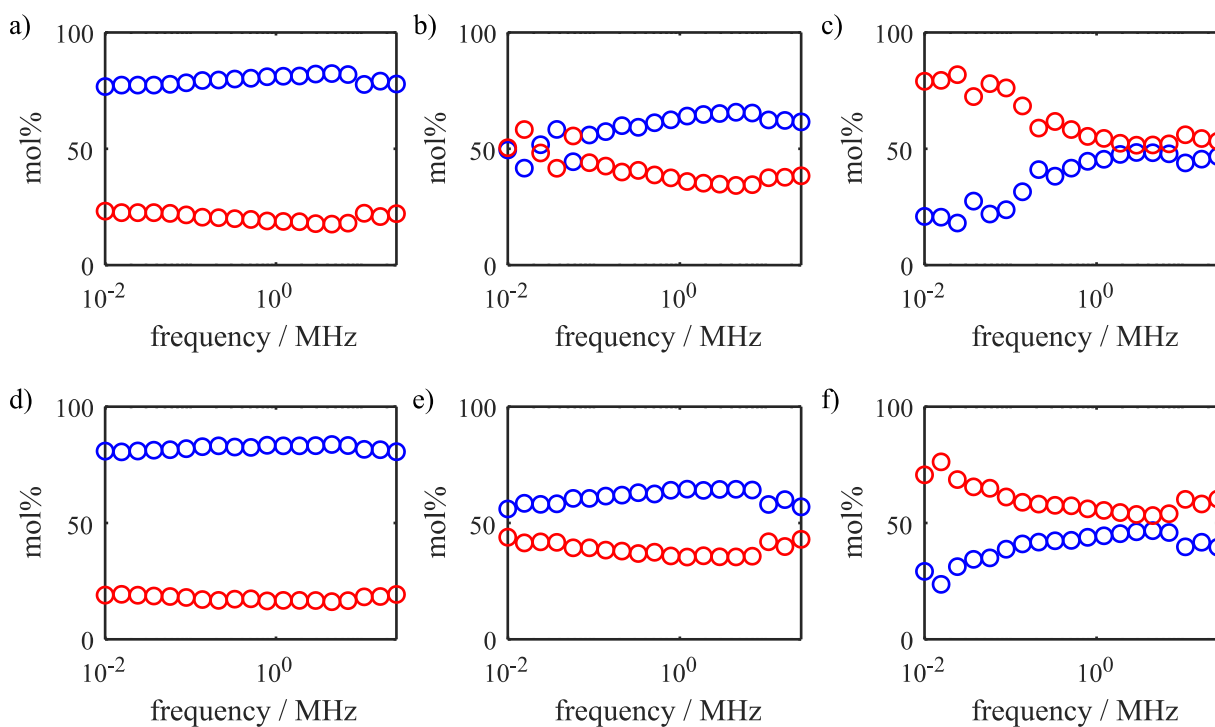


Figure 4.2: THF-water compositions in anatase titania (a-c) and  $\gamma$ -alumina (d-ef), extracted from biexponential fits from FFC-NMR experiments, plotted against the Larmor frequency. The water composition in mol% is shown in blue, THF is shown in red. The THF-water compositions at 7 MHz (shown in appendix A0) are a) 13.3:86.7, b) 32.1:67.9, c) 52.6:47.4, d) 12.1:87.9, e) 29.2:70.8, and f) 52.3:47.7.

The primary reason for this error is that the relaxation rate of water in these mixtures is on the edge of accurate detection, as will be shown in the  $^1\text{H}$  NMRD profiles in section 4.3. In other words, the water signal is decaying too fast for quantitative detection. Additionally, the water  $^1\text{H}$  signal is smaller than its content in mol%, because a water molecule contains two hydrogen atoms, whereas a THF molecule contains eight. This means the accuracy of the composition is further decreased as the water content decreases.

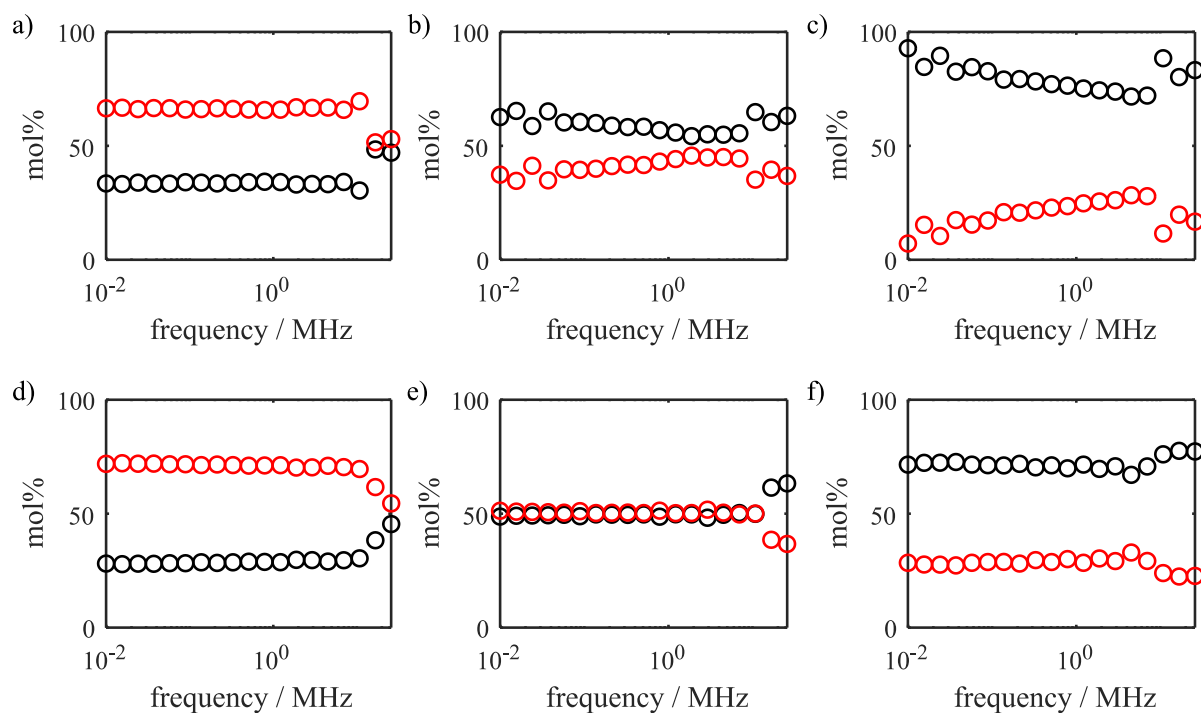


Figure 4.3: THF-decane compositions in anatase titania (a-c) and  $\gamma$ -alumina (d-f), extracted from biexponential fits from FFC-NMR experiments, plotted against the Larmor frequency. The THF composition in mol% is shown in red, decane is shown in black. The THF-decane compositions at 7 MHz (shown in appendix A0) are a) 65.8:34.2, b) 49.4:50.6, c) 27.9:72.1, d) 70.4:29.6, e) 49.7:50.3, and f) 29.2:70.8.

For the THF-decane mixtures, especially when imbibed within  $\gamma$ -alumina, this effect is reduced compared to the THF-water mixtures, see Figure 4.3. The lower relaxation rates of THF and decane, compared to water, result in a smaller loss of signal, and therefore in a smaller, more consistent error in compositions.

Hereafter, the intra-pellet mixture compositions shown for FFC-NMR experiments correspond to the compositions at 7 MHz, in order to avoid any signal loss due to fast relaxation. For fixed field NMR experiments, the mixture compositions that will be shown are those extracted from the  $^1\text{H}$  NMR spectra.

### 4.3 FFC-NMR results

Figure 4.4 shows the NMRD profiles of the THF and water components in a series of THF-water mixtures imbibed within anatase titania and  $\gamma$ -alumina. The equivalent profiles for THF-decane mixtures are shown in Figure 4.5. All NMRD profiles are shown with a logarithmic  $R_1$  axis. It has been previously shown that for similar systems, the NMRD profiles can be fitted to a power law<sup>5,21-23</sup>. The exponent of a power law corresponds to the slope of the profiles in a log-log plot. Therefore it is more suitable to use the logarithmic axis for qualitative interpretation, rather than a linear  $R_1$  axis.

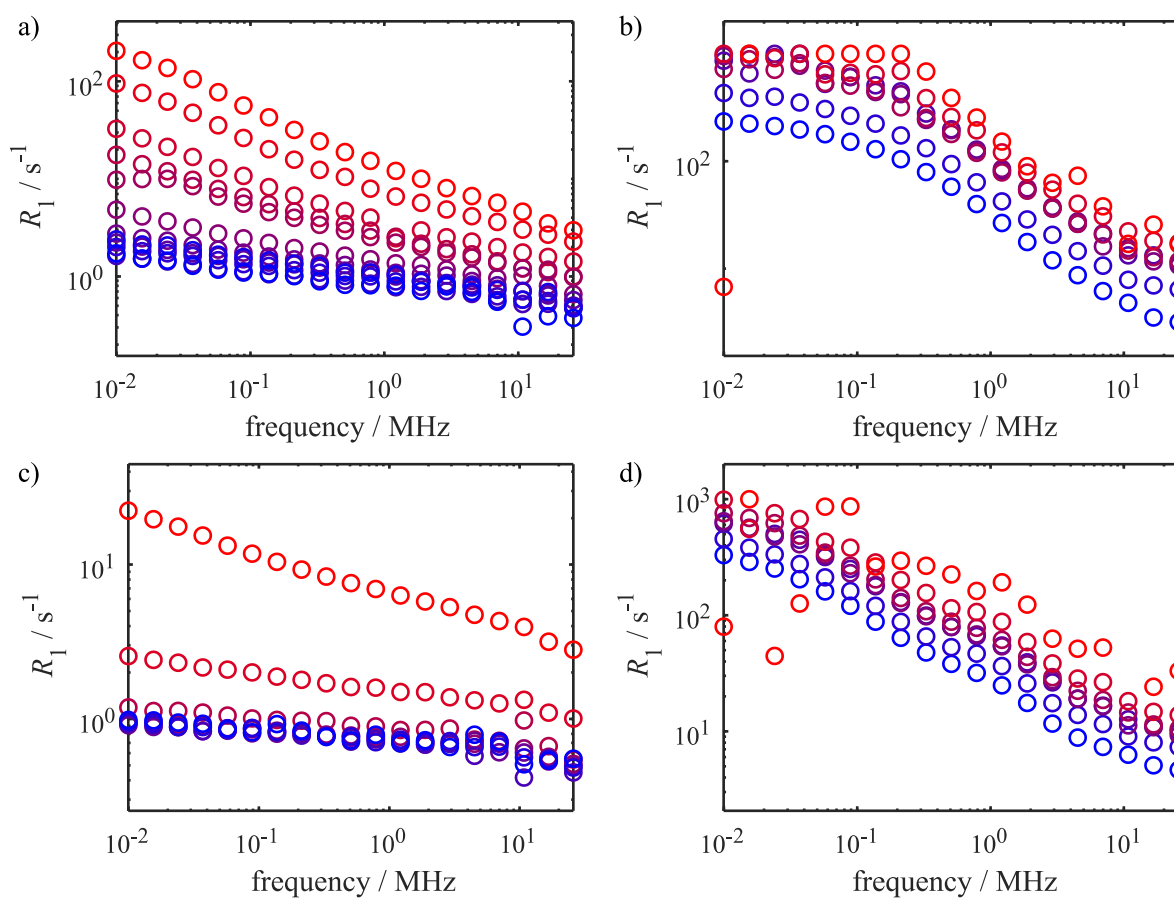


Figure 4.4:  $^1\text{H}$  NMRD profiles for THF (a,c), and water (b,d) components in a series of THF-water mixtures imbibed within anatase titania (a,b) and  $\gamma$ -alumina (c,d). Red profiles correspond to THF-rich mixtures, blue profiles correspond to water-rich mixtures.

An initial visual analysis shows that in the THF-water mixtures, the profiles of the THF component decrease as the THF content decreases. The reduction in relaxation rate is more prominent toward the lower frequency end than at the higher frequency end. As a result, the slope of the THF component also decreases with a decrease in THF content.

For the water component, the relaxation rates increase across the full frequency range as the water content decreases. The lowest water-containing mixture (30% water) shows a clear plateau at  $R_1 \approx 1000 \text{ s}^{-1}$ , corresponding to a relaxation time of approximately 1 ms. Considering the field switching time is 3 ms, this means that only 5% of the original signal will be detected. Therefore the relaxation rates at the low frequency end in this sample, and samples containing less water, are inaccurate. Additionally, the populations of the two components are inaccurate, as was shown in section 4.2.4. As a result, the water component in THF-water mixtures with <30 mol% water will be disregarded.

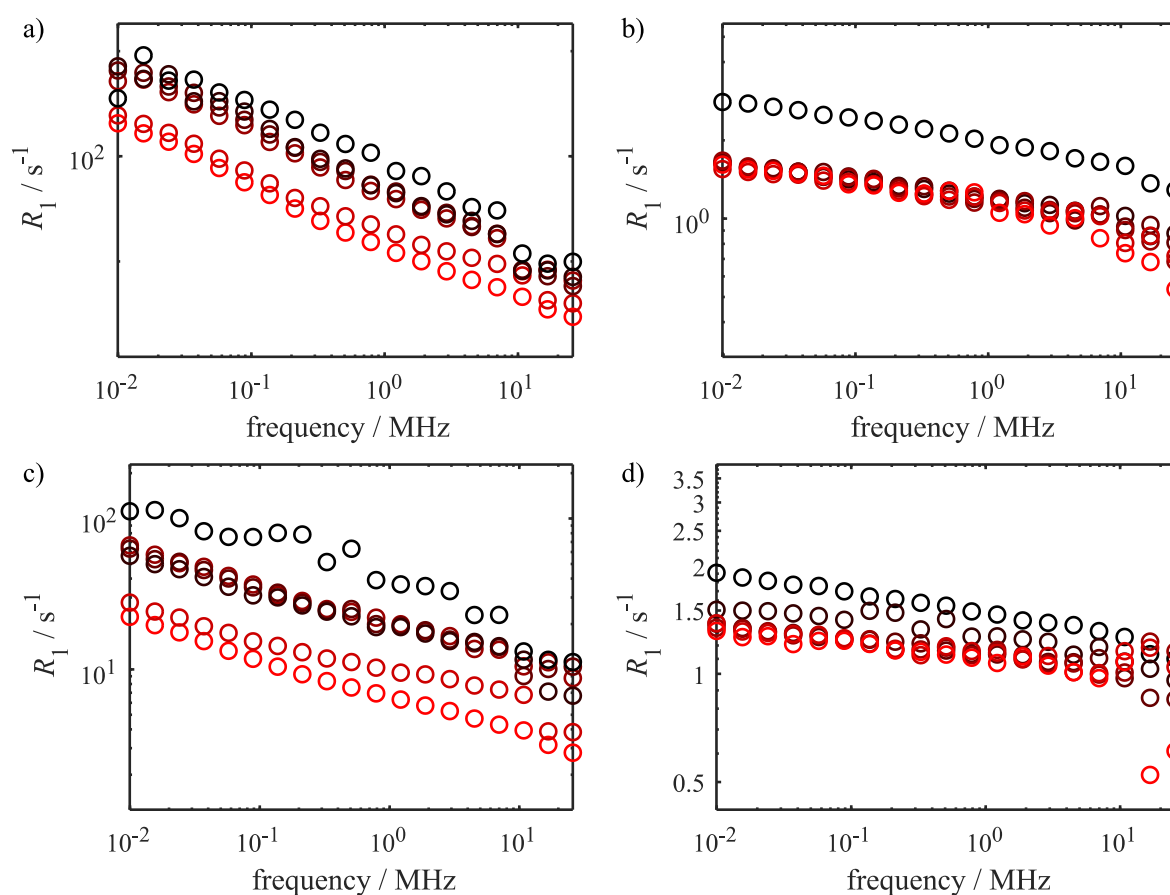


Figure 4.5:  $^1\text{H}$  NMRD profiles for THF (a,c), and decane (b,d) components in a series of THF-decane mixtures imbibed within anatase titania (a,b) and  $\gamma$ -alumina (c,d). Red profiles correspond to THF-rich mixtures, black profiles correspond to decane-rich mixtures.

In the THF-decane mixtures, the NMRD profiles of which are shown in Figure 4.5, the THF relaxation rates increase with a decrease in THF composition, and the decane relaxation rates decrease as the decane content decreases. For both THF and decane, this is the case across the full frequency range. The relaxation rates fall within the limits of detection, therefore the profiles are all considered accurate.

The  $^1\text{H}$  NMRD profiles of liquid mixtures inside a porous medium depend on two factors that affect the relaxation rate, namely the surface mixture composition and the surface dynamics of each component.

#### 4.3.1 Surface composition

The surface mixture composition can be determined through a rearrangement of the two-phase fast exchange (TPFE) model<sup>24</sup> shown in section 2.3.6.1:

$$R_{1i,\text{obs}} = R_{1i,\text{bulk}} + p_{i,\text{surf}}(R_{1i,\text{surf}} - R_{1i,\text{bulk}}), \quad (4.1)$$

where  $R_{1i,\text{obs}}$ ,  $R_{1i,\text{bulk}}$  and  $R_{1i,\text{surf}}$  are the observed, bulk and surface-affected longitudinal relaxation rates respectively, and  $p_{i,\text{surf}} = V_{i,\text{surf}}/(V_{i,\text{surf}} + V_{i,\text{bulk}})$  is the relative surface volume fraction of species  $i = 1,2$ .  $V_{i,\text{surf}}$ , the surface or adsorbed volume, contains all molecules affected by the surface, which may include more than simply the monolayer of molecules directly next to the surface.  $V_{i,\text{bulk}}$  corresponds to the bulk-in-the-pore volume. It is assumed there is no interspecies relaxation.

From this equation, it is clear that  $R_{1i,\text{obs}}$  will vary with the mixture composition. Upon the reduction of a stronger interacting species in a mixture, the value for  $p_{i,\text{surf}}$  of the stronger interacting component will increase, as the value for  $V_{i,\text{bulk}}$  for the stronger interacting component decreases. The result is an increase in the relaxation rate of the stronger interacting species. For the weaker interacting species, the opposite is true. As the content of the weaker interacting species is decreased,  $V_{i,\text{surf}}$  decreases, and therefore the relaxation rate decreases.

Following the two-phase fast exchange model, it can therefore be concluded that in the THF-water mixtures, water is the stronger interacting species, and THF is the weaker interacting species. For THF-decane mixtures, THF is the stronger interacting species, and decane is the weaker interacting species.

### 4.3.1.1 Filling factor analysis

In order to further highlight the difference between stronger and weaker interacting species in a mixture, a filling factor analysis is conducted. The pore filling factor can be expressed as  $f_i = \frac{V_{i,\text{surf}} + V_{i,\text{bulk}}}{V}$ , so that equation (4.1) can be rewritten to:

$$R_{1i,\text{obs}} \approx R_{1i,\text{bulk}} + \frac{V_{i,\text{surf}}}{V f_i} R_{1i,\text{surf}}. \quad (4.2)$$

For the stronger interacting species in a mixture, it is expected that the surface dynamics do not change significantly, i.e. in the TPF model,  $R_{1i,\text{surf}}$  is constant at a given Larmor frequency. In this case, following equation (4.2), the increase in the observed relaxation rate is proportional to the inverse filling factor,  $f_i^{-1}$ . Figure 4.6 and Figure 4.7 show the relaxation rates of the water and THF components in THF-water mixtures, and the THF and decane components in THF-decane mixtures respectively, plotted against the inverse filling factor for a range of relaxation frequencies.

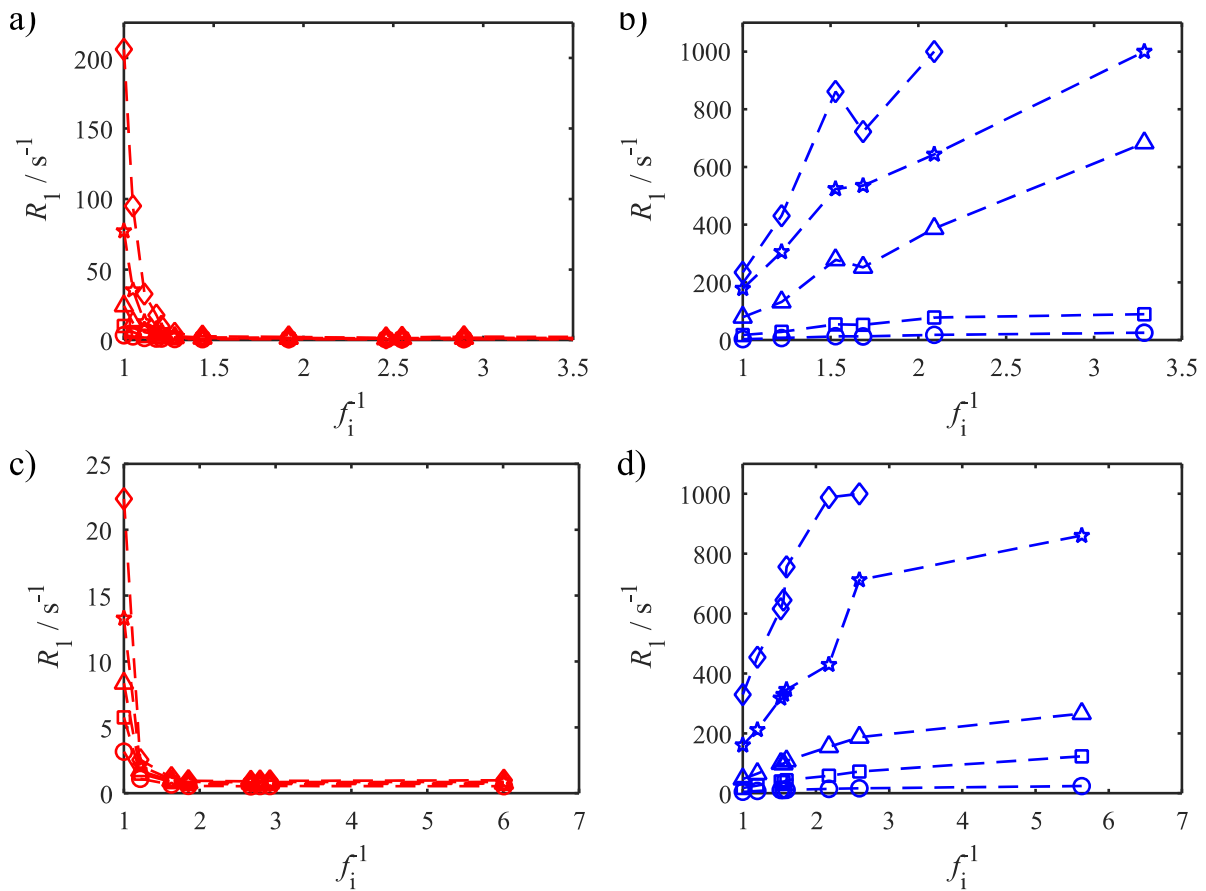


Figure 4.6: Relaxation rates at 10.8 (circle -  $\circ$ ), 1.89 (square -  $\square$ ), 0.33 (triangle -  $\triangle$ ), 0.06 (star -  $\star$ ) and 0.01 (diamond -  $\diamond$ ) MHz plotted against the inverse filling factor for THF (a,c), and water (b,d) components in THF-water mixtures imbibed within anatase titania (a,b) and  $\gamma$ -alumina (c,d). Dashed lines are included to guide the eye.

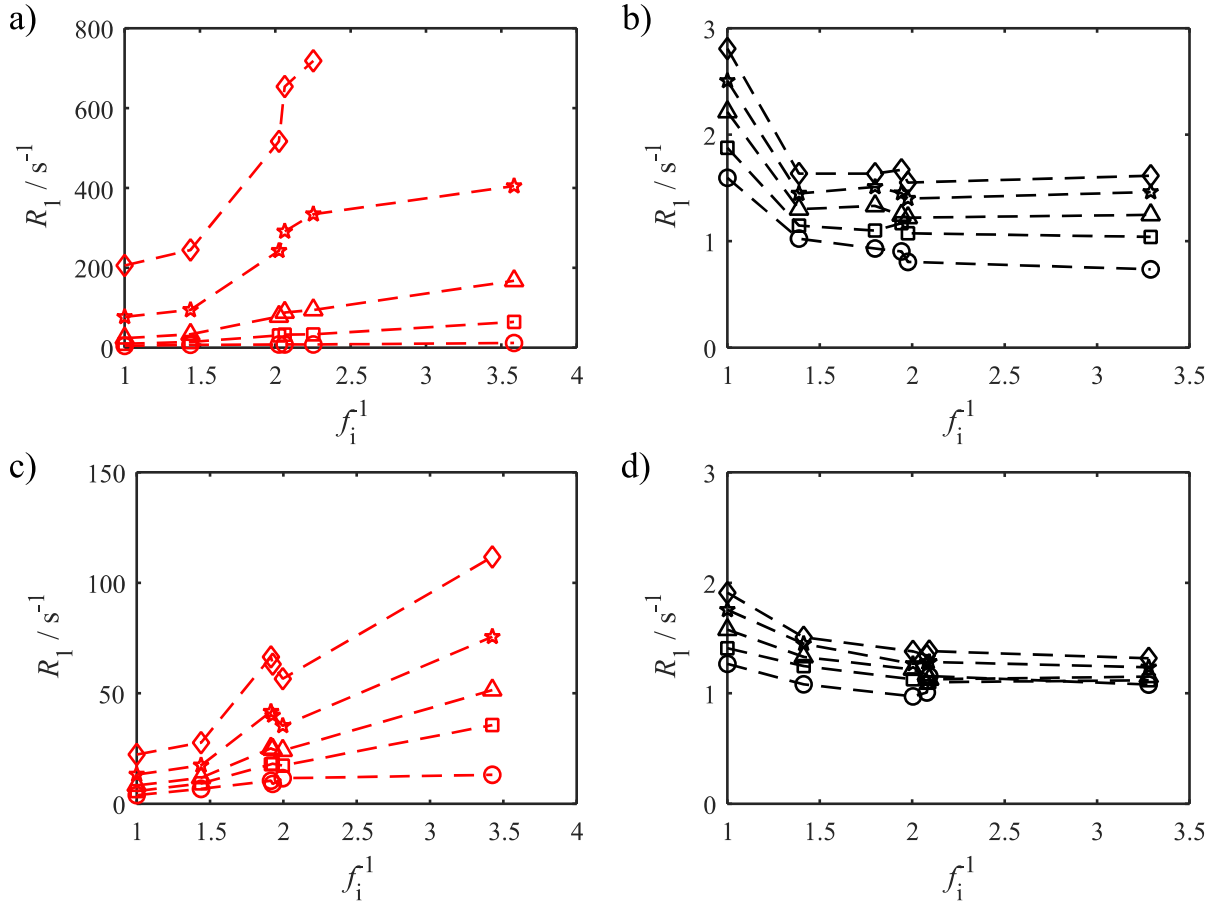


Figure 4.7: Relaxation rates at 10.8 (circle -  $\circ$ ), 1.89 (square -  $\square$ ), 0.33 (triangle -  $\triangle$ ), 0.06 (star -  $\star$ ) and 0.01 (diamond -  $\diamond$ ) MHz plotted against the inverse filling factor for THF (a,c), and decane (b,d) components in THF-decane mixtures imbibed within anatase titania (a,b) and  $\gamma$ -alumina (c,d). Dashed lines are included to guide the eye.

From these plots, it is immediately clear which components correspond to the stronger interacting species. In the THF-water mixtures, the relaxation rate of the water component increases linearly with the inverse filling factor. For the THF-decane, this is true for the THF component. For the weaker interacting species, it is assumed that  $V_{i,\text{surf}} \rightarrow 0$  as  $f_i^{-1}$  increases. Therefore the observed relaxation rate will be approximately equal to the bulk relaxation rate:  $R_{1i,\text{obs}} \approx R_{1i,\text{bulk}}$ . In Figure 4.6a-c and Figure 4.7b-d, the relaxation rates of the weaker interacting species (THF in THF-water and decane in THF-decane) indeed decrease to a relaxation rate  $R_1 \approx 1$  for  $f_i^{-1} > 1.5$ , which is in the order of magnitude expected for  $R_{1i,\text{bulk}}$ .

To conclude, a visual analysis of the NMRD profiles and a more thorough filling factor analysis both indicate that water is the stronger interacting species in THF-water mixtures, and THF is the stronger interacting species in THF-decane mixtures. This corresponds to the expectations based on the polarity of the solvents and the supports, as outlined in the introduction.

### 4.3.2 Surface dynamics

Aside from the surface composition, FFC-NMR experiments contain information about the surface dynamics by probing across a large frequency range, thereby providing information about, for example, the adsorption correlation time<sup>25-27</sup>. In order to examine the surface dynamics without interference from surface composition or  $R_{1i,\text{bulk}}$  effect, the NMRD profiles are renormalized to the relaxation rates at 10 kHz, see Figure 4.8 and Figure 4.9.

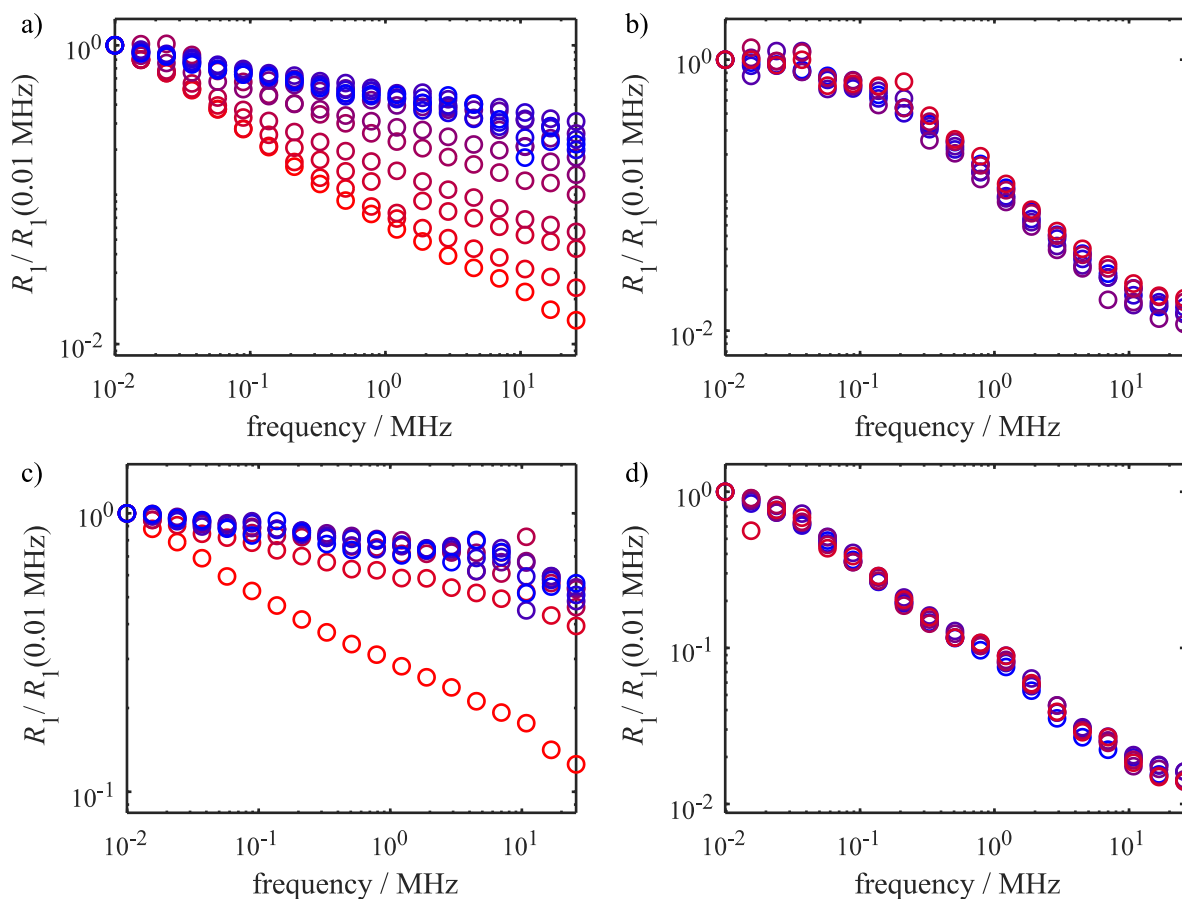


Figure 4.8:  $^1\text{H}$  NMRD profiles of THF (a,c), and water (b,d) components in THF-water mixtures imbibed within anatase titania (a,b) and  $\gamma$ -alumina (c,d), renormalized to the relaxation rate at  $\omega_0 = 10$  kHz.

In Figure 4.8b-d, the profiles for all mixture compositions overlap, indicating that the surface-water interaction does not change. In Figure 4.8a-c, the slope of the THF profiles in THF-water mixtures decrease very significantly, indicating that the surface-THF interaction is reduced by the addition of water to the system. Again, it is clear that water outcompetes THF for interaction with the surface, as is expected due to the polarity of the solvents with respect to that of the support.

For the THF-decane mixtures, Figure 4.9 shows that the slope of both components is independent on the mixture composition, and therefore neither of the surface-adsorbate interactions change. This corresponds to the previous analysis, where THF was concluded to be the stronger interacting species, and the slope of the pure decane profile is already very small, i.e. the surface-decane interaction is minimal to begin with.

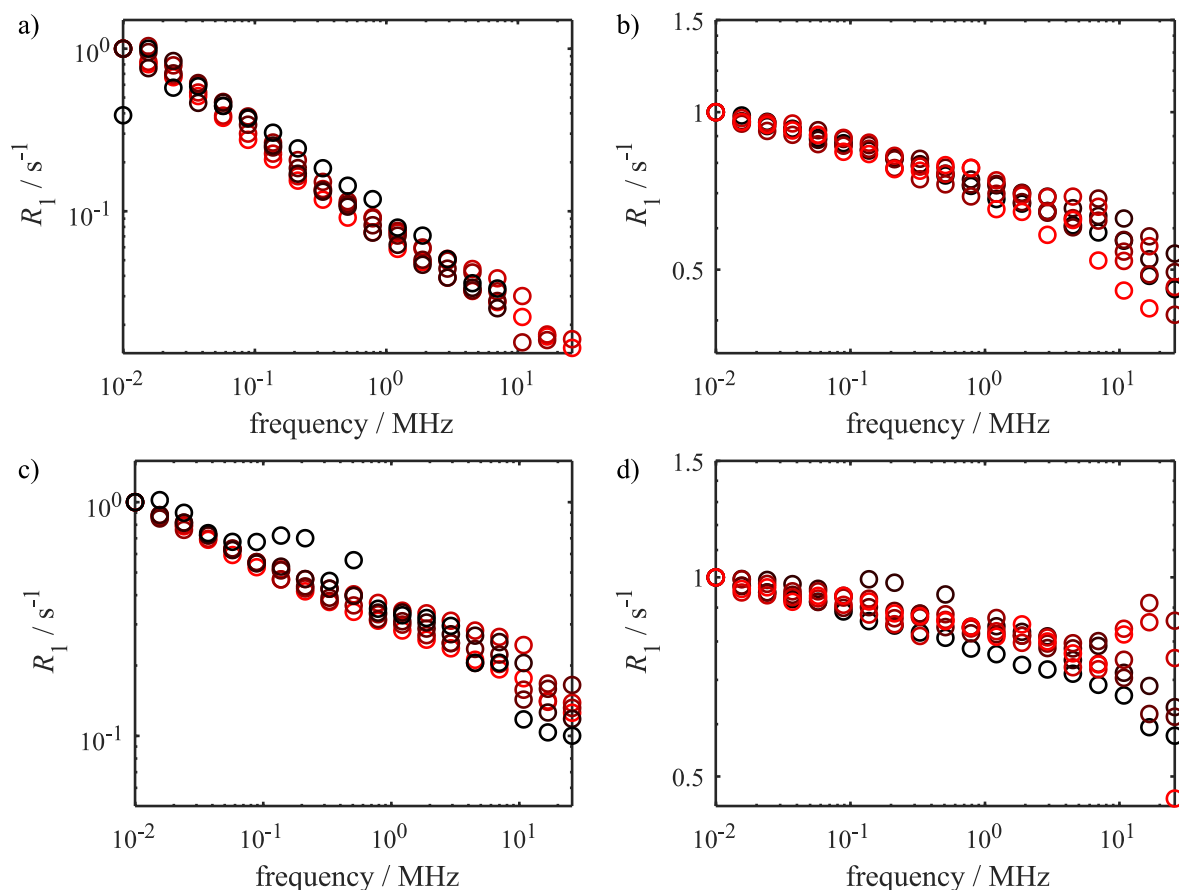


Figure 4.9:  $^1\text{H}$  NMRD profiles of THF (a,c), and decane (b,d) components in THF-decane mixtures imbibed within anatase titania (a,b) and  $\gamma$ -alumina (c,d), renormalized to the relaxation rate at  $\omega_0 = 10$  kHz.

#### 4.3.2.1 Power law analysis

A semi-quantitative analysis of the surface dynamics can be obtained by fitting the profiles to a phenomenological power law of the form  $R_1 = B\omega_0^{-\chi}$ . In a log-log plot, the slope of the profile corresponds to the power law exponent, therefore a higher  $\chi$  value corresponds to a stronger surface-adsorbate interaction. Figure 4.10 shows the power law fits of the pure water, THF and decane profiles.

The power law fit is an oversimplified model to the profiles with no physical significance. This is especially clear for the NMRD profile of water imbibed within anatase titania, for which the quality of the power law fit is very poor, as the curves in the profile are not captured in the power law fit. The THF profiles and the profile for water imbibed within  $\gamma$ -alumina also show slight curvature, however the fits are considered reasonable for a semi-quantitative analysis.

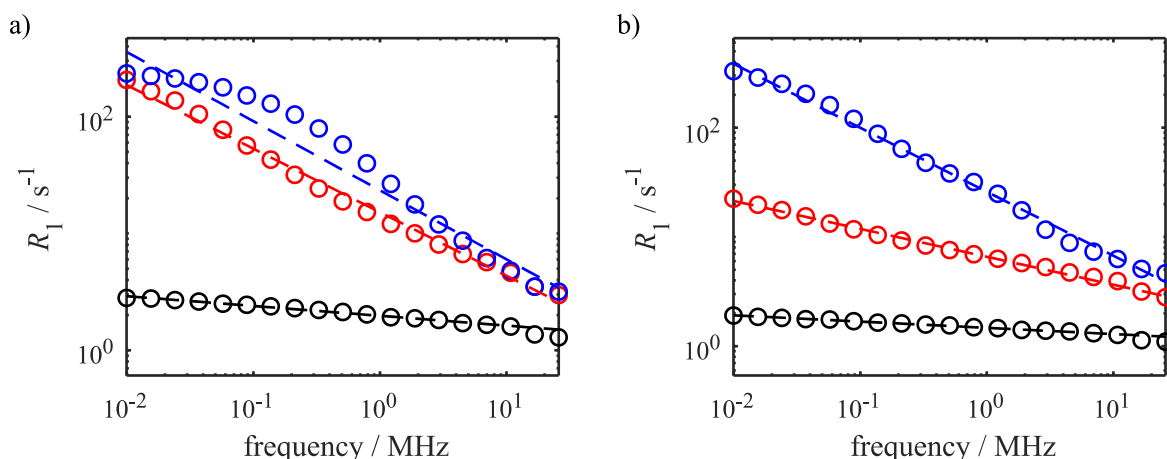


Figure 4.10: Power law fits (dashed line) to the  $^1\text{H}$  NMRD profiles (circles) of single-component water (blue), THF (red) and decane (black) imbibed within a) anatase titania, and b)  $\gamma$ -alumina.

The decane profiles fit to a power law very well, aside from the two high frequency points, where high field relaxation mechanisms start to dominate the profile. It should be noted however, that the slope of these profiles is very low. As a result, a large range of models would appear to fit the decane profiles.

A more detailed description of the profiles and their features requires an analysis by a physical model, such as the Korb model or Levitz-type RMTD models mentioned in section 3.2.3. An approach to identify and apply an appropriate theoretical model will be presented in the following chapter. In the current chapter however, the analysis of the profiles remains relatively qualitative, and therefore a phenomenological power law will be sufficient.

The power law exponents,  $\chi$ , were obtained for each of the components in the THF-water and THF-decane mixtures, and then plotted against the mixture compositions, see Figure 4.11. The  $\chi$  values of water in the THF-water mixtures, and THF and decane in the THF-decane mixtures appear constant with mixture composition. This corresponds to the overlapping renormalized profiles in Figure 4.8 and Figure 4.9. For water in THF-water and THF in THF-decane, the slope and therefore the power law exponent does not change because these are the stronger

interacting species in their respective mixtures. For pure decane, the power law exponents are very low ( $\sim 0.05$ ), which effectively means that there is no interaction with the surface.

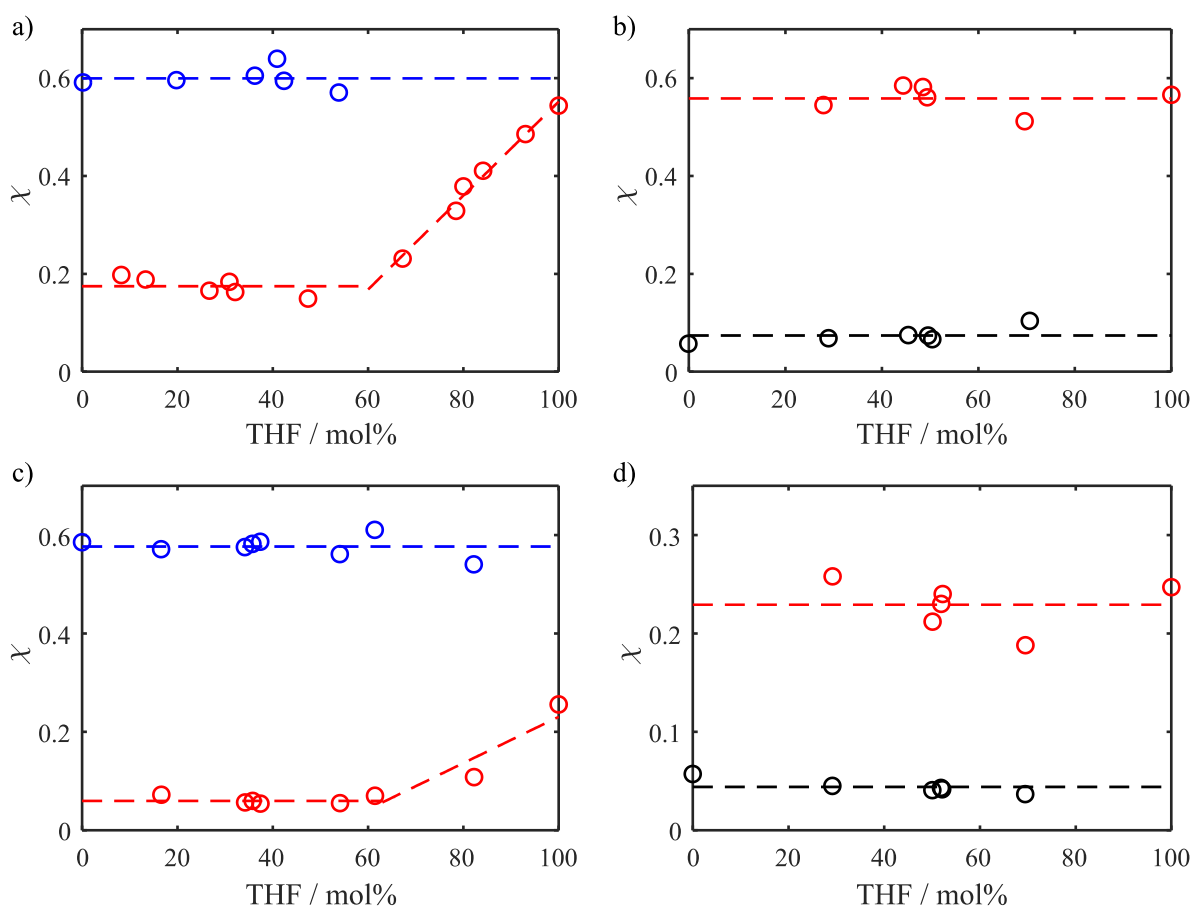
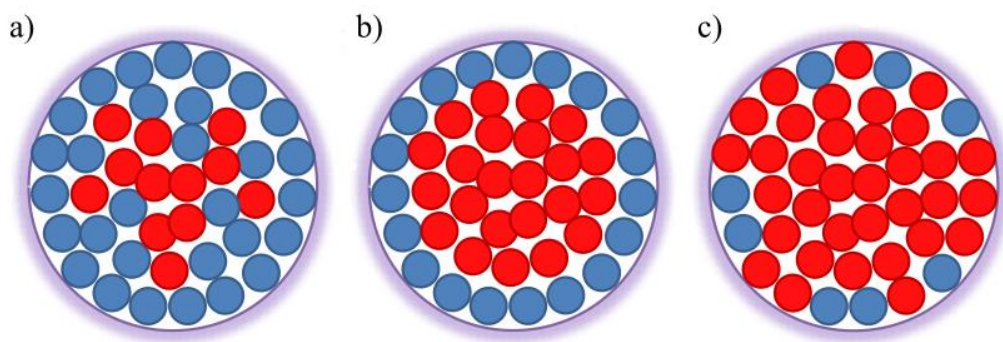


Figure 4.11: Power law exponents  $\chi$  plotted against the mixture composition in THF mol% for THF-water mixtures (a,c), and THF-decane mixtures (b,d), imbibed within anatase titania (a,b) and  $\gamma$ -alumina (c,d). Water data is shown in blue, THF in red, and decane in black.

The surface coverage of water at each of the mixture compositions was calculated based on the surface area and pore volume as shown in section 4.2.1. Due to previous conclusions that water is the stronger interacting species in THF-water mixtures, it is assumed that all the water inside the pore will interact with the surface, until the surface is fully covered with water. The molecular diameter of water was estimated to be  $\delta = 0.3$  nm, following the value used in the literature<sup>21,28</sup>.

For THF in THF-water mixtures imbibed within anatase titania, the power law exponent decreases from 0.55 for the pure liquid to 0.17 at  $\sim 60$  mol% THF. For  $\gamma$ -alumina, the power law extracted from the THF profiles decrease from 0.26 for the pure liquid to 0.06 at  $\sim 60$  mol% THF. For both supports, below this composition, the power law exponent stays constant. For anatase titania, a full monolayer coverage of water corresponds to a composition of 61.4:38.6

mol% THF-water. For  $\gamma$ -alumina, the corresponding composition is 66.5:33.5 mol% THF-water. These values agree very well with the turning points of the THF power law exponents in Figure 4.11a-c, suggesting that indeed all water molecules in the pore attach to the surface, until the surface is fully covered with water. At this stage, a microphase separation between a water-rich surface layer and a THF-rich bulk-like phase is proposed. A schematic overview of the THF-water microphase separation is shown in Figure 4.12.



*Figure 4.12: A schematic overview of THF-water competitive adsorption in anatase titania and  $\gamma$ -alumina, for compositions where a) there is more water than surface access, b) there is precisely one monolayer coverage of water, and c) there is not enough water to cover the surface. Blue circles represent water, red circles represent THF.*

While the decrease in THF power law exponent with an increase in water content is monotonic, it is difficult to make conclusions about the surface dynamics of THF in the THF-water mixtures due to the simplified nature of the power law. A more detailed discussion on the surface dynamics of weaker interacting species in aqueous solutions imbibed within anatase titania, and the microphase separation of these mixtures, is shown in chapter 6.

#### 4.4 Fixed field NMR relaxometry results

In order to validate the use of FFC-NMR as a tool to study surface-adsorption interactions in general, as well as competitive adsorption, conventional fixed field NMR was used as a comparative technique. At fixed fields, relaxometry can be used to describe interaction strengths. For example, the  $T_1/T_2$  ratio has been shown to correlate with the surface-adsorbate interaction strength<sup>29</sup>. Moreover, it has been applied to binary liquid mixtures on a titania support<sup>30-32</sup>. Another fixed field relaxometry tool is to obtain the ratio of  $T_1$  values in the bulk and in the pore, i.e.  $\eta = T_{1,\text{bulk}}/T_{1,\text{pore}}$ <sup>19</sup>. For a close comparison with FFC-NMR, which is fully based on  $T_1$  measurements, the latter fixed field relaxometry method was used in this validation study.

#### 4.4.1 Bulk liquids - $T_{1,\text{bulk}}$

Firstly,  $T_{1,\text{bulk}}$  values were determined for the THF, water and decane components in a series of THF-water and THF-decane bulk liquid mixtures, so that a clear correlation between  $T_{1,\text{bulk}}$  and the composition could be established. All  $T_{1,\text{bulk}}$  values were determined through a monoexponential fit to the integrals of the THF and water peaks, or THF and decane peaks respectively. Subsequently, the  $T_{1,\text{bulk}}$  values were plotted against the composition, see Figure 4.13.

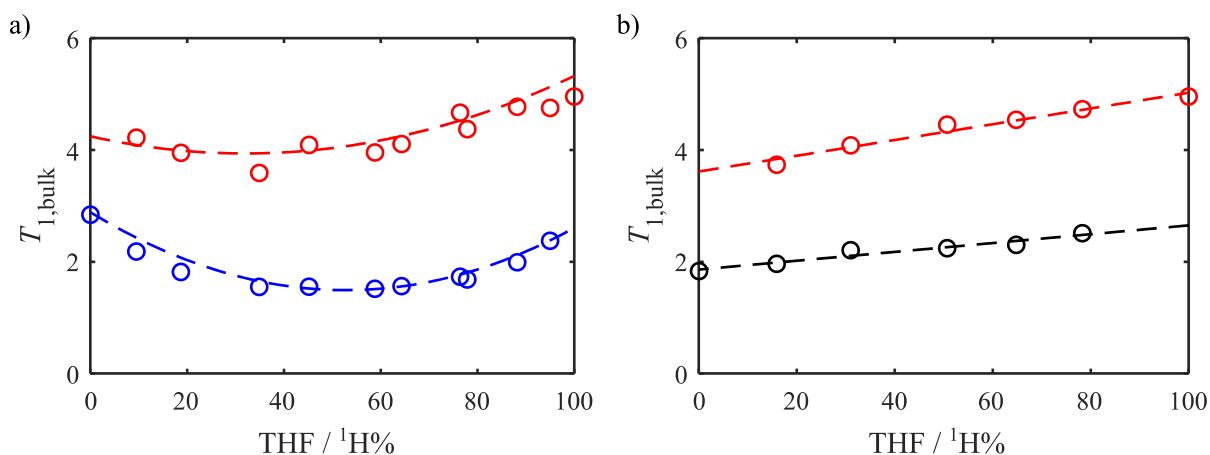


Figure 4.13:  $T_{1,\text{bulk}}$  values of a) THF-water and b) THF-decane mixtures, plotted against the mixture composition in THF  $^1\text{H}\%$ . Water is shown in blue, THF in red, and decane in black. Dashed lines correspond to second order polynomial fits for the THF-water mixtures, and linear fits for the THF-decane mixtures. These fits were only used to interpolate the  $T_{1,\text{bulk}}$  values of other mixture compositions.

For both components in the THF-water mixtures, the  $T_{1,\text{bulk}}$  trends with composition correspond to those shown in the literature<sup>33</sup>. A second order polynomial was fitted to the data, so that the  $T_{1,\text{bulk}}$  values of any composition could be interpolated. For THF-decane, linear fits described the  $T_{1,\text{bulk}}$  trends with composition very well and were used to interpolate the  $T_{1,\text{bulk}}$  values of other mixture compositions.

#### 4.4.2 Imbided liquids - $T_{1,\text{pore}}$

Subsequently, THF-water and THF-decane mixtures were imbided on anatase titania and  $\gamma$ -alumina. The adsorbed liquid mixture composition was determined through the integrals of THF, water and decane peaks in  $^1\text{H}$  NMR spectra, see section 4.2.4. For each of the experiments, at least one of the THF peaks could be separated. For the composition analysis, it was assumed that the integrals of the two THF peaks were equal.

$T_{1,\text{pore}}$  values were determined using inversion recovery experiments. For the pure liquid experiments, a monoexponential fit was used to obtain  $T_{1,\text{pore}}$  values. For the mixtures however, the two mixture components could not be fully resolved. Figure 4.14 shows a 20:80 mol% THF-water mixture in its bulk state, as well as imbibed within anatase titania and  $\gamma$ -alumina.

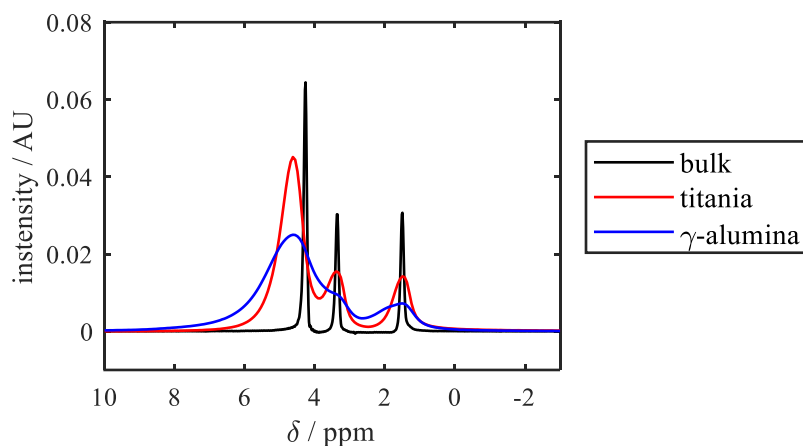


Figure 4.14:  $^1\text{H}$  NMR spectra for a 20:80 mol% THF-water mixture in its bulk state, imbibed within anatase titania, and imbibed within  $\gamma$ -alumina.

It is especially clear for the  $\gamma$ -alumina spectrum that the downfield THF peak and the water peak overlap significantly. Attempting to fit each of the peaks to a monoexponential fit would result in inaccurate  $T_{1,\text{pore}}$  values. Therefore, a biexponential fit was applied to the full spectrum. The initial guess for the populations in the biexponential fit corresponded to the compositions as determined from the  $^1\text{H}$  NMR spectra. The extracted  $T_{1,\text{pore}}$  values were then plotted against the mixture composition, see Figure 4.15.

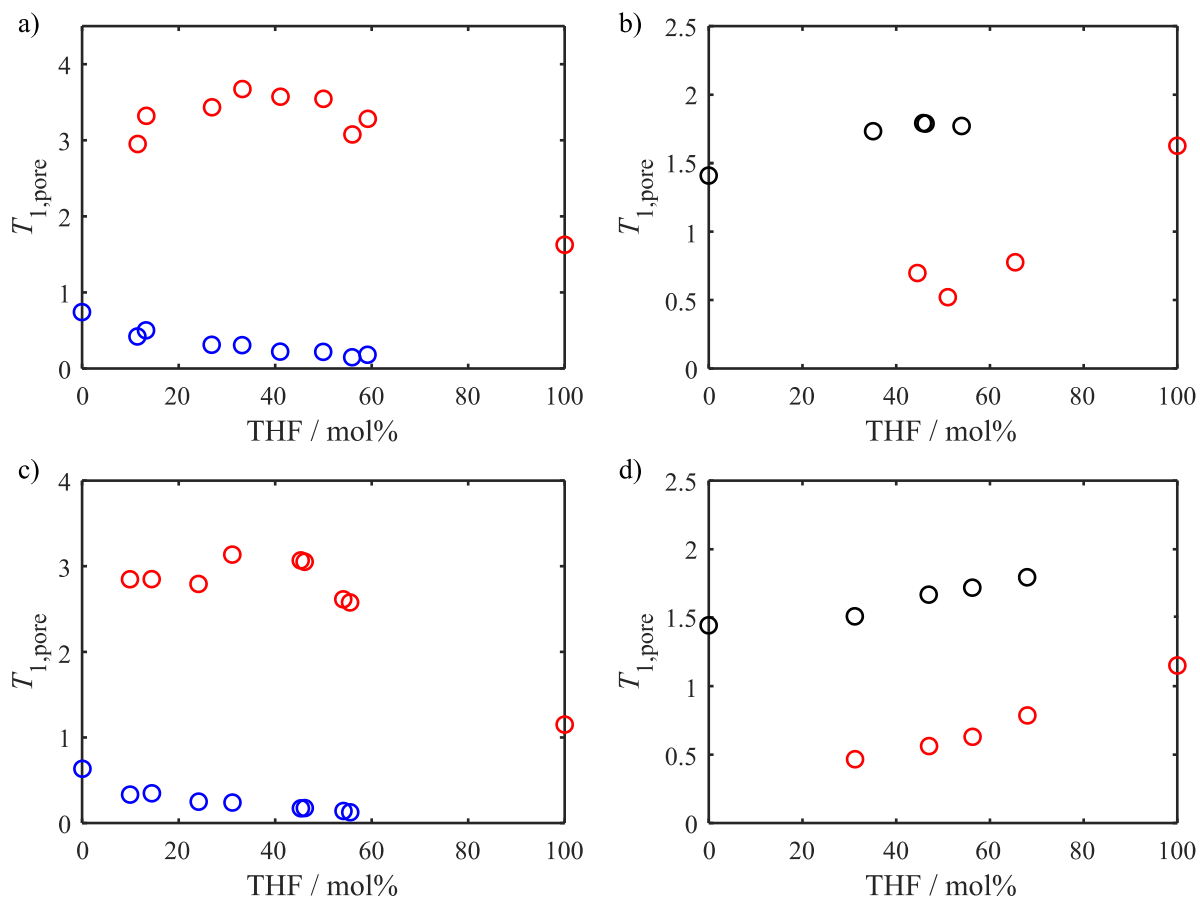


Figure 4.15:  $T_{1,pore}$  values of THF-water mixtures (a,c), and THF-decane mixtures (b,d), imbibed within anatase titania (a,b) and  $\gamma$ -alumina (c,d), plotted against the mixture composition in THF mol%. Water is shown in blue, THF in red, and decane in black.

The  $T_{1,pore}$  values by themselves do not contain much relevant information, as they depend on much more than the surface-adsorbate interaction. The same factors that influence the bulk relaxation rate, will influence the relaxation rate inside the pore. For example, these factors include molecular properties, such as the molecular diameter and weight. Therefore it is impossible to directly compare the trends of the different solvents.

#### 4.4.3 Bulk/imbibed ratio - $\eta$

In order to specifically target surface-adsorbate interactions, the ratio of the bulk and imbibed relaxation rates was determined,  $\eta = T_{1,\text{bulk}}/T_{1,\text{pore}}$ .  $T_{1,\text{bulk}}$  values were determined using the compositions from the  $^1\text{H}$  NMR spectra and the fits shown in Figure 4.13. The  $T_{1,\text{pore}}$  values that were used were shown in Figure 4.15. The resulting  $\eta$  values are again plotted against the composition and shown in Figure 4.16.

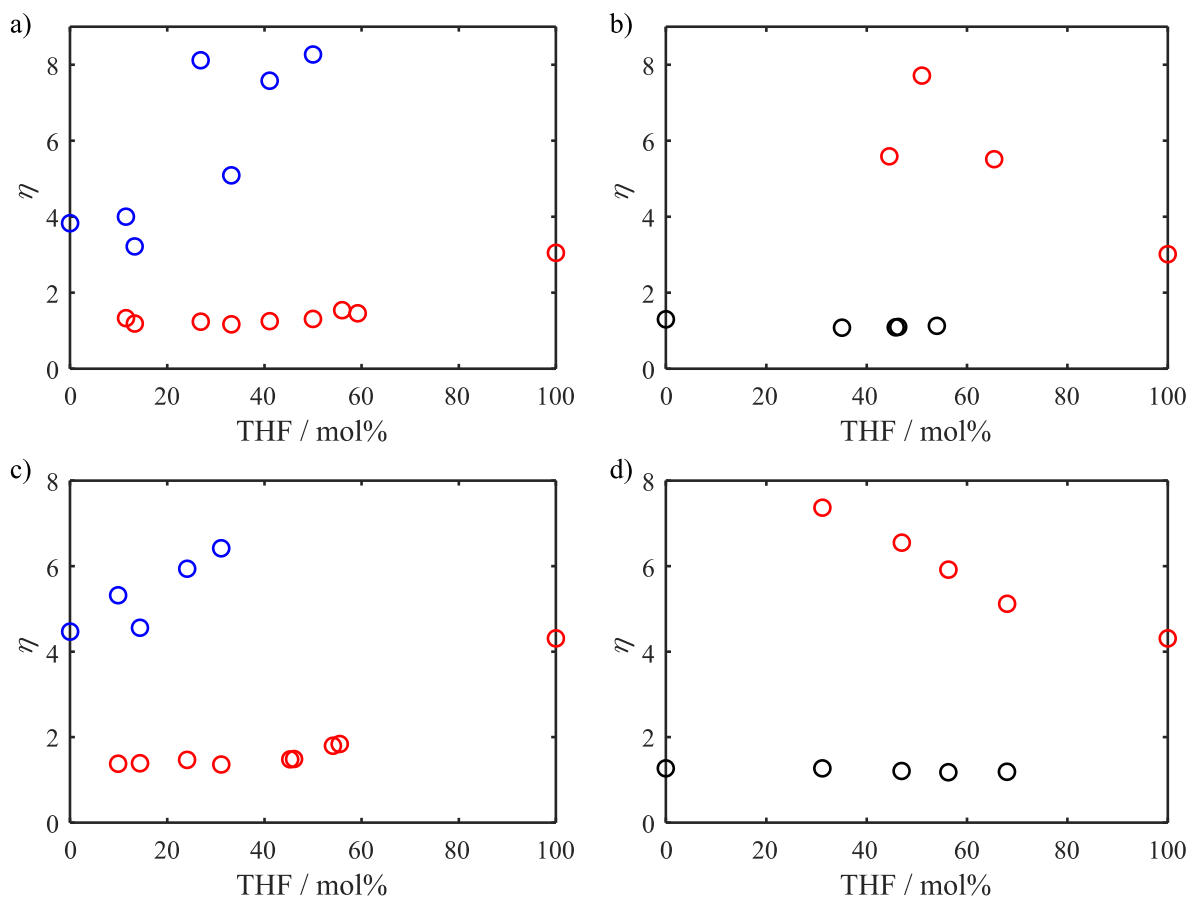


Figure 4.16:  $\eta$  values for THF-water mixtures (a,c), and THF-decane mixtures (b,d), imbibed within anatase titania (a,b) and  $\gamma$ -alumina (c,d), plotted against the mixture composition in THF mol%. Water is shown in blue, THF in red, and decane in black.

The  $\eta$  values for pure water (3.83 for anatase titania and 4.47 for  $\gamma$ -alumina) are only slightly higher than that for pure THF (3.05 for anatase titania and 4.31 for  $\gamma$ -alumina). From this, it is not clear that there is a large difference in interaction strength. The difference between the  $\eta$  values of THF and decane (1.30 for anatase titania and 1.27 for  $\gamma$ -alumina) is much larger, indicating that the decane interaction with the surface is negligible. This corresponds to the FFC-NMR results.

First, the expected weaker interacting species is analysed. For THF-water mixtures, this is THF, and for THF-decane mixtures, this is decane. For THF in THF-water, the  $\eta$  values decrease when water is introduced. For all compositions, the  $\eta$  values are close to 1. Following the TPFE model,  $\eta = 1$  occurs when the relative surface volume fraction is equal to zero. This indicates there is no interaction between THF and the surface of the porous media anymore. It should be noted that no experiments were performed in the range between 60-100 mol% THF, which was shown to correspond to a sub-monolayer water coverage of the surface in section 4.3.2.1. Therefore, based on the limited data set shown in Figure 4.16, the conclusions correspond to the qualitative of FFC-NMR, namely that water is the stronger interacting species, and THF is the weaker interacting species in a THF-water mixture imbibed within anatase titania or  $\gamma$ -alumina, and that the introduction of water reduces the interaction of THF with the surface. However, it is impossible to separate the TPFE or surface composition effects from the surface dynamics using high field  $T_1$ . As shown previously, this is possible with FFC-NMR.

For decane in THF-decane mixtures, the  $\eta$  values are effectively independent of the mixture composition and close to a value of 1, indicating negligible interaction with the surface for all mixture compositions. This again is in agreement with the FFC-NMR results.

The stronger interacting species show interesting behaviour. For water in the THF-water mixtures,  $\eta$  increases as the water content decreases. THF in THF-decane behaves equivalently. This effect could be misinterpreted as an increase in surface-adsorbate interaction strength, however it can again be explained using the TPFE model. As the concentration of the stronger interacting species decreases, there is relatively speaking less of this species in the bulk-like phase inside the pore. Therefore the  $T_{1,\text{pore}}$  value decreases, as can also be seen in Figure 4.15, which in its turn increases the value for  $\eta$ . Due to this surface composition effect, it is difficult to make any conclusions about the surface dynamics or pure surface-adsorbate interaction strengths. In FFC-NMR, the surface composition effect is not present, therefore it is much easier to investigate interaction strengths.

## 4.5 Conclusions and outlook

A case study of FFC-NMR as a tool for studying the surface-adsorbate interactions in binary liquid mixtures imbibed within porous media was presented. THF-water and THF-decane mixtures were imbibed within anatase titania and  $\gamma$ -alumina. Due to the large range of polarities between water, THF and decane, and therefore the large range of interaction strengths, the results shown in this chapter can be generalized to other binary liquid mixtures imbibed within anatase titania and  $\gamma$ -alumina as well.

For all mixtures, it was possible to separate two relaxation environments. Through an analysis based on inverse Laplace transforms, peaks could be assigned to THF, water or decane. The mixtures compositions extracted by the biexponential fits of the FFC-NMR experiments corresponded very well with the compositions extracted through a high field  $^1\text{H}$  NMR spectrum. Inaccuracies in the FFC-NMR mixture compositions due to fast relaxing components should be taken into account, and therefore the mixture compositions extracted at 7 MHz were used in the remainder of this study.

A qualitative analysis of the  $^1\text{H}$  NMRD profiles obtained through FFC-NMR, based on the TPF model, lead to the conclusion that in THF-water mixtures, water is the stronger interacting species, and THF is the weaker interacting species. For THF-decane mixtures, THF is the stronger interacting species, decane is the weaker interacting species. A subsequent filling factor analysis showed the same conclusion in a more quantitative manner.

The surface dynamics were first investigated qualitatively by observing the slope of the renormalized  $^1\text{H}$  NMRD profiles. The slopes of the stronger interacting species, e.g. water in THF-water and THF in THF-decane, were shown to be independent on the mixture composition, indicating no change in surface dynamics. For the weaker interacting species, decane in THF-decane also did not show a change in slope with the mixture composition, this was explained by the inherently weak interaction between pure decane and the titania surface. Interestingly, the THF slope for THF-water mixtures appeared to decrease as water was added into the system, indicating a decrease in the surface-THF interaction.

These conclusions were supported by a power law analysis, where the slope was quantified in the form of a power law exponent. For THF in THF-water mixtures, the power law exponent decreased from 0.55 and 0.26 for the pure liquid imbibed within anatase titania and  $\gamma$ -alumina respectively, to 0.17 and 0.06 at ~60 mol%, which corresponded to precisely one monolayer

water coverage of the surface. It is proposed that for THF-rich mixtures, all water molecules attach to the surface, forming a microphase separation of THF and water inside the pore.

Furthermore, a comparison was made with fixed field NMR relaxometry in the form of  $\eta = T_{1,\text{bulk}}/T_{1,\text{pore}}$  values. For the weaker interacting species, the  $\eta$  value decreased as the concentration of the weaker interacting component decreased. This corresponded to the FFC-NMR results. For the stronger interacting species, the  $\eta$  value increased as the concentration of the stronger interacting component decreased. While this trend could be misinterpreted as a sign of increasing surface-adsorbate interaction strength, it was explained through the TPFE model. For the fixed field NMR relaxometry results, it was impossible to separate surface composition (TPFE) effects and surface dynamics.

This case study of THF-water and THF-decane mixtures imbibed within anatase titania and  $\gamma$ -alumina has shown how to reliably acquire, process and interpret the data in a qualitative and semi-quantitative manner. Further investigations of the surface dynamics require the use of physical models, which will be introduced in chapter 5. The knowledge acquired in chapter 5 and the current chapter will then be combined to investigate the microphase separation of alcohol-water mixtures imbibed within anatase titania in chapter 6.

## References

1. Alnaimi, S. M., Mitchell, J., Strange, J. H. & Webber, J. B. W. Binary liquid mixtures in porous solids. *J. Chem. Phys.* **120**, 2075 (2004).
2. Abdel Hamid, A. R., Mhanna, R., Lefort, R., Ghoufi, A., Alba-Simionesco, C., Frick, B. & Morineau, D. Microphase separation of binary liquids confined in cylindrical pores. *J. Phys. Chem. C* **120**, 9245–9252 (2016).
3. Mhanna, R., Catrou, P., Dutta, S., Lefort, R., Essafri, I., Ghoufi, A., Muthmann, M., Zamponi, M., Frick, B. & Morineau, D. Dynamic heterogeneities in liquid mixtures confined in nanopores. *J. Phys. Chem. B* **124**, 3152–3162 (2020).
4. Baker, L., Renshaw, M. P., Mantle, M. D., Sederman, A. J., Wain, A. J. & Gladden, L. F. Operando magnetic resonance studies of phase behaviour and oligomer accumulation within catalyst pores during heterogeneous catalytic ethene oligomerization. *Appl. Catal. A Gen.* **557**, 125–134 (2018).
5. Stapf, S., Kimmich, R., Seitter, R. O., Maklakov, A. I. & Skirda, V. D. Proton and deuteron field-cycling NMR relaxometry of liquids confined in porous glasses. *Colloids Surfaces A Physicochem. Eng. Asp.* **115**, 107–114 (1996).
6. Korb, J.-P., Whaley Hodges, M., Gobron, T. & Bryant, R. G. Anomalous surface diffusion of water compared to aprotic liquids in nanopores. *Phys. Rev. E* **60**, 3097–3106 (1999).
7. Mattea, C., Kimmich, R., Ardelean, I., Wonorahardjo, S. & Farrher, G. Molecular exchange dynamics in partially filled microscale and nanoscale pores of silica glasses studied by field-cycling nuclear magnetic resonance relaxometry. *J. Chem. Phys.* **121**, 9809 (2004).
8. Korb, J. P., Monteilhet, L., McDonald, P. J. & Mitchell, J. Microstructure and texture of hydrated cement-based materials: A proton field cycling relaxometry approach. *Cem. Concr. Res.* **37**, 295–302 (2007).
9. Chemmi, H., Petit, D., Levitz, P. & Korb, J. P. NMR control of aging and durability of hardened cement pastes. *Comptes Rendus Chim.* **13**, 405–408 (2010).
10. Faux, D. A. & McDonald, P. J. Explicit calculation of nuclear-magnetic-resonance

- relaxation rates in small pores to elucidate molecular-scale fluid dynamics. *Phys. Rev. E* **95**, 33117 (2017).
11. Korb, J. P., Freiman, G., Nicot, B. & Ligneul, P. Dynamical surface affinity of diphasic liquids as a probe of wettability of multimodal porous media. *Phys. Rev. E* **80**, 061601 (2009).
  12. Godefroy, S., Korb, J.-P., Fleury, M. & Bryant, R. G. Surface nuclear magnetic relaxation and dynamics of water and oil in macroporous media. *Phys. Rev. E* **64**, 021605 (2001).
  13. Korb, J.-P., Nicot, B., Louis-Joseph, A., Bubici, S. & Ferrante, G. Dynamics and wettability of oil and water in oil shales. *J. Phys. Chem. C* **118**, 23212–23218 (2014).
  14. Korb, J. P., Godefroy, S. & Fleury, M. Surface nuclear magnetic relaxation and dynamics of water and oil in granular packings and rocks. *Magn. Reson. Imaging* **21**, 193–199 (2003).
  15. Stapf, S., Ren, X., Talnishnikh, E. & Blqmich, B. Spatial distribution of coke residues in porous catalyst pellets analyzed by field-cycling relaxometry and parameter imaging. *Magn. Reson. Imaging* **23**, 383–386 (2005).
  16. Ward-Williams, J., Korb, J.-P. & Gladden, L. F. Insights into functionality-specific adsorption dynamics and stable reaction intermediates using Fast Field Cycling NMR. *J. Phys. Chem. C* **122**, 20271–20278 (2018).
  17. Ward-Williams, J. & Gladden, L. F. Insights into adsorption behaviour of binary liquid mixtures in porous media using fast field cycling NMR. *Magn. Reson. Imaging* **56**, 57–62 (2018).
  18. Reichardt, C. *Solvents and solvent effects in organic chemistry*. (Wiley, 2002).
  19. D’Agostino, C., Mitchell, J., Gladden, L. F. & Mantle, M. D. Hydrogen bonding network disruption in mesoporous catalyst supports probed by PFG-NMR diffusometry and NMR relaxometry. *J. Phys. Chem. C* **116**, 8975–8982 (2012).
  20. Butler, J. P., Reeds, J. A. & Dawson, S. V. Estimating solutions of first kind integral equations with nonnegative constraints and optimal smoothing. *SIAM J. Numer. Anal.* **18**, 381–397 (1981).

21. Korb, J.-P. & Levitz, P. E. Direct probing of the wettability of plaster pastes at the nanoscale by proton Field Cycling Relaxometry. *AIP Conf. Proc.* **1081**, 55 (2008).
22. Levitz, P. E. & Korb, J.-P. Probing glass transition of clay colloids by NMR relaxometry: interplay between fluid Brownian dynamics and particle jamming. *Eurphys. Lett.* **70**, 684 (2005).
23. Korb, J.-P. Multiscale nuclear magnetic relaxation dispersion of complex liquids in bulk and confinement. *Prog. Nucl. Magn. Reson. Spectrosc.* **104**, 12–55 (2018).
24. Brownstein, K. R. & Tarr, C. E. Importance of classical diffusion in NMR studies of water in biological cells. *Phys. Rev. A* **19**, 2446–2453 (1979).
25. Levitz, P. Random flights in confining interfacial systems. *J. Phys. Condens. Matter* **17**, 4059–4074 (2005).
26. Levitz, P., Zinsmeister, M., Davidson, P., Constantin, D. & Poncelet, O. Intermittent Brownian dynamics over a rigid strand: heavily tailed relocation statistics in a simple geometry. *Phys. Rev. E* **78**, 030102 (2008).
27. Levitz, P. Probing interfacial dynamics of water in confined nanoporous systems by NMRD. *Mol. Phys.* **117**, 952–959 (2019).
28. Chemmi, H., Petit, D., Levitz, P., Denoyel, R., Galarneau, A. & Korb, J.-P. Noninvasive experimental evidence of the linear pore size dependence of water diffusion in nanoconfinement. *J. Phys. Chem. Lett* **7**, 45 (2016).
29. Mitchell, J., Broche, L. M., Chandrasekera, T. C., Lurie, D. J. & Gladden, L. F. Exploring surface interactions in catalysts using low-field nuclear magnetic resonance. *J. Phys. Chem.* **117**, 17699–17706 (2013).
30. D’Agostino, C., Brett, G. L., Miedziak, P. J., Knight, D. W., Hutchings, G. J., Gladden, L. F. & Mantle, M. D. Understanding the solvent effect on the catalytic oxidation of 1,4-butanediol in methanol over Au/TiO<sub>2</sub> catalyst: NMR diffusion and relaxation studies. *Chem. - A Eur. J.* **18**, 14426–14433 (2012).
31. D’Agostino, C., Kotionova, T., Mitchell, J., Miedziak, P. J., Knight, D. W., Taylor, S. H., Hutchings, G. J., Gladden, L. F. & Mantle, M. D. Solvent effect and reactivity trend in the aerobic oxidation of 1,3-propanediols over gold supported on titania: NMR

- diffusion and relaxation studies. *Chem. - A Eur. J.* **19**, 11725–11732 (2013).
32. D’Agostino, C., Mitchell, J., Mantle, M. D. & Gladden, L. F. Interpretation of NMR relaxation as a tool for characterising the adsorption strength of liquids inside porous materials. *Chem. - A Eur. J.* **20**, 13009–13015 (2014).
33. Goldammer, E. & Zeidler, M. Molecular motion in aqueous mixtures with organic liquids by nmr relaxation measurements. *Ber. Bunsenges. Phys. Chem.* **73**, 4–15 (1969).



## 5. Quantitative dynamics of alcohols imbibed within anatase titania

### 5.1 Introduction

In chapter 4, a power law analysis of  $^1\text{H}$  NMRD profiles of THF-water mixtures imbibed within anatase titania showed a clear correlation between the surface-THF interaction and the fraction of the titania surface accessible to THF. In this chapter, a systematic study of the dynamics of short linear alcohols imbibed within anatase titania is performed.

As will be shown, the corresponding  $^1\text{H}$  NMRD profiles cannot be analysed with a simple power law, as was the case for THF imbibed within anatase titania. Therefore, a theoretical model is required to gain quantitative insight into the surface-adsorbate interactions of these systems. Extracting correlation times related to adsorption dynamics has been a focus of FFC-NMR scientists for many years, resulting in a number of different theoretical models<sup>1,2</sup>. Each of these models is appropriate for a specific type of interaction and relaxation mechanism. Therefore it is essential to identify the correct model for a particular system, before drawing conclusions on the quantitative dynamics.

The aim of this chapter is to first identify the appropriate theoretical model for describing the dynamics of alcohols imbibed within anatase titania through an in-depth analysis of the  $^1\text{H}$  NMRD profiles and temperature dependent relaxation experiments, and to subsequently apply this model to the data in a reliable manner, leading to an accurate extraction of  $\tau_A$ , the adsorption correlation time.

The identification and optimization of the modelling methodology will be used as a foundation for chapter 6, which covers a study of microphase separation in alcohol-water mixtures imbibed within anatase titania, a poorly understood phenomenon where otherwise fully miscible liquids separate out when imbibed within small pores<sup>3-8</sup>.

## 5.2 Materials and methods

### 5.2.1 Sample preparation

Anatase titania in the form of 1/8" pellets and short, linear alcohols (methanol, ethanol, 1-propanol, 1-butanol, 1-pentanol, subsequently named methanol, ethanol, propanol, butanol and pentanol respectively) were obtained from Alfa Aesar. All alcohols were  $\geq 98\%$  pure and used as received. A BET and BJH analysis of the anatase titania pellets showed a surface area of  $161 \text{ m}^2 \text{ g}^{-1}$  and an average pore diameter of 9.5 nm. The pore volume was determined to be  $0.39 \text{ cm}^3 \text{ g}^{-1}$  by gravimetric measurements. Titania pellets were dried overnight at  $120 \text{ }^\circ\text{C}$ , after which the pellets were imbibed in the alcohols overnight. Extra-pellet liquid was removed by drying the sample with filter paper directly before the NMR experiments, leaving only the desired liquid imbibed within the pellets.

### 5.2.2 FFC-NMR methods

Room temperature FFC-NMR experiments were performed as outlined in section 4.2.2. For the room temperature methanol, propanol and butanol experiments, the  $^1\text{H}$  relaxation frequency range was  $0.01 \leq \omega_0 \leq 40 \text{ MHz}$ . However, for all other experiments, including the room temperature ethanol and pentanol experiments as well as the variable temperature experiments described below, the maximum relaxation field was set to 10 MHz. There were three reasons for this change in parameter. The first and most important reason is that the FFC-NMR relaxometer had several power outages due to metal–oxide–semiconductor field-effect transistor (MOSFET) failures. The maximum field strength was decreased in order to minimize the chance of more MOSFET failures. Additionally, paramagnetic dioxygen, which is dissolved in the liquids in this study, dominates the relaxation behaviour for Larmor frequencies  $\omega_0 > 10 \text{ MHz}$ . As this effect is not relevant to the current study, it was not considered valuable to measure the relaxation rates for these Larmor frequencies. Finally, experiments for  $\omega_0 > 10 \text{ MHz}$  are acquired using the non-polarized (NP) FFC-NMR sequence, while the experiments for  $\omega_0 \leq 10 \text{ MHz}$  are acquired using the pre-polarized (PP) FFC-NMR sequence. In principle, the measured relaxation rate at a chosen Larmor frequency should be the same for the NP and PP experiments, however discrepancies between the two sequences have been shown for low signal-to-noise ratio samples.

### 5.2.2.1 Variable temperature experiments

Variable temperature FFC-NMR experiments were performed on methanol and methanol-d imbibed within anatase titania at 328, 318, 308, 298 and 288 K in order of descending temperature to avoid an inconsistent effect of the evaporation of the probe molecule at higher temperatures on the relaxation rates<sup>9</sup>. The temperatures were checked by placing a thermometer in the sample holder and were found to be within 1 K of the goal temperature for  $T \geq 298$  K. For  $T = 288$  K, the error was found to be 2 K. NMRD profiles were recorded as outlined above. 16-point  $T_1$  curves were recorded at 10 frequency points between 10 kHz and 10 MHz. The polarization time and recycle delay was 4 s.

### 5.2.3 Computational methods

$R_1 = 1/T_1$  values were extracted via a monoexponential fit in Matlab to the  $T_1$  curves obtained by FFC-NMR and plotted against the  $^1\text{H}$  Larmor frequency to obtain NMRD profiles. An in-house script for an inverse Laplace transform using Tikhonov regularisation was used for all  $T_1$  curves to confirm there was only one relaxation environment<sup>10</sup>. The NMRD profiles were then fitted to the Levitz RMTD model and a high field constant relaxation rate<sup>11-15</sup>. The distances between  $^1\text{H}$  atoms were obtained for all alcohols using *Jmol*<sup>16</sup>.

### 5.2.4 Pulsed Field Gradient NMR experiments

Pulsed Field Gradient (PFG) NMR experiments were performed on a 9.4T Bruker Avance NMR spectrometer. Typical pulse lengths were 14.6  $\mu\text{s}$  for a  $\pi/2$  pulse, and 29.2  $\mu\text{s}$  for a  $\pi$  pulse. An inversion recovery experiment with 16 time delays was done to determine the  $T_1$  value, after which the recycle delay was set at  $5T_1$ . The temperature of the sample was calibrated using ethylene glycol and was determined to be  $298 \text{ K} \pm 1 \text{ K}$ . Diffusion experiments were recorded using a pulsed field gradient stimulated echo (PGSTE) sequence with bipolar gradients.  $\delta$  was set at 1 ms,  $\Delta$  was set at 100 ms. 8 scans were recorded at 16 gradients, the range of which was adjusted to each sample, to allow for a full signal decay. Each FID was Fourier Transformed to obtain a  $^1\text{H}$  NMR spectrum. The integrated signal intensities at each gradient strength were fitted to the Stejskal-Tanner equation to obtain the diffusion coefficients for alcohols and THF imbibed within anatase titania<sup>17</sup>.

## 5.3 Results

### 5.3.1 $^1\text{H}$ NMR dispersion profiles of alcohols imbibed within anatase titania

The  $^1\text{H}$  NMRD profiles for a range of short, linear alcohols imbibed within anatase titania are shown in Figure 5.1.

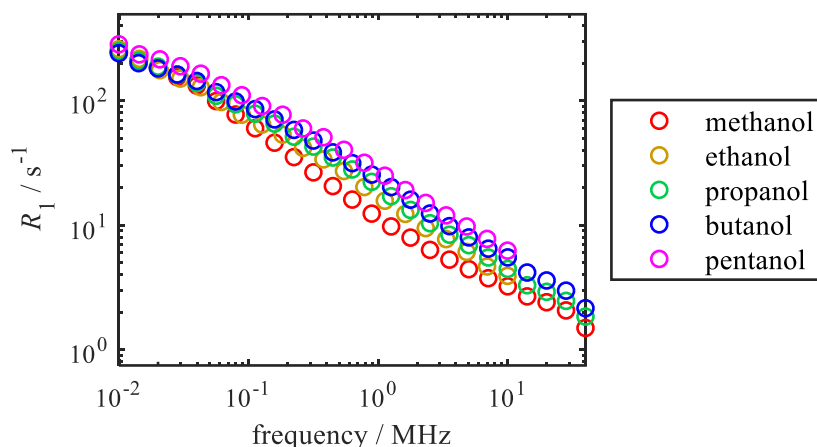


Figure 5.1:  $^1\text{H}$  NMRD profiles for linear alcohols imbibed within anatase titania

The profiles all look very similar in their shape. Due to the polarity of the anatase titania surface, it is expected the strongly interacting component of the alcohol is the hydroxyl group, which stays constant between the different alcohols. Assuming this is correct, the dominant part of the surface-alcohol interaction is expected to be unchanged across the alcohol range, resulting in similar  $^1\text{H}$  NMRD profiles. However, as the alkyl chain increases, the overall polarity of the solvent is decreased, as is shown in Table 5.1.

Table 5.1: The polarity of the alcohols used in the study, relative to the polarity of water

Alcohol	Polarity <sup>18</sup>
Methanol	0.762
Ethanol	0.654
Propanol	0.617
Butanol	0.586
Pentanol	0.568

The effect of the alkyl chain on the polarity of the molecule explains why the steepest slope in the  $^1\text{H}$  NMRD profiles appears to shift to higher frequencies with increasing chain length. The slope, which is a result from the surface-adsorbate interaction, shifting to higher frequencies suggests that these interactions occur at shorter timescales, which indicates weaker surface-alcohol interactions. This observation corresponds with a study of a range of solvents on  $\gamma$ -

alumina, another highly polar support, where interaction parameters extracted from FFC-NMR were shown to correlate with the polarity of the solvent<sup>19</sup>.

A semi-quantitative analysis of the dynamics was done by fitting a power law to the <sup>1</sup>H NMRD profiles. Figure 5.2 shows that the data fluctuates around the power law fitted to the full data, which indicates a simple power law does not describe the data well. Additionally, the power law exponent  $\chi$  varies substantially depending on the frequency range included in the fit. This means that any comparison between the different alcohols will be within the error of the fit, and therefore insignificant. In order to obtain more information about the dynamics of alcohols imbibed within anatase titania, the data must be analysed with a more elaborate model. An overview of the theoretical models that are considered will be given in the next section.

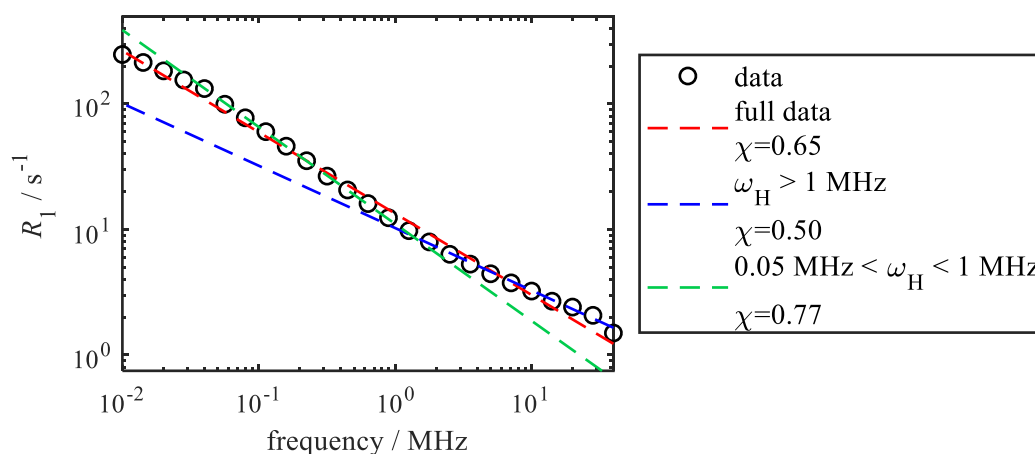


Figure 5.2: The <sup>1</sup>H NMRD profile for methanol imbibed within anatase titania, and corresponding power law fits for varying frequency ranges.

### 5.3.2 <sup>1</sup>H NMR dispersion profiles of methanol-d and methanol-d3

The <sup>1</sup>H NMRD profiles of partially deuterated methanol analogs, see Figure 5.3, show that the methanol (CH<sub>3</sub>OH) profile corresponds to the weighted logarithmic average of the methyl (CH<sub>3</sub>OD) and hydroxyl (CD<sub>3</sub>OH) profiles. This means that alcohol profiles are greatly dominated by the alkyl profiles, especially for longer chain alcohols. For methanol, 75% of the NMR signal must come from alkyl protons, for pentanol, this is 91.7%. This information will be crucial in establishing an appropriate model to obtain a quantitative analysis of the surface-adsorbate interactions.

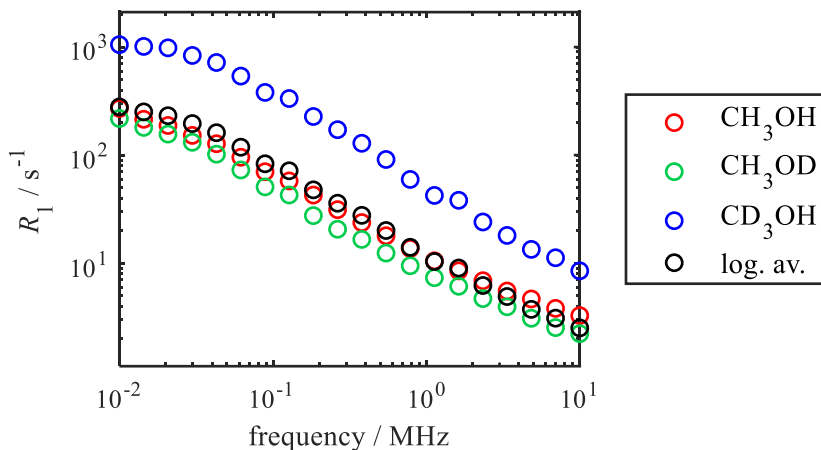


Figure 5.3: NMRD profiles of  $\text{CH}_3\text{OH}$ ,  $\text{CH}_3\text{OD}$ , and  $\text{CD}_3\text{OH}$  imbibed within anatase titania, and the logarithmic weighted average of the  $\text{CH}_3\text{OD}$  and  $\text{CD}_3\text{OH}$  profiles, which is shown to overlap with the  $\text{CH}_3\text{OH}$  profile well.

## 5.4 Theoretical models for FFC-NMR

In this section, a brief overview of a number of theoretical modelling methods used in FFC-NMR of liquids in porous media will be given. For every model, its suitability to model alcohols imbibed within anatase titania will be discussed, in order to identify the best applicable model.

The NMR relaxation mechanisms, which are the basis for theoretical models, can be divided into two main groups, inter- and intramolecular relaxation. Assuming the rotational and translational diffusion are independent, the observed relaxation rate is the superposition between these relaxation mechanisms<sup>1</sup>:

$$R_{1,\text{obs}} = R_{1,\text{inter}} + R_{1,\text{intra}} \quad (5.1)$$

For intermolecular relaxation, the core of the relaxation mechanism is the interaction of adsorbate spins with spins outside of the same adsorbate molecule. For example, in the case of a Korb-like system, which will be discussed in the next section, the mechanism is based on the interaction of adsorbate spins with paramagnetic species at the pore surface. Another example is the interaction of spins that are in the same species, but not within the same *molecule*, which is one of the relaxation mechanisms taken into account by the  $3\tau$  model, which will be discussed later.

For intramolecular relaxation mechanisms, which is the basis for the reorientations mediated by translational diffusion (RMTD) model and the protic model, the relaxation occurs due to

dipolar coupling of spins within the same molecule. For every porous media system, the dominant relaxation mechanism must be identified, in order to clarify which of the theoretical models is suitable to use.

$T_1$  can be expressed as a function of the spectral density. For “like” and “unlike” spins, these expressions are as follows<sup>9</sup>:

$$\frac{1}{T_1} = A[J(\omega_I) + 4J(2\omega_I)], \quad (5.2)$$

$$\frac{1}{T_1} = A[7J(\omega_S) + 3J(2\omega_I)], \quad (5.3)$$

where  $\omega_I$  and  $\omega_S$  are the proton and electron Larmor frequencies respectively.

The spectral density can be described following an analysis of the molecular dynamics of each of the relaxation mechanisms, ultimately providing an expression for the relaxation rate,  $R_1 = 1/T_1$ .

Through the two-phase fast exchange model, discussed before in section 2.3.6.1, the observed relaxation rate will be<sup>20</sup>:

$$R_{1,obs} = R_{1,B} + p(R_{1,S} - R_{1,B}), \quad (5.4)$$

where  $p$  is the population fraction of adsorbed molecules in the pore,  $R_{1,B}$  is the relaxation rate of the bulk liquid and  $R_{1,S}$  is the surface relaxation rate. Figure 5.4 shows that the bulk relaxation rate of methanol is constant within the Larmor frequency used in this study,  $0.01 \text{ MHz} \leq \omega_0 \leq 10 \text{ MHz}$ , corresponding to literature on other bulk liquids<sup>21</sup>.

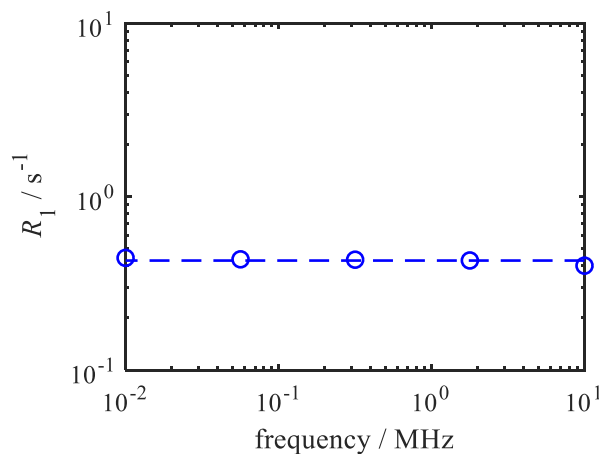


Figure 5.4:  $^1\text{H}$  NMRD profile of bulk methanol. The dotted line represents the mean of the relaxation rates.

It is assumed the bulk relaxation rate for the other alcohols will also be constant in this frequency range. Therefore, for the remainder of this chapter, the bulk relaxation rate will be generalised to a high field relaxation rate,  $R_{1,HF}$ .

#### 5.4.1 Intermolecular relaxation mechanisms

As mentioned before, intermolecular relaxation mechanisms depend on the interaction of spins in one molecule with spins in another molecule or in the support. Two theoretical models based on intermolecular relaxation are widely used for the analysis of liquids in porous media, the Korb model and the  $3\tau$  model.

##### 5.4.1.1 Korb model

The Korb model for aprotic liquids is based on intermolecular relaxation between the proton spins of the liquid and electron spins of paramagnetic impurities in the support<sup>2</sup>. This process is very efficient, which means only small amounts of paramagnetic impurities are required in order for this relaxation mechanism to be dominant. Solvent molecules hop across the surface according to the surface diffusion correlation time,  $\tau_m$ , and after a number of hops, jump off the surface into the bulk-pore space. A ratio of the surface residence correlation time,  $\tau_s$ , and  $\tau_m$  reflects the number of hops a molecule undertakes before leaving the surface. This has been used as a metric for surface affinity<sup>22</sup>.

The spectral density for this model has been explicitly calculated, and results in the following expression for the observed relaxation rate<sup>2</sup>:

$$\begin{aligned} \frac{1}{T_{1,obs}} &= \frac{1}{T_{1,B}} + \left(\frac{\mu_0}{4\pi}\right)^2 \frac{N_s}{N} \frac{\pi\sigma_s(\gamma_I\gamma_S\hbar)^2 S(S+1)}{15d^2\delta'^2} \\ &\times \tau_m \left( 3 \ln \left[ \frac{1 + \omega_I^2\tau_m^2}{\frac{\tau_m^2}{\tau_s^2} + \omega_I^2\tau_m^2} \right] + 7 \ln \left[ \frac{1 + \omega_S^2\tau_m^2}{\frac{\tau_m^2}{\tau_s^2} + \omega_S^2\tau_m^2} \right] \right) \end{aligned} \quad (5.5)$$

The bilogarithmic frequency dependence is a clear difference from the other models that will be discussed later. As was discussed in section 5.3.1, the NMRD profiles of alcohols imbibed within anatase titania show a power law frequency dependence. Therefore, it is unlikely that the Korb model will apply to this system. However, because there is no ESR data for the titania support, it is not possible to fully disregard the Korb model. The Korb model will be fitted to the data in section 5.6 in order to make a full comparison of possible modelling methods and

to establish which of the theoretical models is most appropriate to apply to the NMRD profiles of alcohols imbibed within titania.

#### 5.4.1.2 $3\tau$ model

The  $3\tau$  model is another theoretical model based on intermolecular relaxation<sup>23</sup>. The basis is similar to that of the Korb model. The first of the three  $\tau$ s in this model is  $\tau_l$ , the surface layer diffusion correlation time, corresponding to Korb's hopping time  $\tau_m$ . The second corresponds to Korb's surface residency time,  $\tau_s$ , but is redefined as  $\tau_d$ , the desorption time. The main difference with Korb's model is an additional correlation time:  $\tau_b$ , the bulk fluid diffusion correlation time constant.

As the basis of the relaxation mechanisms used for this model is the same as for the Korb model, it is concluded that it will not apply to the NMRD profiles of alcohols within anatase titania.

#### 5.4.2 Intramolecular relaxation mechanisms

The reorientations mediated by translational diffusion (RMTD) model and the protic model are based on intramolecular relaxation of proton spins within the liquid molecules and therefore follow equation (5.2).

##### 5.4.2.1 Reorientations mediated by translational diffusion

The approach of RMTD is very different to that of the Korb model. The Korb model follows transient surface dynamics, where molecules diffuse along the surface and the main source of relaxation is the interaction with paramagnetic impurities. The RMTD model does not take paramagnetic impurities into account, but is based on intermittent steps between the adsorbed phase, where the adsorbate stays for a time  $\tau_A$ , and bulk excursions, where the adsorbate resides for a time  $\tau_B$ . After  $\tau_B$ , the adsorbate will return to the surface. This process can repeat itself many times before correlation is lost. While this is a general process, called *bulk mediated surface diffusion*<sup>24,25</sup>, the RMTD model applies specifically when there is strong and directional binding of adsorbates to the surface, which reduces the loss of correlation while the adsorbate is on the surface<sup>1,26</sup>. For alcohols on anatase titania, it can be imagined that the hydroxyl will preferentially bind to the polar surface, thereby imposing a preferential orientation of the adsorbate, which follows the RMTD approach.

For the pure RMTD model as described by Kimmich, from here on called the Kimmich model, the relaxation rate is expressed as follows<sup>27</sup>:

$$R_1 = b\Gamma(1 - \chi)c^{-(1-\chi)}\omega^{-\chi}, \quad (5.6)$$

where  $b$  is a constant,  $\Gamma(x)$  is the gamma function, and  $\chi$  characterizes the roughness of the surface. This means that NMRD profiles of different liquids on the same surface, as long as they follow the RMTD processes, will show a power law frequency dependence with the same power law exponent. While systems have been shown to support this hypothesis, where the power law exponent is determined by the surface roughness<sup>28</sup>, rather than the surface-adsorbate interaction, studies have also found different power laws for different liquids on the same surface<sup>29</sup>. For the anatase titania used in this study, the power law exponents for THF (section 4.3.2.1) and alcohols (section 5.3.1) are very different, therefore the Kimmich model does not seem suitable to study this system.

Another approach to RMTD by Levitz, from here on called the Levitz model, is based on the same intermittent dynamics between adsorption steps near the surface and bulk excursions, however now the probability distributions of adsorption and bulk relocations are considered<sup>11</sup>. The model assumes there will only be magnetic noise to induce relaxation during the adsorption steps. The general spectral density for this model is:

$$J(\omega) = \frac{2}{\tau_A \omega^2} \operatorname{Re} \left[ \frac{(1 - \tilde{\Psi}_A(\omega))(1 - \tilde{\Psi}_R(\omega))}{1 - \tilde{\Psi}_A(\omega)\tilde{\Psi}_R(\omega)} \right] \quad (5.7)$$

$\tilde{\Psi}_A(\omega)$  and  $\tilde{\Psi}_R(\omega)$  are the Fourier transforms of the adsorption and bulk relocation probability densities, respectively. This spectral density has not been evaluated for all geometries, however power law type expressions have been found for planar, cylindrical, and rough surfaces<sup>11-13</sup>. The full expressions and further details of the Levitz model will be shown in section 5.5.1, however importantly, these expressions introduce an adsorption correlation time,  $\tau_A$ , which is sensitive to the surface-adsorbate interaction and shifts the power law exponent from  $-1/2$  in the weak adsorption limit to  $-3/2$  in the strong adsorption limit.

The basis of RMTD can be applied to alcohols within anatase titania, and the NMRD profiles of the Levitz model follow a power law frequency dependence, which corresponds with the data shown in section 5.3.1.

#### 5.4.2.2 Protic model

When studying alcohols, the protic nature of the hydroxyl group should not be forgotten. This means that the hydroxyl  $^1\text{H}$  atoms are exchangeable, and can therefore create hydrogen bonds, for example with surface hydroxyls. As a result, the NMR relaxation of  $^1\text{H}$  spins is not controlled by the dynamics of the liquid, but by the dynamics of the surface hydroxyls. If there are paramagnetic impurities in the support, the surface hydroxyls can have strong, efficient, and long-lasting interactions with these paramagnetic species, thereby dominating the NMRD profile<sup>30,31</sup>.

The magnetization transfer due to  $^1\text{H}$  exchange or cross relaxation, can be seen as analogous to the exchange-mediated orientational randomization model of protein relaxation, where the NMRD profile follows a power law dependence with a frequency independent plateau for  $\omega\tau_s \ll 1$ . Additionally, the proximity of the surface hydroxyls to paramagnetic species in the support can give rise to a paramagnetically enhanced relaxation peak in the NMRD profile<sup>2</sup>.

While this model could be applicable to the data, it should be noted that in principle, only the hydroxyl groups of the alcohols are exchangeable. As was shown in section 5.3.2, the alcohol profile corresponds to the weighted average of the alkyl and hydroxyl profiles. For methanol, 75% of the NMR signal must come from non-exchangeable protons, for pentanol, this is 91.7%. This means the alcohol profiles are highly dominated by the alkyl group. However, if the alkyl and hydroxyl groups cross relax, the alkyl group may take on the relaxation mechanism of the protic hydroxyl group, in which the full alcohol will follow the protic model.

#### 5.4.3 Temperature dependent relaxation

For bulk liquids, the temperature dependence of nuclear relaxation is well known, following BPP theory<sup>32</sup>. An increase in temperature leads to an increase in molecular tumbling, which leads to a decrease in the rotational correlation time. Depending on the correlation time relative to the Larmor frequency, the relaxation rate can increase ( $\omega_0\tau_c > 1$ ), decrease ( $\omega_0\tau_c < 1$ ), or stay constant ( $\omega_0\tau_c = 1$ ). For small molecules in bulk, the correlation times are in the order of picoseconds, therefore all FFC-NMR experiments will fall in the range where  $\omega_0\tau_c < 1$ , which means that the relaxation rate will decrease with an increase in temperature.

For liquids in porous media, the temperature dependence is more complex<sup>33</sup>. Depending on the relaxation mechanism, the temperature dependence has been shown to change. Examples

include a bulk-like temperature dependence for acetone within porous silica, however an inverse temperature dependence was shown for water within the same support<sup>30,34</sup>. This means that the temperature dependence of the relaxation rate can be used to identify the appropriate relaxation mechanism, which will then clarify which model can be used to study the dynamics of a porous media system.

Intermolecular relaxation systems, such as those following the Korb and  $3\tau$  model, where molecules diffuse along the surface in a transient manner, have been shown to follow a bulk-like temperature dependence across the full FFC-NMR frequency range<sup>34</sup>.

For the RMTD model, the temperature dependence of the relaxation rate is only determined by the diffusion process during the bulk excursions. At the high field end of the NMRD profiles, fast molecular processes will show a strong temperature dependence of the relaxation rate, similar to bulk liquids. However, at the low field end, the NMRD profile is dominated by the adsorption steps, rather than the bulk diffusion, therefore the relaxation rate is independent on the temperature at lower Larmor frequencies<sup>1</sup>.

Similar to the Korb and RMTD model, there is a bulk-like temperature dependence at the high field end of the NMRD profile for systems following the protic model, however at the low field end, the relaxation rate increases with an increase in temperature. The activation energy of this temperature dependence has been shown to agree with the formation energy of a hydrogen bond<sup>2,30</sup>.

A quantitative analysis of the temperature dependence can be performed by fitting the relaxation rates to an Arrhenius equation<sup>2</sup>:

$$\ln(R_1) = \ln(A) - \frac{E_A}{RT}, \quad (5.8)$$

where  $\ln(A)$  is a prefactor,  $E_A$  is the activation energy,  $R$  is the gas constant and  $T$  is the temperature. The activation energies obtained at high frequencies have previously been shown to correspond to the translational diffusional activation energy of the bulk liquid in the case of water and acetone<sup>2,30,34</sup>. At low frequencies, the activation energy corresponds to an effective activation energy, composed of the diffusion activation energy and the surface interaction energy. For the inverted temperature dependence seen for the protic model, the effective activation energy at the low frequency end will be negative<sup>2,30</sup>.

### 5.4.3.1 Variable temperature experiments results

Variable temperature FFC-NMR experiments were performed on methanol imbibed within anatase titania in a range of 288-328K. The  $^1\text{H}$  NMRD profiles and the corresponding Arrhenius plots are shown in Figure 5.5. At the high frequency end, an increase in temperature resulted in a decrease in relaxation rate. This feature is common for all relaxation models, as the high frequency end of the NMRD profile is dominated by fast, bulk-like relaxation. The apparent activation energy for the three highest frequency points was determined to be  $E_A = 1.8 \pm 0.2 \text{ kJ mol}^{-1}$ . Toward the lower frequency end, the temperature dependence of the relaxation rate inverts. An increase in temperature results in an increase in relaxation rate. This feature is distinctive for a protic relaxation mechanism, where methanol hydroxyl groups exchange or cross relax with surface hydroxyl groups. The apparent activation energy for the three lowest frequency points was determined to be  $E_A = -5.7 \pm 0.5 \text{ kJ mol}^{-1}$ .

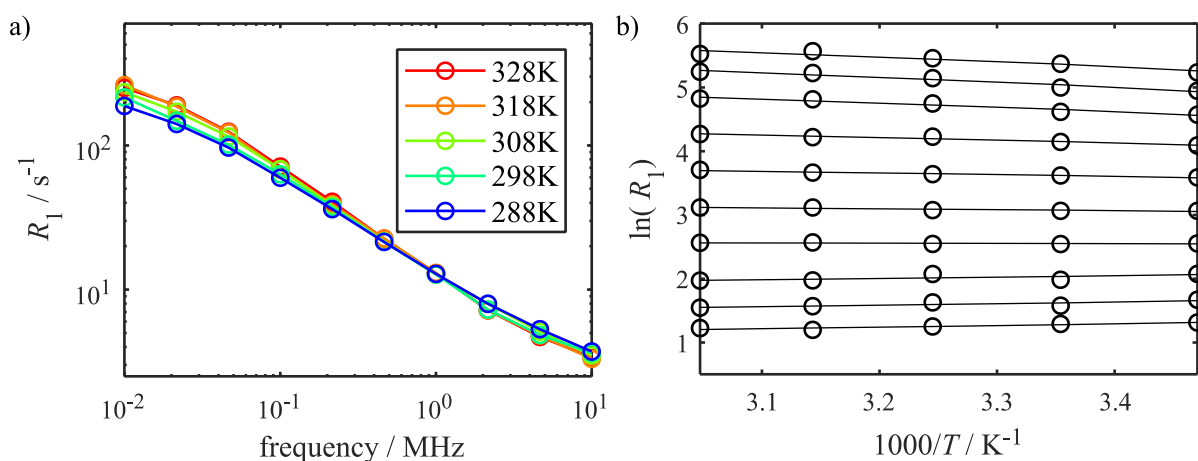


Figure 5.5: a)  $^1\text{H}$  NMRD profiles for methanol imbibed within anatase titania at a temperature range 288-328K. The data points were connected by a line to highlight the trend of the relaxation rate with the temperature. b) Arrhenius plots for methanol imbibed within anatase titania and the corresponding fits to equation (5.8).

Considering the methyl and hydroxyl relaxation rates overlap, it is impossible to determine whether a) the protic model applies to the full molecule, in which case the methyl and hydroxyl groups must cross relax, as the methyl group in itself does not contain protic properties, or b) the protic model applies only to the hydroxyl group. Assuming in the latter case the methyl group follows the RMTD model, there is no temperature dependence at the low frequency end for this part of the molecule. The strong temperature dependence of the hydroxyl group will dominate the profiles. Therefore either of these circumstances will result in a temperature dependence corresponding to the protic model.

#### 5.4.3.1.1 Methanol-d imbibed within anatase titania

In order to investigate the relaxation behaviour of the alkyl group without interference from the hydroxyl group, variable temperature experiments were performed on methanol-d imbibed within anatase titania. It was expected that the temperature dependence of the alkyl group would follow one of the two following trends. The first possibility is to see equivalent trends to those of methanol (from now on called methanol-h, for clarity), showed in the previous section. This would indicate the alkyl and hydroxyl groups of methanol are cross relaxing, in which case the entire molecule follows the protic model. The second possibility is that the alkyl group relaxes independently from the hydroxyl group, in which case it is expected that the alkyl group will follow the RMTD relaxation mechanism. For RMTD, the temperature dependence will go from a bulk-like trend at the high field end, to a temperature independent relaxation rate at the low field end of the  $^1\text{H}$  NMRD profile.

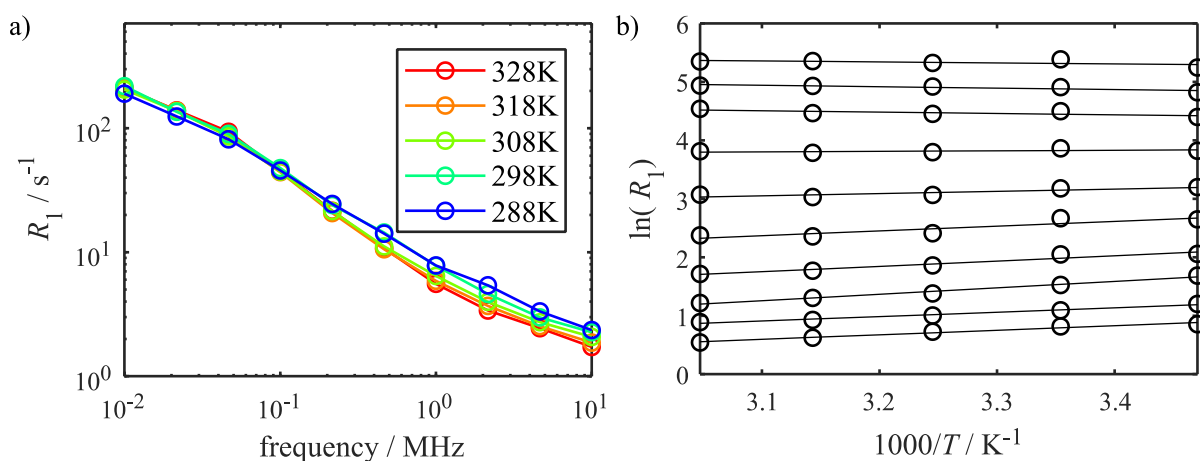


Figure 5.6: a)  $^1\text{H}$  NMRD profiles for methanol-d imbibed within anatase titania at a temperature range 288-328K. The data points were connected by a line to highlight the trend of the relaxation rate with the temperature. b) Arrhenius plots for methanol-d imbibed within anatase titania and the corresponding fits to equation (5.8).

The  $^1\text{H}$  NMRD profiles of methanol-d at a range of temperatures 288-328K and the corresponding Arrhenius plots are shown in Figure 5.6. Again, at the high frequency end, the bulk-like temperature dependence is visible, as is expected. The activation energy for the three highest frequency points,  $E_A = 7.3 \pm 1.6 \text{ kJ mol}^{-1}$ , is much higher than for methanol-h, where  $E_A = 1.8 \text{ kJ mol}^{-1}$ . Going to the lower frequency end, the activation energy for methanol-d ( $-1.8 \pm 0.3 \text{ kJ mol}^{-1}$ ) is again much higher than for methanol-h ( $-5.7 \text{ kJ mol}^{-1}$ ). Moreover, the inversion point for the temperature dependence of methanol-d seems to occur at approximately 0.08 MHz, whereas the inversion point occurred at approximately 1.0 MHz for methanol-h.

Furthermore, the temperature dependence for methanol-d appears to be different between the temperatures 298-328K, where the high frequency end looks the same ( $E_A = 7.6 \text{ kJ mol}^{-1}$ ), but the relaxation rate appears to be independent on the temperature at the low frequency end ( $E_A = 0.05 \text{ kJ mol}^{-1}$ ). This is indicative of a RMTD-type relaxation mechanism. The decrease of the relaxation rates at the low frequency end at 288K can be explained by considering that proton exchange could occur between the methanol-OD group and the surface hydroxyls, resulting in a small amount of methanol-d being converted into methanol-h. As was shown for methanol-h, the effect of the hydroxyl group on the temperature dependence of the relaxation rates is substantial. Therefore even a small amount of methanol-h in the methanol-d sample could show the inverted temperature dependence at low frequencies.

Based on the significant differences between the variable temperature experiments on methanol-h and methanol-d, it is concluded that there is no significant cross relaxation between the methyl and hydroxyl group within methanol. The hydroxyl group appears to follow a protic relaxation mechanism, whereas the methyl group appears to follow the RMTD model.

The contribution of the protic relaxation mechanism to the modeling of the alcohol  $^1\text{H}$  NMRD profiles will be considered constant in the remainder of this thesis, considering the protic model has been shown to be independent on the surface-adsorbate interaction, and considering the hydroxyl group is constant for the short, linear alcohols used in this study. Moreover, the contribution of the hydroxyl group to the  $^1\text{H}$  NMRD profile is small (25%) for methanol, and increasingly smaller for longer alcohols. Therefore any differences between the profiles of the different alcohols are more likely to be caused by changes in the alkyl profile.

#### 5.4.4 High field relaxation

At the high field end, NMRD profiles are dominated by fast relaxation processes, mainly originating from the bulk liquid. As this can include many translational and rotational processes, it is challenging or even impossible to distinguish the different components contributing to the NMRD profile. It has been shown that bulk liquids containing dissolved oxygen, a paramagnetic relaxation source, follow a Lorentzian spectral density<sup>35</sup>:

$$J(\omega) \propto \frac{\tau_L}{1 + \left(\frac{\omega\tau_L}{\tau_L}\right)^2}, \quad (5.9)$$

where  $\tau_L$  is the effective correlation time based on the paramagnetic spin relaxation and the translational diffusion of the liquid, and  $\omega_S$  is the electron Larmor frequency. For accuracy, therefore, the high field relaxation rate,  $R_{1,HF}$  should be modelled to a Lorentzian function. However, this introduces two additional parameters,  $A_{Lor}$ , a pre-factor, and  $\tau_L$ . This means that the complexity of the model is increased and that the effect of one fit parameter on another is increased.

Below a Larmor frequency of 10 MHz, the relaxation rate of bulk liquids is shown to be constant<sup>36</sup>. This also applies to methanol, as was shown in Figure 5.4. Considering the complexity of the RMTD model, as will be shown in the next section, the choice was made to fit the high field relaxation rate to a constant instead. Using a constant  $R_{1,HF}$  produced fits that correspond to the data well, however it should not be forgotten that this term may not be strictly accurate.

#### 5.4.5 Summary

In section 5.4, an overview of several theoretical FFC-NMR models was presented, and for each of the models its applicability to the NMRD profiles of alcohols imbibed within anatase titania, shown in Figure 5.1, was discussed. The five models that were discussed were the Korb model, the  $3\tau$  model, two variations of the RMTD model, and the protic model.

For the Korb model, the physical basis of the models is the interactions of hydrogen spins in the (liquid) probe molecule with paramagnetic impurities on the surface of the support. The corresponding NMRD profiles show a bilogarithmic frequency dependence, contrary to the apparent power law of the alcohol data in Figure 5.1. Additionally, the relaxation rates of a system following the Korb or  $3\tau$  model are expected to decrease upon an increase of the temperature, across the full frequency range of the NMRD profiles. This does not correspond to the temperature dependence of the methanol and methanol-d NMRD profiles in Figure 5.5 and Figure 5.6 respectively, and therefore it is unlikely that the relaxation mechanism of alcohols imbibed within anatase titania matches the Korb or  $3\tau$  model. However, it should be noted that no ESR data is available and therefore it is unclear whether there are paramagnetic impurities in the support. Therefore the alcohol NMRD profiles will be fitted to the Korb model in section 5.6 and compared to the RMTD model fits from section 5.5.

Two approaches to the RMTD mechanism were discussed. The first was the approach by Kimmich, which results in NMRD profiles with a power law frequency dependence. This corresponds to the data in Figure 5.1, however the Kimmich model states that the power law exponent depends only on the surface properties, and not on the surface-adsorbate interactions. In Figure 5.1, the NMRD profiles for the different alcohols do appear to shift, even though the support was the same, suggesting that the surface-adsorbate interactions affect the NMRD profiles. This is taken into account in the intermittent dynamics approach by Levitz, for which the NMRD profiles follow a power law frequency dependence, and the power law exponent is determined by the surface-adsorbate interactions as well as the surface properties. The relaxation rates for systems following the RMTD relaxation mechanism are expected to decrease upon an increase in temperature at the high frequency end, where fast processes are probed. However, at the low frequency end, it is expected that the relaxation rate is independent of the temperature.

Finally, the protic model is based on the interaction and possible exchange of protic groups, in this case the alcohol hydroxyl, with surface hydroxyls that are close to paramagnetic impurities in the support. The corresponding NMRD profiles follow a power law frequency dependence with a frequency independent plateau for  $\omega\tau_s \ll 1$ , and can give rise to a paramagnetic enhancement peak. While these features do correspond with the data in Figure 5.1, only the alcohol hydroxyl group is protic, whereas the alkyl group is not. As for the other relaxation mechanisms, it is expected that the relaxation rates decrease upon an increase in temperature at the high frequency end, however for the protic relaxation mechanism, this temperature dependence inverts toward the low frequency end, resulting in an increase of the relaxation rate with increasing temperature. This corresponds to the variable temperature results for methanol, shown in Figure 5.5, however the inversion was much less clear for methanol-d, shown in Figure 5.6. Therefore it was concluded that there is no significant cross relaxation between the alcohol hydroxyl and alkyl groups, and that the alkyl group likely follows the RMTD mechanism. The protic behaviour of the hydroxyl group is assumed to be constant for the alcohols in this study, and therefore it is expected that any differences between the alcohols are due to the varying alkyl groups and their interactions with the surface.

## 5.5 RMTD modelling

Even though the most suitable model for alcohols imbibed within anatase titania has now been identified, it is not a straightforward task to model the RMTD processes correctly. This section will give an overview of the RMTD background, theory and expressions previously reported in literature. Subsequently the modelling details are described, and the results are presented and discussed.

### 5.5.1 Theory and background

As mentioned previously, the Levitz approach to the RMTD model is based on intermittent dynamics between adsorption steps near the surface and bulk excursions, see Figure 5.7a. In the case of alcohols on a polar titania support, it is expected that the alcohol hydroxyl will bind to the surface strongly, thereby imposing a preferential orientation of the adsorbate. As a result, during the adsorption steps, the loss of correlation is reduced<sup>1,26</sup>. Contrary to the Kimmich approach of the RMTD model, the probability distributions of adsorption (A) and bulk relocations (R) are considered<sup>11</sup>. The probability density functions (p.d.f.),  $\Psi_A(t)$  and  $\Psi_R(t)$  respectively, describe the time distributions of the adsorption and relocation events.  $\Psi_A(t)$  is the p.d.f. describing the time distribution from when a molecule first enters the adsorption layer until its first desorption. The adsorption correlation time,  $\tau_A$ , is the average time spent in the adsorption region between a first entry and the consecutive first exit, shown in Figure 5.7b. In terms of the physical meaning of the correlation times,  $\tau_A$  in the RMTD model has previously been related to the surface diffusion time  $\tau_l$  in the  $3\tau$  model, which corresponds to the surface hopping time  $\tau_m$  in the Korb model<sup>23</sup>.

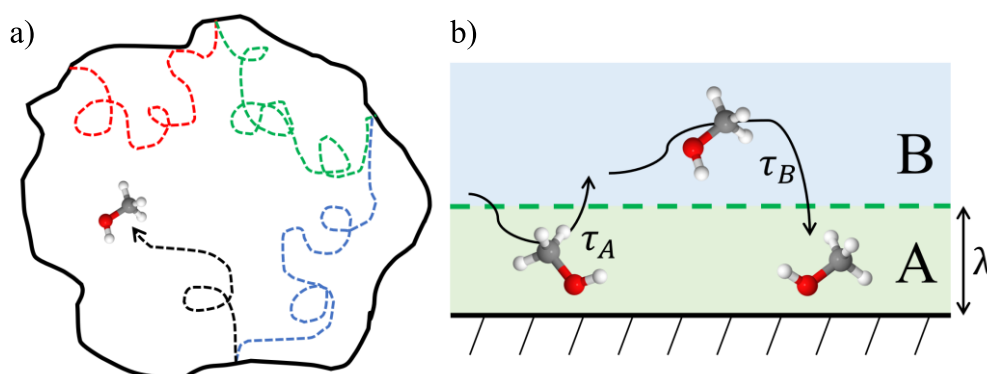


Figure 5.7: a) Intermittent dynamics of a methanol molecule inside a pore, between adsorption steps near the surface, and bridges in the bulk-in-the-pore. b) Schematic of a methanol molecule undergoing intermittent dynamics between the adsorption layer (A) and the confined bulk (B), where the adsorption correlation time,  $\tau_A$ , represents the average time a molecule spends in the adsorption layer before desorption, and the bulk correlation time,  $\tau_B$ , represents the average time a molecule spends in the confined bulk before its first possible re-entry into the adsorption layer.

$\Psi_B(t)$  is the p.d.f. describing the time distribution for the molecule between desorption and its first possible re-entry into the adsorption layer, with a corresponding correlation time  $\tau_B$ . The p.d.f. of relocation ( $\Psi_R(t)$ ) and the p.d.f. of the bulk environment ( $\Psi_B(t)$ ) are related via:

$$\tilde{\Psi}_R(\omega) = \frac{p\tilde{\Psi}_B(\omega)}{1 - (1-p)\tilde{\Psi}_B(\omega)}, \quad (5.10)$$

where  $\tilde{\Psi}_R(\omega)$  and  $\tilde{\Psi}_B(\omega)$  are the Fourier transforms of  $\Psi_R(t)$  and  $\Psi_B(t)$  respectively. The correlation times can be described to find  $\tau_R = \tau_B/p$ , where  $p$  is the probability of readsorption.  $\tau_R$  then describes the average time from a first desorption to a first adsorption. Assuming all molecules will visit the adsorption and bulk phases at a point of time,  $\tau_A(1 - f_{ads}) = \tau_R f_{ads}$ , and therefore  $\tau_A = \frac{\tau_B}{p} \left[ \frac{f_{ads}}{1-f_{ads}} \right]$ , where  $f_{ads}$  is the fraction of molecules within the adsorption layer.

The intermittent dynamics can then be described using an indicator function, where  $I(t) = 1$  during the adsorption steps, and  $I(t) = 0$  when the molecules are in the confined bulk, see Figure 5.8.

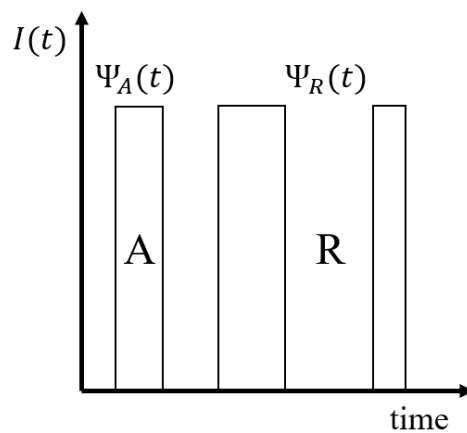


Figure 5.8: An indicator function describing the intermittent dynamics of liquids in a pore. In the adsorption state ( $\Psi_A(t)$ ),  $I(t) = 1$ , and during the bulk relocations ( $\Psi_R(t)$ ),  $I(t) = 0$ .

The corresponding correlation function is then:

$$C(\tau) = \overline{I(\tau) \cdot I(0)} / \eta_a, \quad (5.11)$$

with  $\eta_a = \tau_A / (\tau_A + \tau_R)$ . The brackets stand for an ensemble average over all trajectories, and the bar corresponds to all initial times '0'. Following equation (5.11) and the boundary

conditions for  $\tau_A$  and  $\tau_R$ ,  $C(0) = 1$  and  $C(\infty) = \eta_a$ . Subsequently, the correlation function can be Fourier Transformed into the (normalized) spectral density function:

$$J(\omega) = \frac{2}{\tau_A \omega^2} \text{Real} \left[ \frac{(1 - \tilde{\Psi}_A(\omega))(1 - \tilde{\Psi}_B(\omega))}{1 - \tilde{\Psi}_A(\omega)\tilde{\Psi}_B(\omega)} \right] \quad (5.12)$$

This spectral density function has only been evaluated for a few pore geometries, such as flat, rough or external cylindrical interfaces<sup>11-13</sup>, in which the relocation statistics show an algebraic tail at long times of  $\tilde{\Psi}_B(t)$ . For nanoporous networks however, this algebraic tail is suppressed by an exponential cut-off. As a result, it is more complicated to obtain a closed form expression of the spectral density function.

The spectral density function in the case of a planar surface has been previously applied to spherical silica<sup>38</sup>. In this case, the adsorption and bulk p.d.f.s can be approximated:

$$\Psi_A(t) = \frac{1}{\tau_A} \exp(-t/\tau_A), \quad (5.13)$$

$$\Psi_B(t) = \frac{\delta}{\sqrt{4\pi Dt^3}} \exp(-\delta^2/4Dt), \quad (5.14)$$

where  $\delta$  is the surface layer thickness, and  $D$  the diffusion coefficient of the liquid in the bulk-in-the-pore. By inserting the Fourier Transforms of equations (5.13) and (5.14) into equation (5.12), the spectral density function could be reduced to<sup>14</sup>:

$$J(\omega) = \omega_A^{-1} \left[ \sqrt{\frac{\omega}{\omega_A}} + \frac{\omega}{\omega_A} + \frac{1}{2} \left( \frac{\omega}{\omega_A} \right)^{\frac{3}{2}} \right]^{-1} \quad (5.15)$$

In this expression for the spectral density,  $\omega_A$  is a characteristic frequency for the system, which can be converted to  $\tau_A$ , the adsorption correlation time, via:

$$\omega_A = \frac{\delta^2}{2D\tau_A^2} \quad (5.16)$$

$\tau_A$ , the adsorption correlation time, is arguably the most important parameter that can be extracted from this model, as it represents the average time a molecule spends at the surface before desorption, and therefore it reflects the surface-adsorbate interaction strength. The exponent of the power law relaxation behaviour for weakly adsorbed species (small  $\tau_A$  values)

will be 1/2, whereas strongly adsorbed species (large  $\tau_A$  values) will exhibit a power law exponent of 3/2. Therefore, although the relaxation behaviour between these limits is not strictly a power law, an increase in the surface-adsorbate interaction strength would lead to an increase in the apparent power law exponent. Experimentally determined values for  $\tau_A$  for liquids in mesoporous media are scarce, however values in the nano- to picosecond range have been reported for water in plaster pastes<sup>39</sup>.

### 5.5.2 Fitting expressions and parameters

At the basis of the Levitz model for RMTD processes is an intramolecular relaxation mechanism. This means that the observed relaxation rate can be described as follows<sup>2,15</sup>:

$$R_{1,obs}(\omega) = R_{1,HF} + A_{RMTD}[J(\omega) + 4J(2\omega)], \quad (5.17)$$

with the spectral density function  $J(\omega)$  as described in equation (5.15). In equation (5.17),  $R_{1,HF}$  is the high field relaxation rate, which will be modelled as a constant, as is explained in section 5.4.4. Finally, the pre-factor  $A_{RMTD}$  has been explicitly determined for water in gypsum<sup>39</sup>:

$$A_{RMTD} = \frac{\varepsilon \rho_{Gyp} S}{\varphi} \omega_d^2, \quad (5.18)$$

where  $\varepsilon$  is the adsorption layer,  $\rho_{Gyp}$  is the gypsum density,  $S$  is the specific surface area,  $\varphi$  is the porosity and  $\omega_d^2 = \left(\frac{\mu_0}{4\pi} \gamma_H^2 \hbar\right)^2 \sum \frac{1}{r^6}$  is the proton-water dipole-dipole interaction. The surface weighting term  $\varepsilon \rho_{Gyp} S / \varphi$  corresponds to the surface-to-pore ratio of probed spins  $\frac{N_S}{N}$ . For liquids imbibed within mesoporous media, following the two-phase fast exchange model, this term can be described as  $\frac{N_S}{N} = \frac{\lambda S}{V}$ , where  $\lambda$  is the surface layer thickness, generally estimated to be the molecular diameter,  $S$  is the surface area and  $V$  is the pore volume<sup>37</sup>. As a result, the full model equation is:

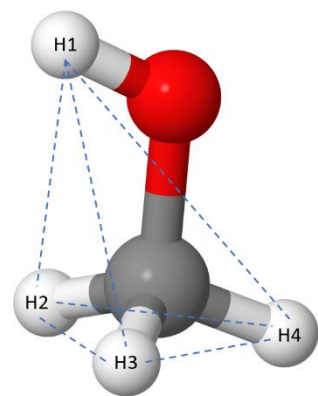
$$R_{1,obs}(\omega) = R_{1,HF} + \frac{\lambda S}{V} \left(\frac{\mu_0}{4\pi} \gamma_H^2 \hbar\right)^2 \sum \frac{1}{r^6} \omega_A^{-1} \times \left[ \left[ \sqrt{\frac{\omega}{\omega_A}} + \frac{\omega}{\omega_A} + \frac{1}{2} \left(\frac{\omega}{\omega_A}\right)^{\frac{3}{2}} \right]^{-1} + 4 \left[ \sqrt{\frac{2\omega}{\omega_A}} + \frac{2\omega}{\omega_A} + \frac{1}{2} \left(\frac{2\omega}{\omega_A}\right)^{\frac{3}{2}} \right]^{-1} \right]. \quad (5.19)$$

In this equation,  $\mu_0$  is the vacuum permeability constant,  $\gamma_H$  is the proton gyromagnetic ratio, and  $\hbar$  is the reduced Planck's constant. These are well-known constants that were fixed in the fitting procedure. The surface area,  $S$ , and the pore volume,  $V$ , were determined through BET/BJH measurements, see section 5.2.1, and were therefore also fixed. The molecular diameter,  $\lambda$ , was estimated by using the density and molecular weight of each of the alcohols to condense the molecules into spheres. The values of  $\lambda$  used in this study are shown in Table 5.2.

Table 5.2: Molecular diameters of the alcohols used in this study, calculated based on the density of the bulk liquid.

Alcohol	$\lambda / \text{\AA}$
Methanol	4.07
Ethanol	4.59
Propanol	4.99
Butanol	5.34
Pentanol	5.64

Values for the intramolecular distances,  $r$ , were estimated via *Jmol* distance measurements<sup>16</sup>. Figure 5.9 shows all intramolecular distances for hydrogen atoms in methanol, and Table 5.3 provides the corresponding values for  $r$ .



<sup>1</sup> H pair	$r / \text{nm}$
H1-H2	0.239
H1-H3	0.239
H1-H4	0.290
H2-H3	0.178
H2-H4	0.178
H3-H4	0.178

Figure 5.9: Intramolecular distances  $r$  between the four hydrogen atoms in methanol, as measured in *Jmol*.

Table 5.3: Intramolecular distances between the hydrogen pairs in methanol, specified in Figure 5.9.

Finally,  $R_{1,HF}$  and  $\omega_A$  were fitted. Importantly,  $\omega_A$  is a characteristic frequency at which the dominant component of the spectral density changes between  $\sqrt{\frac{\omega}{\omega_A}}$  for  $\omega < \omega_A$  and  $\frac{\omega}{\omega_A} +$

$\frac{1}{2} \left( \frac{\omega}{\omega_A} \right)^{\frac{3}{2}}$  for  $\omega > \omega_A$ . This means that for an accurate fit, the value of  $\omega_A$  must be within or close to the NMRD profile frequency range, i.e. ideally in the range of  $10^{-2} - 10^3$  MHz. If  $\omega_A$  does not lie within the FFC frequency range, the power law exponent will converge to the limits of  $1/2$  for  $\omega \ll \omega_A$  and  $3/2$  for  $\omega \gg \omega_A$ . If this is the case, the extracted value of  $\omega_A$  will not be accurate.

Following the fitting procedure,  $\omega_A$  could be converted into  $\tau_A$  via equation (5.16), provided the distance to the surface,  $\delta$ , and the diffusion coefficient,  $D$  are known.

#### 5.5.2.1 Distance to the surface $\delta$

In equation (5.16),  $\delta$  reflects the maximum distance to the surface at which the influence of the surface will be felt by the probe molecule. In other words, it represents a surface-sensitive layer thickness, not to be confused with surface layer thickness  $\lambda$  that is used to determine  $\frac{N_S}{N} = \frac{\lambda S}{V}$ , see section 5.5.1.

As mentioned before, previously the molecular diameter has been used as an estimate for  $\delta$ , so that  $\delta = \lambda$ <sup>38,39</sup>. For water, the molecular diameter is estimated at  $\delta = 0.3$  nm. The molecular diameter can be calculated by using the density and molecular weight to condense the molecules into spheres, or the hydrodynamic radius can be extracted through the self-diffusion coefficient<sup>40</sup>. For small molecules, both methods result in an identical molecular diameter. For longer chain alcohols, the hydrodynamic radius stays constant with carbon number, although the density-based molecular diameter continues to increase.

Assuming  $\delta$  reflects the surface layer thickness,  $\delta$  does not necessarily correspond to the molecular diameter. For longer chain alcohols, the molecules will deviate from a spherical geometry with increasing chain length. Therefore the true value for  $\delta$  will be somewhere between the density-based molecular diameter as calculated above, and the length of the alcohol molecule. In order to obtain a consistent analysis, the density-based molecular diameter shown in Table 5.2 will be used for  $\delta$  and  $\lambda$  in the remainder of this chapter. As expected, the molecular diameter increases with increasing carbon number.

Additionally, it must be noted that when comparing the surface-adsorbate interactions of different liquids on the same surface, the surface-sensitive layer thickness may depend on the surface, rather than the adsorbed liquid. For similar liquids with the same surface-adsorbate

interaction mechanism, such as linear alcohols, it is not necessarily expected that the molecular size affects the interaction. Therefore  $\tau_A$  values will also be determined using a constant value. In order to compare the  $\tau_A$  values with the literature, the molecular diameter of water,  $\delta = 0.3$  nm, will be used.

### 5.5.2.2 Diffusion coefficient $D$

The diffusion coefficient describes the speed at which the molecules diffuse when they are not adsorbed on to the surface, see equation (5.14). Previously, the diffusion coefficient of the bulk liquid has been used to determine  $\tau_A$ , under the assumption that the diffusion coefficient converges to the bulk diffusion coefficient from 1 nm from the surface<sup>14</sup>. The anatase titania pores have an average pore diameter of  $d_p = 9.5$  nm. As was described in the previous section, the surface layer thickness is estimated to correspond to the molecular diameter of each respective alcohol. As was shown in Table 5.2, for methanol, the molecular diameter is approximately 0.41 nm, and for pentanol, the longest alcohol used in this study, the molecular diameter is 0.56 nm. This means that the “bulk” molecules are diffusing close to the surface. Combining these two considerations, using the bulk diffusion coefficient for this system is not valid. Therefore the diffusion coefficient of the liquid imbibed within the pore has been determined using PFG NMR. The diffusion coefficients are shown in Table 5.4.

*Table 5.4: Diffusion coefficients of alcohols imbibed within anatase titania, determined by PFG NMR experiments. The error in diffusion coefficient corresponds to the standard deviation determined from experiments on three different sets of anatase titania pellets imbibed with the appropriate alcohol.*

<b>Alcohol</b>	<b><math>D / 10^{-10} \text{ m}^2\text{s}^{-1}</math></b>
Methanol	$13.4 \pm 0.74$
Ethanol	$5.73 \pm 0.09$
Propanol	$3.15 \pm 0.17$
Butanol	$2.22 \pm 0.10$
Pentanol	$1.70 \pm 0.05$

The diffusion coefficients decrease according to a power law  $D \propto N^{-\beta}$ , where  $N$  is the carbon number, corresponding to similar diffusion trends in alkanes<sup>41</sup>. The slope of this power law was empirically determined at  $\beta = 1.30$ .

### 5.5.3 Modelling results

Equation (5.19) was fitted to the alcohol NMRD profiles shown in Figure 5.1. The fits of methanol and butanol are shown in Figure 5.10 and the corresponding fit parameters are shown in Table 5.5. The least squares fitting is based on the  $\log(R_1)$  values.

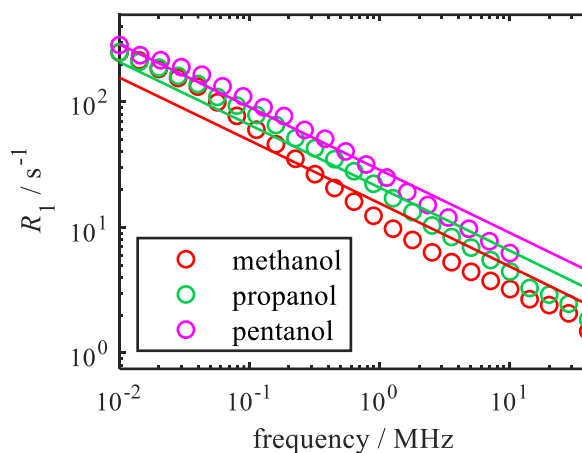


Figure 5.10:  $^1\text{H}$  NMRD profiles for methanol, propanol and pentanol imbibed within anatase titania, and the corresponding RMTD fits as described in equation (5.19). Ethanol and butanol were excluded for clarity.

Table 5.5: Fit parameters  $R_{1,HF}$  and  $\omega_A$ , and their respective standard errors, as well as the  $R^2$  values for the RMTD fits (equation (5.19)) to the alcohol NMRD profiles shown in Figure 5.1. The fits for methanol, propanol and pentanol are shown in Figure 5.10.

Alcohol	$R_{1,HF} / \text{s}^{-1}$	$\omega_A / \text{MHz}$	$R^2$
Methanol	$1.93 \cdot 10^{-11} \pm 0.92$	$9.86 \cdot 10^5 \pm 1.13 \cdot 10^6$	0.9423
Ethanol	$9.05 \cdot 10^{-8} \pm 2.21$	$1.73 \cdot 10^6 \pm 2.86 \cdot 10^6$	0.9602
Propanol	$1.04 \cdot 10^{-8} \pm 1.40$	$3.28 \cdot 10^6 \pm 8.85 \cdot 10^6$	0.9652
Butanol	$8.27 \cdot 10^{-7} \pm 1.36$	$4.97 \cdot 10^6 \pm 1.32 \cdot 10^7$	0.9760
Pentanol	$1.93 \cdot 10^{-7} \pm 3.14$	$4.97 \cdot 10^6 \pm 1.08 \cdot 10^7$	0.9790

In Figure 5.10, the RMTD fits appear to be a single power law, corresponding to a straight line in the log-log plot. The curvature in the NMRD profiles is not considered in the fit. As said before,  $\omega_A$  should fall roughly within the range of the NMRD profile, i.e.  $10^{-2} - 10^3$  MHz, to obtain a sensible fit. The values for  $\omega_A$  in Table 5.5 are all in the order of  $10^6$  MHz. This suggests that the fit is overestimating  $\omega_A$ . Moreover, as can be seen from the very high standard errors and the low  $R^2$  correlation coefficients in Table 5.5, the model does not fit well for any of the alcohols.

Based on the results in Figure 5.10 and Table 5.5 it is concluded that equation (5.19) is not complete, i.e. another fit parameter, from here on called  $A$ , is missing. Therefore the alcohol NMRD profiles were fitted to an adjusted RMTD model equation:

$$R_{1,obs}(\omega) = R_{1,HF} + A \frac{\lambda S}{V} \left( \frac{\mu_0}{4\pi} \gamma_H^2 \hbar \right)^2 \sum \frac{1}{r^6} \omega_A^{-1} \times \left[ \left[ \sqrt{\frac{\omega}{\omega_A} + \frac{\omega}{\omega_A} + \frac{1}{2} \left( \frac{\omega}{\omega_A} \right)^{\frac{3}{2}}} \right]^{-1} + 4 \left[ \sqrt{\frac{2\omega}{\omega_A} + \frac{2\omega}{\omega_A} + \frac{1}{2} \left( \frac{2\omega}{\omega_A} \right)^{\frac{3}{2}}} \right]^{-1} \right] \quad (5.20)$$

The adjusted RMTD fits to the NMRD profiles of alcohols imbibed within anatase titania are shown in Figure 5.11. The fit parameters are shown in Table 5.6. Again, the least squares fitting is based on the  $\log(R_1)$  values.

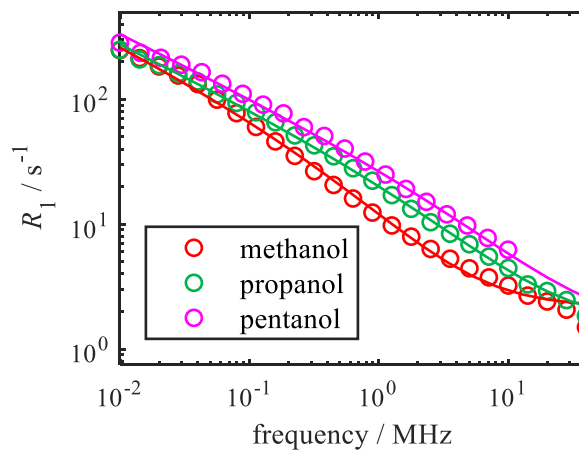


Figure 5.11:  $^1\text{H}$  NMRD profiles for methanol, propanol and pentanol imbibed within anatase titania, and the corresponding adjusted RMTD fits as described in equation (5.20). Ethanol and butanol were excluded for clarity.

Table 5.6: Fit parameters  $R_{1,HF}$ ,  $A$  and  $\omega_A$ , and their respective standard errors, as well as the  $R^2$  values for the adjusted RMTD fits (equation (5.20)) to the alcohol NMRD profiles shown in Figure 5.1. The fits for methanol, propanol and pentanol are shown in Figure 5.11.

Alcohol	$R_{1,HF} / \text{s}^{-1}$	$A$	$\omega_A / \text{MHz}$	$R^2$
Methanol	$2.07 \pm 2.34 \cdot 10^{-2}$	$5.25 \cdot 10^{-3} \pm 5.23 \cdot 10^{-5}$	$8.04 \pm 0.247$	0.9977
Ethanol	$2.08 \pm 3.36 \cdot 10^{-2}$	$5.66 \cdot 10^{-3} \pm 4.87 \cdot 10^{-5}$	$27.1 \pm 0.548$	0.9996
Propanol	$1.51 \pm 2.25 \cdot 10^{-2}$	$5.50 \cdot 10^{-3} \pm 6.16 \cdot 10^{-5}$	$50.1 \pm 1.43$	0.9988
Butanol	$1.60 \pm 5.11 \cdot 10^{-2}$	$5.58 \cdot 10^{-3} \pm 9.86 \cdot 10^{-5}$	$90.1 \pm 2.84$	0.9975
Pentanol	$1.81 \pm 2.55 \cdot 10^{-1}$	$5.54 \cdot 10^{-3} \pm 33.0 \cdot 10^{-5}$	$110 \pm 14.1$	0.9972

As expected, the standard errors of the fit parameters shown in Table 5.6 are lower and the  $R^2$  values are much higher compared to the results shown in Table 5.5. A visual analysis of the fits shown in Figure 5.11 also shows the improved quality of the fits. Moreover, the order of magnitude of the  $\omega_A$  values,  $1 - 10^2$  MHz, falls within the range of the NMRD profiles,  $10^{-2} - 10^3$  MHz. This means that the extracted  $\omega_A$  values are based on the data.

The values for the added fit parameter  $A$  appear to be constant across the alcohol range. With an average value of  $A = 5.50 \cdot 10^{-3} \pm 0.16 \cdot 10^{-3}$ , methanol is the only alcohol for which the  $A$  value is a slight outlier. Because the value for  $A$  is constant for several different liquids on the same support, it is expected that  $A$  is a structural pre-factor that depends on the surface properties. For example,  $A$  could be similar to  $\chi$  in the Kimmich type RMTD model shown in section 5.4.2.1, which represents the surface roughness<sup>27</sup>.

Additionally, the fit parameters  $A$  and  $\omega_A$  are inversely correlated in equation (5.20). To quantify the correlation, a correlation matrix was determined via the variance-covariance matrix, see Table 5.7.

Table 5.7: Correlation matrix for the fit parameters in Table 5.6, produced via the variance-covariance matrix in Matlab. The values shown are the average correlation coefficients for the fits for all alcohols, and the corresponding standard deviations.

	$R_{1,HF}$	$A$	$\omega_A$
$R_{1,HF}$	1.00	$-0.854 \pm 0.112$	$-0.824 \pm 0.126$
$A$	$-0.854 \pm 0.112$	1.00	$0.964 \pm 0.040$
$\omega_A$	$-0.824 \pm 0.126$	$0.964 \pm 0.040$	1.00

From the correlation matrix, it is clear that there is indeed a very high correlation between all fit parameters, and especially  $A$  and  $\omega_A$ , for which the correlation coefficient is nearly 1. The RMTD model could be made more accurate and reliable through further investigation into the value of  $A$ . However, for the current study, the main objective is to establish a modelling method that can distinguish between the surface-adsorbate interactions of alcohols imbibed within anatase titania, such that in chapter 6 the microphase separation of alcohol-water mixtures within the same support can be investigated. Because the relative variation of  $A$  with the alcohol chain length is much less than the variation of  $\omega_A$ , it is concluded that the current modelling method is sufficiently reliable for these purposes.

Now that an appropriate method of modelling RMTD type processes in alcohols imbibed within anatase titania has been established, the appropriate extraction of  $\tau_A$  can be discussed. Values for  $\tau_A$  were calculated based on equation (5.16). The  $\omega_A$  values to determine  $\tau_A$  were those shown in Table 5.6, the diffusion coefficients  $D$  are shown in Table 5.4, and the  $\tau_A$  values were determined for two sets of  $\delta$  values, namely those that correspond to the molecular diameter of the alcohol, shown in Table 5.2, as well as  $\delta = 0.3$  nm, corresponding to the molecular diameter of water. The results are shown in Table 5.8.

Table 5.8:  $\tau_A$  values for alcohols imbibed within anatase titania, determined via equation (5.16), using the  $\omega_A$  values in Table 5.6, diffusion coefficients from Table 5.4, and  $\delta$  values either from Table 5.2, or fixed at  $\delta = 0.3$  nm, corresponding to the molecular diameter of water. The standard errors were estimated by propagating the standard errors of the  $\omega_A$  values and diffusion coefficients.

<b>Alcohol</b>	<b><math>\tau_A</math> / ns (<math>\delta = \lambda</math>)</b>	<b><math>\tau_A</math> / ns (<math>\delta = 0.3</math> nm)</b>
Methanol	$2.77 \pm 0.176$	$2.05 \pm 0.129$
Ethanol	$2.61 \pm 0.067$	$1.70 \pm 0.044$
Propanol	$2.81 \pm 0.172$	$1.69 \pm 0.103$
Butanol	$2.67 \pm 0.147$	$1.50 \pm 0.083$
Pentanol	$2.93 \pm 0.387$	$1.56 \pm 0.206$

The order of magnitude of the  $\tau_A$  values in Table 5.8, nanoseconds, falls within the  $\tau_A$  range found for water in plaster pastes, which was  $64 \cdot 10^{-12} - 5.7 \cdot 10^{-9}$  s and which was shown to be correlated to the nanowettability of the plaster paste<sup>39</sup>. Interestingly, the plaster paste data was also fitted using the  $3\tau$  model<sup>23</sup>, which resulted in  $\tau_l = 40 \pm 5$   $\mu$ s,  $\tau_d = 6.5 \pm 0.5$   $\mu$ s, and  $\tau_i = 17 \pm 0.5$  ps. The surface water diffusion rate was concluded to be related to the desorption rate, as  $\tau_l \approx \tau_d$ . Clearly, there is a large difference between the correlation times from the RMTD model and the  $3\tau$  model. It would be very interesting to model the data presented in the current study with the  $3\tau$  model as well, in order to make a comparison between the models and their respective correlation times. However, this is beyond the scope of the current investigation, which is primarily aimed to obtain a modelling method for alcohols imbibed within anatase titania with the purpose of investigating microphase separation in chapter 6.

For anatase titania, a highly polar support, it is expected that the surface-adsorbate interaction will increase with the solvent polarity, analogous to  $\gamma$ -alumina<sup>19</sup>. For alcohols, as was shown in Table 5.1, the polarity decreases with a longer alkyl chain. Moreover,  $\tau_A$  is believed to

correlate with interaction strength. Therefore, it is expected  $\tau_A$  will decrease with increasing chain length, according to the values for the alcohol polarity.

Table 5.8 indeed shows that  $\tau_A$  decreases with an increasing alkyl chain length when the surface-sensitive layer thickness  $\delta$  is kept constant. When  $\delta$  is set to be equal to the molecular diameter, no clear trend of  $\tau_A$  with the polarity of the alcohol molecule can be distinguished. Therefore it is concluded that  $\delta$  must be kept constant, which suggests the maximum distance at which molecules can feel the influence of the surface depends on the surface, rather than the probe molecule. While this theory has been presented previously in literature<sup>33</sup>, the current study provides evidence that this is indeed the case. It should be noted that while  $\delta$  must be kept constant, it is not necessarily true that  $\delta = 0.3$  nm. This value was merely chosen to simplify a comparison of the current study with the literature. Additional research, including research on multiple types of supports, must be done in order to determine the true value of  $\delta$ , and therefore the true, absolute values of  $\tau_A$ .

### 5.5.3.1 Comparison with THF imbibed within anatase titania

The linear correlation between  $\tau_A$  and the polarity becomes clearer, and importantly, more general, when the RMTD model is applied to the NMRD profile of THF imbibed within anatase titania, the data of which was shown in the previous chapter. The fit parameters are shown in Table 5.9, and values for  $\tau_A$  after conversion via equation (5.20) are shown in Table 5.10. Values for  $\tau_A$  ( $\delta = \lambda = 0.512$ ) are shown for completeness, however the following analysis is based on the values of  $\tau_A$  ( $\delta = 0.3$  nm).

Table 5.9: Fit parameters  $R_{1,HF}$ ,  $A$  and  $\omega_A$ , and their respective standard errors, as well as the  $R^2$  value for the adjusted RMTD fits (equation (5.20)) to the NMRD profile for THF imbibed within anatase titania shown in Figure 4.4a.

Solvent	$R_{1,HF} / s^{-1}$	$A$	$\omega_A / \text{MHz}$	$R^2$
THF	$2.47 \pm 6.08 \cdot 10^{-2}$	$5.60 \cdot 10^{-3} \pm 1.47 \cdot 10^{-4}$	$45.7 \pm 3.99$	0.9944

Table 5.10:  $\tau_A$  values for THF imbibed within anatase titania, determined via equation (5.16), using the  $\omega_A$  value in Table 5.9, a diffusion coefficient  $D = 1.77 \cdot 10^{-9} \text{ m}^2 \text{ s}^{-1}$  as determined by PFG NMR, and  $\delta$  values based on the density of THF, for which  $\delta = 0.512$  nm, or fixed at  $\delta = 0.3$  nm, corresponding to the molecular diameter of water. The standard errors were estimated by propagating the standard errors of the  $\omega_A$  and  $D$  values.

Solvent	$\tau_A / \text{ns}$	$\tau_A / \text{ns}$
	( $\delta = \lambda$ )	( $\delta = 0.3$ nm)
THF	$1.27 \pm 0.112$	$0.745 \pm 0.066$

The linear dependence of  $\tau_A$  on the solvent polarity is shown in Figure 5.12. Not only does this linear correlation provide more evidence that the RMTD processes were modelled appropriately, it also demonstrates how the extraction of  $\tau_A$  can provide insight into the dynamics of a porous media system. For the solvents used in this and the previous chapter, a clear expectation of the dynamical trends could be made. Now, the approach can be applied to systems with unknown dynamics.

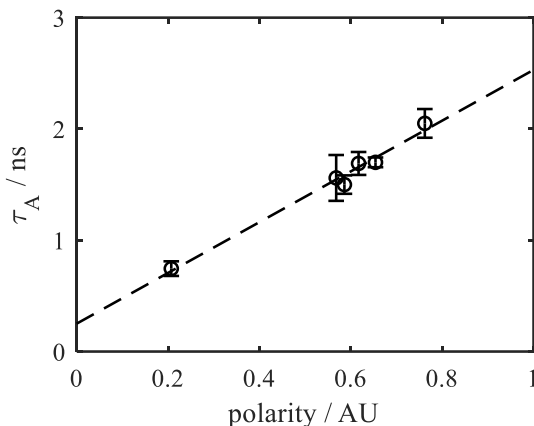


Figure 5.12:  $\tau_A$  as determined by the RMTD model plotted against the solvent polarity, for alcohols and THF imbibed within anatase titania. The  $\tau_A$  values and error bars are specified in Table 5.8 and Table 5.10. A dashed line shows the linearity of the trend.

## 5.6 Comparison with the Korb model

The RMTD model in section 5.5 appears an appropriate modelling method for the NMRD profiles of alcohols imbibed within anatase titania, and the modelling results appear successful and physically sensible. However, it was not possible to completely rule out that a Korb-type model could be appropriate as well, considering the lack of information about the presence of paramagnetic impurities on the anatase titania support. Therefore, this section presents the fitting of the Korb model as shown in section 5.4.1.1 to the NMRD profiles shown in Figure 5.1. Following equation (5.5), the full expression of the fitted model was:

$$R_{1,obs}(\omega) = R_{1,HF} + A_{Korb}\tau_m \times \left[ 3 \ln \left[ \frac{1 + \omega_I^2 \tau_m^2}{\frac{\tau_m^2}{\tau_S^2} + \omega_I^2 \tau_m^2} \right] + 7 \ln \left[ \frac{1 + \omega_S^2 \tau_m^2}{\frac{\tau_m^2}{\tau_S^2} + \omega_S^2 \tau_m^2} \right] \right], \quad (5.21)$$

in which  $R_{1,HF}$  and  $\tau_m$  were fitted. The prefactor  $A_{Korb} = \left(\frac{\mu_0}{4\pi}\right)^2 \frac{N_S \pi \sigma_S (\gamma_I \gamma_S \hbar)^2 S(S+1)}{15d^2 \delta'^2}$  was also fitted, because not all physical properties are known, such as the density of paramagnetic spins,

$\sigma_s$ . The surface residence time,  $\tau_s$ , has previously been shown to yield unphysical correlation times<sup>42</sup>. For the current study, the modelling results did not appear to depend on the value of  $\tau_s$ , because this parameter was larger than the limit that could be measured by the FFC-NMR experiments within a frequency range  $0.01 \leq \omega_0 \leq 40$  MHz. Therefore,  $\tau_s$  was fixed to a value  $\tau_s = 1 \cdot 10^{-5}$  s. Finally,  $\omega_S = 659 \times \omega_I$ . The least squares fitting was based on the  $\log(R_1)$  values. The Korb model fits to the NMRD profiles of alcohols imbibed within anatase titania are shown in Figure 5.13. The fit parameters are shown in Table 5.11.

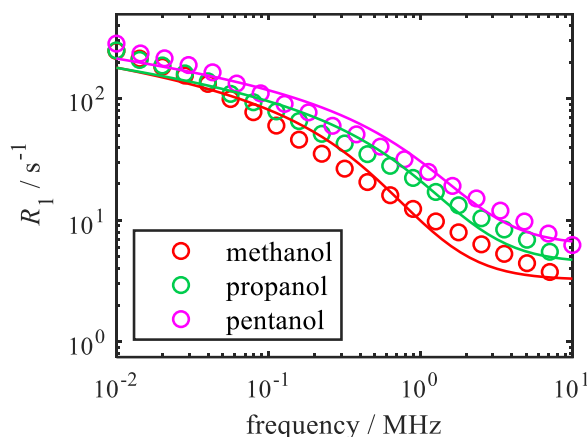


Figure 5.13:  $^1\text{H}$  NMRD profiles for methanol, propanol and pentanol imbibed within anatase titania, and the corresponding Korb model fits as described in equation (5.21). Ethanol and butanol were excluded for clarity.

Table 5.11: Fit parameters  $R_{1,HF}$ ,  $A_{Korb}$  and  $\tau_m$ , and their respective standard errors, as well as the  $R^2$  values for the Korb model fits (equation (5.21)) to the alcohol NMRD profiles shown in Figure 5.1. The fits for methanol, propanol and pentanol are shown in Figure 5.13.

Alcohol	$R_{1,HF} / \text{s}^{-1}$	$A_{Korb}$	$\tau_m / 10^{-7} \text{ s}$	$R^2$
Methanol	$3.23 \pm 9.40 \cdot 10^{-2}$	$2.72 \cdot 10^7 \pm 5.43 \cdot 10^5$	$2.64 \pm 9.53 \cdot 10^{-2}$	0.9739
Ethanol	$3.92 \pm 1.31 \cdot 10^{-1}$	$4.02 \cdot 10^7 \pm 8.91 \cdot 10^5$	$1.50 \pm 5.80 \cdot 10^{-2}$	0.9738
Propanol	$4.46 \pm 1.27 \cdot 10^{-1}$	$4.65 \cdot 10^7 \pm 8.83 \cdot 10^5$	$1.29 \pm 4.23 \cdot 10^{-2}$	0.9794
Butanol	$5.48 \pm 1.33 \cdot 10^{-1}$	$5.14 \cdot 10^7 \pm 8.95 \cdot 10^5$	$1.15 \pm 3.39 \cdot 10^{-2}$	0.9840
Pentanol	$6.24 \pm 1.81 \cdot 10^{-1}$	$6.47 \cdot 10^7 \pm 1.30 \cdot 10^6$	$1.06 \pm 3.58 \cdot 10^{-2}$	0.9812

The quality of the Korb model fits, expressed in  $R^2$  correlation coefficients, is much poorer than that of the RMTD model fits in Figure 5.11 and Table 5.6. Based on a visual analysis of the fits in Figure 5.13, it appears that the Korb model fits underestimate the relaxation rate at high and low frequencies, and overestimate the relaxation rate in the middle of the NMRD profiles. It should be noted that the values for  $\tau_m$  in Table 5.11 decrease with alcohol chain length, which is consistent with a decrease in surface-adsorbate interaction strength and

therefore qualitatively what one would expect. However, given the fit quality of the Korb and RMTD model fits, as well as the results of the variable temperature experiments in section 5.4.3.1, it is concluded that the RMTD model is more appropriate for the currently studied systems.

## 5.7 Conclusions and outlook

In this chapter, the power law analysis as it was performed on THF imbibed within anatase titania, shown in the previous chapter, was deemed insufficient to analyse the dynamics of alcohols imbibed within anatase titania.

Some of the leading theoretical models for FFC-NMR were discussed and variable temperature FFC-NMR experiments were performed on methanol and methanol-d, resulting in the conclusion that the dominant relaxation mechanism for alcohols imbibed within anatase titania likely follow a RMTD type process.

The Levitz RMTD model was then applied to the NMRD profiles. Initially, a model equation based on the literature was fitted to the data, however the quality of the model fits appeared very poor, and the fit parameter  $\omega_A$  did not describe the data. Therefore a structural pre-factor  $A$  was added to the model equation, which produced significantly improved fits. The fitted frequency characteristic to the adsorption process,  $\omega_A$ , was then converted into the adsorption correlation time,  $\tau_A$ . The adsorption correlation time was shown to correlate with the polarity of the solvent, as was expected due to the high polarity of the support. An extension of the study to include some data from the previous chapter regarding THF imbibed within anatase titania, showed the linearity and generality of this correlation.

Finally, the Korb model was fitted to the NMRD profiles. Due to the lack of information on the presence of paramagnetic impurities on the support, it was not possible to fully rule out the relaxation mechanisms corresponding to the Korb model. The quality of the Korb model fits was much poorer than that of the RMTD fits, and therefore it was concluded that the RMTD model is indeed the most appropriate model for the current systems.

The foundation has now been laid for the following chapter, where the competitive adsorption and microphase separation of alcohol-water mixtures imbibed within anatase titania will be investigated. The validation of the RMTD model for pure alcohols means a relatively simple transition to a model for alcohols in a mixture.

## References

1. Kimmich, R. & Anorado, E. Field-cycling NMR relaxometry. *Prog. Nucl. Magn. Reson. Spectrosc.* **44**, 257–320 (2004).
2. Korb, J.-P. Multiscale nuclear magnetic relaxation dispersion of complex liquids in bulk and confinement. *Prog. Nucl. Magn. Reson. Spectrosc.* **104**, 12–55 (2018).
3. Abdel Hamid, A. R., Mhanna, R., Lefort, R., Ghoufi, A., Alba-Simionesco, C., Frick, B. & Morineau, D. Microphase separation of binary liquids confined in cylindrical pores. *J. Phys. Chem. C* **120**, 9245–9252 (2016).
4. Guo, X.-Y., Watermann, T. & Sebastiani, D. Local microphase separation of a binary liquid under nanoscale confinement. *J. Phys. Chem. B* **118**, 10207–10213 (2014).
5. Muthulakshmi, T., Dutta, D., Maheshwari, P. & Pujari, P. K. Evidence for confinement induced phase separation in ethanol-water mixture: a positron annihilation study. *J. Phys. Condens. Matter* **30**, 025001 (2018).
6. Krycka, K. L., Dura, J. A., Langston, L. J. & Burba, C. M. Nanoconfinement-induced phase segregation of binary benzene-cyclohexane solutions within a chemically inert matrix. *J. Phys. Chem. C* **122**, 7676–7684 (2018).
7. Barnette, A. L. & Kim, S. H. Coadsorption of n-propanol and water on SiO<sub>2</sub>: study of thickness, composition, and structure of binary adsorbate layer using attenuated total reflection infrared (ATR-IR) and sum frequency generation (SFG) vibration spectroscopy. *J. Phys. Chem. C* **116**, 9909–9916 (2012).
8. Harrach, M. F., Drossel, B., Winschel, W., Gutmann, T. & Buntkowsky, G. Mixtures of isobutyric acid and water confined in cylindrical silica nanopores revisited: a combined solid-state NMR and molecular dynamics simulation study. *J. Phys. Chem. C* **119**, 28961–28969 (2015).
9. Ward-williams, J. A. Applying NMR relaxation methods to the study of liquids in porous media. (University of Cambridge, 2019).
10. Butler, J. P., Reeds, J. A. & Dawson, S. V. Estimating solutions of first kind integral equations with nonnegative constraints and optimal smoothing. *SIAM J. Numer. Anal.* **18**, 381–397 (1981).

11. Levitz, P. Random flights in confining interfacial systems. *J. Phys. Condens. Matter* **17**, 4059–4074 (2005).
12. Levitz, P., Grebenkov, D. S., Zinsmeister, M., Kolwankar, K. M. & Sapoval, B. Brownian flights over a fractal nest and first-passage statistics on irregular surfaces. *Phys. Rev. Lett.* **96**, 180601 (2006).
13. Levitz, P., Zinsmeister, M., Davidson, P., Constantin, D. & Poncelet, O. Intermittent Brownian dynamics over a rigid strand: heavily tailed relocation statistics in a simple geometry. *Phys. Rev. E* **78**, 030102 (2008).
14. Levitz, P., Bonnaud, P. A., Cazade, P.-A., Pellenq, J.-M. & Coasne, B. Molecular intermittent dynamics of interfacial water: probing adsorption and bulk confinement. *Soft Matter* **9**, 8654–8663 (2013).
15. Levitz, P. Probing interfacial dynamics of water in confined nanoporous systems by NMRD. *Mol. Phys.* **117**, 952–959 (2019).
16. Jmol: An open-source Java viewer for chemical structures in 3D. <http://www.jmol.org/> accessed May 2020.
17. Stejskal, E. O. & Tanner, J. E. Spin diffusion measurements: spin echoes in the presence of a time-dependent field gradient. *J. Chem. Phys.* **42**, 288 (1965).
18. Reichardt, C. *Solvents and solvent effects in organic chemistry*. (Wiley, 2002).
19. Ward-Williams, J., Korb, J.-P. & Gladden, L. F. Insights into functionality-specific adsorption dynamics and stable reaction intermediates using Fast Field Cycling NMR. *J. Phys. Chem. C* **122**, 20271–20278 (2018).
20. Brownstein, K. R. & Tarr, C. E. Importance of classical diffusion in NMR studies of water in biological cells. *Phys. Rev. A* **19**, 2446–2453 (1979).
21. Korb, J. P., Godefroy, S. & Fleury, M. Surface nuclear magnetic relaxation and dynamics of water and oil in granular packings and rocks. *Magn. Reson. Imaging* **21**, 193–199 (2003).
22. Korb, J. P., Freiman, G., Nicot, B. & Ligneul, P. Dynamical surface affinity of diphasic liquids as a probe of wettability of multimodal porous media. *Phys. Rev. E* **80**,

- 061601 (2009).
23. Faux, D. A. & McDonald, P. J. A model for the interpretation of nuclear magnetic resonance spin-lattice dispersion measurements on mortar, plaster paste, synthetic clay and oil-bearing shale. *Microporous Mesoporous Mater.* **269**, 39–42 (2018).
  24. Bychuk, O. V. & O'Shaughnessy, B. Anomalous surface diffusion: a numerical study. *J. Chem. Phys.* **101**, 772–780 (1994).
  25. Stapf, S., Kimmich, R. & Seitter, R.-O. Field-Cycling NMR relaxometry of liquids confined in porous glass: evidence for Levy-walks. *Magn. Reson. Imaging* **14**, 772–780 (1996).
  26. Zavada, T. & Kimmich, R. The anomalous adsorbate dynamics at surfaces in porous media studied by nuclear magnetic resonance methods. The orientational structure factor and Lévy walks. *J. Chem. Phys.* **109**, 6929 (1998).
  27. Kimmich, R. & Fatkullin, N. Self-diffusion studies by intra- and inter-molecular spin-lattice relaxometry using field-cycling: liquids, plastic crystals, porous media, and polymer segments. *Prog. Nucl. Magn. Reson. Spectrosc.* **101**, 18–50 (2017).
  28. Stapf, S., Kimmich, R., Seitter, R. O., Maklakov, A. I. & Skirda, V. D. Proton and deuteron field-cycling NMR relaxometry of liquids confined in porous glasses. *Colloids Surfaces A Physicochem. Eng. Asp.* **115**, 107–114 (1996).
  29. Stapf, S., Ren, X., Talnishnikh, E. & Blqmich, B. Spatial distribution of coke residues in porous catalyst pellets analyzed by field-cycling relaxometry and parameter imaging. *Magn. Reson. Imaging* **23**, 383–386 (2005).
  30. Korb, J.-P., Whaley Hodges, M., Gobron, T. & Bryant, R. G. Anomalous surface diffusion of water compared to aprotic liquids in nanopores. *Phys. Rev. E* **60**, 3097–3106 (1999).
  31. Korb, J.-P. Surface dynamics of liquids in porous media. *Magn. Reson. Imaging* **19**, 363–368 (2001).
  32. Bloembergen, N., Purcell, E. M. & Pound, R. V. Relaxation effects in nuclear magnetic resonance absorption. *Phys. Rev.* **73**, 679–712 (1948).

33. Ward-Williams, J., Korb, J.-P., Rozing, L., Sederman, A. J., Mantle, M. D. & Gladden, L. F. Characterizing solid-liquid interactions in a mesoporous catalyst support using variable-temperature Fast Field Cycling NMR. *J. Phys. Chem. C* **125**, 8767–8778 (2021).
34. Korb, J.-P., Whaley-Hodges, M. & Bryant, R. G. Translational diffusion of liquids at surfaces of microporous materials: theoretical analysis of field-cycling magnetic relaxation measurements. *Phys. Rev. E* **56**, 1934–1945 (1997).
35. Teng, C. L., Hong, H., Kiihne, S. & Bryant, R. G. Molecular oxygen spin-lattice relaxation in solutions measured by proton magnetic relaxation dispersion. *J. Magn. Reson.* **148**, 31–34 (2001).
36. Abragam, A. *The principles of nuclear magnetism*. (Clarendon Press, 1983).
37. Fripiat, J. J., Letellier, M. & Levitz, P. Interaction of water with clay surfaces. *Philos. Trans. R. Soc. London. Ser. A, Math. Phys. Sci.* **311**, 287–299 (1984).
38. Chemmi, H., Petit, D., Levitz, P., Denoyel, R., Galarneau, A. & Korb, J.-P. Noninvasive experimental evidence of the linear pore size dependence of water diffusion in nanoconfinement. *J. Phys. Chem. Lett* **7**, 45 (2016).
39. Korb, J.-P. & Levitz, P. E. Direct probing of the wettability of plaster pastes at the nanoscale by proton Field Cycling Relaxometry. *AIP Conf. Proc.* **1081**, 55 (2008).
40. Iwahashi, M., Ohbu, Y., Kato, T., Suzuki, Y., Yamauchi, K., Yamaguchi, Y., Muramatsu, M. The dynamical structure of normal alcohols in their liquids as determined by the viscosity and self-diffusion measurements. *Bull. Chem. Soc. Jpn.* **59**, 3771–3774 (1986).
41. Freed, D. E., Burcaw, L. & Song, Y. Q. Scaling laws for diffusion coefficients in mixtures of alkanes. *Phys. Rev. Lett.* **94**, 067602 (2005).
42. Faux, D. A. & McDonald, P. J. Explicit calculation of nuclear-magnetic-resonance relaxation rates in small pores to elucidate molecular-scale fluid dynamics. *Phys. Rev. E* **95**, 33117 (2017).

## 6. Microphase separation of alcohol-water mixtures imbibed within anatase titania

### 6.1 Introduction

While pure liquids imbibed within porous media have been extensively studied, as was shown in chapter 3, the understanding of nanoconfined liquid mixtures is much more limited. Section 3.3.2 presented a literature overview of liquid mixtures imbibed within porous media, with a specific focus towards microphase separation, the phenomenon where liquid mixtures that are miscible in their bulk state, separate under confinement<sup>1-7</sup>.

In biofuel production, the separation of alcohol-water mixtures, and in particular ethanol-water mixtures, is a challenge<sup>8</sup>. While it is difficult to separate ethanol-water mixtures through distillation, which is the most common separation method, nanoconfinement has been shown to be a promising alternative separation technique<sup>9-11</sup>. Therefore, in this chapter, the microphase separation of ethanol-water mixtures as well as other alcohol-water mixtures imbibed within anatase titania is investigated.

FFC-NMR has been shown to be sensitive to variations in the dynamics of liquids imbibed within porous media<sup>12-14</sup>. As was shown in chapter 5 of this thesis, in the particular case of a system that follows the Reorientations Mediated by Translational Diffusion (RMTD) model,  $\tau_A$ , the adsorption correlation time, is expected to correlate with the surface-adsorbate interaction strength<sup>15,16</sup>.

Moreover, studies of binary tetrahydrofuran(THF)-water and THF-decane mixtures imbibed within anatase titania were reported in chapter 4, providing insight into the capabilities of FFC-NMR in separating the signals of different liquids, and into challenges that arise when investigating liquid mixtures with FFC-NMR. It was shown that the gradient of the <sup>1</sup>H NMR dispersion (NMRD) profile of THF in THF-water mixtures, the weaker interacting species, could be quantified in a power law exponent. The relative surface-adsorbate interaction strength could be determined through the power law exponent, which decreased monotonically as water was added to the system, until it stabilised once one monolayer of water had formed at the pore surface. It was concluded that the interaction of THF with the surface was blocked by a water-rich surface layer, and therefore the THF was located in the centre of the pore.

Following the experimental approach to obtain, process and interpret FFC-NMR data for confined liquid mixtures shown in chapter 4, and the theoretical analysis of alcohols imbibed within anatase titania presented in chapter 5, the microphase separation of alcohol-water mixtures imbibed within anatase titania is investigated. As was shown in section 3.3.2, microphase separation is a newly studied phenomenon and different techniques are shown to contradict each other. For ethanol-water mixtures imbibed within silica, molecular dynamics and positron annihilation lifetime spectroscopy (PALS) studies have shown a phase-segregated system where ethanol sticks to the surface and water resides in the bulk-in-the-pore, due to the strong hydrogen network of water<sup>17,18</sup>. However, a fixed field NMR relaxation study concluded the opposite, namely that water is strongly attached to the surface, and ethanol has a weak interaction with the surface, corresponding to the bulk-in-the-pore<sup>19</sup>. More details about these studies can be found in section 3.3.2.

This chapter aims to provide an unambiguous method of studying microphase separation. FFC-NMR is an ideal technique for the investigation of surface-adsorbate interactions, because it shows relatively little interference from other dynamical processes, such as the fast relaxation processes seen in high field NMR relaxometry, and it is a chemically selective technique, unlike for example PALS. This chapter will show which conclusions can be drawn from FFC-NMR experiments with respect to microphase separation, and which questions still need to be answered.

A range of alcohol-water mixtures were imbibed within anatase titania. Investigating a range of linear alcohols allowed for a systematic analysis of the microphase separation effects, across a range in polarities and bulk miscibilities with water, while the surface-adsorbate interaction mechanisms for different alcohols remain the same. Chapter 5 has shown the RMTD analysis of the pure alcohols imbibed within this porous medium. Assuming the relaxation mechanism remains the same, an identical analysis could be performed on the alcohol component of the <sup>1</sup>H NMRD profiles of the alcohol-water mixtures.

Initially, the product of the surface-to-volume ratio and the adsorption correlation time,  $\frac{N_S}{N} \times \tau_A$  was used to create a basic understanding of the chemistry of the system, i.e. whether microphase separation occurs or not. A comparison between different alcohols and the THF-water data from chapter 4 resulted in a quantitative analysis of the structure of the mixture, reflected by  $\frac{N_S}{N}$ , and the dynamics inside the pores through the adsorption correlation time,  $\tau_A$ .

## 6.2 Adaptation of the RMTD model to mixtures

The Levitz-type RMTD model for pure liquids imbibed within porous, as it was applied in chapter 5, has the following form<sup>12,20</sup>:

$$R_{1,obs} = R_{1,HF} + A_{RMTD}[J(\omega) + 4J(2\omega)] \quad (6.1)$$

In this equation,  $R_{1,obs}$  is the observed relaxation rate and  $R_{1,HF}$  is the high field relaxation rate, which is modelled as a constant for simplicity.  $A_{RMTD}$  can be estimated as<sup>12</sup>:

$$A_{RMTD} = A \frac{N_S}{N} \omega_d^2 = A \frac{N_S}{N} \left( \frac{\mu_0}{4\pi} \gamma_H^2 \hbar \right)^2 \sum \frac{1}{r^6}, \quad (6.2)$$

where  $\frac{N_S}{N}$  is the surface-to-pore ratio of spins,  $\omega_d^2$  is the intramolecular dipole-dipole frequency of the system,  $\mu_0$  is the vacuum permeability constant,  $\gamma_H$  is the proton gyromagnetic ratio,  $\hbar$  is the reduced Planck's constant,  $r$  is the intramolecular proton-proton distance and  $A$  is an unknown variable, however it is assumed to be a constant, following the analysis performed in chapter 5.

The spectral density,  $J(\omega)$ , has the form:

$$J(\omega) = \omega_A^{-1} \left[ \sqrt{\frac{\omega}{\omega_A}} + \frac{\omega}{\omega_A} + \frac{1}{2} \left( \frac{\omega}{\omega_A} \right)^{\frac{3}{2}} \right]^{-1}, \quad (6.3)$$

where  $\omega_A = \frac{\delta^2}{2D\tau_A^2}$  is a characteristic frequency for the system, which is fitted. If the molecular diameter,  $\delta$ , and diffusion coefficient,  $D$ , are known,  $\omega_A$  can be converted to  $\tau_A$ , which can provide information about the dynamics of microphase separation.

In the limit where  $\omega \ll \omega_A$ , the spectral density can be reduced to  $J(\omega) = \omega_A^{-1} \left( \frac{\omega}{\omega_A} \right)^{-1/2} = \omega_A^{-1/2} \omega^{-1/2}$ , so that equations (5.17)-(5.18) can be rearranged to:

$$R_{1,obs} = R_{1,HF} + \frac{N_S}{N} A \left( \frac{\mu_0}{4\pi} \gamma_H^2 \hbar \right)^2 \sum \frac{1}{r^6} \frac{\sqrt{2D}\tau_A}{\delta} [\omega^{-1/2} + 4(2\omega)^{-1/2}] \quad (6.4)$$

The unknown variables in equation (6.4) are  $\frac{N_S}{N}$  and  $\tau_A$ .

For pure liquids following the two phase fast exchange model, the surface-to-pore ratio of spins can be estimated as  $\frac{N_S}{N} \approx \frac{\lambda S}{V}$ , where  $\lambda$  is the surface layer thickness, generally estimated to be the molecular diameter,  $S$  is the surface area and  $V$  is the pore volume<sup>21</sup>. However, for mixtures,

$\frac{N_S}{N}$  must be changed to  $\frac{N_{S,i}}{N_i}$ , the surface-to-pore ratio of spins of species  $i$ . This ratio will depend on the chemistry of the system, i.e. whether or not microphase separation occurs. Moreover, the dependence of  $\tau_A$  on the mixture composition depends on the chemistry of the system. The following scenarios can be considered:

1. A system without competitive adsorption between species A and B. In this system, the two components are balanced and therefore the values for  $\frac{N_S}{N}$  and  $\tau_A$  for both species will stay constant across the composition range.
2. Component A outcompetes component B for adsorption sites, however the liquids remain fully miscible within the pore. For component A, as its concentration decreases, relatively more molecules will attach to the surface. Therefore  $\frac{N_{S,A}}{N_A}$  will increase from a value of  $\frac{N_{S,A}}{N_A} \approx \frac{\lambda S}{V}$  for pure A, to  $\frac{N_{S,A}}{N_A} = 1$  in the limit of 0% A.  $\tau_{A,A}$  will remain the “true” value of  $\tau_{A,A}$ , i.e. the value of the pure liquid A, across the composition range. For component B, the opposite situation will occur. As its concentration decreases, the surface population of component B and  $\tau_{A,B}$  decrease.  $\frac{N_{S,B}}{N_B}$  will decrease from a value of  $\frac{N_{S,B}}{N_B} \approx \frac{\lambda S}{V}$  for pure B, to  $\frac{N_{S,B}}{N_B} = 0$  in the limit of 0% B.  $\tau_{A,B}$  will decrease from the pure value to very short timescales, corresponding to other relaxation processes than RMTD, such as rotational relaxation. It is expected these correlation times will be in the order of  $10^{-11}$  s, similar to the high field contribution of the relaxation model.
3. Component A outcompetes component B for adsorption sites, and full demixing occurs. Similarly to scenario 2, the value of  $\frac{N_{S,A}}{N_A}$  will increase from  $\frac{N_{S,A}}{N_A} \approx \frac{\lambda S}{V}$  for pure A, to  $\frac{N_{S,A}}{N_A} = 1$ , however the composition at which  $\frac{N_{S,A}}{N_A} = 1$  will be equal to the composition corresponding to the surface being covered by one monolayer of component A. Below this composition,  $\frac{N_{S,A}}{N_A}$  will remain 1, as all molecules in the system will attach to the pore.  $\tau_{A,A}$  is expected to stay constant across the composition range. For component B, similarly to scenario 2,  $\frac{N_{S,B}}{N_B}$  and  $\tau_{A,B}$  decrease with a decrease in concentration. The composition at which  $\frac{N_{S,B}}{N_B} = 0$  corresponds to the composition where the surface is covered by one monolayer of component A. At any lower composition of component

B, the molecules of component A will effectively shield the surface from component B molecules. Therefore there will not be any interaction between the surface and component B. This means that  $\tau_{A,B}$  will decrease to the high field value at the composition where the surface is covered with one monolayer of component A, and stay at this value for any lower concentrations of component B.

The three outlined scenarios and their corresponding trends for  $\frac{N_S}{N}$  and  $\tau_A$  with the mixture composition are shown in Figure 6.1.

It must be noted that the scenarios described above are model systems. Experimentally, the behaviour of liquid mixtures imbibed within porous media will likely fall between these scenarios, e.g. the liquids could demix partially, instead of fully, as described in scenario 3.

Based on these scenarios, it is expected that the trends of  $\frac{N_S}{N}$  and  $\tau_A$  with the mixture composition are similar for the weaker interacting species (component B). Therefore, the product  $\frac{N_S}{N} \times \tau_A$  can be used to investigate microphase separation semi-quantitatively, and to compare the microphase separation of different liquids. In this systematic study a range of alcohol-water mixtures and THF-water mixtures are investigated to provide more information on the basis of microphase separation effects.

Further to this,  $\frac{N_S}{N}$  and  $\tau_A$  can be estimated, under the assumption that the trend of  $\frac{N_S}{N} \times \tau_A$  with composition is equal to those of  $\frac{N_S}{N}$  and  $\tau_A$ . This results in a quantitative analysis of structural,  $\frac{N_S}{N}$ , and dynamical,  $\tau_A$ , behaviour of microphase separation.

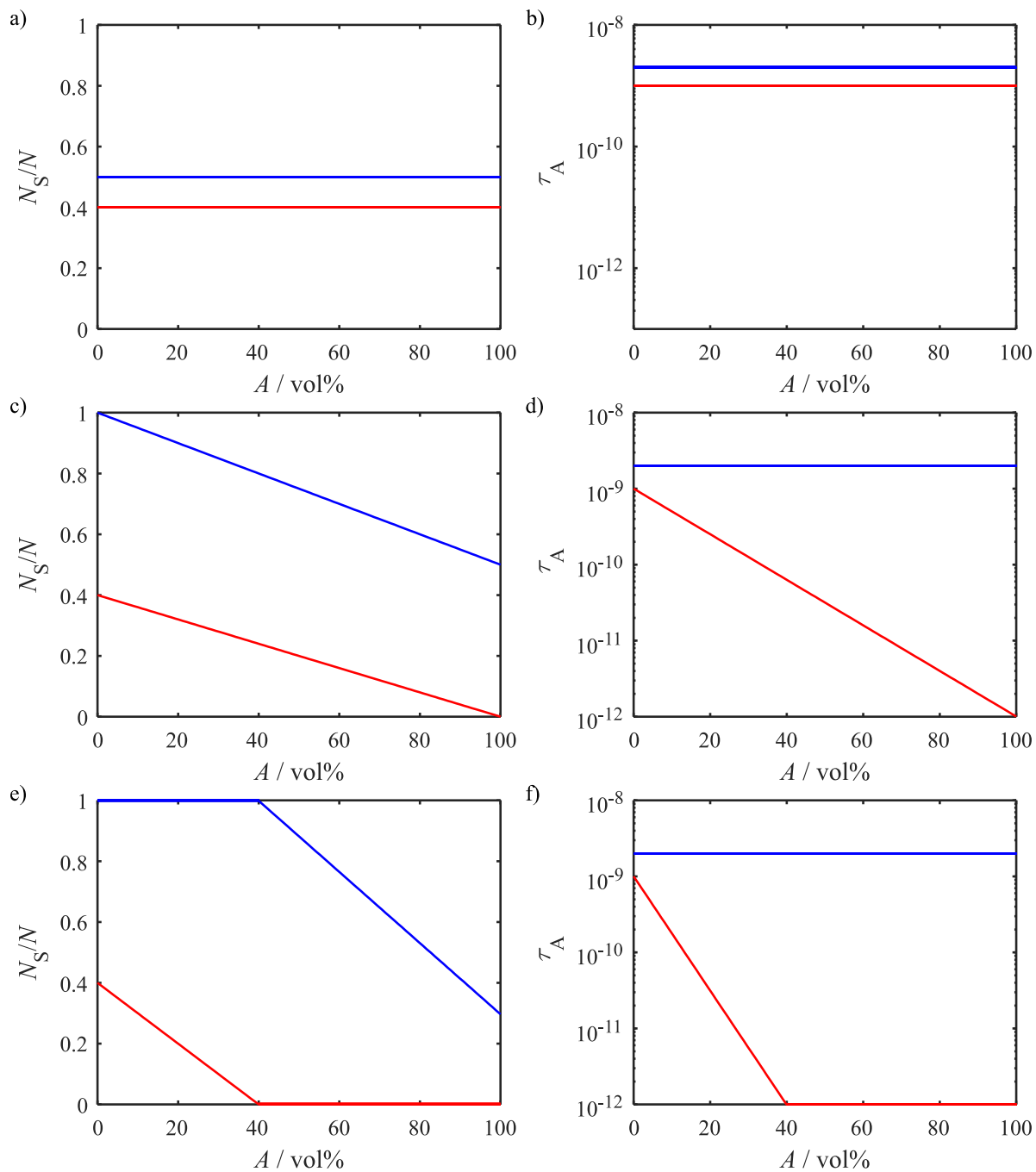


Figure 6.1: Expected trends for the surface-to-volume ratios  $\frac{N_S}{N}$  (a,c,e) and adsorption correlation times  $\tau_A$  (b,d,f), plotted against the mixture composition in A vol%, for scenarios 1(a,b), 2 (c,d), and 3 (e,f), as outlined in the text. In each plot, the blue line represents component A (the stronger interacting component) and the red line represents component B (the weaker interacting species). For the pure liquids,  $\left(\frac{N_S}{N}\right)_A = 0.5$ ,  $\left(\frac{N_S}{N}\right)_B = 0.4$ ,  $\tau_{A,A} = 2$  ns,  $\tau_{A,B} = 1$  ns, and the minimum  $\tau_{A,\min} = 1$  ps.

## 6.3 Experimental

The materials that were used were the same as those used in the previous chapter, see section 5.2.1. Additionally, the sample preparation, FFC-NMR and PFG-NMR experiments, and computational methods were equal to those in section 5.2. This section will briefly describe a composition analysis, where the mixture compositions determined by different methods will be compared.

### 6.3.1 Composition analysis

The bulk and intra-pore compositions of methanol-water, ethanol-water and propanol-water mixtures were determined by  $^1\text{H}$  NMR spectroscopy on a Magritek Spinsolve 43 MHz NMR spectrometer. Intra-pore butanol-water and pentanol-water mixtures could not be spectroscopically resolved and are therefore omitted from the following analysis. The bulk and intra-pore compositions were compared in order to investigate preferential adsorption.

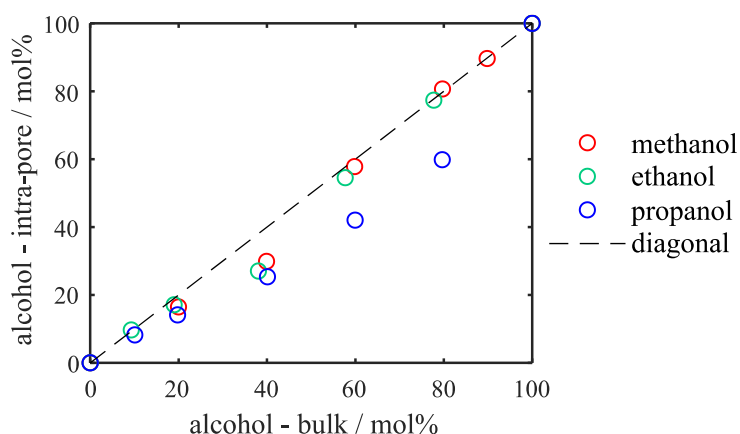


Figure 6.2: The intra-pore alcohol mole percent plotted against the corresponding bulk composition, both extracted from  $^1\text{H}$  NMR spectra obtained on a 43 MHz NMR spectrometer.

In Figure 6.2, the diagonal represents the system in the case of no preferential adsorption, i.e. the bulk and intra-pore compositions are equal. The methanol and ethanol compositions follow the diagonal well, however the intra-pore propanol compositions are found to be lower than the bulk compositions. This indicates that for propanol-water mixtures, water is preferentially adsorbed into the pore. It is expected that this trend continues for butanol and pentanol.

Additionally, the spectroscopically determined intra-pore mixture compositions were compared to the mixture compositions obtained through a biexponential fit of the FFC-NMR data. The FFC-NMR based compositions were determined follow two methods. The first method assumes that the two components of the biexponential fit correspond to water and the

corresponding alcohol. The second method assumes there is fast exchange between water and the alcohol hydroxyl group, resulting in a (water + hydroxyl) relaxation environment, and an alkyl relaxation environment.

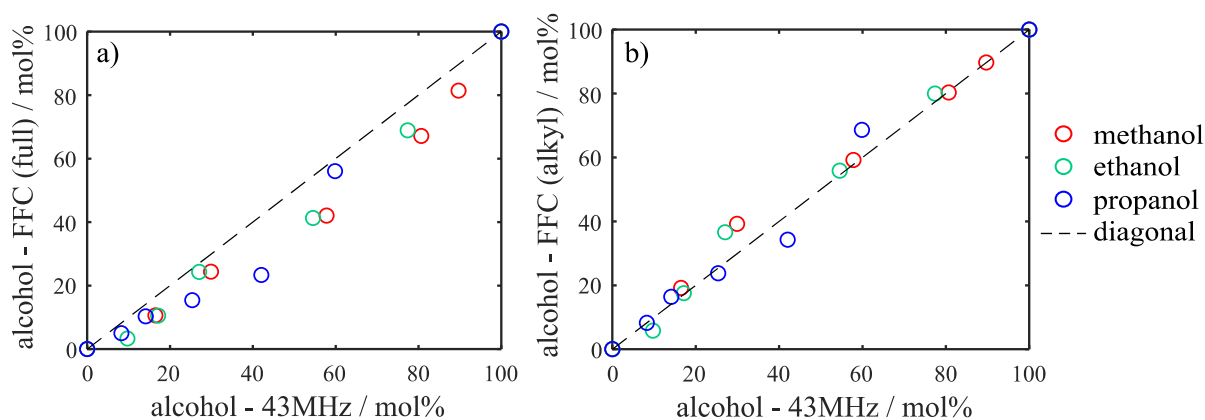


Figure 6.3: Intra-pore compositions as determined by FFC-NMR assuming the two relaxation components correspond to a) the full alcohol and water molecules, or b) the alkyl group of the alcohol and a (water+hydroxyl) environment. The FFC-NMR based compositions are plotted against the intra-pore compositions extracted spectroscopically on a 43 MHz NMR spectrometer.

It can be seen in Figure 6.3a that the FFC (alcohol – water) composition underestimates the alcohol component, especially for higher methanol and ethanol concentration samples. In contrast, Figure 6.3b shows that the FFC (alkyl – water/hydroxyl) compositions correspond to those measured spectroscopically very well. From this it can be concluded that the  $^1\text{H}$  NMR dispersion profiles of the alcohol component actually correspond to the alkyl group only, not to the full alcohol. For simplicity, the profiles for the alkyl component and the (water + hydroxyl) component will be denoted alcohol and water components respectively.

## 6.4 Results and discussion

### 6.4.1 FFC-NMR dispersion profiles

$^1\text{H}$  NMR dispersion (NMRD) profiles were recorded for alcohol-water mixtures imbibed within anatase titania. The profiles of the alcohol and water components in each of the mixtures were extracted through a biexponential fit of the relaxation data, and are shown in Figure 6.4 and Figure 6.5. In order to simplify a visual comparison of the different alcohol-water mixtures, the axes for the different plots within the same figure were kept equal.

Upon addition of water to the system, the alcohol relaxation rates decrease for all alcohols, see Figure 6.4. For the water component in all mixtures, see Figure 6.5, the relaxation rate increases as the water concentration decreases. Following the two-phase fast exchange model, this indicates that water is the stronger interacting species, and therefore the alcohols are the weaker interacting species in each mixture<sup>22</sup>. This agrees with the correlation of the surface-adsorbate interaction strength with the polarity of the liquid, as previously described in chapter 5. Water, being the most polar liquid in any of the mixtures, will interact more strongly with the surface than alcohols.

The methanol NMRD profiles for water-methanol mixtures with a high water concentration (Figure 6.4a) show high levels of scatter, indicative of a low signal-to-noise ratio. This is not a problem for the other alcohols. There are two explanations for the large scatter of methanol. Firstly, the alkyl group in methanol contains three hydrogen atoms that are detected by NMR. For longer alcohols, this number increases, and therefore the NMR signal per alcohol molecule increases. This means that the alcohol component in low alcohol concentration samples will be detected more easily for longer alcohols than for methanol. However, the methanol profile for the lowest methanol concentration mixture contains 20% of the  $^1\text{H}$  signal. The alkyl profile of the lowest ethanol concentration mixture contains only 9% of the  $^1\text{H}$  signal, but the scatter for the ethanol profile is much smaller than for that of the methanol component. Therefore another reason is required to explain the high scatter for methanol.

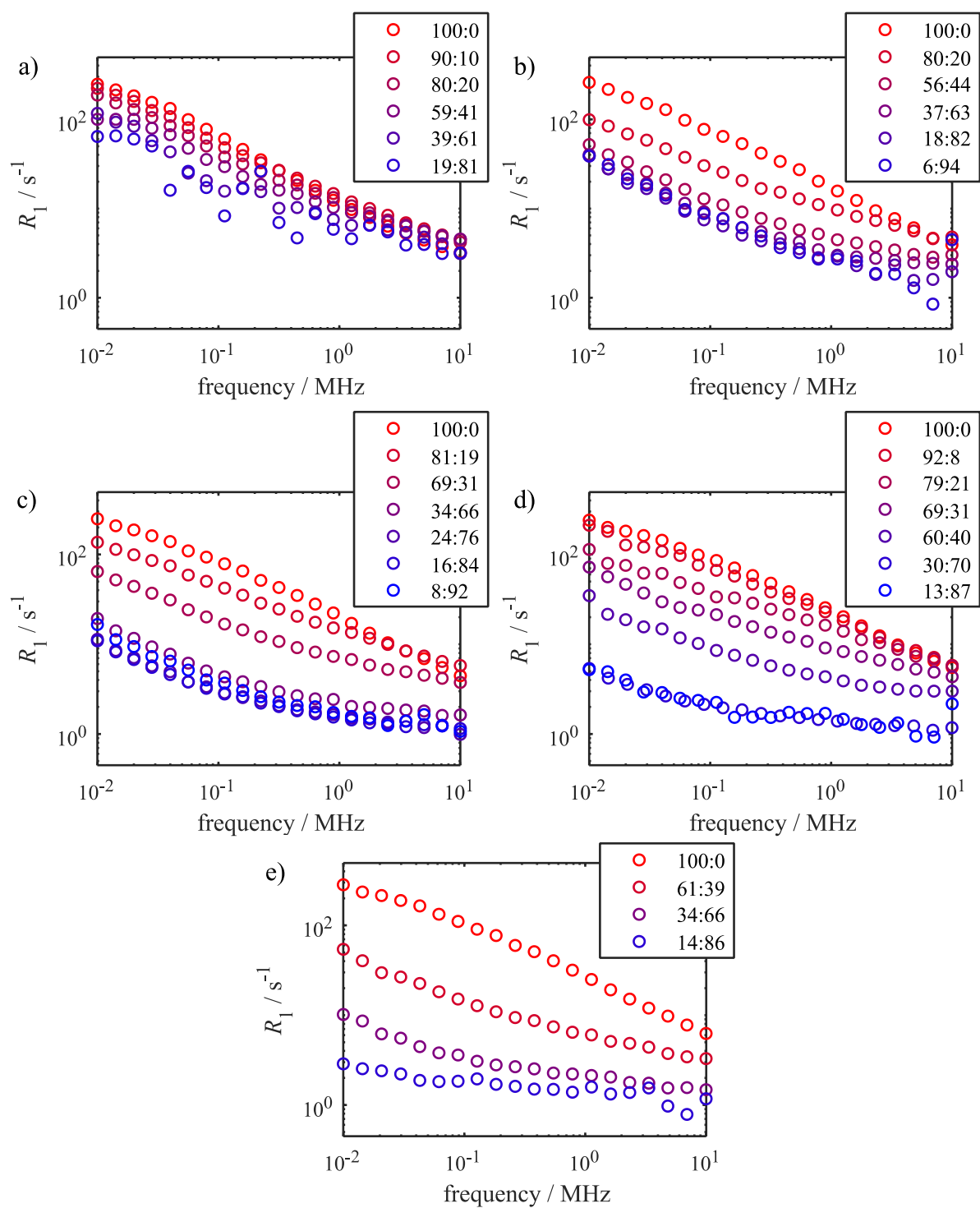


Figure 6.4:  $^1\text{H}$  NMRD profiles of the alcohol component in alcohol-water mixtures imbibed within anatase titania, for a) methanol, b) ethanol, c) propanol, d) butanol, and e) pentanol. The legend shows the mixture composition in alcohol-water mole percent.

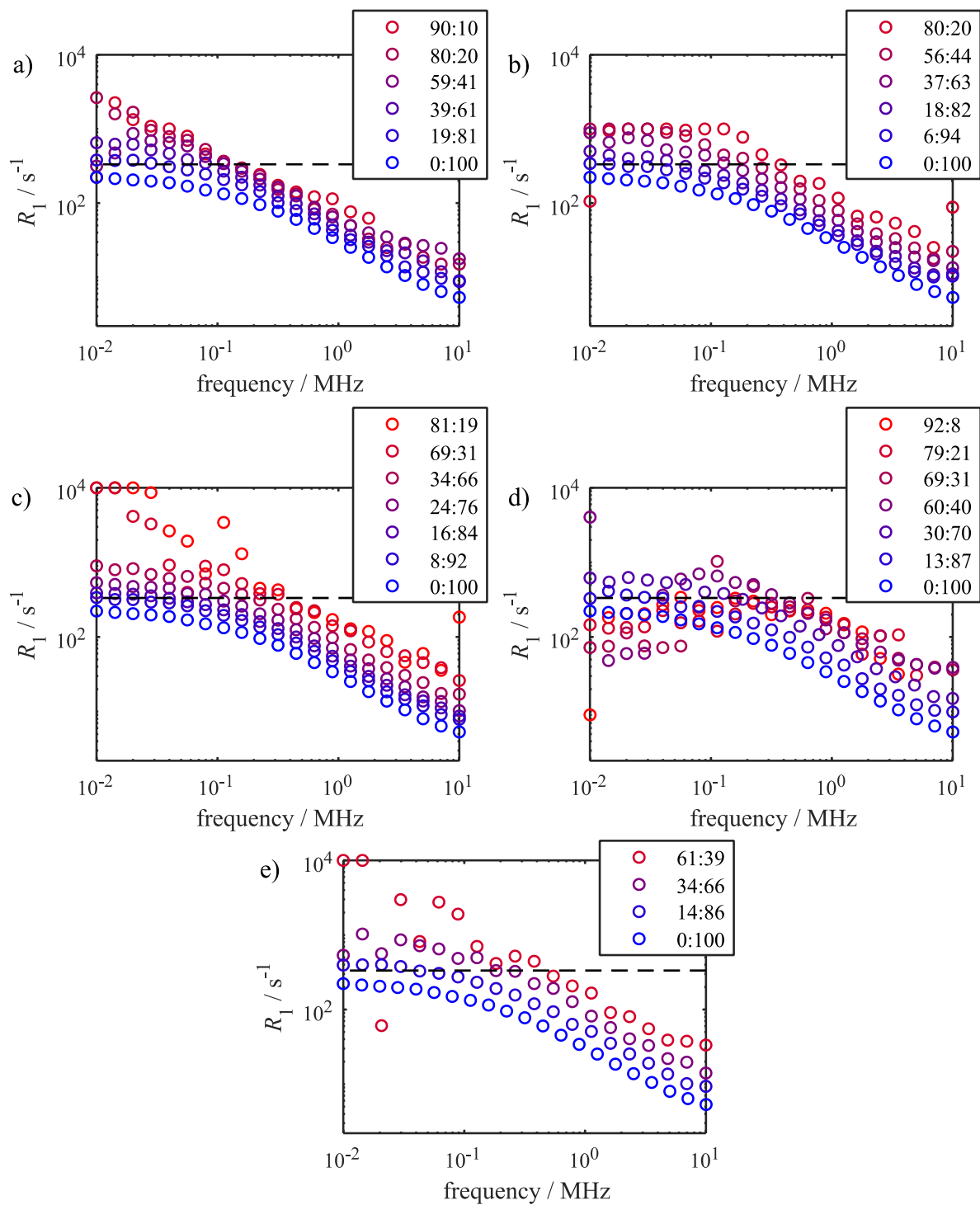


Figure 6.5:  $^1\text{H}$  NMRD profiles of the water component in alcohol-water mixtures imbibed within anatase titania, for a) methanol, b) ethanol, c) propanol, d) butanol, and e) pentanol. The legend shows the mixture composition in alcohol-water mole percent. A dashed line shows the magnetic field switching rate  $R_{1,\text{switch}} = 1/3 \text{ ms}$ , which can be considered a limit above which the observed relaxation rate cannot be accurately detected.

The second explanation is that the relaxation rates for the water and methanol components in low methanol mixtures are too close to each other. Figure 6.6 shows the ratio of the water to alkyl component  $^1\text{H}$  NMRD profiles at the lowest alcohol content mixture for each of the alcohol-water mixtures.

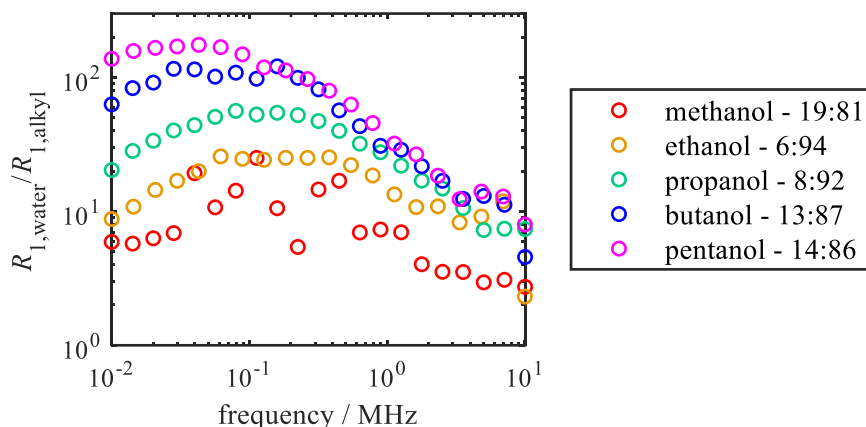


Figure 6.6: The ratio of water to alkyl  $^1\text{H}$  NMRD profiles for the lowest alcohol content mixtures of each of the alcohol-water mixtures. The legend shows the mixture composition in alcohol-water mol%.

It is clear that the difference between the alkyl and water relaxation rates increases for longer chain alcohols. For the 19:81 methanol sample, the average ratio of water to alkyl relaxation rates across the frequency range is 7.6, including all scattered points. When the scattered points between  $0.03 \text{ MHz} < \omega_0 < 0.5 \text{ MHz}$  are excluded, the average ratio is only 4.3. For the 6:94 ethanol sample, this ratio is already 16.4, showing that the ethanol-water profiles are much further apart than the methanol-water profiles. For the 8:92 propanol-water mixture, the 13:87 butanol-water mixture and the 14:86 pentanol-water mixture the average ratio of water to alkyl relaxation rate is 28.0, 58.0, and 88.3 respectively.

The combination of a small amount of signal and the similar relaxation rates for water and alkyl components causes high scatter in the methanol profiles at low methanol concentrations. In order to obtain a higher quality methanol profile, experiments could be performed using deuterated water, however it will be difficult to determine the intra-pore composition. Another option is to use a Carr-Purcell-Meiboom-Gill (CPMG)-FFC-NMR pulse sequence, which allows for extra resolution through the addition of a  $T_2$  relaxation component<sup>23</sup>. A more detailed discussion of this pulse sequence will be presented in chapter 8.

Despite the scatter in some of the methanol profiles, it appears the relaxation rates of the alkyl component decrease more for longer alcohol chains, indicating a stronger alcohol-surface interaction suppression by the water. Methanol, ethanol and propanol are all fully miscible with water in the bulk, however this difference in interaction suppression may indicate not all alcohols are equally miscible in the pore. A more detailed investigation of the intra-pore miscibilities of alcohol-water mixtures requires a quantitative analysis in the form of the RMTD model.

For the water component profiles, there is large scatter for most low water content mixtures. Similarly to the alcohol profiles, the signal-to-noise ratio decreases as the water content decreases, thereby decreasing the accuracy of the relaxation rates. More importantly however, the relaxation rates of the water component in low water content mixtures are very high. In Figure 6.5, a dashed line is shown in each of the graphs, which reflects the magnetic field switching rate  $R_{1,\text{switch}} = 1/3$  ms. Relaxation rates higher than  $R_{1,\text{switch}}$  cannot be detected accurately, because most of the signal has decayed before the signal detection starts. The same effect was shown for water in water-THF mixtures imbibed within anatase titania in section 4.2.4.

Considering only the parts of the water component profiles for which  $R_1 \leq R_{1,\text{switch}}$ , it appears that the full profile shifts to higher relaxation rates as the water content decreases. There is no clear indication that the slope or shape of the profile is changing, therefore it can be concluded that the water-surface interaction does not change. Only the surface-to-volume ratio  $\frac{N_S}{N}$  changes with the alcohol-water mixture composition. This conclusion again indicates that water is the stronger interacting species in the alcohol-water mixtures.

#### 6.4.2 RMTD modelling

In order to analyse the  $^1\text{H}$  NMRD profiles in a quantitative manner, the profiles were fitted using the Levitz-type RMTD model. The RMTD model was also applied to the  $^1\text{H}$  NMRD profiles of THF-water mixtures imbibed within anatase titania shown in section 4.3. This allowed for a comparison among the alcohols, as well as a comparison of the alcohols with a less polar solvent.

Because the two unknown parameters in the RMTD model,  $\frac{N_S}{N}$  and  $\tau_A$ , are correlated, a semi-quantitative analysis on the product of these two parameters,  $\frac{N_S}{N} \times \tau_A$ , was performed. This

analysis requires an accurate value for the diffusion coefficient, therefore the effect of the diffusion coefficient on the  $\frac{N_S}{N} \times \tau_A$  values is discussed. Subsequently, the full  $\frac{N_S}{N} \times \tau_A$  analysis is presented.

#### 6.4.2.1 Effect of the diffusion coefficient

In the RMTD model, the fitted characteristic frequency,  $\omega_A$ , can be converted to the adsorption correlation time,  $\tau_A$ , if the molecular diameter,  $\delta$ , and the diffusion coefficient,  $D$ , are known. Therefore, an accurate value for  $\tau_A$  requires the correct diffusion coefficient to be determined. Following the intermittent dynamics theory underlying the Levitz RMTD model, the diffusion coefficient of the liquid in the centre of the pore should be used<sup>4</sup>.

Previously, it was assumed that the diffusion coefficient converges to the bulk diffusion coefficient at more than 1 nm distance from the surface, and therefore the bulk diffusion coefficient was used<sup>4</sup>. However, in chapter 5 it was shown that for the alcohol range methanol-pentanol the surface layer thickness is approximately 0.41-0.56 nm, which means “bulk” molecules are diffusing close to the surface, and therefore the use of the bulk diffusion coefficient was deemed invalid. The intra-pore diffusion coefficient must be measured for an accurate estimate of  $\tau_A$ .

Moreover, for liquid mixtures, the effect of one component on the diffusion coefficient of the other component needs to be considered. Previously reported diffusion coefficients show that the alcohol diffusion coefficients in bulk alcohol-water mixtures heavily depend on the mixture composition<sup>24,25</sup>.

In order to take both the effect of confinement and the effect of mixing into account, the intra-pore diffusion coefficients were determined for a range of different alcohol-water mixtures through PFG-NMR experiments. The obtained diffusion coefficients are plotted against the composition in Figure 6.7.

The trend of the diffusion coefficient with the composition corresponds to the trends of the bulk diffusion coefficients for alcohol-water mixtures reported in the literature<sup>24,25</sup>. A second order polynomial fit was applied to the diffusion data, so that the diffusion coefficient of mixtures at any composition could be interpolated.

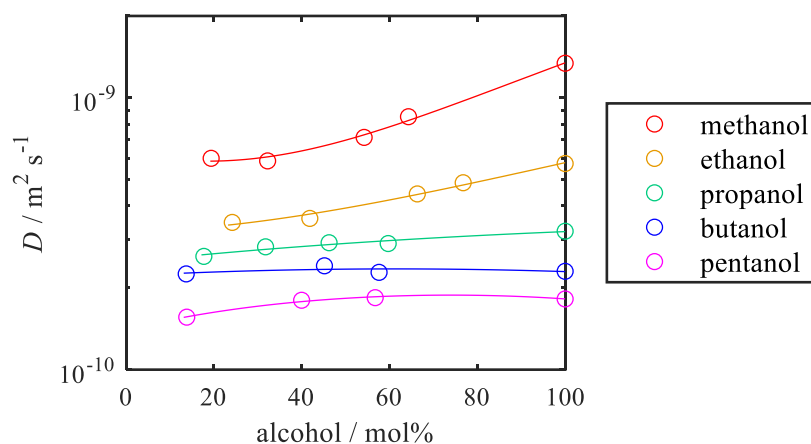


Figure 6.7: Intra-pore diffusion coefficients of alcohols in alcohol-water mixtures imbibed within anatase titania, plotted against the mixture composition in alcohol mole fraction. For each data point, three experiments were performed on three different sets of pellets from the same prepared sample. The standard deviation between these experiments was too small to see by eye. The lines correspond to second order polynomial fits to the diffusion data, which is used to interpolate the diffusion coefficients for other mixture compositions.

However, it should be noted that the diffusion coefficient of mixtures below the lowest measured alcohol mol% cannot simply be extrapolated. It has been shown that the diffusion coefficient of alcohols in bulk alcohol-water mixtures increases rapidly for very low alcohol contents, and similar trends are expected for intra-pore diffusion coefficients<sup>24,25</sup>. Therefore, the RMTD analysis will be limited to FFC-NMR experiments on samples that fall within the composition range shown in Figure 6.7.

The effect of the pore on the diffusion coefficient, in terms of confinement effects and interaction effects, can be quantified in the PFG interaction parameter. The PFG interaction parameter,  $\xi = D_{\text{bulk}}/D_{\text{pore}}$ , provides information on the enhancement or reduction of the self-diffusivity<sup>15-17</sup>. A reduction of the diffusion coefficient of a liquid or a liquid mixture inside a pore, compared to its bulk equivalent, i.e.  $\xi > 1$ , has previously been ascribed to effects regarding the chemical functionalities of the molecule, i.e. the chemical interactions of the molecule with the surface. An enhancement of the diffusion coefficient,  $\xi < 1$ , has been shown for polyols, where it is believed that the molecules move faster inside the pore than in the bulk because the hydrogen bond network is disrupted by interactions with the surface.

In order to distinguish between confinement and interaction effects, the PFG interaction parameter must be scaled to the tortuosity of the system,  $\tau$ . The tortuosity can be defined as the PFG interaction parameter for a non-interacting liquid, and therefore provides insight into the confinement effects of the pore, without the interference of chemical interactions between the liquid and the support. Previously, the  $\xi$  value for strongly nonpolar alkanes have been used to

determine the tortuosity of liquids in strongly polar supports, such as  $\gamma$ -alumina and titania<sup>26</sup>. The PFG interaction parameter for any liquid,  $\xi$ , can then be normalized to the tortuosity, resulting in the normalized PFG interaction parameter,  $\xi_N \equiv \xi/\tau$ , which allows for comparison across different supports.

In this study, all experiments were performed on the same support, and therefore the tortuosity is assumed to be constant for all samples. As a result, the differences and trends for  $\xi$  reflect the trends of the surface-adsorbate interactions. Figure 6.8a shows the  $\xi$  values for the alcohol components in methanol-, ethanol- and propanol-water mixtures, plotted against the composition. The experimental data for the intra-pore diffusion coefficients shown in Figure 6.7 was used as  $D_{\text{pore}}$ , the  $D_{\text{bulk}}$  values are extracted from literature<sup>24,25</sup>.

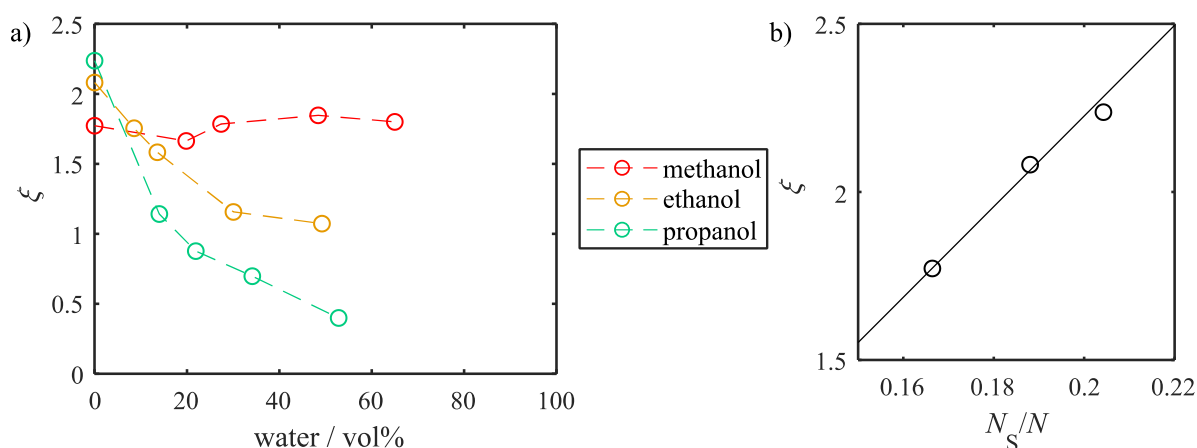


Figure 6.8: a) The PFG interaction parameter,  $\xi = D_{\text{bulk}}/D_{\text{pore}}$ , of alcohols in alcohol-water mixtures, plotted against the mixture composition in water vol%. b) The PFG interaction parameter of pure alcohols plotted against the surface-to-volume ratio,  $\frac{N_S}{N}$ , extracted from the RMTD fits shown in chapter 5. A linear fit to the data illustrates the proportionality of  $\xi$  with  $\frac{N_S}{N}$ .

For the pure alcohols in Figure 6.8a, it is clear that the PFG interaction parameter increases with increasing chain length. This can be interpreted as a sign of stronger interaction with the surface for longer alcohols, however Figure 6.8b shows that the increase of  $\xi$  is proportional to  $\frac{N_S}{N}$ , the surface-to-volume ratio. Therefore it can be concluded that this increase of  $\xi$  is a surface composition effect, rather than a dynamical effect.

The PFG interaction parameter for methanol in methanol-water mixtures stays constant for all mixture compositions, indicating that the pore does not affect the mixture dynamics, with respect to the bulk mixture. For ethanol and propanol, the PFG interaction parameter decreases as water is introduced into the system. The ethanol  $\xi$  values appear to stabilize at approximately

$\xi = 1$ , whereas the propanol  $\xi$  values continue to decrease as the water vol% increases. The decrease of the PFG interaction parameter can generally be interpreted as a decrease in the surface-alcohol interaction, therefore it can be concluded that water reduces the interaction of ethanol with the surface, and that this competitive adsorption effect is more pronounced for propanol.

To further highlight the importance of using the correct diffusion coefficient, Figure 6.9 shows the  $\frac{N_S}{N} \times \tau_A$  values for ethanol in ethanol-water mixtures, determined using the diffusion coefficients shown in Figure 6.7, the pure ethanol intra-pore diffusion coefficient, and the bulk diffusion coefficients for pure ethanol and ethanol-water mixtures extracted from the literature<sup>14</sup>. The  $\frac{N_S}{N} \times \tau_A$  values are plotted against the water vol%, for a simpler comparison with the later figures in this study.

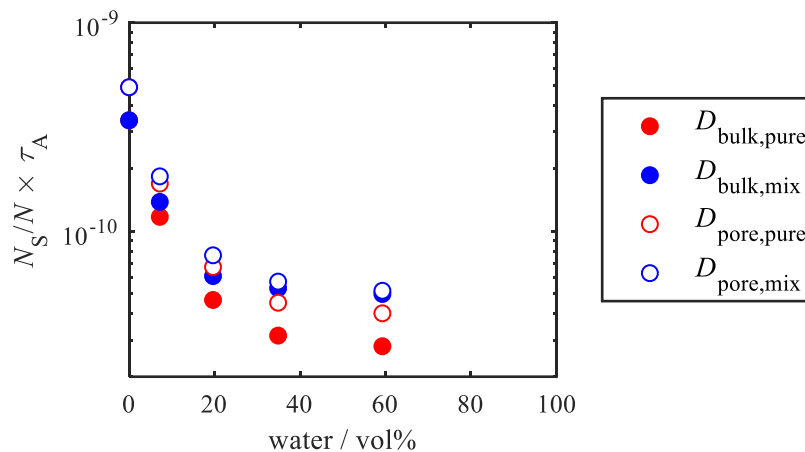


Figure 6.9:  $\frac{N_S}{N} \times \tau_A$  values plotted against the water vol% for ethanol in ethanol-water mixtures, determined using different sets of diffusion coefficients. Red symbols correspond to the use of the diffusion coefficient of the pure liquid, blue symbols correspond to the diffusion coefficients from ethanol-water mixtures. Closed symbols are for bulk liquid diffusion coefficients, open symbols correspond to intra-pore diffusion coefficients.

In comparing the  $\frac{N_S}{N} \times \tau_A$  based on the pure ethanol diffusion coefficients, it can be seen that the use of the bulk diffusion coefficient,  $D_{\text{bulk,pure}}$ , instead of the intra-pore diffusion coefficient,  $D_{\text{pore,pure}}$  reduces the  $\frac{N_S}{N} \times \tau_A$  values consistently across the composition range by a factor of  $\sqrt{\frac{D_{\text{bulk,pure}}}{D_{\text{pore,pure}}}}$ . For ethanol, this means that the value of  $\frac{N_S}{N} \times \tau_A$  will be inaccurate to a factor of 1.38.

However, when the mixture diffusion coefficients,  $D_{\text{bulk,mix}}$  and  $D_{\text{pore,mix}}$ , are compared, Figure 6.9 shows that the difference between  $\frac{N_S}{N} \times \tau_A$  values decreases toward higher water vol%. This

indicates that the diffusion coefficients of ethanol-water mixtures in confinement are affected differently than the bulk mixture diffusion coefficients, which matches the conclusions from the PFG interaction parameters.

This section has shown that it is of utmost importance to use the correct diffusion coefficients when applying the RMTD model to FFC data. Figure 6.7 showed the trends of the intra-pore diffusion coefficients with the mixture composition for different alcohols, Figure 6.8 highlighted how each of the alcohol-water mixtures behaves differently, and the effects of the different diffusion coefficients for ethanol were shown in Figure 6.9. Therefore no assumptions can be made about the diffusion coefficients, they must be directly measured for accurate RMTD modelling.

#### 6.4.2.2 $\frac{N_S}{N} \times \tau_A$ initial analysis

Due to the correlation of  $\frac{N_S}{N}$  and  $\tau_A$  in the RMTD model, an initial analysis is presented using the product of these two parameters. In order to test its reliability, the model has been applied using two different fitting methods. Firstly, the fits of the alcohol component in the mixtures were performed using the  $\frac{N_S}{N}$  value of the corresponding pure alcohol. In other words, the  $\frac{N_S}{N}$  value was kept constant across the composition range. For the second fitting method,  $\frac{N_S}{N}$  was set to correlate with the composition (alcohol vol%). For a simpler comparison between the different alcohols and THF, the  $\frac{N_S}{N} \times \tau_A$  values were normalized to the pure alcohol value, and the composition is shown in water vol% instead of the previously used alcohol mol%. The results are shown in Figure 6.10.

The results for all solvents in Figure 6.10 appear to be independent of the fitting method. This means that the  $\frac{N_S}{N} \times \tau_A$  values do not depend on the initial guesses of  $\frac{N_S}{N}$  and  $\tau_A$  much, and therefore the RMTD fitting is considered robust, i.e. it is possible to reproduce the fitting results.

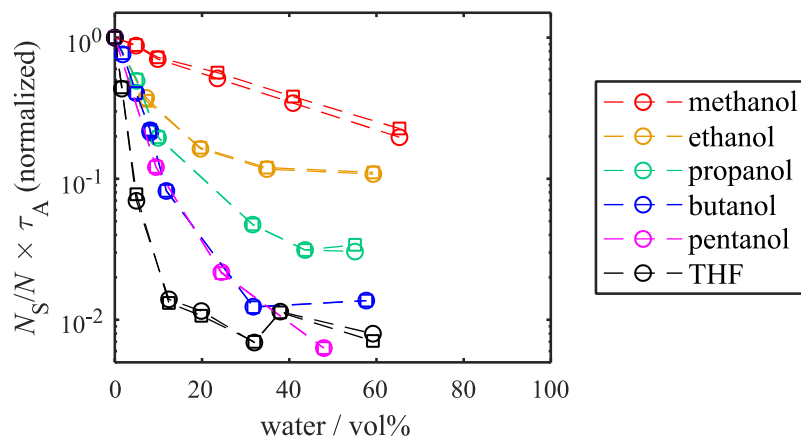


Figure 6.10:  $\frac{N_S}{N} \times \tau_A$  values extracted from RMTD fits to the  $^1\text{H}$  NMRD profiles shown in Figure 6.4, plotted against the water volume percent. The THF data corresponds to the THF-water mixture data shown in chapter 4. The  $\frac{N_S}{N} \times \tau_A$  values were normalized to the  $\frac{N_S}{N} \times \tau_A$  value of the pure alcohol and THF, in order to compare between the different solvents. Circles correspond to  $\frac{N_S}{N} \times \tau_A$  values determined using a constant  $\frac{N_S}{N}$  value across the composition range, squares correspond to  $\frac{N_S}{N} \times \tau_A$  values when  $\frac{N_S}{N}$  was set to correlate with the alcohol volume composition.

For all solvents, the  $\frac{N_S}{N} \times \tau_A$  values decrease as the water composition increases. This is consistent with the visual analysis in section 6.4.1, where it was concluded that water is the stronger interacting species, and the alcohols are the weaker interacting species. Moreover, the results in Figure 6.10 are consistent with the results from chapter 4, where the same conclusions were made: water is the stronger interacting species in THF-water mixtures imbibed within anatase titania, and THF is the weaker interacting species.

In comparing the different alcohols with each other, the  $\frac{N_S}{N} \times \tau_A$  values decrease more for longer chain alcohols. Similar trends were shown for the PFG interaction parameter in Figure 6.8. This suggests that for longer chain alcohols, the alcohol-surface interaction is suppressed more strongly by the water, resulting in a stronger phase separation. For alcohols, the polarity decreases with increasing chain length, as was shown in Table 5.1. The miscibility of alcohols with water also decreases with chain length, however methanol, ethanol and propanol are considered to be 100% miscible with water in their bulk state. Therefore it is proposed that the level of microphase separation depends to a large extent on the pure alcohol-surface interaction strength, and not only on the bulk miscibility of the mixture. This means that the microphase separation inside the anatase titania pores is a confinement effect, and not simply a mixing effect.

The comparison of the alcohols with the THF data reinforces the proposed hypothesis. The  $\frac{N_S}{N} \times \tau_A$  values of THF are decreased more, especially at low water content, than any of the alcohols. The bulk miscibility of THF with water is higher than those of butanol and pentanol, 30g THF/100g water versus 7.7g butanol/100g water and 2.2 g pentanol/100g water, however the relative polarity of THF is much lower (0.207) than those of butanol (0.586) and pentanol (0.568)<sup>29</sup>. Therefore again the data suggests that the level of microphase separation depends on the pure surface-adsorbate interaction, rather than the bulk miscibility.

#### 6.4.2.3 $\frac{N_S}{N} \times \tau_A$ fits

In order to quantify the level of microphase separation, the trends shown in Figure 6.10 were fitted to an empirical exponential trend and a constant:

$$\frac{N_S}{N} \times \tau_A = A \exp(-Bx_{\text{water}}) + C \quad (6.5)$$

The fits are shown in Figure 6.11 and the corresponding parameters are shown in Table 6.1.

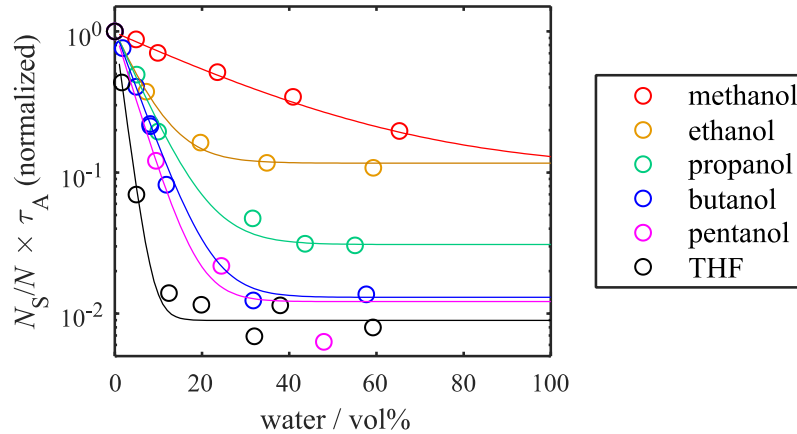


Figure 6.11: The  $\frac{N_S}{N} \times \tau_A$  values plotted against the water volume percent, and the corresponding fits of the data to  $\frac{N_S}{N} \times \tau_A = A \exp(-Bx_{\text{water}}) + C$ .

Table 6.1: Fit parameters of equation (6.5) to the data shown in Figure 6.11.

Alcohol	<i>A</i>	<i>B</i>	<i>C</i>
Methanol	0.88	0.03	0.13
Ethanol	0.90	0.16	0.11
Propanol	0.98	0.16	0.03
Butanol	1.00	0.19	0.01
Pentanol	1.00	0.23	0.01
THF	0.99	0.54	0.01

The interesting parameters are  $B$  and  $C$ . First, the constant  $C$ . In equation (6.5), the constant  $C$  reflects the system in abundance of water. A lower constant indicates a weaker alcohol/THF-surface interaction in the presence of a lot of water. In Table 6.1 it is shown that the value for  $C$  decreases with increasing alcohol chain length.

In Figure 6.11,  $C$  is reflected by the plateau of  $\frac{N_S}{N} \times \tau_A$  at high water content. It is clear that the plateau indeed decreases with increasing alcohol chain length. A lower  $\frac{N_S}{N} \times \tau_A$  value indicates a weaker interaction with the surface, and therefore can be interpreted as a sign of stronger microphase separation. In other words, the water-rich surface layer and alcohol/THF-rich bulk-like phase are more clearly separated for longer chain alcohols.

For butanol, pentanol and THF,  $C$  has reached a minimum. At this point, it can be interpreted there is full microphase separation. Interestingly, the value of  $C$  for propanol is significantly lower than for methanol and ethanol, even though these three alcohols are all fully miscible with water in the bulk. This indicates that the level of microphase separation depends strongly on the surface-adsorbate interaction of the pure alcohol, rather than the bulk miscibility.

The exponent  $B$  is a measure for the amount of water that is required to break the alcohol-surface interactions. In Figure 6.11, this corresponds to the steepness of the decrease of  $\frac{N_S}{N} \times \tau_A$ . For methanol, the normalized product  $\frac{N_S}{N} \times \tau_A$  never fully plateaus. This corresponds to a low value for  $B$ , as can also be seen in Table 6.1. This suggests that water cannot easily displace adsorbed methanol molecules. In contrast, the  $\frac{N_S}{N} \times \tau_A$  values for THF decrease rapidly as water is introduced, reaching equilibrium at approximately 15 vol% water. This corresponds to a high  $B$  value, see Table 6.1.

Figure 6.12 shows the exponent  $B$  plotted against the relative polarity of the alcohols and THF. There is a clear correlation between  $B$  and the polarity, which was previously shown to correlate with the surface-adsorbate interaction strength. Therefore it can be concluded that the weaker the surface-adsorbate interaction of the pure liquids, the easier it is for water to displace this liquid. This again supports to the hypothesis that the level of microphase separation depends on the pure surface-adsorbate interaction, rather than the bulk miscibility.

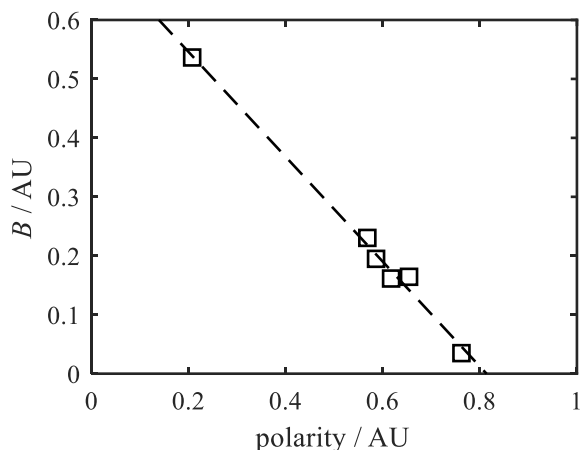


Figure 6.12: Exponent  $B$  from equation (6.5) correlates directly with the relative polarity of the alcohols and THF<sup>29</sup>.

#### 6.4.2.4 Estimating $\frac{N_S}{N}$ and $\tau_A$

Finally, values for the surface composition,  $\frac{N_S}{N}$ , and the adsorption correlation time,  $\tau_A$ , will be estimated. Because both of these parameters depend on the surface-adsorbate interaction, it is expected that the trends for  $\frac{N_S}{N}$  and  $\tau_A$  with the composition will be equivalent to each other. This means that the product  $\frac{N_S}{N} \times \tau_A$  can be decomposed to  $\frac{N_S}{N}$  and  $\tau_A$  based on the fits shown in section 6.4.2.3 and the values for the pure alcohol/THF fits as shown in section 5.5.3. The extracted values for  $\frac{N_S}{N}$  and  $\tau_A$  are shown in Figure 6.13.

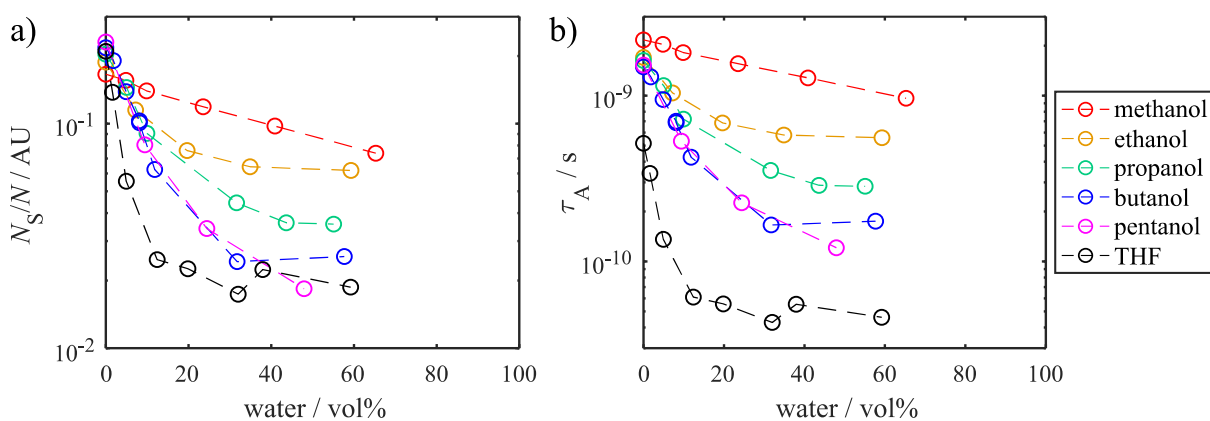


Figure 6.13: Estimated values of a)  $\frac{N_S}{N}$ , and b)  $\tau_A$ , based on a decomposition of  $\frac{N_S}{N} \times \tau_A$  values as explained in the text, plotted against the water vol%.

From the  $\frac{N_S}{N}$  values, the surface composition can be determined for each of the mixtures, thereby giving quantitative insight into the structure of the mixture throughout the pore. For pure alcohols/THF, the surface-to-volume ratio ranges between 0.17-0.23, which means that on average one in 4-6 molecules interacts with the surface.

As an example to demonstrate the level of quantification the  $\frac{N_S}{N}$  values provide, the following equation can be made to obtain the number of molecules of species  $i$  interacting with the surface in an average pore:

$$n_{i,\text{surf}} = \left(\frac{N_S}{N}\right)_i \times \frac{f_i \times V_{\text{pore}}}{V_i} \quad (6.6)$$

where  $f_i$  is the filling factor of species  $i$  corresponding to the mixture composition in vol%,  $V_{\text{pore}}$  is the pore volume based on a spherical pore with diameter  $d = 9.5$  nm, and  $V_i$  is the volume of a spherical molecule of species  $i$ , calculated using the molecular diameter. The molecular diameters of the alcohols in this study and THF are shown in sections 5.5.2.2 and 5.5.3.4.

For pure THF,  $n_{\text{THF},\text{surf}} \approx 1319$ . In comparison, for one of the weakest interacting mixtures, THF at 59.2 vol% water,  $\frac{N_S}{N} = 0.018$ , corresponding to approximately one in 53 molecules interacting with the surface. Following equation (6.6) it can be calculated that there are on average  $n_{\text{THF},\text{surf}} \approx 48$  THF molecules interacting with the surface in one nominal pore, only 3.6% of the number of THF molecules at the surface for pure THF.

The  $\tau_A$  values shown in Figure 6.13 fall within a range of 50 ps to 2.2 ns. The higher end of this range corresponds to the expected order of magnitude for  $\tau_A$  based on the literature<sup>15,20,30,31</sup>. For the lower end of this range, the order of magnitude of picoseconds corresponds to fast relaxation processes, such as reorientational and translational processes of the bulk liquid, see section 5.4.4. In essence, it can be concluded that adsorption correlation times in the order of picoseconds can be interpreted as a sign that there is no adsorption of the liquid on the surface at all. The successful estimation of  $\tau_A$  values provides quantitative insight into the dynamics of the liquid mixtures inside the pore.

## 6.5 Conclusions and outlook

In previous chapters, it has been shown that FFC-NMR provides quantitative insight into the dynamics of alcohols within titania, in the form of the adsorption correlation time,  $\tau_A$ , which can be determined through the application of the RMTD model to the  $^1\text{H}$  NMRD profiles. Moreover, it has been shown that FFC-NMR can be used to investigate the competitive adsorption of liquid mixtures imbibed within anatase titania. The combination of this knowledge has led to an investigation of microphase separation of alcohol-water mixtures imbibed within anatase titania.

Based on a qualitative analysis of the  $^1\text{H}$  NMRD profiles, it is concluded that for all mixtures, water is the stronger interacting species and the alcohols are the weaker interacting species. It appeared that the  $^1\text{H}$  NMRD profiles for longer chain alcohols were suppressed more by the addition of water than  $^1\text{H}$  NMRD profiles of shorter chain alcohols, indicating the surface-alcohol interaction is more affected for longer chain alcohols.

Subsequently, the RMTD model was applied to the alcohol component of the  $^1\text{H}$  NMRD profiles. In order to obtain accurate modelling results, it is of utmost importance to use the appropriate diffusion coefficient. For this study, the intra-pore diffusion coefficients of alcohols in alcohol-water mixtures were determined on a 400 MHz spectrometer using PFG-NMR.

Considering the surface-to-volume ratio,  $\frac{N_S}{N}$ , and the adsorption correlation time,  $\tau_A$ , are correlated within the RMTD model, initially, the product of these parameters,  $\frac{N_S}{N} \times \tau_A$ , was obtained. Several fitting methods were applied and no difference was found between the fitting methods, indicating the robustness of the model. The  $\frac{N_S}{N} \times \tau_A$  values were normalized to the  $\frac{N_S}{N} \times \tau_A$  value of each pure alcohol, and plotted against the composition. It was shown that for all alcohols and THF, the  $\frac{N_S}{N} \times \tau_A$  values decreased as the water content increased. This indicated that the surface-adsorbate interaction of alcohols/THF was reduced. The reduction of  $\frac{N_S}{N} \times \tau_A$  was more prominent for longer chain alcohols, and even more pronounced for THF, which is more miscible with water in the bulk, but has a lower polarity and is therefore expected to have a weaker interaction with the surface. Therefore it was hypothesized that the degree of microphase separation depends not only on the bulk miscibility of the liquid mixture, but rather on the surface-adsorbate interaction strength of the weaker interacting species.

To further quantify the microphase separation, the  $\frac{N_S}{N} \times \tau_A$  trends with composition were fitted to an exponential function and a constant. The constant was thought to reflect the system in abundance of water, where a lower constant corresponds to a higher level of microphase separation. The fitted values for the constant decreased with alcohol chain length, until stabilization at  $\sim 0.01$  for butanol, pentanol and THF. It is believed that at such a low constant value, there is full microphase separation. The exponent extracted from the fits can be interpreted as a measure for the efficiency with which water displaces the alcohols/THF. The exponent was shown to correlate inversely with the polarity of the alcohols/THF, which has previously been linked to the surface-adsorbate interaction strength. Therefore, it could again be concluded that the degree of microphase separation depends on the surface-adsorbate interaction strength of the weaker interacting species.

Finally, values for the surface-to-volume ratio,  $\frac{N_S}{N}$ , and the adsorption correlation time,  $\tau_A$ , were estimated based on the assumption that both of these parameters depend on the surface-interaction strength, and therefore will have equivalent trends with the composition as the product  $\frac{N_S}{N} \times \tau_A$ . From the  $\frac{N_S}{N}$  values, the surface composition at any mixture composition can be determined, providing quantitative insight into the structural properties of the mixture inside the pores. In contrast,  $\tau_A$  values provide information about the dynamics of the system, which has not yet previously been reported, according to the author's knowledge.

Future work will contain investigations of the microphase separation of different mixtures in different supports and the comparison between them. In the next chapter of this thesis, challenges will be described regarding microphase separation studies on mesoporous silica, for which the RMTD model is not appropriate, and for which the relaxation environments of the two liquids are much closer to each other, and therefore not easily distinguishable. Other interesting systems include tert-butanol (TBA)-benzene and TBA-toluene mixtures in silica, in order for a comparison with the work of Morineau *et al.*<sup>1-4</sup>, or aqueous alcohol solutions in MCM-41<sup>5-7</sup>. Furthermore, work can be done to expand from binary to ternary mixtures, and in terms of applications, the microphase separation studies can be combined with catalytic activity studies or separations studies.

## References

1. Abdel Hamid, A. R., Mhanna, R., Lefort, R., Ghoufi, A., Alba-Simionesco, C., Frick, B. & Morineau, D. Microphase separation of binary liquids confined in cylindrical pores. *J. Phys. Chem. C* **120**, 9245–9252 (2016).
2. Mhanna, R., Abdel Hamid, A. R., Dutta, S., Lefort, R., Noirez, L., Frick, B. & Morineau, D. More room for microphase separation: an extended study on binary liquids confined in SBA-15 cylindrical pores. *J. Chem. Phys.* **146**, 024501 (2017).
3. Essafri, I., Morineau, D. & Ghoufi, A. Microphase separation of a miscible binary liquid mixture under confinement at the nanoscale. *npj Comput. Mater.* **5**, 1–10 (2019).
4. Mhanna, R., Catrou, P., Dutta, S., Lefort, R., Essafri, I., Ghoufi, A., Muthmann, M., Zamponi, M., Frick, B. & Morineau, D. Dynamic heterogeneities in liquid mixtures confined in nanopores. *J. Phys. Chem. B* **124**, 3152–3162 (2020).
5. Elamin, K., Jansson, H., Kittaka, S. & Swenson, J. Different behavior of water in confined solutions of high and low solute concentrations. *Phys. Chem. Chem. Phys.* **15**, 18437–18444 (2013).
6. Swenson, J., Elamin, K., Chen, G., Lohstroh, W. & Sakai, V. G. Anomalous dynamics of aqueous solutions of di-propylene glycol methylether confined in MCM-41 by quasielastic neutron scattering. *J. Chem. Phys.* **141**, 214501 (2014).
7. Elamin, K., Jansson, H. & Swenson, J. Dynamics of aqueous binary glass-formers confined in MCM-41. *Phys. Chem. Chem. Phys.* **17**, 12978–12987 (2015).
8. Kumar, S., Singh, N. & Prasad, R. Anhydrous ethanol: A renewable source of energy. *Renew. Sustain. Energy Rev.* **14**, 1830–1844 (2010).
9. Wang, C. H., Bai, P., Siepmann, J. I. & Clark, A. E. Deconstructing hydrogen-bond networks in confined nanoporous materials: Implications for alcohol-water separation. *J. Phys. Chem. C* **118**, 19723–19732 (2014).
10. El-Roz, M., Bazin, P., Birsa Čelič, T., Zabukovec Logar, N. & Thibault-Starzyk, F. Pore occupancy changes water/ethanol separation in a metal-organic framework - quantitative map of coadsorption by IR. *J. Phys. Chem. C* **119**, 22570–22576 (2015).

11. Gravelle, S., Yoshida, H., Joly, L., Ybert, C. & Bocquet, L. Carbon membranes for efficient water-ethanol separation. *J. Chem. Phys.* **145**, 124708 (2016).
12. Korb, J.-P. Multiscale nuclear magnetic relaxation dispersion of complex liquids in bulk and confinement. *Prog. Nucl. Magn. Reson. Spectrosc.* **104**, 12–55 (2018).
13. Kimmich, R. & Anordo, E. Field-cycling NMR relaxometry. *Prog. Nucl. Magn. Reson. Spectrosc.* **44**, 257–320 (2004).
14. Ward-Williams, J., Korb, J.-P. & Gladden, L. F. Insights into functionality-specific adsorption dynamics and stable reaction intermediates using Fast Field Cycling NMR. *J. Phys. Chem. C* **122**, 20271–20278 (2018).
15. Levitz, P., Bonnaud, P. A., Cazade, P.-A., Pellenq, J.-M. & Coasne, B. Molecular intermittent dynamics of interfacial water: probing adsorption and bulk confinement. *Soft Matter* **9**, 8654–8663 (2013).
16. Korb, J.-P. & Levitz, P. E. Direct probing of the wettability of plaster pastes at the nanoscale by proton Field Cycling Relaxometry. *AIP Conf. Proc.* **1081**, 55 (2008).
17. Guo, X.-Y., Watermann, T. & Sebastiani, D. Local microphase separation of a binary liquid under nanoscale confinement. *J. Phys. Chem. B* **118**, 10207–10213 (2014).
18. Muthulakshmi, T., Dutta, D., Maheshwari, P. & Pujari, P. K. Evidence for confinement induced phase separation in ethanol-water mixture: a positron annihilation study. *J. Phys. Condens. Matter* **30**, 025001 (2018).
19. Robertson, C. I. Characterising adsorption and mass transfer in porous media. (Doctoral thesis, University of Cambridge, 2017).
20. Levitz, P. Probing interfacial dynamics of water in confined nanoporous systems by NMRD. *Mol. Phys.* **117**, 952–959 (2019).
21. Fripiat, J. J., Letellier, M. & Levitz, P. Interaction of water with clay surfaces. *Philos. Trans. R. Soc. London. Ser. A, Math. Phys. Sci.* **311**, 287–299 (1984).
22. Ward-Williams, J. & Gladden, L. F. Insights into adsorption behaviour of binary liquid mixtures in porous media using fast field cycling NMR. *Magn. Reson. Imaging* **56**, 57–62 (2018).

23. Neudert, O., Mattea, C. & Stapf, S. Application of CPMG acquisition in Fast-Field-Cycling relaxometry. *Microporous Mesoporous Mater.* **269**, 103–108 (2018).
24. Derlacki, Z. J., Easteal, A. J., Edge, A. V. J., Woolf, L. A. & Roksandic, Z. Diffusion coefficients of methanol and water and the mutual diffusion coefficient in methanol-water solutions at 278 and 298 K. *J. Phys. Chem.* **89**, 5318–5322 (1985).
25. Harris, K. R., Goscinska, T. & Lam, H. N. Mutual diffusion coefficients for the systems water-ethanol and water-propan-1-ol at 25 °C. *J. Chem. Soc. Faraday Trans.* **89**, 1969–1974 (1993).
26. D’Agostino, C., Mitchell, J., Gladden, L. F. & Mantle, M. D. Hydrogen bonding network disruption in mesoporous catalyst supports probed by PFG-NMR diffusometry and NMR relaxometry. *J. Phys. Chem. C* **116**, 8975–8982 (2012).
27. D’Agostino, C., Kotionova, T., Mitchell, J., Miedziak, P. J., Knight, D. W., Taylor, S. H., Hutchings, G. J., Gladden, L. F. & Mantle, M. D. Solvent effect and reactivity trend in the aerobic oxidation of 1,3-propanediols over gold supported on titania: NMR diffusion and relaxation studies. *Chem. - A Eur. J.* **19**, 11725–11732 (2013).
28. D’Agostino, C., Brett, G. L., Miedziak, P. J., Knight, D. W., Hutchings, G. J., Gladden, L. F. & Mantle, M. D. Understanding the solvent effect on the catalytic oxidation of 1,4-butanediol in methanol over Au/TiO<sub>2</sub> catalyst: NMR diffusion and relaxation studies. *Chem. - A Eur. J.* **18**, 14426–14433 (2012).
29. Reichardt, C. *Solvents and solvent effects in organic chemistry.* (Wiley, 2002).
30. Levitz, P. Random flights in confining interfacial systems. *J. Phys. Condens. Matter* **17**, 4059–4074 (2005).
31. Levitz, P., Zinsmeister, M., Davidson, P., Constantin, D. & Poncelet, O. Intermittent Brownian dynamics over a rigid strand: heavily tailed relocation statistics in a simple geometry. *Phys. Rev. E* **78**, 030102 (2008).

## **7. Competitive adsorption of ethanol-water mixtures imbibed within mesoporous silicas. Part I: a fixed field relaxometry study**

### 7.1 Introduction

The previous chapter has shown that FFC-NMR can be used to obtain quantitative information about the microphase separation of binary liquid mixtures imbibed within porous media. Now that the first microphase separation system has been successfully investigated, we aim to generalize the FFC-NMR approach by studying other porous media systems. Ideally, the systems that are studied next, have already been investigated using methods different to FFC-NMR, and reported in the literature, so that a comparison can be made between the FFC-NMR approach and other techniques used in the literature. Therefore, the system studied in this chapter, as well as chapter 9, is ethanol-water imbibed within mesoporous silicas.

Ethanol-water mixtures imbibed within mesoporous silicas were investigated previously by Muthulakshmi *et al.*<sup>1</sup> and Robertson<sup>2</sup>, as was described in chapter 3. Robertson concluded from NMR relaxometry experiments that the ethanol-water mixtures, when imbibed into a mesoporous silica, separate into a water-rich surface layer and an ethanol-rich pore centre. In contrast, Muthulakshmi *et al.* concluded based on a positron annihilation lifetime spectroscopy (PALS) study that between ethanol concentrations of 30–45%, “inverse” microphase separation occurs, resulting in an ethanol-rich surface layer and a water-rich pore centre. This conclusion supported MD simulations, which predicted that ethanol is more likely to bind to silanol pore walls than water, because the hydrogen bonding network between water molecules outweighs the surface-water interaction<sup>3</sup>.

There are two clear differences between the studies by Muthulakshmi *et al.* and Robertson. Firstly, Muthulakshmi *et al.* investigated silicas with average pore diameters of 4, 6, and 10 nm, whereas Robertson used silicas with a 15 nm pore diameter. In order to directly compare our results with both studies, we will investigate silicas with pore sizes ranging from 3 to 30 nm.

Secondly, Robertson investigated as-received silicas as well as dehydroxylated silicas, in order to study the effect of the surface hydroxyl density on the microphase separation. Muthulakshmi *et al.* did not report surface hydroxyl densities. In this study, we will investigate as-received and rehydroxylated silicas to investigate the surface chemistry, particularly for smaller pore size silicas.

The ultimate goal of this study is to gain quantitative insight into the microphase separation of ethanol-water mixtures in silicas in the form of correlation times, however the FFC-NMR data is significantly more complex than the data shown in previous chapters, due to the overlap of the ethanol and water  $T_1$  relaxation times. Therefore a  $T_1 - T_2$  FFC-NMR pulse sequence was implemented, for which the optimization is shown in chapter 8. The FFC-NMR results of ethanol-water mixtures in silicas are shown in chapter 9.

This chapter focuses on the use of fixed field NMR relaxometry to investigate microphase separation.  $T_1 - T_2$  correlation experiments have been shown to provide insight into surface-adsorption interactions<sup>4-13</sup>. Moreover, a  $T_1 - T_2$  analysis for different mixture compositions has already been shown by Robertson to be an effective tool to study competitive adsorption.

We will apply the methodology used by Robertson for different pore size silicas, as well as silicas with varying surface hydroxyl densities. The fixed field results can then be used as validation for the FFC-NMR results shown in chapter 9, as well as to provide qualitative insight into the microphase separation of ethanol-water mixtures imbibed within mesoporous silicas.

$T_1 - T_2$  correlation experiments are performed at Larmor frequencies of 400 MHz (high field), to directly compare with Robertson, and 43 MHz (low field). The low field data is added for two reasons. Firstly, the echo time could be reduced more on the 43 MHz magnet than on the 400 MHz magnet, which was necessary in order to detect fast-relaxing components. Secondly, at low field, we can more easily distinguish surface-adsorbate interaction effects from faster processes such as liquid mixing effects. A detailed comparison of high and low field results will be made to highlight advantages and challenges of each of the magnetic fields.

## 7.2 Experimental

### 7.2.1 Materials

As-received CARiACT Q-series silicas (Q3, Q6, Q10, Q15, Q30) were obtained in the form of 2–4 mm spherical pellets. The labelling of the silicas corresponds to the characteristic pore diameter, e.g. Q6 corresponds to a 6 nm pore size, Q15 corresponds to 15 nm. All of the following characterization of the Q6–Q30 silicas was performed by another PhD student (Callum Penrose) in our research group, however the results are mentioned here explicitly due to their immediate relevance to the work presented. No characterization was done on the Q3 silica.

The surface areas were measured by Brunauer–Emmett–Teller (BET) nitrogen adsorption measurements<sup>14</sup>, and surface hydroxyl densities,  $\alpha_{OH}$ , were determined using a simple liquid <sup>1</sup>H NMR based deuterium exchange method<sup>15</sup>. The surface areas and surface hydroxyl densities for the Q-series silicas are shown in Table 7.1.

Table 7.1: As-received Q-series silicas surface areas, and surface hydroxyl densities<sup>15</sup>. The surface area error is estimated at  $\pm 2.0\%$ .

Silica	Surface area / $\text{m}^2\text{g}^{-1}$	$\alpha_{OH}$ / $\text{nm}^{-2}$
Q6	407	$1.51 \pm 0.13$
Q10	312	$1.29 \pm 0.17$
Q15	207	$4.52 \pm 0.36$
Q30	107	$5.35 \pm 0.81$

It can be seen that with increasing Q-number, the surface area decreases. This is consistent with an increasing pore diameter, as is expected. The surface hydroxyl densities show a sharp difference between Q6 and Q10 on one side, and Q15 and Q30 on the other side, where the surface hydroxyl densities of Q15 and Q30 are much higher than those of Q6 and Q10.

In order to separate the effect of the pore size from the effect of the surface hydroxyl density, rehydroxylated Q6 and Q10 silicas were investigated. The rehydroxylation was performed by boiling the silica pellets in water for 100 hours. A BET analysis showed that following the rehydroxylation, the surface areas of Q6 and Q10 decreased to 191 and 233  $\text{m}^2\text{g}^{-1}$  respectively. This means that the pore size is comparable to the as-received Q15 silica. The surface hydroxyl densities increased to 6.56 and 4.75  $\text{nm}^{-2}$  for Q6 and Q10 respectively.

Mixtures of ethanol ( $\geq 98\%$ , Alfa Aesar) and deionized water ranging between 10 and 80 mol% ethanol were made gravimetrically. Silica pellets were dried overnight at 200 °C, after which the pellets were imbibed in the ethanol-water mixtures overnight. Extra-pellet liquid was removed by drying the sample with filter paper directly before the NMR experiments, leaving only the desired liquid imbibed within the pellets.

### 7.2.2 NMR relaxometry experiments

High field NMR relaxometry experiments were performed on the as-received Q6, Q10, and Q15 silicas using a 9.4T Bruker Avance NMR spectrometer. Typical pulse lengths on this spectrometer were 14.4  $\mu\text{s}$  for a  $\pi/2$  pulse, and 28.8  $\mu\text{s}$  for a  $\pi$  pulse. Low field NMR relaxometry experiments were performed on all as-received and rehydroxylated Q-series silicas using a Magritek Spinsolve 43 MHz NMR spectrometer. For these experiments, the pulse length was set to 22  $\mu\text{s}$  and the pulse amplitude was adjusted to obtain  $\pi/2$  and  $\pi$  pulses.

For each sample at high and low field, an initial inversion recovery experiment with 16 time delays was done to determine the  $T_1$  value, after which the recycle delay was set at  $5T_1$ . 2D  $T_1 - T_2$  correlation data was obtained using a one-shot CPMG-inversion recovery pulse sequence. At high field, PROJECT acquisition was used in order to suppress J-modulation effects<sup>2</sup>. For all experiments, 32  $T_1$  time delays between 1 ms and  $5T_1$  were used, and 8 repeat scans were recorded. At high field, 512 echoes with an echo time of 2 ms were recorded to obtain  $T_2$  relaxation times. At low field, the echo time was 125  $\mu\text{s}$  and 10000 were recorded. The 2D data sets were processed using an in-house script for a 2D inverse Laplace transform using Tikhonov regularisation<sup>16</sup>.  $T_1$  and  $T_2$  values were determined from the logarithmic average of each of the dimensions of the peaks in the 2D  $T_1 - T_2$  plots.

The intra-pore compositions of ethanol-water mixtures were determined from the  $^1\text{H}$  NMR spectrum. For all mixtures, the ethanol- $\text{CH}_3$  peak could be clearly distinguished from the ethanol- $\text{CH}_2$ , ethanol-OH, and water peaks.

## 7.3 Results and discussion

### 7.3.1 High field NMR relaxometry results

High field NMR relaxometry experiments were performed on ethanol-water mixtures imbibed within as-received Q6, Q10, and Q15 silicas. The 2D  $T_1 - T_2$  correlation plots for pure water, pure ethanol, and the mixture with 40 mol% ethanol are shown in Figure 7.1.

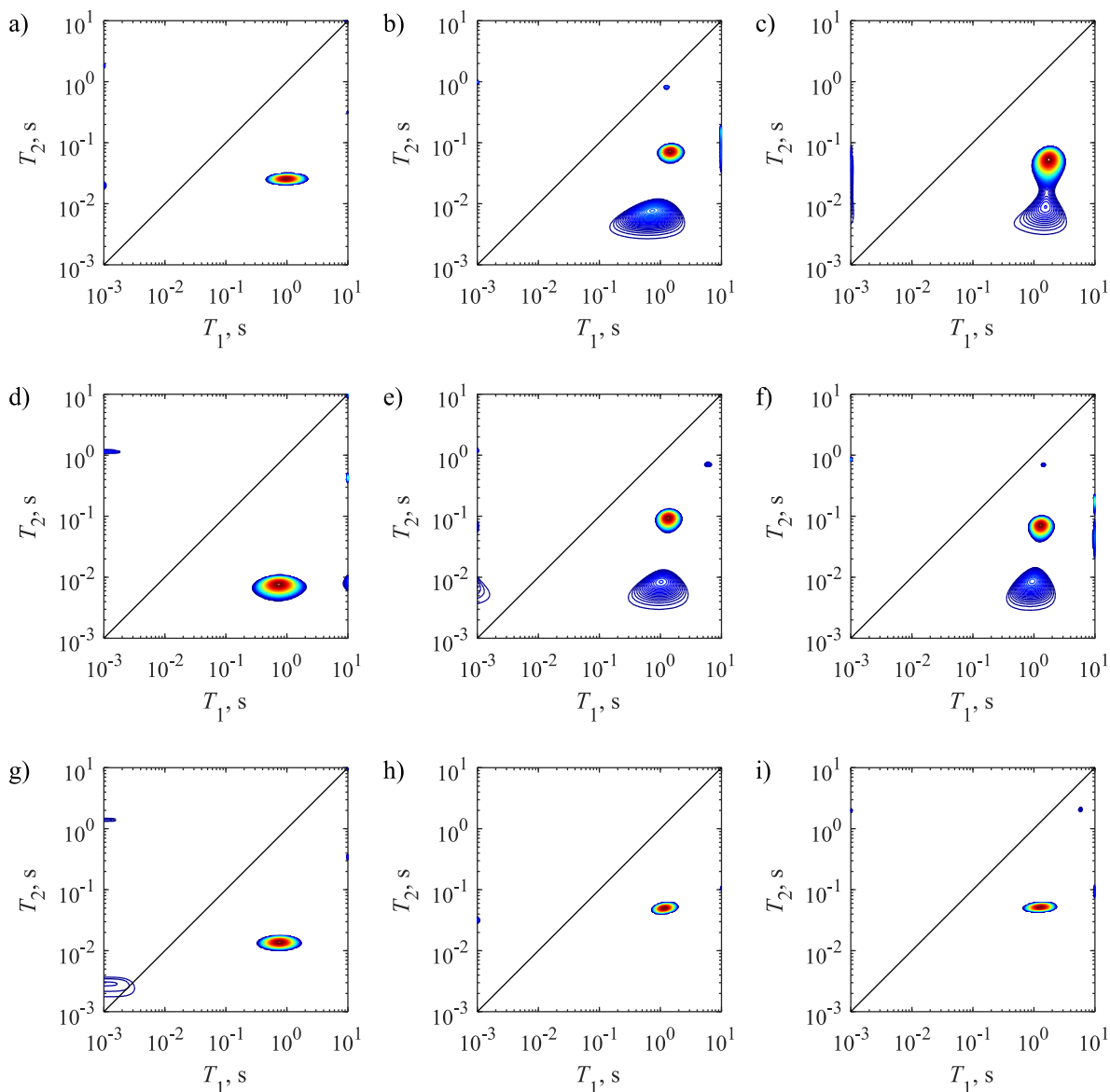


Figure 7.1: 2D  $T_1$ - $T_2$  correlation plots for (a,d,g) water, (b,e,h) 60:40 mol% ethanol-water, and (c,f,i) ethanol imbibed within (a-c) Q15, (d-f) Q10, and (g-i) Q6 silica, recorded at a Larmor frequency of 400 MHz.

For the Q10 and Q15 silicas, shown in Figure 7.1a-f, two components could be distinguished. Based on the populations of the components compared to the intra-pore mixture compositions, it could be concluded that the component with long  $T_1$  and  $T_2$  times corresponds to the alkyl chain of ethanol. As was also shown for alcohol-water mixtures imbibed within anatase titania in chapter 6, there appears to be fast exchange between water and the ethanol-hydroxyl, therefore the component with short  $T_1$  and  $T_2$  times corresponds to the water signal, as well as the ethanol-hydroxyl. For simplicity, the profiles for the alkyl component and the (water + hydroxyl) component will be denoted ethanol and water components respectively.

For Q6 silica, see Figure 7.1g-i, the 2D inverse Laplace transform only shows one  $T_1 - T_2$  peak, regardless of the mixture composition. There are two possible explanations for this. Firstly, the  $T_2$  values are expected to decrease with decreasing pore size, following the two-phase fast exchange model. The echo time that was used is 2 ms, which means that most of the water signal will have decayed after only a few echoes. Unfortunately, the echo time is restricted in order to limit the duty cycle. Therefore the echo time could not be reduced to obtain two components. The second explanation is that the  $T_1$  and  $T_2$  values of ethanol and water are too similar to distinguish.

Because we cannot separate out two components in Q6, we cannot make any conclusions about competitive adsorption within this support. In order to investigate the Q6 silica further, low field NMR relaxometry experiments will be presented later in this chapter. On the low field Spinsolve spectrometer, the echo time could be reduced to 125  $\mu$ s, which means shorter  $T_2$  components can be detected.

For the Q10 and Q15 silicas, the  $T_1/T_2$  ratio was plotted against the mixture composition, see Figure 7.2. The results correspond very well with the  $T_1/T_2$  ratios shown by Robertson. The  $T_1/T_2$  ratio of the water component generally increases with ethanol composition. Following the two-phase fast exchange model, this indicates that, as the concentration of water inside the pores decreases, the ratio between water in the surface layer and in the centre of the pore increases. For the ethanol component, the  $T_1/T_2$  ratio decreases upon addition of water to the system, indicating a decrease of ethanol molecules in the surface layer. From these observations, we can conclude that water is the stronger-interacting species in these systems, and will preferentially adsorb on the pore surface, whereas ethanol is the weaker-interacting species that will reside in the centre of the pore.

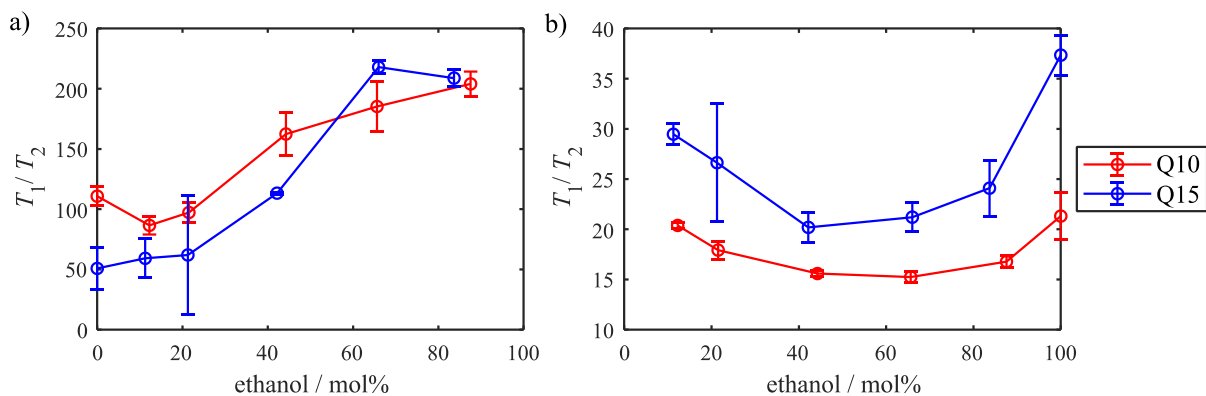


Figure 7.2:  $T_1/T_2$  ratios of a) water, and b) ethanol components in ethanol-water mixtures imbibed within Q10 and Q15 silica, plotted against the mixture composition in ethanol mol%, recorded at  $\nu_0 = 400$  MHz. The error bars represent the standard deviation of  $T_1/T_2$  ratios from experiments on three different sets of silica pellets.

For ethanol concentrations  $<30\%$ , the ethanol  $T_1/T_2$  ratio appears to increase. For the same concentrations in Q10 silica, the water  $T_1/T_2$  ratio appears to decrease. This may indicate the presence of ethanol clusters at the pore surface, which corresponds to the low-ethanol mixtures in the paper by Muthulakshmi *et al.*

In order to compare the Q10 and Q15 results in more detail, the  $T_1/T_2$  ratios were normalized to the  $T_1/T_2$  ratio of the pure water and ethanol imbibed within the corresponding support. The normalized  $T_1/T_2$  ratios are shown in Figure 7.3. Based on these plots, it appears that the trends of the  $T_1/T_2$  ratios with the mixture composition are more pronounced in Q15 silica than in Q10 silica. This could indicate that the competitive adsorption of ethanol-water mixtures is different between the two supports. However, it remains crucial to obtain information about the other silicas, especially toward smaller pore sizes, in order to establish correlations between microphase separation and the silica pore size and surface chemistry. Therefore low field NMR relaxometry experiments on silicas with pore diameters ranging between 3–30 nm will now be discussed.

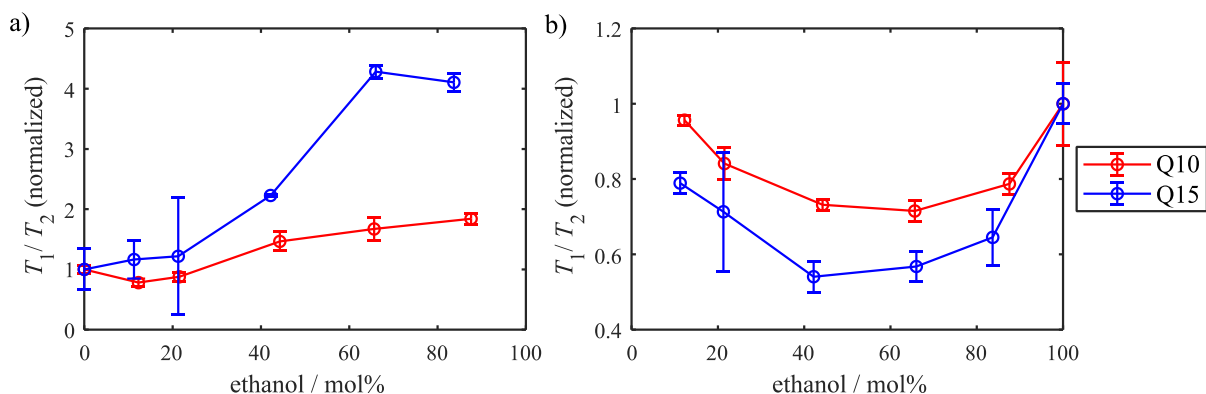


Figure 7.3:  $T_1/T_2$  ratios of a) water, and b) ethanol components in ethanol-water mixtures imbibed within Q10 and Q15 silica, normalized to the pure water and ethanol  $T_1/T_2$  ratios respectively, plotted against the composition in ethanol mol%. The error bars represent the standard deviation of  $T_1/T_2$  ratios from experiments on three different sets of silica pellets.

### 7.3.2 Low field NMR relaxometry results

Low field  $T_1 - T_2$  correlation experiments were performed on a Magritek Spinsolve 43 MHz NMR spectrometer. The echo time was set to 125  $\mu$ s, which allowed for the detection of faster-relaxing components compared to the high field relaxometry experiments. The 2D  $T_1 - T_2$  correlation plots for pure water, pure ethanol, and the mixture with 40 mol% ethanol are shown in Figure 7.4.

The 2D plots show that two components can be distinguished for all pore size silicas. The  $T_2$  values of the water component in Q3 silica (Figure 7.4m-o) are as small as 3 ms, however they can still be reliably detected and distinguished from the slower-relaxing ethanol component on the Magritek spectrometer.

The  $T_1/T_2$  ratios for the water and ethanol components are again plotted against the mixture composition, and the  $T_1/T_2$  ratios are renormalized to the  $T_1/T_2$  ratio of the pure component, see Figure 7.5. First, we discuss the water component. The  $T_1/T_2$  ratios for the water component in Q15 and Q30 increase with the ethanol concentration, see Figure 7.5a-c. This corresponds to the high field results and is consistent with a system where water preferentially adsorbs onto the silica surface. For Q6 and Q10 silica however, the water  $T_1/T_2$  ratios decrease as the water concentration decreases, indicating that the water resides preferentially in the centre of the pore, rather than at the surface. These results are consistent with the “inverse” microphase separation described by Muthulakshmi *et al.* Finally, in Q3 silica, the  $T_1/T_2$  ratio does not appear to be dependent on the mixture composition. It is expected that for such small pore sizes, microphase separation does not occur, because there are simply not enough molecules within a pore to create a surface layer and a bulk-like phase. An investigation of pore size effects in microphase separation has not yet been reported in the literature, according to the author’s knowledge. For the ethanol component, see Figure 7.5b-d, the  $T_1/T_2$  ratios are independent of the mixture composition for all pore sizes. It is expected that the dominant surface-ethanol interaction is that of the polar ethanol hydroxyl with the polar silica surface. As a result, the alkyl chain of ethanol is not directly involved in the surface-ethanol interaction. The ethanol  $T_1/T_2$  component corresponds to the alkyl chain only and is therefore not a sensitive probe for the surface-ethanol interaction. The  $T_1/T_2$  ratio of the ethanol component in Q3 silica is much higher than for all other silicas. This again indicates that the pores of Q3 silica are so small, that there is no surface layer and bulk-like phase.

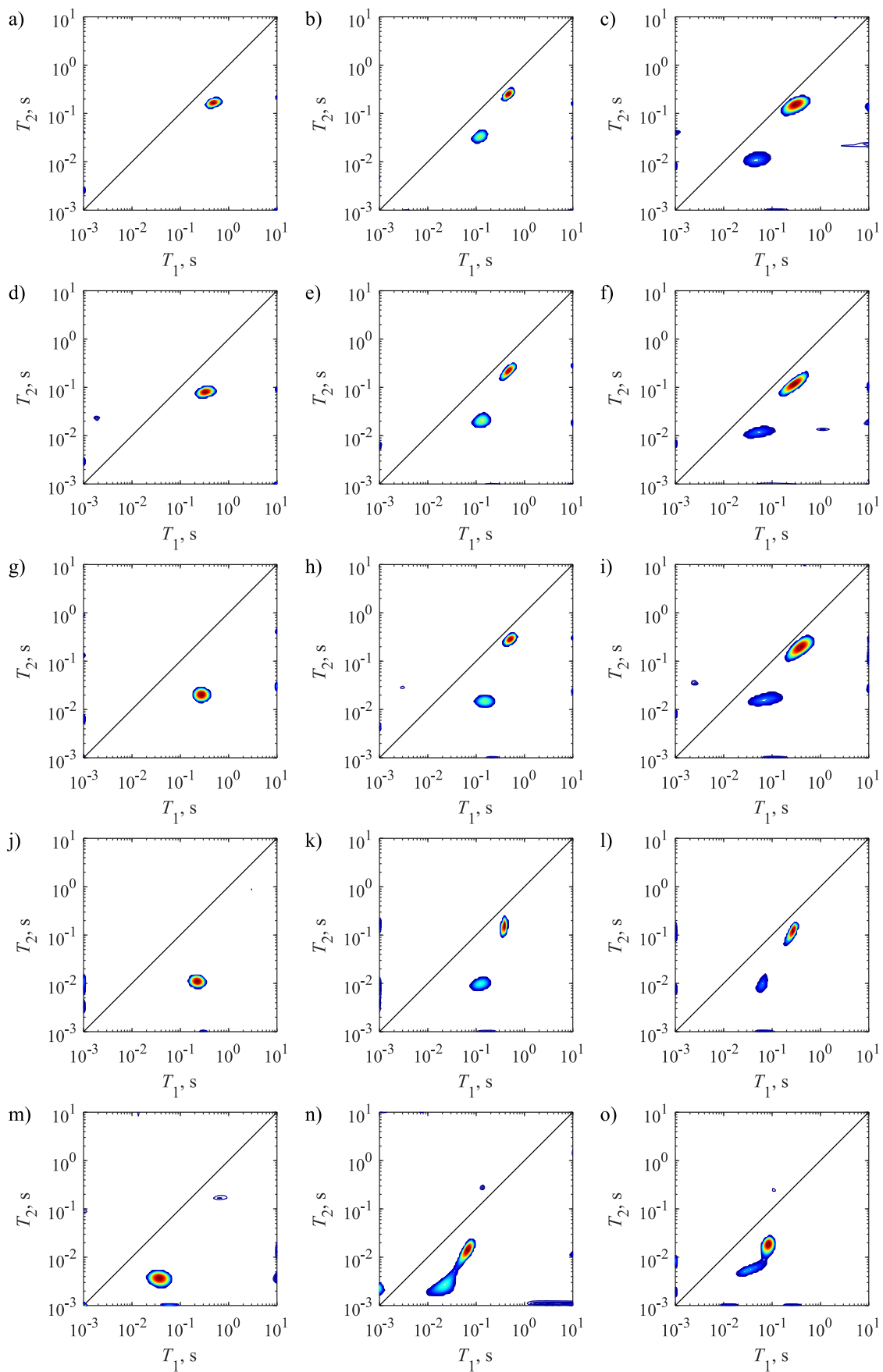


Figure 7.4: 2D  $T_1$ - $T_2$  correlation plots for (a,d,g,j,m) water, (b,e,h,k,n) 60:40 mol% ethanol-water, and (c,f,i,l,o) ethanol imbibed within (a-c) Q30, (d-f) Q15, (g-i) Q10, (j-l) Q6, and (m-o) Q3 silica, recorded at a Larmor frequency of 400 MHz.

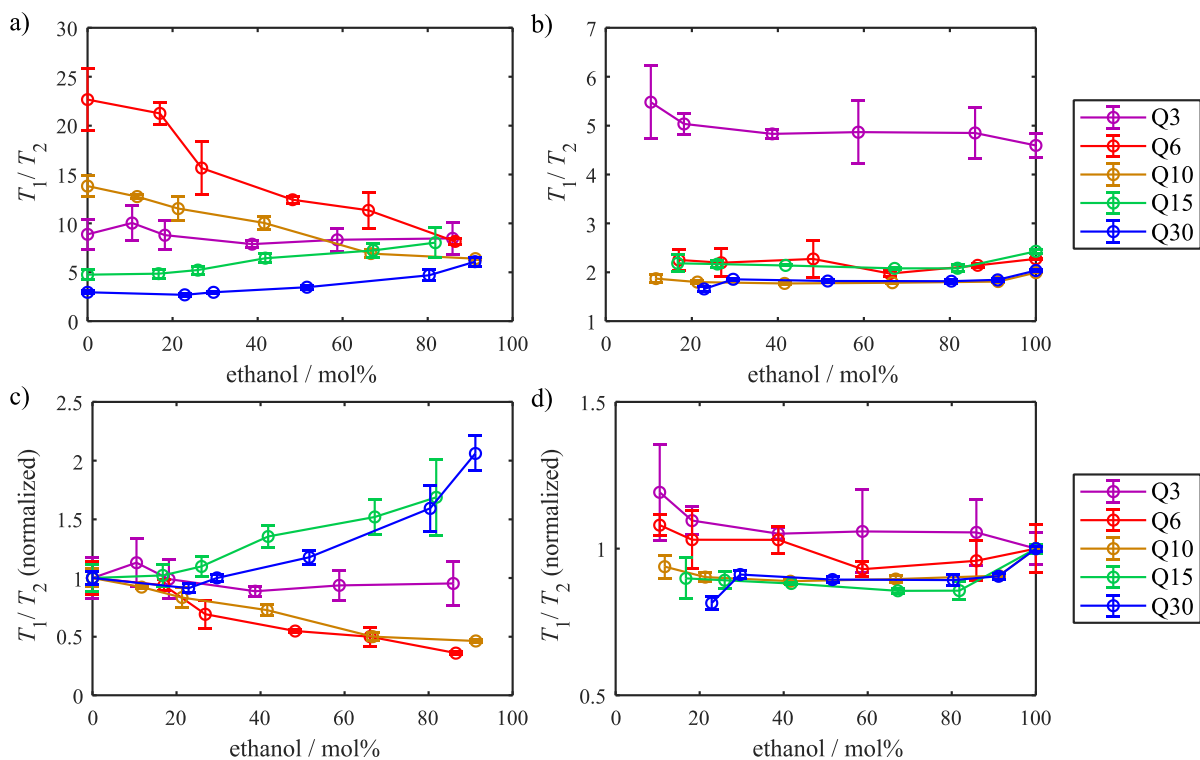


Figure 7.5: (a,b) Absolute and (c,d) renormalized  $T_1/T_2$  ratios of (a,c) water, and (b,d) ethanol components in ethanol-water mixtures imbibed within Q3–Q30 silicas, plotted against the mixture composition in ethanol mol%, recorded at  $\nu_0 = 43$  MHz. The error bars represent the standard deviation of  $T_1/T_2$  ratios from experiments on three different sets of silica pellets. Error bars are shown for all samples, however some are too small to see by eye.

While it is clear from the water  $T_1/T_2$  ratios that the microphase separation inverts between Q6/Q10 and Q15/Q30 silica, the reason behind this significant change cannot be concluded without further research. This is because two main variables change between Q6/Q10 and Q15/Q30 silica: first, the pore size, and second, the surface hydroxyl density. As was shown in section 7.2.1, the surface hydroxyl densities for Q6 and Q10 silica are 1.29 and 1.51 OH/nm<sup>-2</sup>, whereas Q15 and Q30 have much higher surface hydroxyl densities at 4.52 and 5.35 OH/nm<sup>-2</sup>. A lower surface hydroxyl density suggests a weaker surface-water interaction, which could result in the water molecules favouring a strongly hydrogen bonded network with other water molecules, rather than a water-rich surface layer, i.e. “inverse” microphase separation. In order to investigate the effect of the surface hydroxyl density on microphase separation, the  $T_1/T_2$  experiments were repeated on rehydroxylated Q6 and Q10 silica.

### 7.3.2.1 Rehydroxylated silicas

$T_1 - T_2$  correlation data was recorded for ethanol-water mixtures imbibed within rehydroxylated Q6 and Q10 silica. First, the  $T_1/T_2$  ratios of pure water and pure ethanol were plotted against the pore size, see Figure 7.6.

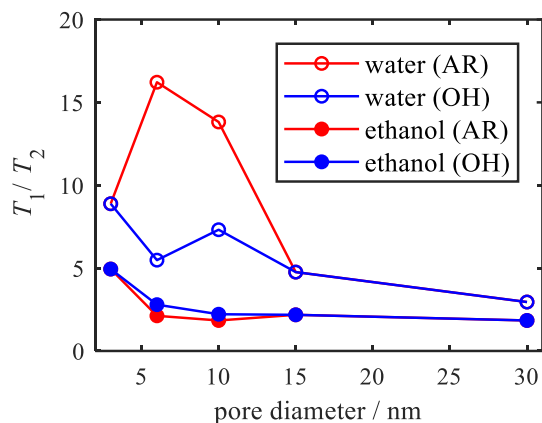


Figure 7.6:  $T_1/T_2$  ratios of pure water and ethanol in as-received (AR) and rehydroxylated (OH) silicas. Because the as-received Q15 and Q30 silicas were already fully hydroxylated, and there was no surface hydroxyl density for Q3 silica, the same  $T_1/T_2$  ratios were used for the as-received and rehydroxylated data points.

The water  $T_1/T_2$  ratios for the rehydroxylated silicas are significantly lower than for the as-received silicas. This is consistent with the work done by Robertson, and is an effect following the change in surface chemistry, i.e. the different silanol properties within the silicas. Figure 7.7 shows the water and ethanol  $T_1/T_2$  ratios of the as-received and rehydroxylated Q6 and Q10 samples, plotted against the mixture composition. For the ethanol component, the  $T_1/T_2$  ratios of the rehydroxylated samples increase across the full composition range. However, the  $T_1/T_2$  ratio still does not depend on the mixture composition, as is expected following the previous conclusion that the alkyl chain of ethanol is not directly involved in the surface-ethanol interaction.

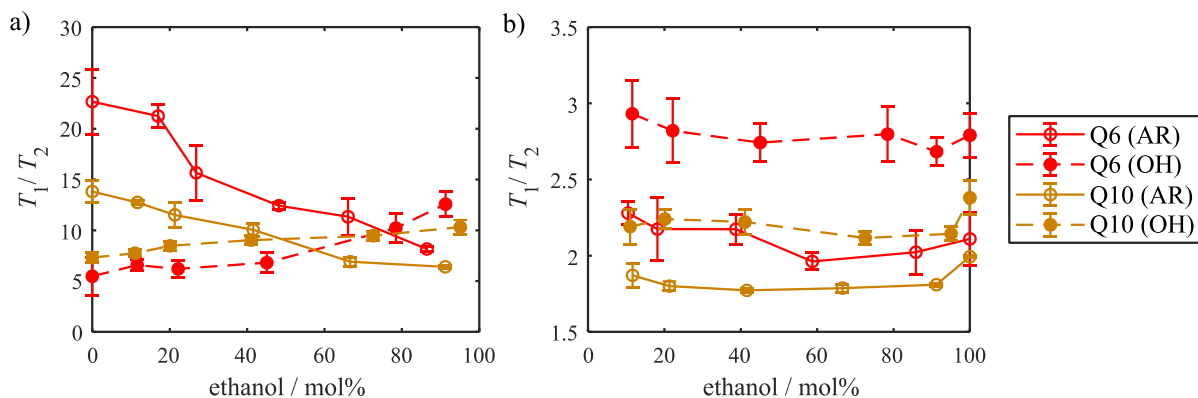


Figure 7.7:  $T_1/T_2$  ratios of a) water, and b) ethanol components in ethanol-water mixtures imbibed within as-received (AR) and rehydroxylated (OH) Q6 and Q10 silicas, plotted against the mixture composition in ethanol mol%.

The  $T_1/T_2$  ratios of the water component show a significant change between the as-received and rehydroxylated silicas. The  $T_1/T_2$  ratio of the rehydroxylated samples increases with the ethanol concentration, indicating that water is the stronger-interacting species for the rehydroxylated samples, just like for Q15 and Q30 silica. It is clear that the microphase separation has been inverted, showing the effect the rehydroxylation has on the competitive adsorption characteristics. It should however be noted that the rehydroxylation process resulted in larger pore sizes as well as higher surface hydroxyl densities, see section 7.2.1, therefore it cannot be unambiguously concluded whether the microphase separation depends more on the surface hydroxyl density or on the pore size. In order to distinguish between the two effects, a small-pore silica with a high surface hydroxyl density should be tested. This system could be created through a gentler rehydroxylation method.

### 7.3.3 Comparison between high and low field NMR relaxometry

While the high and low field  $T_1/T_2$  ratios for the Q15 silica support were consistent with each other, those for the as-received Q10 silica were not. In Figure 7.2a it can be seen that the high field water  $T_1/T_2$  ratio increases with ethanol mol%, whereas the low field  $T_1/T_2$  ratio decreases, see Figure 7.5a. In order to understand the different results between high and low field, the separate  $T_1$  and  $T_2$  components were compared, see Figure 7.8. The  $T_1$  and  $T_2$  values were renormalized to the pure liquid to highlight competitive adsorption effects.

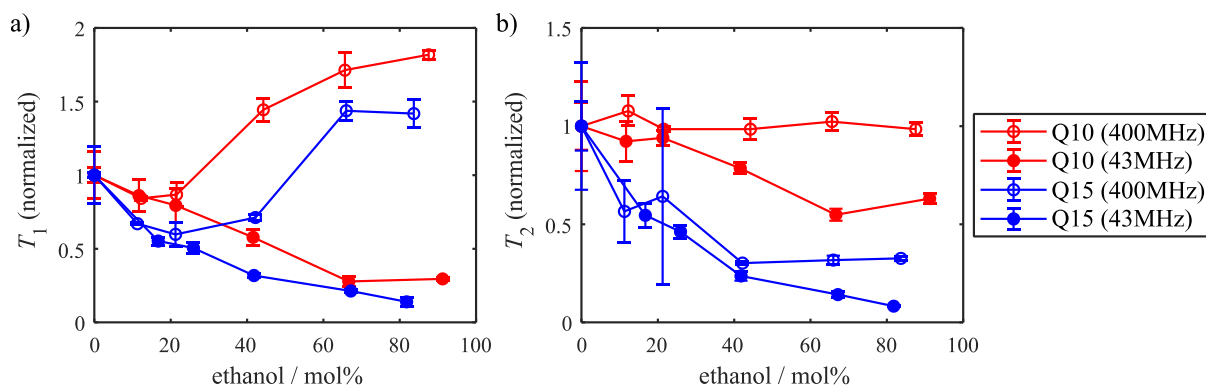


Figure 7.8: Normalized (a)  $T_1$  and (b)  $T_2$  values for the water component in ethanol-water mixtures imbibed within as-received Q10 and Q15 silicas, at Larmor frequencies of 400 MHz and 43 MHz, plotted against the mixture composition in ethanol mol%.

It is immediately clear in Figure 7.8a that for both Q10 and Q15 silica, the high and low field  $T_1$  values follow different trends with ethanol mol%. At low field (43 MHz) the water  $T_1$  values decrease as the ethanol concentration increases. In contrast, the  $T_1$  values at high field (400 MHz) first decrease as ethanol is added to the system, but then increase for >20 mol% ethanol. For the  $T_2$  values shown in Figure 7.8b the differences between high and low field are much smaller. The renormalized  $T_2$  values of Q15 appear to follow the same trend at high and low field, but for Q10 silica, the high field  $T_2$  appears to be independent on the mixture composition, whereas the low field  $T_2$  still decreases.

The differences between the high and low field results are due to the different timescales on which we measure relaxation. At high Larmor frequencies, we measure fast processes, whereas at low Larmor frequencies, slow processes are measured, such as surface-adsorbate interactions. Because we are mainly interested in competitive adsorption, we first discuss the low field results.

At low field, both  $T_1$  and  $T_2$  relaxation times for both silicas decrease with increasing ethanol mol%. It has been long established that bulk water relaxation times vary upon addition of ethanol due to mixing effects<sup>17</sup>. These mixing effects are equivalent to the bulk mixing effects on the diffusion coefficient as discussed in section 6.4.2.1. It is expected that mixing effects dominate the change in relaxation times with mixture composition. Therefore it is important to renormalize the relaxation times to remove bulk mixing effects. This can be done for example by obtaining  $T_{1,\text{bulk}}/T_{1,\text{pore}}$  ratios, or, in this study, by measuring  $T_1/T_2$  ratios.

In general, a reduction in relaxation times is consistent with a decrease in the molecular mobility. However, the  $T_2$  relaxation time is much more affected by surface adsorption effects than the  $T_1$  relaxation time<sup>8,18</sup>. Therefore the stronger interacting species in a mixture will exhibit an increase in  $T_1/T_2$  ratio, and the weaker interacting species will show a decreasing  $T_1/T_2$  ratio.

In this study, for the 67% ethanol mixture in Q10 silica, the  $T_1$  value is reduced by 72% with respect to the pure water  $T_1$ . The  $T_2$  value of the same mixture is reduced by 45%. As the  $T_1$  is reduced more than the  $T_2$ , the  $T_1/T_2$  ratio decreases. In contrast, for Q15 silica, the same mixture shows a 79% reduction in  $T_1$  and a 86% reduction in  $T_2$ , resulting in an overall increase in the  $T_1/T_2$  ratio. Both results are consistent with the above theory.

The high field relaxation times show different trends. While the  $T_2$  values for Q15 silica match the low field trend quite well, for Q10 the high field  $T_2$  values appear to be independent of the mixture composition. However, the most significant difference between high and low field is in the  $T_1$  trends. The increase in  $T_1$  for mixture compositions >20 mol% ethanol suggests enhanced rotational mobility.

Previously, an increase in  $T_1$  for polyols imbibed within porous media compared to their bulk equivalents was explained as an increase in the tumbling rate following a disruption to the intermolecular hydrogen bonding network<sup>19</sup>. For the water component in confined ethanol-water mixtures, it is expected that the water hydrogen bonding network is similarly disrupted, thereby causing an increase in  $T_1$ .

A comparison between high and low field relaxation times has shown that at low field, competitive adsorption effects can be distinguished, whereas at high field, other effects are dominant in changing the relaxation times, in particular the  $T_1$ . Because it is difficult to distinguish these effects from surface-adsorbate interaction effects, the relaxometry results can easily be misinterpreted. Therefore, it is more appropriate to use low field relaxometry to investigate surface-adsorbate interactions compared to high field relaxometry.

## 7.4 Conclusions and outlook

Fixed field  $T_1 - T_2$  correlation experiments were used to investigate the microphase separation of ethanol-water mixtures in a range of silicas with pore sizes between 3–30 nm and with different surface hydroxyl densities. The literature on similar systems contradicted each other. While the studies agree that microphase separation occurs, some studies concluded that ethanol sticks to the pore surface<sup>1,3</sup>, whereas another study showed the opposite, that water is the stronger interacting species<sup>2</sup>. The work presented here has been able to shed light on the discrepancies in the literature.

First, the experiments were performed at high field, at a Larmor frequency of 400 MHz. The results on Q10 and Q15 silica were consistent with one of the previously mentioned studies, showing a steep increase in the water  $T_1/T_2$  ratio with increasing ethanol mol%<sup>2</sup>. This indicated that water is the stronger interacting species and therefore adsorbs onto the surface, while ethanol is in the centre of the pore. The ethanol  $T_1/T_2$  ratio appeared to be much less dependent on the mixture composition than the water component. This is because the alkyl chain of ethanol is not directly involved in the surface-ethanol interaction. Unfortunately, ethanol and water signals could not be separated for Q6 silica. Therefore, the experiments were repeated at low field, at a Larmor frequency of 43 MHz. This allowed for the detection of shorter  $T_2$  values and for a better separation of the ethanol and water components.

The low field  $T_1/T_2$  trends for Q15 silica matched those at high field, however the  $T_1/T_2$  ratios of the water component in smaller pore silicas decreased upon addition of ethanol, indicating an “inverse” microphase separation, with an ethanol-rich surface layer and water residing in the centre of the pore. This “inverse” microphase separation is consistent with the other studies previously mentioned<sup>1,3</sup>. In observing both forms of microphase separation, we can conclude that the discrepancy found in the literature is due to the difference in silica characteristics, namely the pore size and surface hydroxyl density.

In order to investigate whether the change of microphase separation is a primarily pore size effect or whether it is caused by varying the surface chemistry, rehydroxylated Q6 and Q10 silicas were tested. The water  $T_1/T_2$  ratios in the rehydroxylated Q6 and Q10 silicas increased upon addition of ethanol, similarly to the as-received Q15 and Q30 silicas. Therefore the microphase separation is likely largely dependent on the surface chemistry, however it should be noted that the rehydroxylation process appears to increase the average pore size<sup>14</sup>.

A definitive conclusion requires additional experiments on small-pore size silicas with a high surface hydroxyl density, for example created via a gentler rehydroxylation process.

The  $T_1/T_2$  results on Q10 silica were inconsistent between high and low field experiments. An analysis of the separate  $T_1$  and  $T_2$  values showed that at low field, all water relaxation times for Q10 and Q15 silica decrease with increasing ethanol mol% due to liquid mixing effects. The difference in  $T_1/T_2$  trends is determined by which relaxation time is reduced more. In the case of Q15 and Q30 silicas, the  $T_2$  is reduced more than the  $T_1$ , resulting in an increasing  $T_1/T_2$  ratio with ethanol composition, indicating that water is the stronger interacting species. For the as-received small-pore silicas, the opposite is true. The  $T_2$  value is reduced less than the  $T_1$  value, resulting in a decreasing  $T_1/T_2$  ratio, consistent with water being in the centre of the pore.

At high field, the  $T_1$  relaxation times of the water component increase with ethanol mol%, suggesting an enhanced rotational mobility, which is expected to be caused by a disruption to the water hydrogen bonding network. Because the variation in  $T_1$  is thought to be due to hydrogen bonding network effects, rather than surface-adsorbate interactions, the high field  $T_1/T_2$  results can easily be misinterpreted, highlighting the advantage of using low field NMR relaxometry to study adsorption compared to high field NMR relaxometry.

This chapter shows how fixed field NMR relaxometry can be used to gain insight into the competitive adsorption of confined liquid mixtures, and how two opposite forms of microphase separation can be distinguished through  $T_1 - T_2$  correlation experiments. However, the quantitative information about the dynamics of the liquids is limited. In the next chapters, FFC-NMR will be used to extract correlation times related to the microphase separation of ethanol-water mixtures imbibed within silicas, creating a more complete and quantitative description of these systems.

## References

1. Muthulakshmi, T., Dutta, D., Maheshwari, P. & Pujari, P. K. Evidence for confinement induced phase separation in ethanol-water mixture: a positron annihilation study. *J. Phys. Condens. Matter* **30**, 025001 (2018).
2. Robertson, C. I. Characterising adsorption and mass transfer in porous media. (Doctoral thesis, University of Cambridge, 2017).
3. Guo, X.-Y., Watermann, T. & Sebastiani, D. Local microphase separation of a binary liquid under nanoscale confinement. *J. Phys. Chem. B* **118**, 10207–10213 (2014).
4. Peemoeller, H., Shenoy, R. K. & Pintar, M. M. Two-dimensional nmr time evolution correlation spectroscopy in wet lysozyme. *J. Magn. Reson.* **45**, 193–204 (1981).
5. Song, Y.-Q., Venkataramanan, L., Hürlimann, M. D., Flaum, M., Frulla, P., Straley, C.  $T_1$ – $T_2$  Correlation Spectra Obtained Using a Fast Two-Dimensional Laplace Inversion. *J. Magn. Reson.* **154**, 261–268 (2002).
6. McDonald, P. J., Korb, J.-P., Mitchell, J. & Monteilhet, L. Surface relaxation and chemical exchange in hydrating cement pastes: A two-dimensional NMR relaxation study. *Phys. Rev. E* **72**, 011409 (2005).
7. Weber, D., Mitchell, J., McGregor, J. & Gladden, L. F. Comparing Strengths of Surface Interactions for Reactants and Solvents in Porous Catalysts Using Two-Dimensional NMR Relaxation Correlations. *J. Phys. Chem.* **113**, 6610–6615 (2009).
8. Gladden, L. F. & Mitchell, J. Measuring adsorption, diffusion and flow in chemical engineering: applications of magnetic resonance to porous media. *New J. Phys.* **13**, 35001 (2011).
9. D’Agostino, C., Brett, G. L., Miedziak, P. J., Knight, D. W., Hutchings, G. J., Gladden, L. F. & Mantle, M. D. Understanding the Solvent Effect on the Catalytic Oxidation of 1,4-Butanediol in Methanol over Au/TiO<sub>2</sub> Catalyst: NMR Diffusion and Relaxation Studies. *Chem. - A Eur. J.* **18**, 14426–14433 (2012).
10. D’Agostino, C., Kotionova, T., Mitchell, J., Miedziak, P. J., Knight, D. W., Taylor, S. H., Hutchings, G. J., Gladden, L. F. & Mantle, M. D. Solvent Effect and Reactivity Trend in the Aerobic Oxidation of 1,3-Propanediols over Gold Supported on Titania:

- NMR Diffusion and Relaxation Studies. *Chem. - A Eur. J.* **19**, 11725–11732 (2013).
11. D’Agostino, C., Mitchell, J., Mantle, M. D. & Gladden, L. F. Interpretation of NMR Relaxation as a Tool for Characterising the Adsorption Strength of Liquids inside Porous Materials. *Chem. - A Eur. J.* **20**, 13009–13015 (2014).
  12. D’Agostino, C., Feaviour, M. R., Brett, G. L., Mitchell, J., York, A. P. E., Hutchings, G. J., Mantle, M. D. & Gladden, L. F. Solvent inhibition in the liquid-phase catalytic oxidation of 1,4-butanediol: understanding the catalyst behaviour from NMR relaxation time measurements. *Catal. Sci. Technol.* **6**, 7896–7901 (2016).
  13. D’Agostino, C., Brett, G., Divitini, G., Ducati, C., Hutchings, G. J., Mantle, M. D. & Gladden, L. F. Increased Affinity of Small Gold Particles for Glycerol Oxidation over Au/TiO<sub>2</sub> Probed by NMR Relaxation Methods. *ACS Catal.* **7**, 4235–4241 (2017).
  14. Brunauer, S.; Emmett, P. H.; Teller, E. Adsorption of gases in multimolecular layers. *J. Am. Chem. Soc.* **60**, 309–319 (1938).
  15. Penrose, C., Steiner, P., Gladden, L.F., Sederman, A.J., York, A.P.E., Bentley, M. & Mantle, M.D. A simple liquid state <sup>1</sup>H NMR measurement to directly determine the surface hydroxyl density of porous silica. *Chem. Commun.* (2021) Advance Article.
  16. Butler, J. P., Reeds, J. A. & Dawson, S. V. Estimating solutions of first kind integral equations with nonnegative constraints and optimal smoothing. *SIAM J. Numer. Anal.* **18**, 381–397 (1981).
  17. Goldammer, E. & Zeidler, M. Molecular motion in aqueous mixtures with organic liquids by nmr relaxation measurements. *Ber. Bunsenges. Phys. Chem.* **73**, 4–15 (1969).
  18. Liu, G., Li, Y. & Jonas, J. Confined geometry effects on reorientational dynamics of molecular liquids in porous silica glasses. *J. Chem. Phys.* **95**, 288 (1991).
  19. D’Agostino, C., Mitchell, J., Gladden, L. F. & Mantle, M. D. Hydrogen Bonding Network Disruption in Mesoporous Catalyst Supports Probed by PFG-NMR Diffusometry and NMR Relaxometry. *J. Phys. Chem. C* **116**, 8975–8982 (2012).

## 8. Optimization of a FFC-NMR pulse sequence with CPMG-acquisition for enhanced resolution through $T_2$ -encoding

### 8.1 Introduction

The previous chapters in this thesis have shown the suitability of NMR relaxometry, and in particular FFC-NMR as a tool to study surface-adsorbate interactions and competitive adsorption of liquid mixtures inside porous media. The  $\gamma$ -alumina and titania systems studied in chapters 4-6 show easily distinguishable  $T_1$  environments, that can be processed and modelled further to obtain insight into the chemistry of the systems. However, the  $T_1$ s cannot always be so easily separated.

Chapter 9 shows an FFC-NMR study on ethanol-water mixtures imbibed within silicas, the systems previously investigated by fixed field NMR relaxometry in chapter 7. For the Q6 and Q10 silicas, it is clear that the  $T_1$  environments of ethanol and water overlap for low ethanol mixture compositions. As a result, the NMRD profiles are very noisy and it is impossible to extract quantitative information about microphase separation, which is the goal of these experiments.

Unfortunately, the homogeneity of the magnetic field in FFC-NMR is very poor. Therefore we cannot add chemical resolution to the experiments. However, it is possible to add a  $T_2$  component by adding a CPMG echo-train in the acquisition part of the pulse sequence. Previously, this pulse sequence was used to provide “ $T_2$ -Encoded Acquisition of Relaxation Dispersion for Resolution of Pore Sizes” (TEARDROPS), separating out the NMRD profiles of water inside a range of different pore-size silicas<sup>1</sup>. To the best of our knowledge, this CPMG-FFC NMR pulse sequence has not yet been applied for the purpose of separating overlapping  $T_1$  environments by anyone other than the research group previously mentioned. Therefore it is crucial to implement the sequence in an appropriate manner.

While the pulse sequence is installed in the AcqNMR software and therefore relatively easy to access, there are many experimental parameters and hardware considerations which may cause artefacts or high errors in the  $T_1$  and  $T_2$  domains. This chapter highlights some of these

challenges and how to manage them, and validates the use of this sequence for the ethanol-water mixtures imbibed within silicas shown in the next chapter.

## 8.2 Background and literature review

The Carr-Purcell-Meiboom-Gill (CPMG) pulse sequence is a well-established method in NMR to refocus magnetization and measure  $T_2$ , the spin-spin relaxation time, see section 2.2.2<sup>2,3</sup>. Moreover, the one-shot CPMG echo-train can be easily connected to other pulse sequences to create correlation experiments, e.g.  $T_1$ - $T_2$  correlation experiments like the experiments in chapter 7<sup>4-13</sup>.

Another possible correlation experiment is a CPMG-FFC-NMR experiment<sup>14</sup>, for which the pulse sequence consists of a conventional pre-polarized or non-polarized FFC-NMR sequence with one-shot CPMG acquisition instead of FID acquisition. The pre-polarized CPMG-FFC-NMR pulse sequence is shown in Figure 8.1<sup>1,14</sup>. The non-polarized sequence is equivalent, except the polarization step is removed. The relaxation time,  $t_{rel}$ , and field,  $B_{rel}$ , are varied to obtain  $T_1$  decays at a range of Larmor frequencies, identically to the “standard” 1D FFC-NMR sequence.

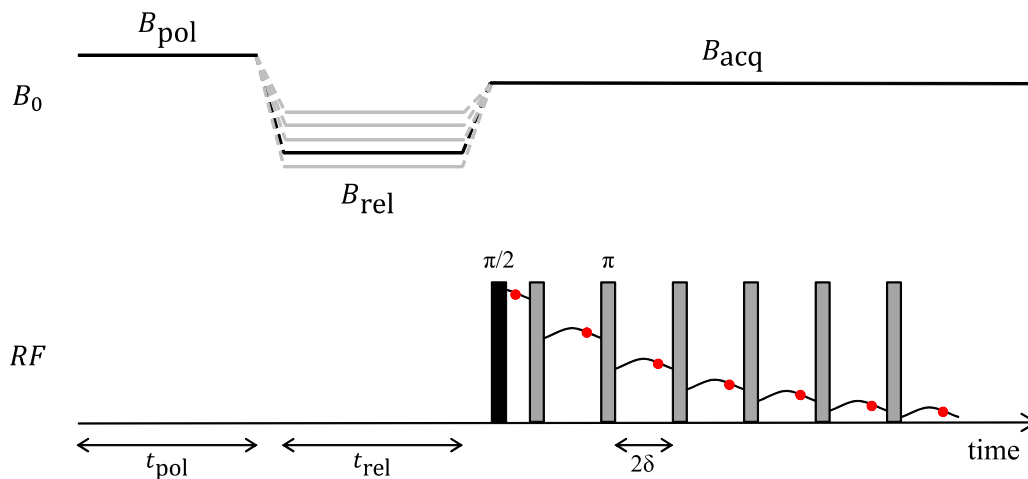


Figure 8.1: The pre-polarized CPMG-FFC-NMR pulse sequence.

From this experiment,  $T_1$ - $T_2$  correlation data can be obtained, where the  $T_1$  is measured at the relaxation Larmor frequency,  $B_{rel}$ , and the  $T_2$  is recorded at the acquisition frequency,  $B_{acq}$ .

### 8.2.1 Applications

CPMG-FFC-NMR has already been demonstrated to be a useful tool for several purposes. First, the sequence was used to provide field-cycling weighting to  $T_1$ - $T_2$  correlation experiments regarding foods and proteins<sup>15-17</sup>. Based on the  $T_1$  dispersion of a relaxation environment, peaks can be better separated and assigned. Secondly, the addition of the CPMG echo-train has been used for phase encoding and for refocusing pulse imperfections in FFC-MRI studies<sup>18,19</sup>.

Another application for CPMG acquisition is the increase in signal-to-noise ratio it can bring. The  $\pi$  pulses in CPMG trains refocus inhomogeneous spectral broadening and can therefore be used to significantly extend NMR signals compared to standard FID acquisition, especially in the case of inhomogeneous magnetic fields<sup>14,20</sup>. The increased sensitivity is often used in FFC-NMR studies in combination with dynamic nuclear polarization (DNP)<sup>21-24</sup>.

Finally, CPMG acquisition can be used to distinguish different relaxation environments in NMRD profiles<sup>1,14,24,25</sup>. The first practical demonstration of this resulted in the separation of water NMRD profiles in different pore-size silicas based on their  $T_2$  components, therefore the technique was called  $T_2$ -Encoded Acquisition of Relaxation Dispersion for Resolution of Pore Sizes (TEARDROPS)<sup>1</sup>.

CPMG and FFC-NMR have been shown to be a valuable combination with a range of applications, as shown above, and the CPMG-FFC-NMR pulse sequence is one of the default sequences in the AcqNMR software that controls Stellar FFC-NMR relaxometers. This means that the pulse sequence is easily accessible and ready to use, however it is important to understand the limitations of the sequence and the relaxometer in general and consequently optimize the experimental parameters.

### 8.2.2 Field noise effects

Some of the most important effects to take into account in implementing the CPMG-FFC-NMR sequence are field noise effects<sup>14,26,27</sup>. Fluctuations in the magnetic field strength and/or RF offset can cause artefacts in NMR signals. The contributions to field noise effects can be split into two parts.

First, fluctuations in the RF offset will affect the accuracy and efficiency of the pulses. For FID acquisition, there is only one ( $90^\circ$ ) pulse and therefore RF fluctuations will have a relatively small effect on the NMR signal<sup>26</sup>. However, for CPMG acquisition, several thousand  $180^\circ$

pulses are used in one scan, and therefore low RF fluctuations are crucial for reliable experiments<sup>27</sup>. As a result, it is necessary to manually optimize the RF offset before each experiment. Additionally, phase cycling should be used to refocus remaining inaccuracies in the 180° pulses.

Second, the homogeneity and stability of the electromagnetic field in FFC-NMR relaxometers can cause field drift related phase artefacts. When using FID acquisition, the magnitude NMR signal is generally used to obtain NMRD profiles, thereby avoiding phase artefacts. For CPMG-FFC-NMR however, the echo delay,  $\delta$ , must be optimized. When  $\delta$  is shorter than the magnetic field fluctuations, most field noise effects can be refocused. Previously reported values for  $\delta$  range between 50-100  $\mu\text{s}$ <sup>1,14</sup>.

Previously, a correlation between the magnet temperature and experimental errors was found<sup>1</sup>. This is because the magnetic field stability depends on the magnet temperature. For our system, the magnet is cooled via water that is stored on the roof of the lab building. As a result, the temperature of the cooling water and the magnet depends on the outdoor temperature and cannot be easily controlled. Therefore, it was impossible to do an extensive study on the effect of the magnet temperature on the results. However the maximum observed magnet temperature was 18.8°C, which is below the 19°C threshold set by Neudert.

### 8.3 Aims and objectives

The main aim of this chapter is simple: to optimize and validate the CPMG-FFC-NMR pulse sequence on our relaxometer, so that it can be used to quantitatively investigate the microphase separation of ethanol-water mixtures in silicas, following chapter 7. In order to optimize the sequence, the following experiments were carried out:

- Acquisition field fluctuations are measured for two different probes, a 10 mm probe and a 5 mm probe. The results can then be compared to the fluctuations measured by Neudert *et al.*<sup>1</sup> and the threshold set by Ferrante and Sykora<sup>14</sup>, to confirm that the relaxometer should be able to run CPMG-FFC-NMR experiments without large artefacts.
- Tuning and matching stability for the two different probes is compared. The tuning and matching capacitors of the 10 mm probe were damaged in unrelated experiments, and it is expected this will affect the accuracy of the CPMG-FFC-NMR experiments.

- The effect of the echo delay,  $\delta$ , on the NMR signal is investigated and an optimal value for  $\delta$  is set.
- The FFC-acquired  $T_2$  values for a range of manganese(II) chloride solutions are compared to the  $T_2$  values obtained on a permanent 23.8 MHz magnet. For an appropriate comparison, the acquisition field,  $B_{\text{acq}}$ , is changed to 23.8 MHz.
- Finally, once all  $T_2$  parameters are optimized, the  $T_1$  NMRD profiles using FID and CPMG-acquisition are compared.

## 8.4 Experimental

### 8.4.1 Materials

Manganese(II) chloride solutions (0.25 mM, 0.5 mM, 1 mM and 2 mM) were freshly prepared before each set of FFC-NMR experiments. The 0.5 mM and 2 mM solutions are generally used as a reference for NMRD profiles due to their high  $R_1$  dispersion. The addition of 0.25 mM and 1 mM solutions allowed for a  $R_1$  range between approximately 3–120 s<sup>-1</sup>, which spans the relaxation rates measured for ethanol-water mixtures imbibed within silicas shown in chapter 9.

### 8.4.2 FFC-NMR experimental parameters

FFC-NMR experiments with FID acquisition were recorded as outlined in section 4.2.2. First, a 10 mm probe was used, which was the same probe as in chapters 4–6. For this probe, the transmitter attenuation was set to 12 and the 90° pulse was 8  $\mu$ s. Additionally, a 5 mm probe was used to compare field fluctuations. For this probe, the transmitter attenuation was set to 18 and the 90° pulse length was 3  $\mu$ s. Following the phase cycle, four scans were recorded at each point.

For the CPMG-FFC-NMR experiments, the PPCPMG/s pulse sequence was used, see Figure 8.1. The duration of the 180° pulse was defined as twice the duration of the 90° pulse. The CPMG data points were recorded at 3/4 echo time, i.e.  $3/2\delta$  after a  $\pi$  pulse, which allowed for shorter echo times without pulse transients causing artefacts in the signal<sup>1</sup>.

As discussed in section 8.2.2, it is important to (manually) optimize the frequency offset before an experiment to make sure the magnetic field does not drift too far and the RF pulses remain

efficient<sup>14</sup>. Because the offset was optimized, the real signal was processed instead of the magnitude signal, as is the usual method for FID-FFC-NMR processing.

Due to memory restrictions, no more than 64k data points could be recorded in one  $T_1$  experiment. As a result, the maximum number of echoes was 4096 when 16  $T_1$  delays were used, and 2048 echoes for 32  $T_1$  delays.

FID-FFC-NMR data and CPMG-FFC-NMR  $T_1$  data were processed as outlined in section 4.2.2, and fitted to a monoexponential decay to obtain  $T_1$  values. For the CPMG-FFC-NMR  $T_2$  data, the CPMG decays for  $t_{\text{rel}} = 1$  ms were fitted to a monoexponential or biexponential fit to obtain  $T_2$  values.

#### 8.4.3 NMR relaxation experiments on a permanent 23 MHz magnet

CPMG-NMR experiments were performed on a Magritek Tomograph with a hydrogen Larmor frequency of 23.8 MHz. The pulse length was set to 25  $\mu\text{s}$ , the power level was adjusted to optimize the  $90^\circ$  and  $180^\circ$  pulses. 16 scans and 128 echoes were recorded with echo delays ranging between 1 ms for the 2 mM solution and 4 ms for the 0.25 mM solution.

## 8.5 Results and discussion

### 8.5.1 Acquisition field fluctuations

First, the variations in the acquisition frequency were measured according to the method by Neudert *et al.* to allow for an appropriate comparison. Using a standard pre-polarized FFC-NMR pulse sequence without relaxation interval, 64 single-scan FIDs were recorded 0.8 ms after the  $90^\circ$  pulse, and 64 FIDs were recorded 3.3 ms after the  $90^\circ$  pulse to test for later fluctuations. Like in the Neudert paper, no systematic differences between the sets of FIDs were found.

The FIDs were processed using a moving Fourier Transform with a Hamming window and 16-fold zerofilling, after which the frequency relative to the acquisition frequency,  $B_{\text{acq}} = 16.3$  MHz, could be calculated. Table 8.1 shows the scatter in the average frequency, the maximum variation in frequency over the course of the FID, and the overall range of frequencies that was detected.

Table 8.1: Acquisition field fluctuations. Data for comparison extracted from Neudert et al.<sup>1</sup>

Variation ( $\mu\text{T}$ / ppm / kHz)	10 mm probe	5 mm probe (16.3 MHz)	5 mm probe (23.8 MHz)	Neudert <sup>1</sup>
Average frequency	63 / 165 / 2.7	58 / 150 / 2.5	68 / 179 / 2.9	70 / 183 / 3.0
Variation over time	102 / 267 / 4.4	29 / 77 / 1.3	38 / 100 / 1.6	40 / 105 / 1.7
Overall range	139 / 364 / 5.9	76 / 199 / 3.3	82 / 215 / 3.5	120 / 313 / 5.1

The acquisition field fluctuations for the experiments where the 5 mm probe was used, both at 16.3 and 23.8 MHz, are relatively small, compared to the fluctuations observed by Neudert. The highest fluctuations recorded using this probe are 3.5 kHz, this corresponds to a fluctuation time of  $\sim 285 \mu\text{s}$ , which means the fluctuations should be easily refocused by the  $\pi$  pulses in the CPMG sequence.

Field fluctuations up to  $\sim 5$  kHz are expected to be acceptable, however the variations for the 10 mm probe reach up to 5.9 kHz<sup>14</sup>. As a result, the CPMG sequence may not be able to refocus phase errors, which can lead to inaccurate NMR signal decays. The  $T_2$  value will then be underestimated, and this will propagate to a systematic error in the  $T_1$  domain.

On the other hand, fluctuations with a frequency of 5.9 kHz correspond to a fluctuation time of  $\sim 170 \mu\text{s}$ . Echo delays that are suggested in the literature are in the range of 50–100  $\mu\text{s}$ <sup>14</sup>, which is significantly shorter than the fluctuation time of  $\sim 170 \mu\text{s}$ . Therefore, the  $\pi$  pulses may still be able to refocus the acquisition field fluctuations for experiments using the 10 mm probe, especially when relatively short echo delays are applied.

### 8.5.2 Tuning and matching stability

During experiments unrelated to this study, the tuning and matching capacitors of the 10 mm probe were damaged. Because it was still possible to obtain a signal stable enough for FID acquisition, and because the 10 mm probe was the only suitable probe for other experiments, the probe was not repaired while the current study was carried out. For CPMG acquisition, however, higher tuning and matching stability is necessary, as the acquisition time is three orders of magnitude longer ( $\sim 0.25$  s for the following experiments) compared to standard FID acquisition ( $\sim 120 \mu\text{s}$ ). Moreover, the tuning and matching stability appeared to deteriorate over time.

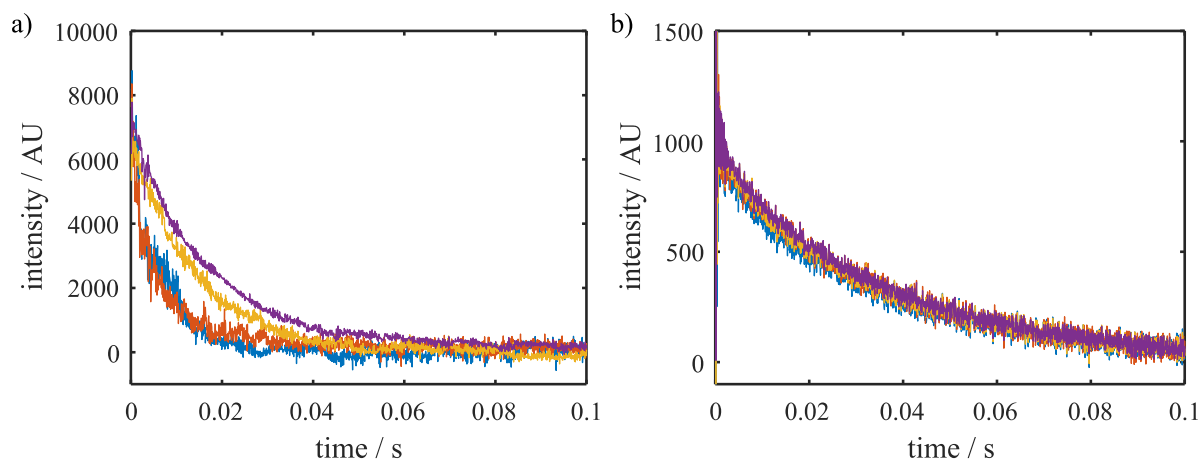


Figure 8.2: CPMG decays of a 2 mM manganese(II) chloride solution, measured using the a) 10 mm probe, and b) 5 mm probe. For both probes, 4 scans were recorded under identical conditions.

Figure 8.2 shows the effect of poor tuning and matching stability in the 10 mm probe. Four CPMG decays were recorded for a 2 mM manganese(II) chloride solution, under identical conditions. For these experiments, the echo delay was  $\delta = 60 \mu\text{s}$ , on the short side of the recommended 50–100  $\mu\text{s}$  range, to maximize the chances of effective refocusing of field instabilities.

It is expected, for a stable probe, that the four scans give identical NMR signals. This is the case for the 5 mm probe, as is shown in Figure 8.2b, but the CPMG traces for the 10 mm probe, see Figure 8.2a, vary significantly, indicating the increased field noise effects due to poor tuning and matching stability. Moreover, even the most stable NMR signal for the 10 mm probe, coloured purple in Figure 8.2, decays faster than the 5 mm probe signals, showing that the signal obtained on the 10 mm probe is highly unreliable.

For the remainder of this chapter, and chapter 9, only the 5 mm probe was used. Once the tuning and matching capacitors on the 10 mm probe are repaired, the experiments in this chapter should be repeated to check whether the CPMG-FFC-NMR sequence is accurate enough using this probe.

### 8.5.3 The effect of the echo delay

As was explained in section 8.2.2, the  $\pi$  pulses in the CPMG acquisition can refocus field instabilities, under the condition that the timescale of the field fluctuations is significantly longer than that of the echo delay. Neudert *et al.* determined a maximum echo delay of  $\delta = 72 \mu\text{s}$  for their system<sup>1</sup>, and generally the recommended range for the echo delay is 50–100  $\mu\text{s}$ <sup>14</sup>.

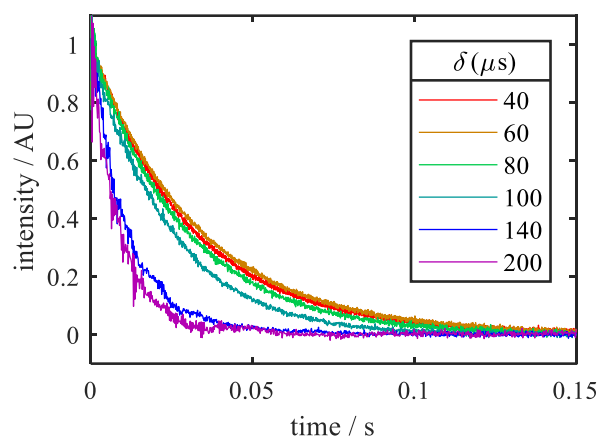


Figure 8.3: CPMG decays of a 1 mM manganese(II) chloride solution, measured using varying echo delays, at an acquisition frequency  $B_{acq} = 16.3$  MHz.

As can be seen in Figure 8.3, the CPMG trains for echo delays  $> 100$   $\mu\text{s}$  decay considerably faster than when shorter echo delays are used. Even the signal for  $\delta = 100$   $\mu\text{s}$  already shows a somewhat faster decay compared to the shorter echo delays. As is expected from the literature, the field fluctuations cannot be effectively refocused, resulting in dephasing of the magnetization and therefore faster decaying NMR signal.

The differences between  $\delta = 40$  and  $60$   $\mu\text{s}$  appear to be negligible, indicating that field noise effects do not significantly affect the NMR signal using these echo delays. Considering the limited number of echoes that can be recorded in one measurement, a longer echo delay means that longer  $T_2$  values can be measured accurately. Therefore for the remaining experiments in this chapter, and for the experiments in chapter 9, the echo delay was set to  $\delta = 60$   $\mu\text{s}$ .

#### 8.5.4 Comparison of $T_2$ with a permanent magnet

Once the echo delay was optimized, the accuracy of the  $T_2$  component was tested against a permanent magnet with a Larmor frequency of 23.8 MHz. Therefore, the acquisition frequency of the FFC-NMR experiments was adjusted to be 23.8 MHz. Considering the substantial effect that field noise effects can have on the CPMG decays, the echo delay was reoptimized, see Figure 8.4.

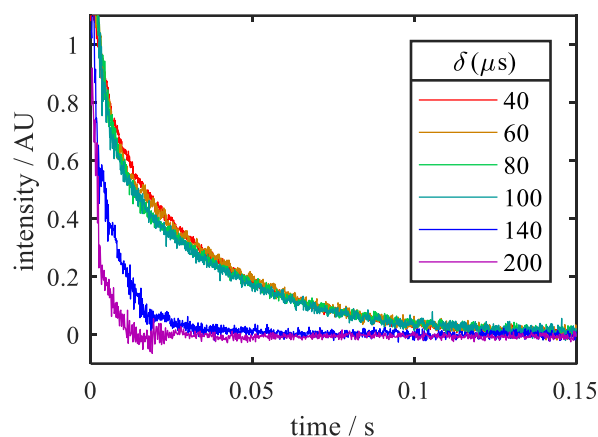


Figure 8.4: CPMG decays of a 1 mM manganese(II) chloride solution, measured using varying echo delays, at an acquisition frequency  $B_{acq} = 23.8$  MHz.

It is clear that echo delays  $> 100$   $\mu\text{s}$  are still subject to significant field noise effects, however the NMR traces for echo delays up to 100  $\mu\text{s}$  overlap very well, indicating the field instabilities can be appropriately refocused. The echo delay was set to  $\delta = 60$   $\mu\text{s}$  to be consistent with the CPMG-FFC-NMR experiments shown in section 8.5.2.

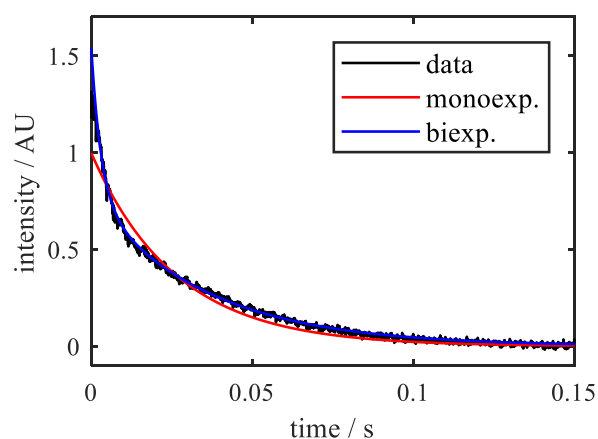


Figure 8.5: The CPMG decay for  $\delta = 30$   $\mu\text{s}$ , see Figure 8.4, and the corresponding monoexponential and biexponential fits.

Interestingly, the CPMG decays at 23.8 MHz do not appear monoexponential, see Figure 8.5. Therefore, two  $T_2$  components were fitted to the data. The biexponential fit matches the data very well, however only one  $T_2$  component is expected for a doped water sample. The data from the permanent 23.8 MHz magnet clearly shows one  $T_2$  component, see Figure 8.6, and therefore confirms the second  $T_2$  component in the FFC-NMR data is an artefact.

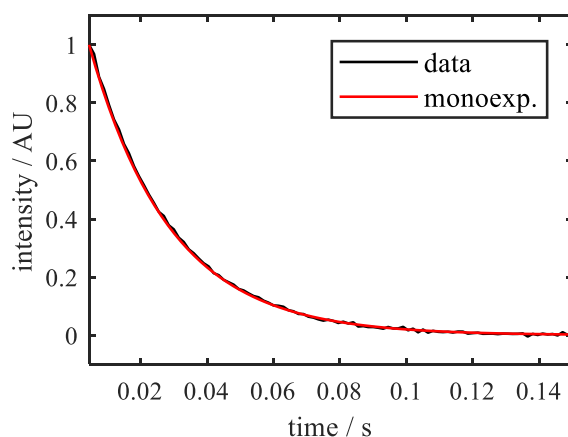


Figure 8.6: The CPMG decay of a 1 mM manganese(II) chloride solution, measured using a permanent 23.8 MHz magnet, and its corresponding monoexponential fit.

In order to try to explain the second  $T_2$  component, the  $T_2$  values for the permanent magnet and for the FFC-NMR fits are compared. The results are shown in Figure 8.7.

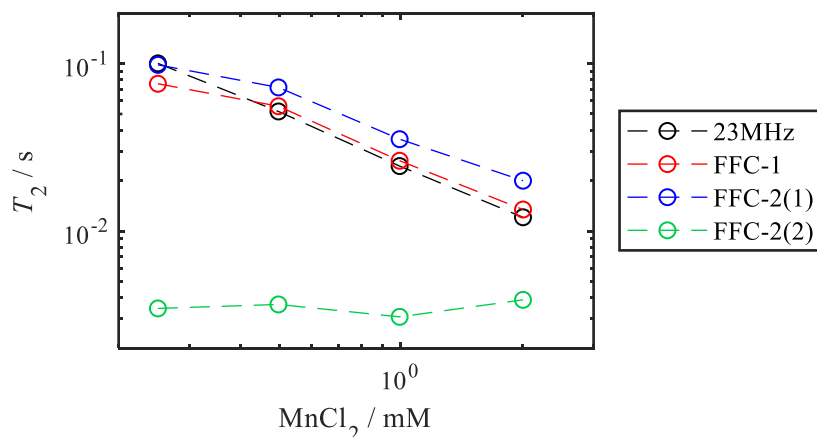


Figure 8.7: Observed  $T_2$  relaxation times plotted against the manganese(II) chloride concentration, extracted from the permanent magnet (23 MHz), a monoexponential fit to the FFC-NMR data (FFC-1), and a biexponential fit to the FFC-NMR data (FFC-2(1) and FFC-2(2)).

The  $T_2$  values extracted from the data acquired on the permanent magnet appear to follow a power law trend with the dopant concentration, where the  $T_2$  value decreases as the concentration increases. As the dopant is expected to dominate the relaxation mechanism, this trend follows our expectation.

The monoexponential FFC-NMR fit (FFC-1) appears to coincide with the 23 MHz magnet  $T_2$  values, especially for the solutions  $\geq 0.5$  mM, indicating again that the biexponential properties of the FFC-NMR results are artefacts rather than true  $T_2$  values.

For the biexponential fits, the primary component (FFC-2(1)) overestimates the  $T_2$  value consistently by approximately 50%. The secondary component (FFC-2(2)) on the other hand

appears to be independent on the concentration, with a value of  $T_2 \sim 3.5$  ms. It is expected the second component is an artefact caused by field instabilities.

At an acquisition frequency  $B_{\text{acq}} = 16.3$  MHz, the data was very well described by a monoexponential fit. The main difference between the experiments 16.3 MHz and 23.8 MHz is that 23.8 MHz is at the edge of the tuning range of the FFC-NMR relaxometer. As a result, it is likely that the tuning and matching stability is slightly poorer at 23.8 MHz compared to 16.3 MHz, which is the frequency the machine is optimized to work at.

Because the data at 16.3 MHz appears monoexponential, there is good overlap between the data from the permanent 23 MHz magnet and the monoexponential fit to the FFC-NMR data at 23.8 MHz, and because it is expected that the relaxometer operates more accurately at 16.3 MHz than at 23.8 MHz, the  $T_2$  measurements are expected to be more accurate at 16.3 MHz than at 23.8 MHz.

#### 8.5.5 $T_2$ NMRD profiles analysis

Finally, the  $T_2$  components were determined for experiments across the  $T_1$  Larmor frequency range. The  $T_2$  value should only depend on the acquisition frequency, and therefore remain constant as the  $T_1$  relaxation frequency is varied. The  $T_2$  NMRD profiles are shown in Figure 8.8.

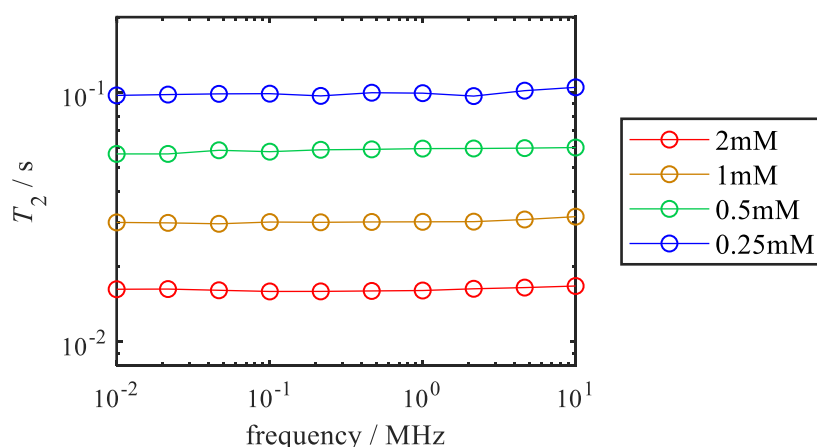


Figure 8.8:  $T_2$  values for a range of manganese(II) chloride solutions, plotted against the  $T_1$  relaxation frequency

Upon visual inspection, it is clear that the  $T_2$  value indeed is independent on the relaxation frequency. The highest standard deviation for the  $T_2$  values is 2.4%, which is significantly lower than the error up to 10% that is expected for the experiments in chapter 9 due to pore

inhomogeneities. It can therefore be concluded that the  $T_2$  component of the CPMG-FFC-NMR experiment is accurate enough to separate relaxation environments in porous media.

### 8.5.6 $T_1$ NMRD profiles analysis

Now that the CPMG aspect of the CPMG-FFC-NMR pulse sequence has been validated, the  $T_1$  NMRD profiles using the CPMG sequence and the 1D FID sequence are compared. The  $^1\text{H}$  NMRD profiles of a range of manganese(II) chloride solutions is shown in Figure 8.9.

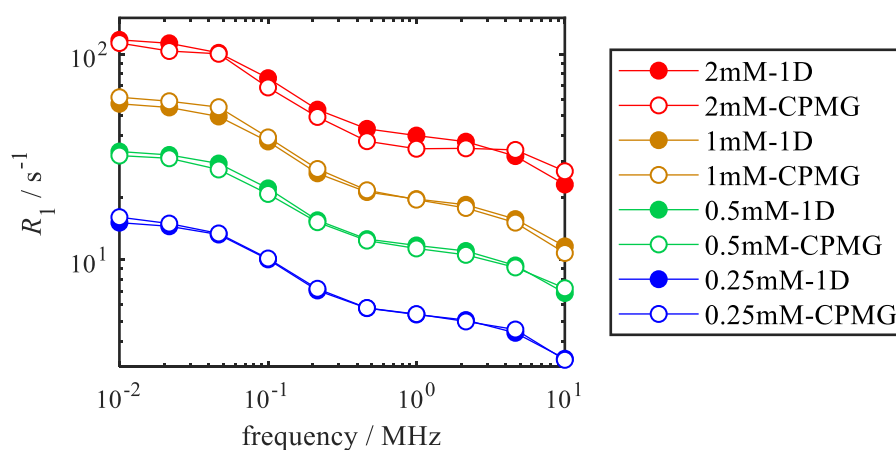


Figure 8.9:  $^1\text{H}$  NMRD profiles of a range of manganese(II) chloride solutions, using the 1D FID pulse sequence (filled symbols) and the CPMG-FFC-NMR pulse sequence (open symbols).

All experiments were performed twice, using freshly made  $\text{MnCl}_2$  solutions, and the resulting error bars are too small to see by eye.

In general, the CPMG-acquired NMRD profiles correspond reasonably well with the 1D FID profiles. The highest errors can be seen in the 2 mM  $\text{MnCl}_2$  solution. In order to further analyse the accuracy of the experiment, the errors were quantified and plotted, see Figure 8.10.

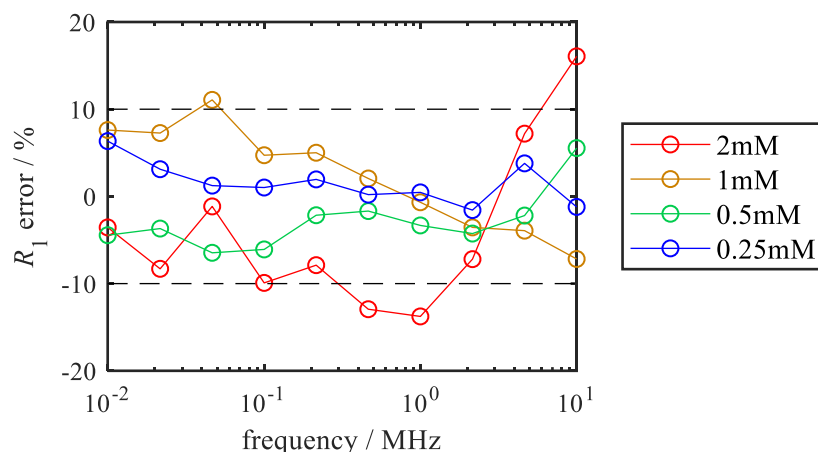


Figure 8.10: The error, defined as the relative difference between the CPMG and FID-acquired  $R_1$  value, for each of the  $^1\text{H}$  NMRD profiles shown in Figure 8.9.

In this analysis, it is assumed that errors up to 10% are acceptable, because the aim of the CPMG-FFC-NMR sequence is to separate NMRD profiles of liquid mixtures imbibed within porous media. In these materials, pore inhomogeneities are expected to induce similar errors in the relaxation rate.

Unfortunately, there are several data points where the error exceeds the imposed 10% threshold. All but one of these data points are in the 2 mM  $\text{MnCl}_2$  solution data. For this solution, the  $T_2$  value is approximately 12 ms, which means that after just 460 data points, the signal intensity is only 10%. As a result, the signal-to-noise ratio is lower than for the other solutions. However, considering the error does not often exceed the 10% threshold, it is concluded that in general the accuracy of the  $T_1$  NMRD profiles is adequate for porous media studies.

## 8.6 Conclusions and outlook

In previous chapters, FFC-NMR has been shown to provide quantitative information about the microphase separation of liquid mixtures imbibed within porous media. However, the  $T_1$  relaxation environments of the liquid mixtures cannot always be easily distinguished, as was the case in chapters 4–6.

In order to separate relaxation environments, a  $T_2$  component can be added by means of CPMG acquisition. This CPMG-FFC-NMR pulse sequence has previously been applied to FFC-encoded  $T_1 - T_2$  correlation experiments, FFC-MRI experiments, DNP-FFC-NMR experiments and to obtain “ $T_2$ -Encoded Acquisition of Relaxation Dispersion for Resolution of Pore Sizes” (TEARDROPS).

Following the large range of applications of the CPMG-FFC-NMR pulse sequence, it has been installed as a default sequence on Stellar FFC-NMR relaxometers. However, the pulse sequence comes with technical challenges that must be dealt with and optimized, namely field noise effects.

First, the acquisition field fluctuations for two different probes were measured. The maximum measured field noise for the 10 mm probe was 5.9 kHz, which is higher than the fluctuations measured by Neudert *et al.*<sup>1</sup>, and the threshold set by Ferrante and Sykora<sup>14</sup>. As a result, it is not certain that this probe is able to perform the CPMG-FFC-NMR experiment accurately. The measured field fluctuations for the 5 mm probe, however, were significantly lower than the reference values, and therefore it is expected that this probe can obtain reliable CPMG-FFC-NMR data.

Unfortunately, the 10 mm probe was damaged in experiments unrelated to this study. As a result, the tuning and matching stability was shown to be impaired and no reliable CPMG decays could be measured anymore. Once the probe has been repaired, the experiments in this chapter should be repeated to confirm its suitability to run CPMG-FFC-NMR experiments.

For the 5 mm probe, the effect of the echo delay,  $\delta$ , on the NMR signal was investigated. Echo delays  $\geq 100 \mu\text{s}$  showed rapid  $T_2$  decays, indicating the field noise effects could not be effectively refocused. The echo delay for further experiments was set to  $\delta = 60 \mu\text{s}$ .

After optimization, the  $T_2$  component was compared to the  $T_2$  values measured on a permanent 23.8 MHz magnet. CPMG-FFC-NMR experiments at  $B_{\text{acq}} = 23.8 \text{ MHz}$  unexpectedly showed

two relaxation environments. It is likely that this artefact is caused by poor tuning stability, as 23.8 MHz is at the edge of the tuning range of the FFC-NMR relaxometer. However, the  $T_2$  values for the FFC-NMR experiments were consistent with the values measured on the permanent magnet, and other CPMG-FFC-NMR experiments are performed at  $B_{\text{acq}} = 16.3$  MHz, where the tuning stability is better. Therefore it was concluded that the  $T_2$  component of the CPMG-FFC-NMR experiment is accurate enough.

Finally, the  $T_1$  NMRD profiles using FID and CPMG-acquisition were compared. In general the overlap was very good, however the 2 mM manganese(II) chloride solution showed a few data points with errors  $>10\%$ . This is likely due to the short  $T_2$  value for this solution. For samples with sufficiently long  $T_2$  components, it is concluded that the CPMG-FFC-NMR pulse sequence can accurately obtain  $T_1$  NMRD profiles.

In summary, this chapter contains a highly detailed description of the implementation of a relatively new and unexplored pulse sequence to separate different chemical environments based on their  $T_2$  components. The optimized CPMG-FFC-NMR pulse sequence will be applied in the following chapter, where the  $T_1$  relaxation environments of certain water-ethanol mixtures imbibed within porous silicas cannot be separated. Aside from these experiments, the CPMG-FFC-NMR sequence can now be used, provided the optimized parameters are used.

## References

1. Neudert, O., Mattea, C. & Stapf, S. Application of CPMG acquisition in Fast-Field-Cycling relaxometry. *Microporous Mesoporous Mater.* **269**, 103–108 (2018).
2. Carr, H. Y. & Purcell, E. M. Effects of Diffusion on Free Precession in Nuclear Magnetic Resonance Experiments. *Phys. Rev.* **94**, 630 (1954).
3. Meiboom, S. & Gill, D. Modified Spin-Echo Method for Measuring Nuclear Relaxation Times. *Rev. Sci. Instrum.* **29**, 688 (1958).
4. Peemoeller, H., Shenoy, R. K. & Pintar, M. M. Two-dimensional nmr time evolution correlation spectroscopy in wet lysozyme. *J. Magn. Reson.* **45**, 193–204 (1981).
5. Song, Y.-Q., Venkataramanan, L., Hürlimann, M. D., Flaum, M., Frulla, P., Straley, C.  $T_1$ – $T_2$  Correlation Spectra Obtained Using a Fast Two-Dimensional Laplace Inversion. *J. Magn. Reson.* **154**, 261–268 (2002).
6. McDonald, P. J., Korb, J.-P., Mitchell, J. & Monteilhet, L. Surface relaxation and chemical exchange in hydrating cement pastes: A two-dimensional NMR relaxation study. *Phys. Rev. E* **72**, 011409 (2005).
7. Weber, D., Mitchell, J., McGregor, J. & Gladden, L. F. Comparing Strengths of Surface Interactions for Reactants and Solvents in Porous Catalysts Using Two-Dimensional NMR Relaxation Correlations. *J. Phys. Chem.* **113**, 6610–6615 (2009).
8. Gladden, L. F. & Mitchell, J. Measuring adsorption, diffusion and flow in chemical engineering: applications of magnetic resonance to porous media. *New J. Phys.* **13**, 35001 (2011).
9. D’Agostino, C., Brett, G. L., Miedziak, P. J., Knight, D. W., Hutchings, G. J., Gladden, L. F. & Mantle, M. D. Understanding the Solvent Effect on the Catalytic Oxidation of 1,4-Butanediol in Methanol over Au/TiO<sub>2</sub> Catalyst: NMR Diffusion and Relaxation Studies. *Chem. - A Eur. J.* **18**, 14426–14433 (2012).
10. D’Agostino, C., Kotionova, T., Mitchell, J., Miedziak, P. J., Knight, D. W., Taylor, S. H., Hutchings, G. J., Gladden, L. F. & Mantle, M. D. Solvent Effect and Reactivity Trend in the Aerobic Oxidation of 1,3-Propanediols over Gold Supported on Titania: NMR Diffusion and Relaxation Studies. *Chem. - A Eur. J.* **19**, 11725–11732 (2013).

11. D'Agostino, C., Mitchell, J., Mantle, M. D. & Gladden, L. F. Interpretation of NMR Relaxation as a Tool for Characterising the Adsorption Strength of Liquids inside Porous Materials. *Chem. - A Eur. J.* **20**, 13009–13015 (2014).
12. D'Agostino, C., Feaviour, M. R., Brett, G. L., Mitchell, J., York, A. P. E., Hutchings, G. J., Mantle, M. D. & Gladden, L. F. Solvent inhibition in the liquid-phase catalytic oxidation of 1,4-butanediol: understanding the catalyst behaviour from NMR relaxation time measurements. *Catal. Sci. Technol.* **6**, 7896–7901 (2016).
13. D'Agostino, C., Brett, G., Divitini, G., Ducati, C., Hutchings, G. J., Mantle, M. D. & Gladden, L. F. Increased Affinity of Small Gold Particles for Glycerol Oxidation over Au/TiO<sub>2</sub> Probed by NMR Relaxation Methods. *ACS Catal.* **7**, 4235–4241 (2017).
14. Ferrante, G. & Sykora, S. Technical Aspects of Fast Field Cycling. *Adv. Inorg. Chem.* **57**, 405–470 (2005).
15. Hills, B., Benamira, S., N. Marigheto & Wright, K. T<sub>1</sub>-T<sub>2</sub> correlation analysis of complex foods. *Appl. Magn. Reson.* **26**, 543–560 (2004).
16. Marigheto, N., Venturi, L., Hibberd, D., Wright, K. M., Ferrante, G. & Hills, B. P. Methods for peak assignment in low-resolution multidimensional NMR cross-correlation relaxometry. *J. Magn. Reson.* **187**, 327–342 (2007).
17. Venturi, L., Woodward, N., Hibberd, D., Marigheto, N., Gravelle, A., Ferrante, G. & Hills, B. P. Applied Magnetic Resonance Multidimensional Cross-Correlation Relaxometry of Aqueous Protein Systems. *Appl. Magn. Reson* **33**, 213–234 (2008).
18. Matter, N. I., Scott, G. C., Grafendorfer, T., MacOvski, A. & Conolly, S. M. Rapid polarizing field cycling in magnetic resonance imaging. *IEEE Trans. Med. Imaging* **25**, 84–93 (2006).
19. Broche, L. M., James Ross, P., Pine, K. J. & Lurie, D. J. Rapid multi-field T<sub>1</sub> estimation algorithm for Fast Field-Cycling MRI. *J. Magn. Reson.* **238**, 44–51 (2014).
20. Hürlimann, M. D. Diffusion and Relaxation Effects in General Stray Field NMR Experiments. doi:10.1006/jmre.2000.2263
21. Überrück, T., Neudert, O., Kreuer, K.-D., Granwehr, J., Stapf, S. & Han, S. Effect of nitroxide spin probes on the transport properties of Nafion membranes. *Phys. Chem.*

- Chem. Phys.* **20**, 26660–26674 (2018).
22. Gizatullin, B., Mattea, C. & Stapf, S. X-nuclei hyperpolarization for studying molecular dynamics by DNP-FFC. (2019). doi:10.1016/j.jmr.2019.106583
  23. Gizatullin, B., Mattea, C. & Stapf, S. Molecular Dynamics in Ionic Liquid/Radical Systems. *J. Phys. Chem. B* **125**, 4862 (2021).
  24. Gizatullin, B., Mattea, C. & Stapf, S. Field-cycling NMR and DNP – A friendship with benefits. *J. Magn. Reson.* **322**, 106851 (2021).
  25. Steele, R. M., Korb, J.-P., Ferrante, G. & Bubici, S. New applications and perspectives of fast field cycling NMR relaxometry. *Magn. Reson. Chem.* **54**, 502–509 (2016).
  26. Sykora, S. Field noise effects on NMR signals: FID's and 1D spectra. *Stan's Library* (2006). doi:10.3247/SL1Nmr06.002
  27. Sykora, S. Field noise effects on NMR signals: Hahn echoes and CPMG. *Stan's Library* (2006). doi:10.3247/SL1Nmr06.003



## 9. Competitive adsorption of ethanol-water mixtures imbibed within mesoporous silicas. Part II: correlation times through FFC-NMR relaxometry

### 9.1 Introduction

Chapter 7 showed an investigation of the microphase separation of ethanol-water mixtures imbibed within a range of different pore size silicas with varying surface chemistries.  $T_1 - T_2$  correlation experiments were performed across the full ethanol-water composition range. While not much information about competitive adsorption was found in the ethanol component, the  $T_1/T_2$  ratios of the water component showed clear trends. For the large pore silicas with a high surface hydroxyl density (Q15, Q30), the normalized water  $T_1/T_2$  ratio increased with ethanol mol%, suggesting a phase-separated system with a water-rich surface layer and ethanol residing in the centre of the pore. For the smaller pore silicas with low surface hydroxyl densities (Q6, Q10), the trend was opposite: the normalized water  $T_1/T_2$  ratio decreased with ethanol mol%, indicating an ethanol-rich surface layer and water in the centre of the pore.

In this chapter, the goal is to obtain quantitative information about the microphase separation and the dynamics of these systems in the form of correlation times. Correlation times can be extracted from  $^1\text{H}$  NMRD profiles, as was previously shown in chapters 5 and 6. However, as will be shown in section 9.3.1, the NMRD profiles for the water and ethanol components in the smaller pore silicas (Q6, Q10) cannot be distinguished, because the  $T_1$  values of the components are too similar.

Therefore, we will apply the FFC-NMR pulse sequence with CPMG acquisition that was optimized in chapter 8. This pulse sequence can be used to distinguish NMRD profiles based on  $T_2$  values, as was previously demonstrated for water imbibed within different pore size silicas<sup>1,2</sup>. However, because the acquisition period for CPMG acquisition is significantly longer than for FID acquisition, it was necessary to characterize the acquisition field fluctuations and confirm that field noise effects are not affecting the accuracy of the FFC-NMR experiments<sup>3-5</sup>. After the CPMG-FFC-NMR pulse sequence was optimized, it can now be used to separate the water and ethanol NMRD profiles shown in section 9.3.1.

Finally, the NMRD profiles of the water component will be modelled to obtain correlation times. In this study, the approach by Chemmi will be used, because this modelling method has been applied to similar water in silica systems before and provided clear quantitative information<sup>6</sup>. In this approach, the NMRD profiles are fitted to two simple spectral densities, from which a fast and a slow correlation time can be extracted.

## 9.2 Experimental

The materials and sample preparation methods in this chapter are identical to those used in chapter 7, see section 7.2.1. Experiments were performed on the as-received silicas only. FID-FFC-NMR experiments were performed as outlined in section 4.2.2, variable temperature FFC-NMR experiments were performed as outlined in chapter 5.2.2.1, and CPMG-FFC-NMR experiments were performed following the optimization procedures in chapter 8. The CPMG-FFC-NMR experiments were performed under identical conditions to the FID-FFC-NMR experiments to avoid discrepancies between the sets of experiments.

For the FID-FFC-NMR experiments,  $T_1$  curves were processed using a monoexponential fit for pure water samples, and using a biexponential fit for ethanol and ethanol-water mixtures. For CPMG-FFC-NMR experiments, the pure water samples were processed using the same method, however the ethanol and ethanol-water mixtures were analysed following a different approach:

1. First,  $T_2$  values were extracted through a biexponential fit to the CPMG decays. Importantly, only the CPMG decays for  $t_{\text{rel}} = 1$  ms were used in order to avoid  $T_1$  weighting effects. This procedure was done for all frequency points, and the results were averaged to obtain reliable  $T_2$  values.
2. Each CPMG decay within the  $T_1$  curves was fitted to a biexponential function with fixed  $T_2$  values, extracted in step 1, which provided populations for each of the  $T_2$  components. The populations depend on the mixture composition as well as the  $T_1$  relaxation time of each of the components.
3. Based on the  $T_2$  values and populations, two  $T_1$  curves were constructed that could be separately fitted to a monoexponential fit, resulting in two reliable  $T_1$  values.

## 9.3 Results and discussion

### 9.3.1 FID-FFC-NMR experiments

#### 9.3.1.1 Pure liquids

The  $^1\text{H}$  NMRD profiles of pure water and of the ethyl component for pure ethanol imbibed within the silica supports are shown in Figure 9.1.

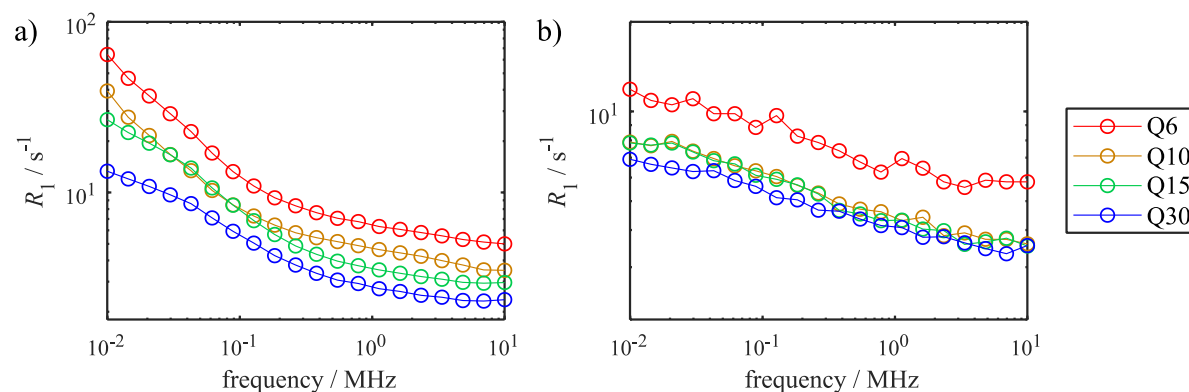


Figure 9.1:  $^1\text{H}$  NMRD profiles for pure (a) water, and (b) ethanol, imbibed within a range of silicas.

For water, the relaxation rate towards the high frequency end appears to scale with the pore size; smaller pores result in higher relaxation rate. This observation corresponds to the high field NMR relaxometry results on the same systems reported by Robertson<sup>7</sup>. There are two explanations for the increase of  $R_1$  with decreasing pore size. Firstly, it can be explained by the two-phase fast exchange model. In smaller pores, the surface-to-volume ratio is higher than for larger pores. The surface relaxation rate is higher than the bulk relaxation rate, and therefore the observed relaxation rate is higher for smaller pores. Alternatively, the confinement upon decreasing the pore size restricts the motion of the water and thereby increases  $R_1$ .

Toward the low frequency end, the NMRD profiles show interesting differences. The relaxation rate appears to plateau for the Q15 and Q30 profiles, but not for the Q6 and Q10 profiles. It is likely that this big distinction is due to the difference in surface hydroxyl densities between the Q6/Q10 and Q15/Q30 silicas. A difference in surface hydroxyl density leads to a difference in the surface-adsorbate dynamics, and therefore shows different NMRD profiles.

In section 7.3.2, it was shown that the high surface hydroxyl density silicas (Q15, Q30 and the rehydroxylated Q6 and Q10) displayed lower  $T_1/T_2$  ratios than the low surface hydroxyl density silicas (as-received Q6 and Q10). The plateau in the NMRD profiles is indicating the

same effect. As will be shown in more detail in section 9.4, the surface-adsorbate interaction strength correlates with the plateau; a stronger interaction is described by a higher plateau at lower frequencies. In Figure 9.1a, qualitatively, it is clear that the plateaus for Q15 and Q30 are lower and at higher frequencies than for Q6 and Q10 silica, for which the relaxation rates do not reach a plateau within the current frequency range.

For ethanol, the slopes of the NMRD profiles are identical and shallow, indicating the ethyl group only weakly interacts with the surface. This is consistent with the results from section 7.3.2, where the  $T_1/T_2$  ratio of the ethanol component stayed approximately constant across the composition range, for all silica supports. The increase in the absolute relaxation rates for Q6 silica is again explained by the two-phase fast exchange model; as the pore size decreases, the surface-to-volume ratio and therefore the relaxation rate increases. The difference between Q10, Q15 and Q30 silica is small due to the weak nature of the surface-ethyl interactions. Because the ethyl profiles are not very sensitive to surface interactions, we will focus only on the water profiles for the remainder of this chapter.

#### 9.3.1.2 Mixtures

The  $^1\text{H}$  NMRD profiles of the water component in ethanol-water mixtures imbibed within the silica supports, measured using the FID-FFC-NMR pulse sequence, are shown in Figure 9.2. It is clear that for all silicas, the water relaxation rates increase as the water content decreases. This corresponds to the  $T_1$  and  $T_2$  values at 43 MHz decreasing with ethanol mol%, as was shown in chapter 7. However, for the fixed field experiments it was important to analyse the  $T_1/T_2$  ratio instead of the separate  $T_1$  and  $T_2$  components, to avoid mixing effects. For the FFC-NMR results, it is also important to take mixing effects into account. In order to analyse the information about surface-adsorbate interactions contained within the NMRD profiles, it is necessary to apply a theoretical model.

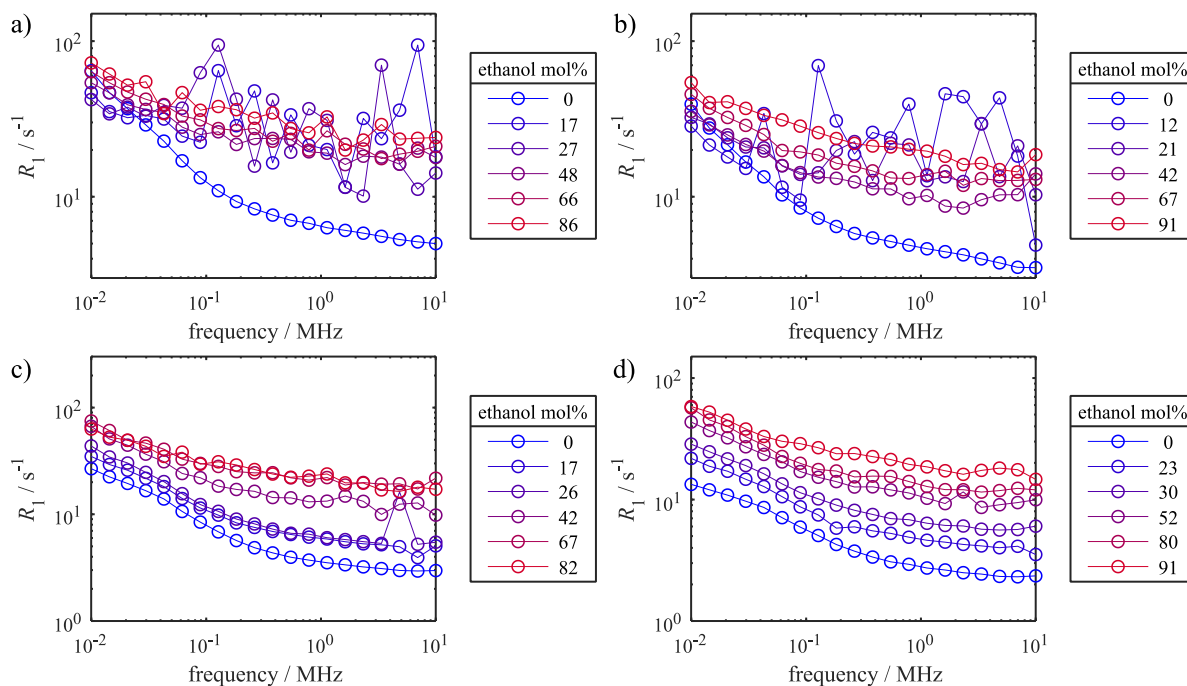


Figure 9.2:  $^1\text{H}$  NMRD profiles of the water component in ethanol-water mixtures imbibed within (a) Q6, (b) Q10, (c) Q15, and (d) Q30 silica, obtained using the FID-FFC-NMR pulse sequence.

While the NMRD profiles for all mixtures in Q15 and Q30 silica (Figure 9.2c-d) look reasonably smooth, and can therefore be modelled, the NMRD profiles for the low-ethanol mixtures in Q6 and Q10 silica (Figure 9.2a-b) are extremely noisy, which means that a data interpretation in terms of surface-adsorbate interactions is impossible.

The reason for these noisy NMRD profiles is that the water and ethanol  $T_1$  components are too similar and therefore overlap. This explanation is confirmed by an inverse Laplace transform analysis shown in Figure 9.3. The 86:14% ethanol-water mixture clearly shows two separate  $T_1$  environments, whereas for the 27:73% mixture, at many frequency points, only one  $T_1$  environment is visible.

Following the results in chapter 7, where the  $T_1/T_2$  components could be easily separated for all mixtures in all silica supports, it is expected that the NMRD profiles of the water and ethanol components can be separated based on their  $T_2$  values. Therefore, the CPMG-FFC-NMR pulse sequence that was introduced in chapter 8 is applied.

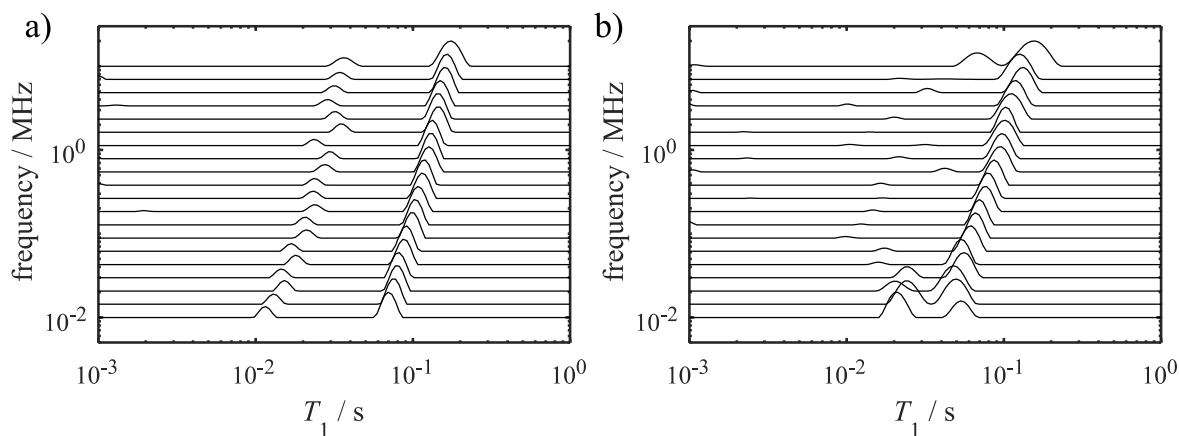


Figure 9.3:  $T_1$  inverse Laplace transform plots at each frequency point of (a) 86:14% and (b) 27:73% ethanol-water mixtures imbibed within Q6 silica.

### 9.3.2 CPMG-FFC-NMR experiments

#### 9.3.2.1 Validation: a comparison of FID and CPMG acquisition

In order to validate the CPMG-FFC-NMR experiment on the current systems, the pure water NMRD profiles using CPMG acquisition are compared to the FID-FFC-NMR experiments, see Figure 9.4.

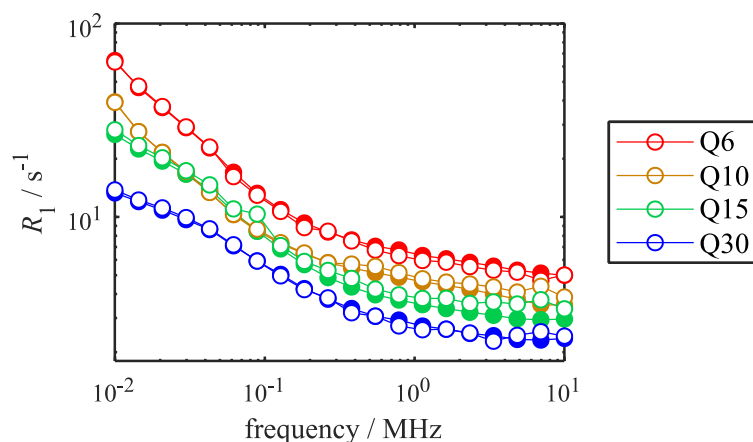


Figure 9.4:  $^1\text{H}$  NMRD profiles of pure water imbibed within silicas, obtained using the FID-FFC-NMR pulse sequence (filled symbols) and using the CPMG-FFC-NMR pulse sequence (open symbols).

For all silica supports, the pure water profiles using FID and CPMG acquisition match reasonably well, especially towards the lower frequency end. At the higher frequency end, the highest difference between the FID and CPMG profiles is approximately 16%, which is significant, even if a 10% error is accepted based on the inhomogeneity of the supports. However, the changes in the NMRD profiles as a function of the mixture composition are much larger, as was shown in Figure 9.2. Therefore, the CPMG-FFC-NMR experiments are considered accurate enough for the current study.

Additionally, the FID- and CPMG-acquired profiles for the water component in ethanol-water mixtures are compared. Figure 9.5 shows the water component profile in the 86:14% ethanol-water mixture imbibed within Q6 silica, and the 91:9% ethanol-water mixture in Q30 silica. These were the mixtures with the highest ethanol content, for which the FID-FFC-NMR pulse sequence was able to distinguish the water and ethanol components. The results for Q10 and Q15 silica are not shown in Figure 9.5 for clarity, although the results were equivalent.

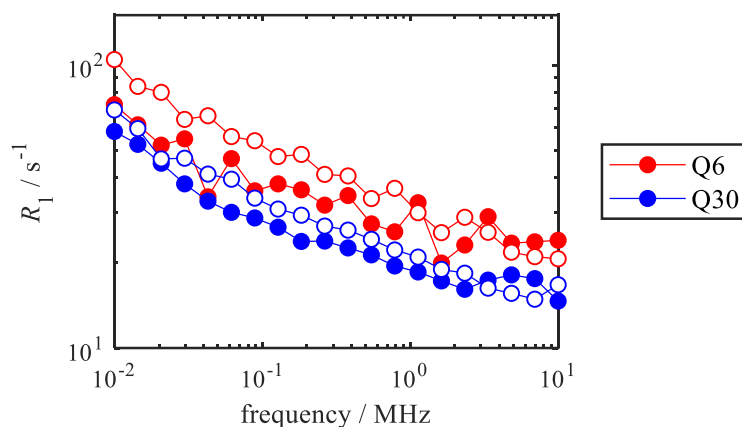


Figure 9.5:  $^1\text{H}$  NMRD profiles of the water component in the 86:14% ethanol-water mixture imbibed within Q6 silica, and the 91:9% ethanol-water mixture in Q30 silica, obtained using the FID-FFC-NMR pulse sequence (filled symbols) and using the CPMG-FFC-NMR pulse sequence (open symbols).

There are clear differences between the FID- and CPMG-acquired NMRD profiles. The CPMG relaxation rates are up to 30% higher than the FID relaxation rates. There are two explanations for this. First, this could be a real error, in which case, the CPMG-FFC-NMR pulse sequence is not accurate enough to measure the NMRD profiles of the mixtures in this study.

Alternatively, the error lies with the FID-NMRD profiles. Even though the ethanol and water components appeared to be separated successfully for the mixtures shown in Figure 9.5, this separation may not be perfect. This hypothesis is supported by the good agreement between the FID- and CPMG-NMRD profiles of pure water shown in Figure 9.4, and by the difference between the Q6 and Q30 results. The differences between the FID- and CPMG-acquired relaxation rates in Q30 silica in Figure 9.5 are approximately 15%, whereas the differences for Q6 silica are approximately 30%. Based on the NMRD profiles in Figure 9.2, the ethanol and water components could be distinguished more easily in Q30 than in Q6 silica, and therefore we would expect a better overlap of FID- and CPMG-methods for Q30 than Q6 silica. Based on these observations, we conclude that the latter explanation is more likely, and therefore the CPMG-FFC-NMR pulse sequence is adequately accurate for the current study.

### 9.3.2.2 Mixture NMRD profiles

The NMRD profiles of the water component in the ethanol-water mixtures, obtained using the CPMG-FFC-NMR sequence, are shown in Figure 9.6. The NMRD profiles for Q6 and Q10 silica using CPMG acquisition appear much smoother than the FID-acquired profiles shown in Figure 9.2a-b, suggesting that the  $T_2$ -encoded acquisition facilitated the goal of distinguishing the  $T_1$  components of ethanol-water mixtures in silicas.

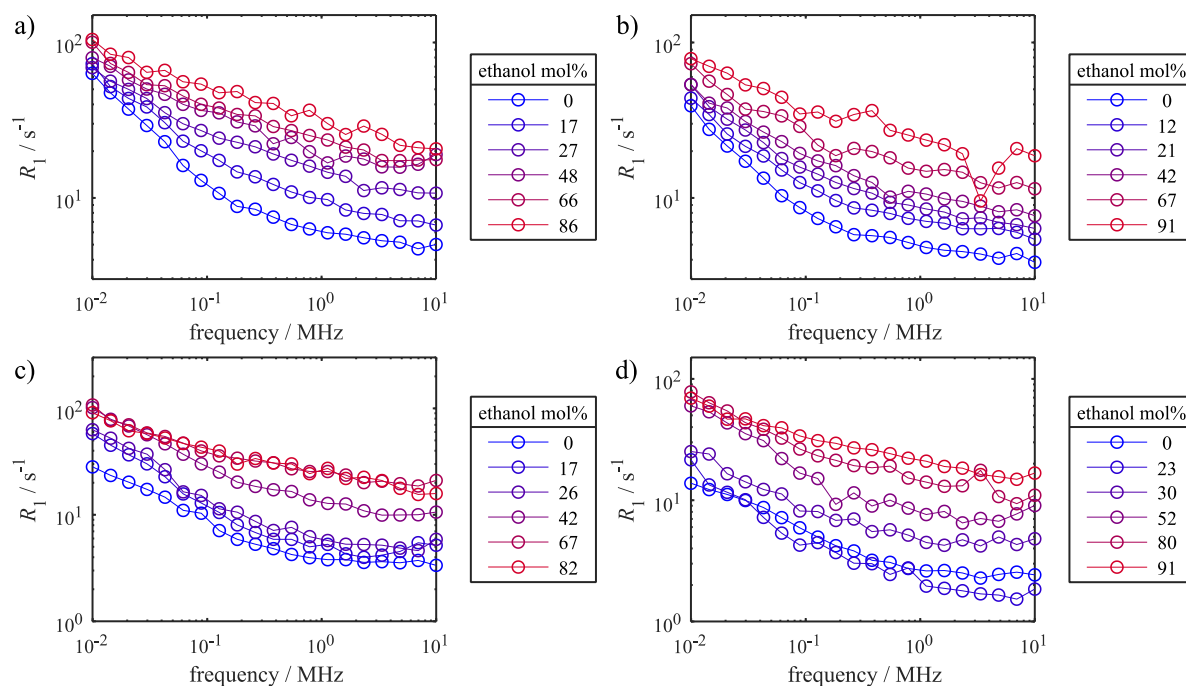


Figure 9.6:  $^1\text{H}$  NMRD profiles of the water component in ethanol-water mixtures imbibed within (a) Q6, (b) Q10, (c) Q15, and (d) Q30 silica, obtained using the CPMG-FFC-NMR pulse sequence.

The quality of the Q15 and Q30 profiles, however, is less when CPMG-acquisition is used compared to the 1D FID experiments. This is especially evident for the 23% ethanol mixture in Q30 silica, where the relaxation rates of the water component in the mixture are lower than those of the pure water, see Figure 9.6d. Based on the NMRD profiles in Figure 9.2, and the other profiles in Figure 9.6, it is expected that the relaxation rate of the water component increases with the ethanol composition. It appears that the NMRD profile of the 23% ethanol mixture shown in Figure 9.6 is between the true water and ethanol profiles, suggesting that the components cannot be accurately distinguished.

The reason for the poor separation of the water and ethanol components in this mixture is due to similar  $T_2$  values. Figure 9.7 shows the  $T_2$  fits to the 91% and 23% ethanol mixture CPMG decays for Q30 silica. For the 91% mixture, the  $T_2$  components are significantly different and therefore can be easily separated. However, for the 23% mixture, the short  $T_2$  component is much longer compared to the 91% mixture, and the  $T_2$  values are much more similar. This leads to inaccuracies in the  $T_2$  fits and therefore in inaccuracies in the  $T_1$  fits and NMRD profiles.

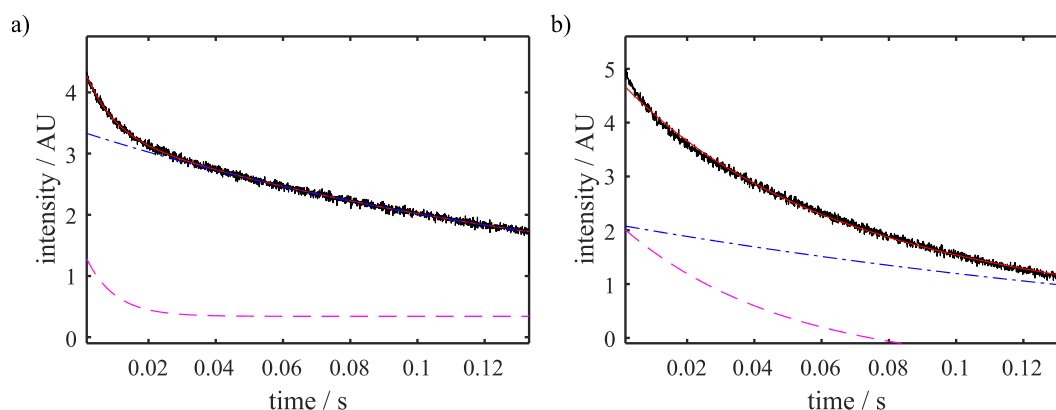


Figure 9.7:  $T_2$  fits to the CPMG decays of (a) the 91% ethanol mixture, and (b) the 23% ethanol mixture imbibed within Q30 silica.

To avoid artefacts due to similar  $T_2$  values, for further analysis and modelling, the CPMG-acquired NMRD profiles will be used for the Q6 and Q10 silicas only, and the FID-acquired NMRD profiles will be used for Q15 and Q30 silica.

## 9.4 Modelling

As was shown in sections 3.2.3 and 5.4, NMRD profiles can be fitted to many different types of theoretical models. For simple bulk liquids, the BPP model can be used<sup>8</sup>. For liquids in porous media, complex models can be applied such as the Korb model<sup>9,10</sup>, the  $3\tau$  model<sup>11</sup>, the Levitz<sup>12–14</sup> and Kimmich<sup>15,16</sup> type RMTD models, and many more models that are being developed.

One difficult aspect of applying these models is choosing the most appropriate model for the investigated system. In order to do this, it is important to identify the relaxation mechanism, for which variable temperature FFC-NMR experiments can be used<sup>17</sup>. For more details about variable temperature FFC-NMR and relaxation mechanisms, see section 5.4.3.

Figure 9.8 shows the results for the variable temperature FFC-NMR experiments on pure water in Q6 silica. It is assumed that the relaxation behaviour for water in all silicas is dominated by the same mechanism, thus the variable temperature results can be extrapolated to the other silica supports.

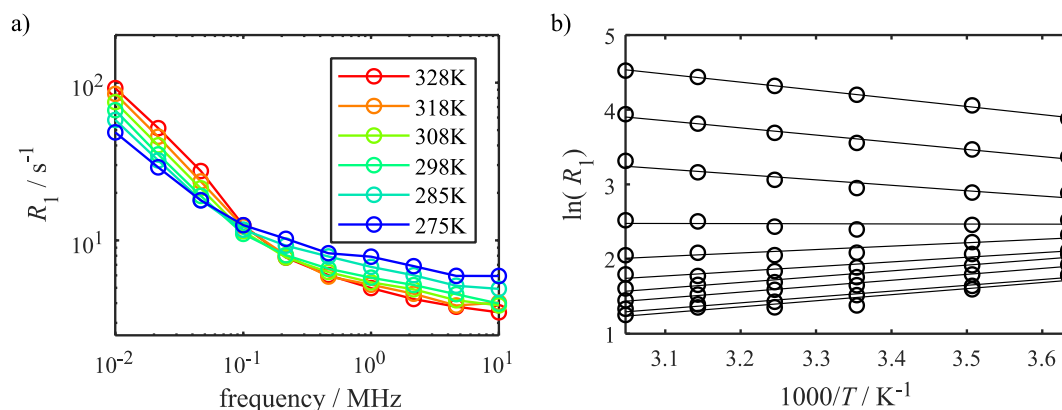


Figure 9.8: (a)  $^1H$  NMRD profiles of pure water imbibed within Q6 silica as a function of temperature, and (b) its corresponding Arrhenius plot.

At the high frequency end, the relaxation rate increases as the temperature decreases, following a bulk-like temperature dependence. Toward the lower frequency end, the temperature dependence inverts and the relaxation rate increases as the temperature increases. The inversion of the temperature dependence is indicative of a protic relaxation mechanism, which is based on the exchange or cross relaxation between water and surface hydroxyl groups. Identical relaxation behaviour has been seen previously for other silica systems imbibed with water<sup>9,18</sup>. As a result, it can be concluded with certainty that the dominant interaction mechanism between water and the surface is exchange with the surface hydroxyl groups.

Two modelling methods have been found for water-silica systems that are consistent with the protic relaxation mechanism<sup>7,18</sup>. For the first, the NMRD profiles followed a power law-like trend and the model was based on the interaction of water with paramagnetic ferric ions<sup>18</sup>. A power law will not very well describe the NMRD profiles shown in Figure 9.1a, as the profiles do not appear to be a straight line in a plot with logarithmic frequency and relaxation rate axes. Therefore, we consider the second method.

In the approach by Chemmi *et al.*, the NMRD profiles of water imbibed within different types of silica supports were fitted to a linear combination of two spectral densities, representing slow and fast processes respectively<sup>6</sup>. In essence, the approach by Chemmi *et al.* is a simplified version of the Korb model as previously presented in sections 3.2.3 and 5.4.1.1. This means that the underlying relaxation mechanism is based on the interaction of <sup>1</sup>H spins in the probe liquid with paramagnetic impurities in the support<sup>9,19</sup>. For the fast and slow processes, the autocorrelation function describes the loss of the dipolar correlation while the molecules undergo surface diffusion:

$$G(t) = \frac{\tau_m}{|\tau|} \left[ 1 - \exp\left(\frac{|\tau|}{\tau_m}\right) \right], \quad (9.1)$$

where  $\tau_m$  corresponds to the translational correlation time<sup>19</sup>. Following a Fourier Transform, the spectral density has the following form:

$$J(\omega) = \tau_m \ln \left[ 1 - \frac{1}{(\omega/\tau_m)^2} \right]. \quad (9.2)$$

The Chemmi *et al.* model fits to the pure water NMRD profiles are shown in Figure 9.9.

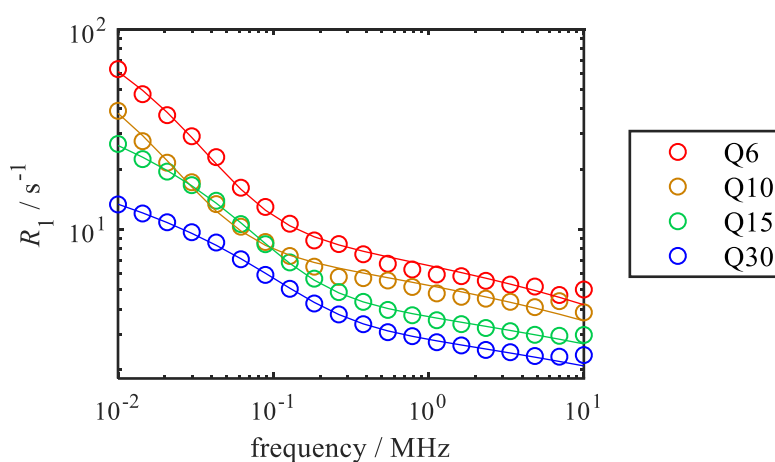


Figure 9.9: <sup>1</sup>H NMRD profiles of pure water in silicas, and their corresponding Chemmi *et al.* model fits.

The model appears to describe the profiles very well. A range of initial parameters was used to test the reliability of the model. The correlation time of the fast component appears to depend on the initial parameters reasonably heavily. This component contains information about fast processes, for the mixtures we are investigating this includes bulk mixing effects. The slow component on the other hand provides us with information about the surface-adsorbate interactions, which is the topic of the current study. The correlation time of the slow component did not significantly vary with initial parameters, indicating that this component can be modelled robustly, i.e. independent of other model parameters.

Subsequently, the NMRD profiles of the water component in ethanol-water mixtures were fitted to the Chemmi *et al.* model, see Figure 9.10. For all mixtures, the Chemmi *et al.* model appears to describe the water NMRD profiles very well, and again, the correlation time of the slow component could be extracted in a reliable manner, as it stayed constant with different input parameters.

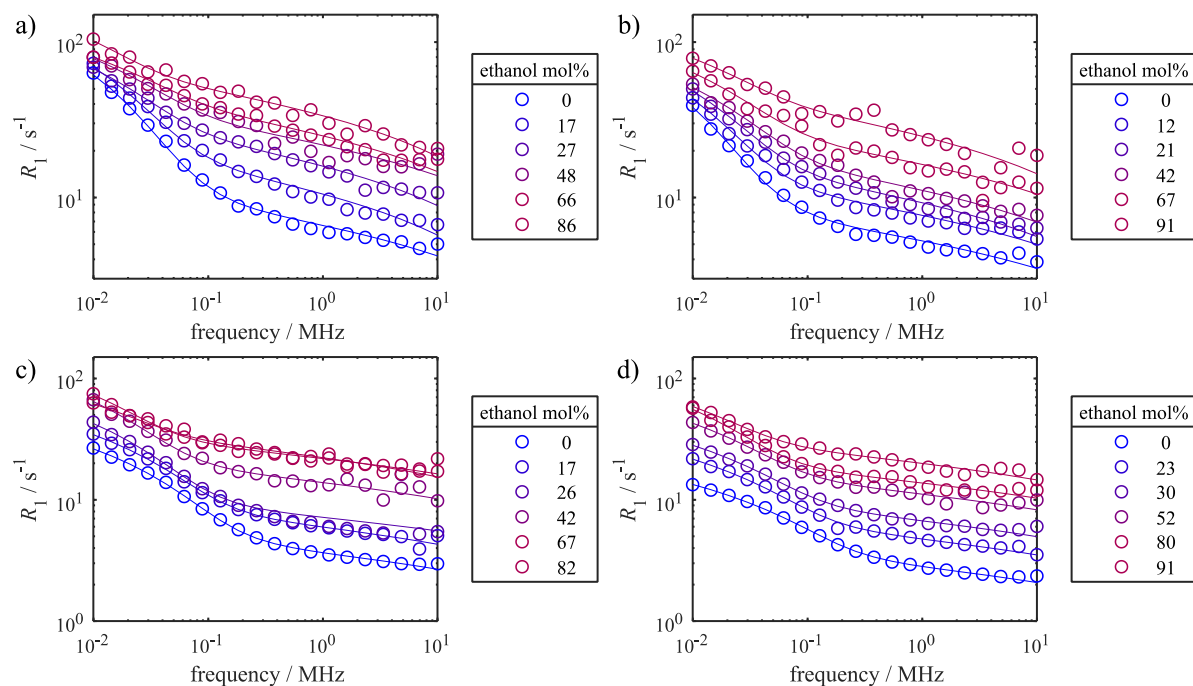


Figure 9.10:  $^1H$  NMRD profiles of the water component in ethanol-water mixtures imbibed within (a) Q6, (b) Q10, (c) Q15, and (d) Q30 silica, and their corresponding Chemmi model fits.

In order to investigate microphase separation, the correlation time of the slow component,  $\tau_m(\text{slow})$ , was plotted against the mixture composition, see Figure 9.11a. The slow correlation times are in the order of microseconds, which corresponds to the slow correlation times as reported by Chemmi *et al.*<sup>6</sup>, as well as previously reported surface diffusion correlation times,  $\tau_l$  extracted from the  $3\tau$  model<sup>11</sup>. As such, the correlation times presented in Figure 9.11a are considered to be physically sensible. Interestingly, these correlation times are significantly longer than the correlation times presented for alcohols and THF in chapters 5 and 6, as these were in the order of nanoseconds.

The correlation times were also normalized against the pure water correlation time, see Figure 9.11b, to allow for a straightforward comparison between the different silica supports. For Q15 and Q30 silica, the slow water correlation times increase as the ethanol composition increases, indicating that an average water molecule resides at the surface longer when there is less water in the system. This is consistent with microphase separation with water at the surface and

ethanol in the centre of the pore. For Q6 and Q10 silica, an opposite trend can be seen; the water correlation times decrease with ethanol composition, suggesting water resides in the centre of the pore and there is an ethanol-rich surface layer. The  $\tau_m(\text{slow})$  for Q10 silica appears to plateau for ethanol compositions  $>40$  mol%, however this is likely a fit error, as these NMRD profiles are reasonably noisy, see Figure 9.10b.

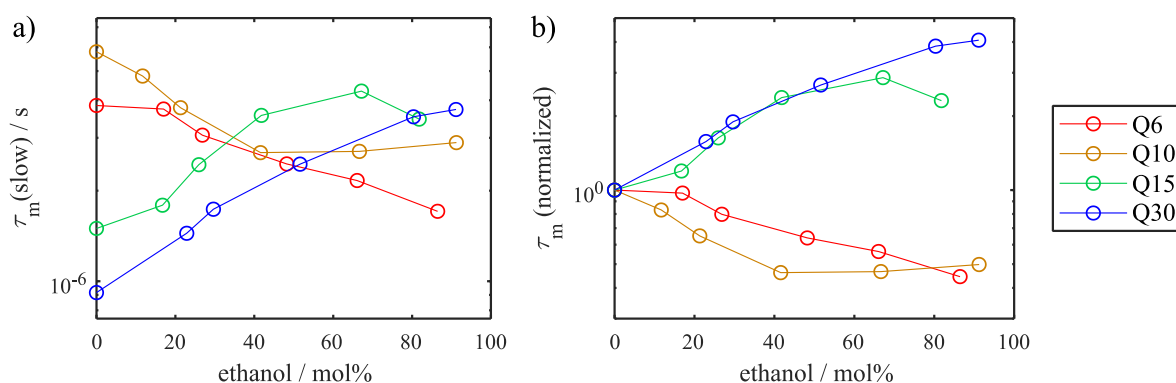


Figure 9.11: (a) Absolute and (b) normalized correlation times of the slow process, extracted from the Chemmi model fits, plotted against the mixture composition.

There is excellent agreement between the  $\tau_m(\text{slow})$  results and the fixed field  $T_1/T_2$  ratios of the water component of ethanol-water mixtures in the as-received silicas, shown in Figure 7.5. This reassures us that the results from both techniques are interpreted in an appropriate manner. Thereby we conclude that FFC-NMR experiments followed by modelling using the Chemmi approach is a valid method in terms of investigating microphase separation of ethanol-water mixtures imbibed within porous silicas.

The FFC-NMR method is much more complex and time consuming than the fixed field  $T_1 - T_2$  correlation experiments, in terms of data acquisition, especially when the CPMG-FFC-NMR sequence is used, data processing, modelling and interpretation. However, comparing the  $T_1/T_2$  ratios of different liquid mixtures in different supports is not a straightforward task, as the fixed field  $T_1$  and  $T_2$  values are highly dependent on the system characteristics. The FFC-NMR method on the other hand allows for a quantitative analysis of the dynamics in the form of correlation times. Under the assumption that the experiments are performed in an adequately accurate manner, and that an appropriate modelling method is chosen, correlation times are independent of the investigated system. This means that the same FFC-NMR method can be applied to different supports and liquid mixtures, and the extracted correlation times can be easily compared.

## 9.5 Conclusions and outlook

In chapter 7, the microphase separation of ethanol-water mixtures imbibed within silicas was investigated. Based on fixed field  $T_1 - T_2$  correlation experiments, it was concluded that for the larger pore silicas with high surface hydroxyl densities, the liquids phase segregated into a water-rich surface layer and an ethanol-rich pore centre. For smaller pore silicas with low surface hydroxyl densities, inverse microphase separation occurred, resulting in an ethanol-rich surface layer and water residing in the centre of the pore.

However, the ultimate goal was to gain quantitative insight into the dynamics and competitive adsorption of these liquids imbibed within porous media. For fixed field NMR relaxometry experiments, this is not straightforward, as the relaxation times depend strongly on the environment, and not only on the surface-adsorbate interactions. Therefore, in this chapter, FFC-NMR is used to obtain translational correlation times, which are a direct probe for the surface dynamics.

A typical FFC-NMR experiment with FID acquisition was not able to provide two relaxation environments for all mixtures, because the water and ethanol  $T_1$  relaxation times were too similar. Consequently, the CPMG-FFC-NMR pulse sequence that was optimized in chapter 8 was used to provide enhanced resolution through  $T_2$ -encoding. A comparison of FID- and CPMG-acquired NMRD profiles of pure water in the silica supports confirmed that the  $T_1$  values measured using CPMG acquisition were sufficiently accurate for the current study.

Subsequently, the CPMG-NMRD profiles of the water-ethanol mixtures were compared to their FID-acquired equivalents, and it was concluded that the  $T_2$ -encoding facilitated the resolution of two  $T_1$  relaxation environments in Q6 and Q10 silica. For Q15 and Q30 silica, the quality of the FID-NMRD profiles was higher than that of the CPMG-NMRD profiles, and therefore further analysis was performed on the FID-NMRD profiles for these supports.

In order to identify an appropriate modelling method, the relaxation mechanism of pure water in Q6 silica was determined through variable temperature FFC-NMR experiments. A distinctive inversion of the temperature behaviour confirmed that the dominant relaxation mechanism is based on the exchange between water and the surface hydroxyl groups of the silicas.

Following the determination of the relaxation mechanism, the NMRD profiles were modelled according to the approach of Chemmi *et al.*, which provided a fast and slow translational correlation time. In this model, the fast component is essentially a fit parameter and does not provide physically sensible correlation times. However, the model provided slow correlation times that were independent of the fast component. Moreover, the slow correlation times were found to be in the order of microseconds, which is consistent with surface diffusion correlation times presented in the literature, and therefore considered reliable and physically sensible. The slow correlation time was also shown to display identical behaviour as the fixed field water  $T_1/T_2$  ratios measured in chapter 7, confirming the chemistry of the system as described in that chapter, and validating the FFC-NMR approach in this chapter for the investigated systems.

Finally, it was concluded that while the FFC-NMR approach was more complex and challenging, the ability to determine correlation times is a clear advantage over other techniques, including fixed field NMR relaxometry. This is because correlation times are not constrained by which liquid mixtures or supports are investigated, and therefore the competitive adsorption of different systems can be compared in a straightforward manner.

## References

1. Neudert, O., Mattea, C. & Stapf, S. Application of CPMG acquisition in Fast-Field-Cycling relaxometry. *Microporous Mesoporous Mater.* **269**, 103–108 (2018).
2. Steele, R. M., Korb, J.-P., Ferrante, G. & Bubici, S. New applications and perspectives of fast field cycling NMR relaxometry. *Magn. Reson. Chem.* **54**, 502–509 (2016).
3. Ferrante, G. & Sykora, S. Technical aspects of Fast Field Cycling. *Adv. Inorg. Chem.* **57**, 405–470 (2005).
4. Sykora, S. Field noise effects on NMR signals: FID's and 1D spectra. *Stan's Library* (2006). doi:10.3247/SL1Nmr06.002
5. Sykora, S. Field noise effects on NMR signals: Hahn echoes and CPMG. *Stan's Library* (2006). doi:10.3247/SL1Nmr06.003
6. Chemmi, H. , Petit, D., Levitz, P., Denoyel, R., Galarneau, A. & Korb, J.-P. Noninvasive experimental evidence of the linear pore size dependence of water diffusion in nanoconfinement. *J. Phys. Chem. Lett* **7**, 45 (2016).
7. Robertson, C. I. Characterising adsorption and mass transfer in porous media. (Doctoral thesis, University of Cambridge, 2017).
8. Bloembergen, N., Purcell, E. M. & Pound, R. V. Relaxation effects in nuclear magnetic resonance absorption. *Phys. Rev.* **73**, 679–712 (1948).
9. Korb, J.-P. Multiscale nuclear magnetic relaxation dispersion of complex liquids in bulk and confinement. *Prog. Nucl. Magn. Reson. Spectrosc.* **104**, 12–55 (2018).
10. Korb, J. P., Freiman, G., Nicot, B. & Ligneul, P. Dynamical surface affinity of diphasic liquids as a probe of wettability of multimodal porous media. *Phys. Rev. E* **80**, 061601 (2009).
11. Faux, D. A. & McDonald, P. J. A model for the interpretation of nuclear magnetic resonance spin-lattice dispersion measurements on mortar, plaster paste, synthetic clay and oil-bearing shale. *Microporous Mesoporous Mater.* **269**, 39–42 (2018).
12. Levitz, P. Random flights in confining interfacial systems. *J. Phys. Condens. Matter* **17**, 4059–4074 (2005).

13. Levitz, P., Grebenkov, D. S., Zinsmeister, M., Kolwankar, K. M. & Sapoval, B. Brownian flights over a fractal nest and first-passage statistics on irregular surfaces. *Phys. Rev. Lett.* **96**, 180601 (2006).
14. Levitz, P., Zinsmeister, M., Davidson, P., Constantin, D. & Poncelet, O. Intermittent Brownian dynamics over a rigid strand: heavily tailed relocation statistics in a simple geometry. *Phys. Rev. E* **78**, 030102 (2008).
15. Zavada, T. & Kimmich, R. The anomalous adsorbate dynamics at surfaces in porous media studied by nuclear magnetic resonance methods. The orientational structure factor and Lévy walks. *J. Chem. Phys.* **109**, 6929 (1998).
16. Kimmich, R. & Fatkullin, N. Self-diffusion studies by intra- and inter-molecular spin-lattice relaxometry using field-cycling: liquids, plastic crystals, porous media, and polymer segments. *Prog. Nucl. Magn. Reson. Spectrosc.* **101**, 18–50 (2017).
17. Ward-Williams, J. Korb, J.-P., Rozing, L. Sederman, A. J., Mantle, M. D. & Gladden, L. F. Characterizing solid-liquid interactions in a mesoporous catalyst support using variable-temperature Fast Field Cycling NMR. *J. Phys. Chem. C* **125**, 8767–8778 (2021).
18. Korb, J.-P., Whaley Hodges, M., Gobron, T. & Bryant, R. G. Anomalous surface diffusion of water compared to aprotic liquids in nanopores. *Phys. Rev. E* **60**, 3097–3106 (1999).
19. Godefroy, S., Korb, J.-P., Fleury, M. & Bryant, R. G. Surface nuclear magnetic relaxation and dynamics of water and oil in macroporous media. *Phys. Rev. E* **64**, 021605 (2001).



## 10. Conclusions and future work

### 10.1 Conclusions

The main objective of this thesis was to develop NMR relaxometry methods to gain insight into the competitive adsorption and microphase separation of binary liquid mixtures imbibed within mesoporous media. Fixed field NMR relaxometry methods were used in several chapters, however the primary method in this thesis is Fast Field Cycling (FFC) NMR. FFC-NMR is a promising tool to provide quantitative information about surface-adsorbate interactions in the form of correlation times. By measuring the  $T_1$  relaxation time across a large Larmor frequency range, molecular motions over a broad range of timescales can be investigated. As a result, it is possible to identify and describe the underlying relaxation mechanisms related to surface adsorption in a quantitative manner. Whilst FFC-NMR and other NMR relaxometry methods are continuously developed, literature examples describing the application of these methods to competitive adsorption and microphase separation remain scarce.

One of the reasons that the literature on FFC-NMR applied to liquid mixtures imbibed within porous media is so limited, and one of the main disadvantages to FFC-NMR, is the lack of spectral resolution, which complicates the application of multicomponent systems. However, previously it was shown that it is possible to distinguish different components by their relaxation behaviour<sup>1</sup>. The possibilities and challenges in obtaining reliable FFC-NMR data for multicomponent systems were examined in chapter 4. A case study on tetrahydrofuran (THF):water and THF-decane mixtures imbibed within anatase titania and  $\gamma$ -alumina was used to create a general approach towards these experiments, processing methods and their interpretation. The NMR dispersion or NMRD profiles for the THF, water and decane components in their respective mixtures were interpreted in a qualitative as well as a semi-quantitative manner. The slope of the NMRD profiles could be quantified in the form of a power law exponent, which showed that a microphase separation occurs for THF-water mixtures, where water binds strongly to the surface. For THF-decane mixtures, THF is the stronger interacting species. The FFC-NMR results were also compared with high field  $T_{1,\text{bulk}}/T_{1,\text{pore}}$  measurements, from which it was concluded that FFC-NMR provides information that is more reliable and more difficult to misinterpret than high field relaxometry.

In chapter 5, a theoretical approach was described to characterize the dynamics of short, linear alcohols imbibed within anatase titania, in order to gain fully quantitative information in the form of correlation times. Several widely applied FFC-NMR models for liquids in porous media were discussed, and following a variable temperature FFC-NMR study, it could be concluded that the NMRD profiles of alcohols imbibed within anatase titania could be appropriately described by a Levitz-type Reorientations Mediated by Translational Diffusion (RMTD) model. Several methods of applying the RMTD model were used to verify the reliability of the model. The adsorption correlation time,  $\tau_A$ , could be extracted from the RMTD model fits to the NMRD profiles, and correlated very well with the polarity of the alcohols, which reflects the surface-adsorbate interaction strength. Thereby it was concluded that the modelling approach was valid.

Based on the work in chapter 5, the RMTD modelling approach was used to investigate the microphase separation of alcohol-water mixtures imbibed within anatase titania in chapter 6. A qualitative analysis illustrated that water is the stronger interacting species in all alcohol-water mixtures imbibed within anatase titania. However, the application of the RMTD model to the alcohol component NMRD profiles provided quantitative information about the extent of microphase separation for each of the mixtures. The surface-to-volume ratio,  $N_S/N$ , and the adsorption correlation time,  $\tau_A$ , are correlated within the RMTD model. Therefore, the product  $\frac{N_S}{N} \times \tau_A$  was analysed. The  $\frac{N_S}{N} \times \tau_A$  values decreased with the water composition for all alcohols. This effect scaled with the alcohol chain length, independently of the bulk alcohol-water solubility. Therefore, it was concluded that the level of microphase separation depends on the surface-adsorbate interaction strength of the weaker interacting species, in this case the alcohols, and not on the bulk miscibility. Finally, the  $\frac{N_S}{N} \times \tau_A$  values were deconstructed to obtain estimates for the surface-to-volume ratio as a function of mixture composition, as well as the adsorption correlation times. The adsorption correlation times provide quantitative information about the dynamics of a confined binary liquid system, which has not yet previously been reported, to the best of the author's knowledge.

In chapter 7, a different type of mesoporous material was introduced, namely a series of silicas with pore sizes ranging between 3–30 nm and with varying surface chemistries. The literature on the microphase separation of ethanol-water mixtures in similar silicas contradicted each other; one study concluded that water is the stronger interacting species<sup>2</sup>, however other investigations have reported that ethanol binds strongly to the surface<sup>3,4</sup>. This chapter sought

to elucidate the discrepancies in the literature through fixed field  $T_1 - T_2$  correlation experiments. Initially, the experiments were performed at high field ( $\omega_0 = 400$  MHz). The  $T_1/T_2$  ratios for the water and ethanol components in 10 and 15 nm pore size silicas were consistent with one of the previously mentioned studies, from which it was concluded that water adsorbs onto the surface<sup>2</sup>. Unfortunately, the ethanol and water signals could not be separated for smaller pore size (6 nm) silicas. Therefore, the experiments were repeated at low field ( $\omega_0 = 43$  MHz). For the 15 nm pore size silica, the low field results were in agreement with the high field results. For the 6 and 10 nm silicas however, the trend in the  $T_1/T_2$  ratio of the water component was inverted, and therefore it was concluded that for these silicas, the surface layer was ethanol-rich, which is consistent with the other studies previously mentioned<sup>3,4</sup>. As both forms of microphase separation were observed, it was concluded that the discrepancy found in the literature is caused by different silica characteristics, such as the pore size and the surface chemistry. A rehydroxylation study sought to clarify whether the pore size or the surface hydroxyl density is the main cause for the microphase separation behaviour, however due to the harshness of the rehydroxylation method, the pore size and surface hydroxyl density could not be properly controlled and therefore it is not possible to definitively conclude which of the silica properties controls the microphase separation behaviour. Another important conclusion from this chapter is that the high and low field  $T_1 - T_2$  correlation experiments showed different results. It was shown that at high field, the water  $T_1$  relaxation time is affected not only by the surface-adsorbate interactions, but also by the disruption of the water hydrogen network caused by the addition of ethanol. At low field, the relaxation behaviour is dominated by the adsorption dynamics, and therefore these results provide a less ambiguous result which is more difficult to misinterpret.

Chapters 8 and 9 were focused on describing the ethanol-water mixtures imbibed within silicas quantitatively by means of FFC-NMR. However, the acquisition of FFC-NMR data for ethanol-water mixtures imbibed within these silicas was more complex than for the previously studied titania and  $\gamma$ -alumina systems, therefore a FFC-NMR pulse sequence with CPMG acquisition was optimized in chapter 8. This pulse sequence, previously used to obtain “ $T_2$ -Encoded Acquisition of Relaxation Dispersion for Resolution of Pore Sizes” (TEARDROPS)<sup>5</sup>, allows for different environments to be distinguished based on their  $T_2$  relaxation times, rather than their  $T_1$  values. The implementation of this pulse sequence required a characterization of the field noise effects that can cause artefacts in both the  $T_1$  and  $T_2$  domains. It was shown that the 10 mm probe used in previous chapters was damaged in experiments unrelated to this thesis,

which meant that this probe was unsuitable for CPMG-FFC-NMR experiments. However, validation experiments were performed on a 5 mm probe and the field fluctuations were deemed sufficiently small to obtain reliable data. The effect of the echo delay,  $\delta$ , was investigated and it was shown that field noise effects could not be effectively refocused for echo delays  $\geq 100 \mu\text{s}$ . Finally, CPMG-FFC-NMR experiments were performed on doped water samples. The  $T_2$  values were compared to  $T_2$  relaxation times obtained on a permanent magnet, and the  $T_1$  values were compared to the standard FFC-NMR sequence with FID acquisition. From these experiments, it was concluded that the errors were sufficiently small, such that the CPMG-FFC-NMR pulse sequence can accurately obtain NMRD profiles for liquids imbibed within porous media.

Finally, in chapter 9, the CPMG-FFC-NMR pulse sequence was applied to ethanol-water mixtures imbibed within silicas. A comparison was made for the FID- and CPMG-acquired NMRD profiles of pure water in the silica supports, which showed that the CPMG-FFC-NMR experiment was sufficiently accurate for these systems. A similar comparison was made for the ethanol-water mixtures, which showed that  $T_2$ -encoding indeed facilitated the resolution of two  $T_1$  relaxation environments in the 6 and 10 nm silicas. For the 15 and 30 nm silica, two relaxation components could be distinguished already using FID-acquisition, and these NMRD profiles were used for further analysis. Similarly to the alcohols imbibed within anatase titania shown in chapter 5, the relaxation mechanism of water in silica was determined through variable temperature FFC-NMR experiments. Based on the relaxation mechanism, the NMRD profiles were modelled according to the approach of Chemmi *et al.*<sup>6</sup> From this model, a fast and slow correlation time were extracted, and the slow correlation time was shown to display identical behaviour as the low field  $T_1/T_2$  ratios for the water component shown in chapter 7. Therefore, the current FFC-NMR approach was considered to be validated. Whilst the FFC-NMR experiments were more complex, time-consuming and challenging than the fixed field  $T_1 - T_2$  correlation experiments, its ability to provide correlation times is a distinct advantage over other techniques, as correlation times are not constrained by the system, therefore allowing a straightforward comparison of the competitive adsorption of different liquids in different porous media.

## 10.2 Future work

The chapters in this thesis have described approaches to investigating competitive adsorption and microphase separation of binary liquid mixtures imbibed within mesoporous media using FFC-NMR and other NMR relaxometry methods. Therefore, extensions to this work are considered in three directions:

- Different types of liquid mixtures, such as catalytically relevant binary mixtures, or the investigation of more components, for example in ternary mixtures;
- Different types of porous media, for example by extending the current work to include the effect of paramagnetic impurities on the surface, or investigating microporous media such as zeolites;
- The development of FFC-NMR for liquids in porous media, to investigate how more reliable or more complete quantitative information can be extracted from these experiments.

### 10.2.1 Different types of liquid mixtures

The liquid mixtures investigated in this thesis were limited to THF-water, THF-decane, and alcohol-water mixtures. Therefore, a natural extension of this work is to apply the presented methods to other types of liquid mixtures. Notably, there are two directions to investigate. First, binary liquid mixtures that are directly relevant to the chemical industry should be investigated. Secondly, more complex systems could be investigated. Many processes relevant to chemical industry involve more than two chemical components, and as such, it would be beneficial to investigate liquid mixtures with three or more components. Figure 10.1 shows the NMRD profiles of a THF-water-pyridine mixture imbibed within anatase titania. This ternary mixture experiment was performed as a proof of principle, and shows that it is indeed possible to distinguish three relaxation environments using FFC-NMR, assuming the  $T_1$  values are sufficiently dissimilar. However, the competitive adsorption of the three components in this mixture was not investigated in the current work.

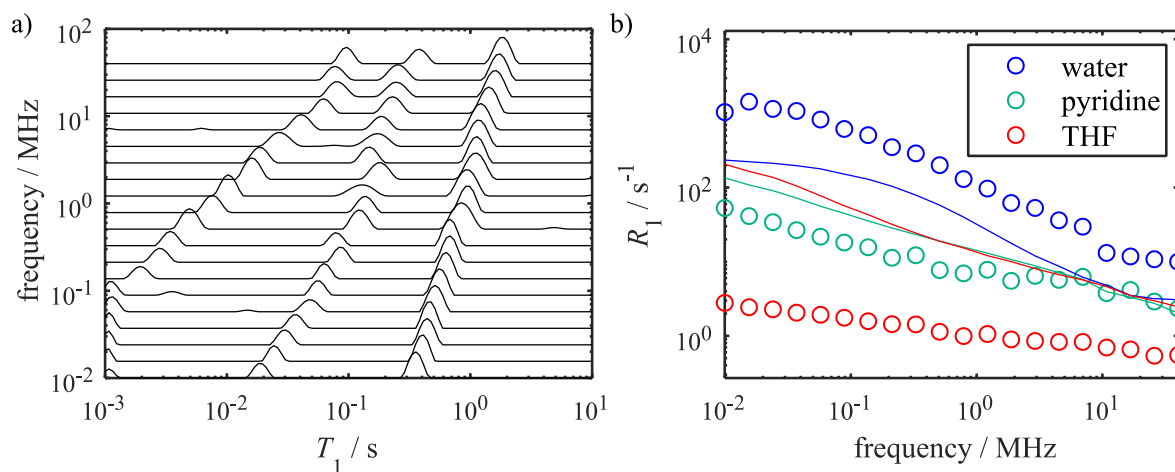


Figure 10.1: a) The inverse Laplace transform and b)  $^1\text{H}$  NMRD profiles of a THF-water-pyridine mixture imbibed within anatase titania. For the NMRD profiles, the lines correspond to the pure water (blue), pyridine (green) and THF (red) profiles, and the circles correspond to their respective mixture components.

### 10.2.2 Different types of porous media

Of course, as the liquid mixtures in this thesis were limited, so were the types of porous media. While the FFC-NMR methods were applied to different species of mesoporous metal oxides, it has been shown that the porous material characteristics significantly affect the relaxation behaviour, as is expected. This was especially clear for the silica studies in chapters 7–9, where the pore size and surface chemistry of the silicas completely altered the microphase separation behaviour of ethanol-water mixtures. Another property of porous materials that was not investigated in this thesis is the effect of paramagnetics on the surface. While paramagnetic impurities are included in the Korb model, and therefore frequently studied, investigations of competitive adsorption or microphase separation as a function of the paramagnetic impurities could be of great interest to the chemical industry, where paramagnetic species are often used as catalysts.

Another direction for future research is to develop FFC-NMR studies on liquids and liquid mixtures imbibed within microporous media, such as zeolites. FFC-NMR studies on zeolites are scarce in the literature<sup>7</sup>. Zeolites are difficult to pelletize, and therefore exist in powder form. As such, it is difficult to distinguish intra-pore liquid from inter-crystalline liquid. Therefore special sample preparation methods are required, which make the experiments challenging. However, zeolites remain some of the most used catalysts, and therefore it is necessary to increase our scientific knowledge about zeolites.

### 10.2.3 Development of FFC-NMR for liquids in porous media

Even though FFC-NMR is a greatly promising tool for obtaining information about the surface-adsorbate interactions of liquids imbibed within porous media, the technique requires much more development to fulfil its full potential. The studies in this thesis have clarified that, in the case of liquid mixture investigations, sometimes it is possible to distinguish different relaxation environments. However, the separation of relaxation environments is not always straightforward, and may require additional method development. For example, CPMG-FFC-NMR has been demonstrated to facilitate the resolution of multiple relaxation environments through  $T_2$ -encoding. However, the implementation of the technique is not straightforward and imposes significant limits on the investigated systems. As such, development is required to improve the stability and usability of this experiment.

Moreover, on fixed field NMR spectrometers, combining pulse sequences to obtain a 2D or 3D data set is a relatively common procedure. The CPMG-FFC-NMR pulse sequence has shown that this is also possible on FFC-NMR relaxometers. Therefore, the standard FFC-NMR pulse sequences could also be combined with other pulse sequences to obtain more information about the systems. An example of a promising combination that has been recently published is FFC-NMR with ultra-low field NMR<sup>8-10</sup>. In this combination, the frequency range of FFC-NMR is expanded by measuring  $T_1$  relaxation at Larmor frequencies as low as 10 Hz, thereby providing a more complete data set, which will improve the reliability of theoretical models fitted to the NMRD profiles. However, the main advantage of this combination in terms of competitive adsorption studies, is that ultra-low field NMR measures the J-coupling frequency of samples. Therefore, although the samples are limited to those that exhibit J-coupling, this means that different relaxation environments can be distinguished based on their respective J-coupling frequencies, providing chemical resolution to FFC-NMR data<sup>10</sup>.

## References

1. Ward-Williams, J. & Gladden, L. F. Insights into adsorption behaviour of binary liquid mixtures in porous media using fast field cycling NMR. *Magn. Reson. Imaging* **56**, 57–62 (2018).
2. Robertson, C. I. Characterising adsorption and mass transfer in porous media. (Doctoral thesis, University of Cambridge, 2017).
3. Muthulakshmi, T., Dutta, D., Maheshwari, P. & Pujari, P. K. Evidence for confinement induced phase separation in ethanol-water mixture: a positron annihilation study. *J. Phys. Condens. Matter* **30**, 025001 (2018).
4. Guo, X.-Y., Watermann, T. & Sebastiani, D. Local microphase separation of a binary liquid under nanoscale confinement. *J. Phys. Chem. B* **118**, 10207–10213 (2014).
5. Neudert, O., Mattea, C. & Stapf, S. Application of CPMG acquisition in Fast-Field-Cycling relaxometry. *Microporous Mesoporous Mater.* **269**, 103–108 (2018).
6. Chemmi, H., Petit, D., Levitz, P., Denoyel, R., Galarneau, A. & Korb, J.-P. Noninvasive experimental evidence of the linear pore size dependence of water diffusion in nanoconfinement. *J. Phys. Chem. Lett* **7**, 45 (2016).
7. Hsu, C.-W. Chen, Y.-W., Rana, B. S., Kumar, R., Sinha, A. K. & Hwang, D. W. Dynamics of water in hierarchical mesoporous H-ZSM-5 by Fast Field-Cycling NMR relaxometry. *J. Phys. Chem. C* **118**, 20481–20487 (2014).
8. Tayler, M. C. D., Ward-Williams, J. & Gladden, L. F. NMR relaxation in porous materials at zero and ultralow magnetic fields. *J. Magn. Reson.* **297**, 1–8 (2018).
9. Barskiy, D. A., Tayler, M. C. D., Marco-Rius, I., Kurhanewicz, J., Vigneron, D. B., Cikrikci, S., Aydogdu, A., Reh, M., Pravdivtsev, A. N., Hövener, J.-B., Blanchard J. W., Wu, T., Budker, D. & Pines, A. Zero-field nuclear magnetic resonance of chemically exchanging systems. *Nat. Commun.* **10**, 3002 (2019).
10. Bodenstedt, S., Mitchell, M. W. & Tayler, M. C. D. Fast-field-cycling ultralow-field nuclear magnetic relaxation dispersion. *Nat. Commun.* **12**, 4041 (2021).

## Appendix A: THF-water and THF-decane mixture compositions

Table A.1: THF-water mol% mixture compositions - anatase titania

Sample	Bulk	Intra-pellet (high field NMR)		Intra-pellet (FFC-NMR)	
		<sup>1</sup> H spectrum	$T_1$ fit	7 MHz	Average
1.1	20.0:80.0	11.5:88.5	11.1:88.9	8.2:91.8	8.4:91.6±0.8
1.2	20.0:80.0	13.3:86.7	11.9:88.1	-	-
1.3	19.8:80.2	-	-	13.3:86.7	14.8:85.2±1.5
2.1	49.6:50.4	26.9:73.1	28.8:71.2	-	-
2.2	50.5:49.5	33.2:66.8	31.7:68.3	-	-
2.3	49.9:50.1	-	-	32.1:67.9	38.0:62.0±6.0
2.4	49.7:50.3	-	-	30.9:69.1	36.3:63.7±5.7
3.1	69.1:30.9	50.0:50.0	46.7:53.3	-	-
3.2	69.3:30.7	41.1:58.9	46.4:53.6	-	-
3.3	67.7:32.3	-	-	47.4:52.6	53.5:46.5±11.6
4.1	82.5:17.5	59.2:40.8	57.3:42.7	-	-
4.2	82.6:17.4	56.0:44.0	61.7:38.3	-	-
4.3	81.8:18.2	-	-	61.2:38.8	42.2:57.8±71.3

Table A.2: THF-decane mol% mixture compositions - anatase titania

Sample	Bulk	Intra-pellet (high field NMR)		Intra-pellet (FFC-NMR)	
		<sup>1</sup> H spectrum	$T_1$ fit	7 MHz	Average
1.1	73.5:26.5	65.4:34.6	59.4:40.6	65.8:34.2	64.5:35.5±4.9
2.1	50.6:49.4	51.0:49.0	46.3:53.7	-	-
2.2	50.4:49.6	44.5:55.5	40.6:59.4	48.6:51.4	42.6:57.4±3.4
2.3	50.4:49.6	-	-	49.4:50.6	44.9:55.1±3.0
3.1	23.5:76.5	27.9:72.1	22.5:77.5	-	-
3.2	24.4:75.6	-	-	27.9:72.1	19.7:80.3±6.0

Table A.3: THF-water mol% mixture compositions -  $\gamma$ -alumina

Sample	Bulk	Intra-pellet (high field NMR)		Intra-pellet (FFC-NMR)	
		$^1\text{H}$ spectrum	$T_1$ fit	7 MHz	Average
1.1	20.0:80.0	9.9:90.1	11.0:89.0	7.6:92.4	7.9:92.1 $\pm$ 1.3
1.2	20.0:80.0	14.4:85.6	12.5:87.5	-	-
1.3	19.8:80.2	-	-	12.1:87.9	12.9:87.1 $\pm$ 0.8
2.1	49.7:50.3	24.1:75.9	20.9:79.1	21.5:78.5	23.1:76.9 $\pm$ 2.4
2.2	50.5:49.5	31.1:68.9	29.4:70.6	-	-
2.3	49.9:50.1	-	-	29.2:70.8	32.3:67.7 $\pm$ 2.9
3.1	69.1:30.9	46.1:53.9	42.0:58.0	-	-
3.2	69.3:30.7	45.3:54.7	44.6:55.4	-	-
3.3	67.7:32.3	-	-	44.8:55.2	51.5:48.5 $\pm$ 6.8
4.1	82.5:17.5	54.1:45.9	60.5:39.5	-	-
4.2	82.6:17.4	55.5:44.5	59.6:40.4	-	-
4.3	81.8:18.2	-	-	52.3:47.7	58.1:41.9 $\pm$ 7.1

Table A.4: THF-decane mol% mixture compositions -  $\gamma$ -alumina

Sample	Bulk	Intra-pellet (high field NMR)		Intra-pellet (FFC-NMR)	
		$^1\text{H}$ spectrum	$T_1$ fit	7 MHz	Average
1.1	73.5:26.5	74.3:25.7	68.0:32.0	70.4:29.6	68.4:31.6 $\pm$ 7.9
2.1	50.1:49.9	56.3:43.7	47.0:53.0	49.7:50.3	48.4:51.6 $\pm$ 5.6
2.2	50.6:49.4	59.7:40.3	56.3:43.7	-	-
2.3	50.4:49.6	-	-	52.0:48.0	51.1:48.9 $\pm$ 2.6
3.1	23.5:76.5	38.4:61.6	31.2:68.8	-	-
3.2	24.4:75.6	-	-	29.2:70.8	28.1:71.9 $\pm$ 2.6